Single-Molecule Magnets and Multifunctional Molecular Magnetic Materials Based on Polynuclear Metal Complexes

Dimitrios I. Alexandropoulos, MSc

PhD Chemistry

Submitted in partial fulfillment of the

requirements for the Degree of Doctor of Philosophy

Faculty of Mathematics and Science,

Brock University

St. Catharines, Ontario

Abstract

Our work on single molecule magnets and multifunctional magnetic materials is presented in four projects. In the first project we show for first time that heteroatomic-type pseudohalides, such as OCN^-, can be employed as structure-directing ligands and ferromagnetic couplers in higher oxidation state metal cluster chemistry. The initial use of cyanato groups in Mn cluster chemistry has afforded structurally interesting $Mn^{II/III}_{14}$ (**1**) and $Mn^{II/III/IV}_{16}$ (**2**) clusters in which the end-on bridging cyanates show a preference in binding through their O-atom. The Mn_{14} compound shows entirely visible out-of-phase alternating currect signals below 5 K and large hysteresis loops below 2 K. Furthermore, the amalgamation of azido groups with the triethanolamine tripodal ligand in manganese carboxylate cluster chemistry has led to the isolation of a new ferromagnetic, high-nuclearity and mixed-valence $Mn^{II/III}_{15}Na_2$ (**3**) cluster with a large ground-state spin value of $S = 14$.

In the second project we demonstrate a new synthetic route to purely inorganic-bridged, transition metal-azido clusters [Co^{II}_7 (**4**) and Ni^{II}_7 (**5**)] and coordination polymers [$\{Fe^{II/III}_2\}_n$ (**6**)] which exhibit strong ferromagnetic, SMM and long-range magnetic ordering behaviors. We also show that access to such a unique ferromagnetic class of inorganic, N-rich and O-free materials is feasible through the use of Me_3SiN_3 as the azido-ligand precursor without requiring the addition of any organic chelating/bridging ligand.

In the last projects we have tried to bring together molecular magnetism and optics via the synthesis of multifunctional magnetic materials based on 3*d*- or 4*f*-metal ions. We decided to approach such challenge from two different directions: firstly, in our third project, by the deliberate replacement of non-emissive carboxylato ligands in known 3*d*-SMMs with their fluorescent analogues, without perturbing the metal-core structure and SMM properties (complexes **7**, **8**, and **9**). The second route (last project) involves the use of naphthalene or pyridine-based polyalcohol bridging ligands for the synthesis of new polynuclear Ln^{III} metal clusters (Ln = lanthanide) with novel topologies, SMM behaviors and luminescent properties arising from the increased efficiency of the "antenna" organic group. This approach has led us to the isolation of two new families of Ln^{III}_8 (complexes **10**-**13**) and Ln^{III}_4 (complexes **14**-**20**) clusters.

Acknowledgements

Firstly, I would like to express my sincere gratitude to my supervisor Prof. Theocharis C. Stamatatos for his continuous support during my Ph.D studies, for his patience, motivation, and immense knowledge. His guidance helped me throughout my research development and the writing of this thesis. I could not have imagined having a better supervisor and mentor for my Ph.D. Besides my supervisor, I would like to thank the other members of my advisory committee, Prof. Georgii Nikonov and Prof. Tony Yan for their insightful comments and encouragement, but also for their hard questions which incented me to broaden my research in various perspectives and new directions. My special thanks go also to Prof. Melanie Pilkington for her support and very helpful discussions throughout the entire duration of my thesis.

I would like to thank each one of our research collaborators because without their precious support it would not be possible to conduct this research. More specifically, I am utterly grateful to Dr. Luís Cunha-Silva, Dr. Manolis J. Manos, Prof. Anastasios J. Tasiopoulos, Dr. Simon J. Teat and Prof. Melanie Pilkington, for solving and refining the structures of all the reported complexes. Furthermore, I am grateful to Prof. George Christou and all his group members, Dr. Wolfgang Wernsdorfer and Prof. Albert Escuer who acquired the magnetic data of all synthesized compounds, as well as Dr. Vlasoula Bekiari who performed the solid-state photoluminescence studies on the reported compounds.

I thank my fellow labmates for the stimulating discussions, for the sleepless nights we were working together before deadlines, and for all the fun we have had in the last four years. I am also grateful to the Ontario Trillium Foundation for the financial support of my entire Ph.D research the last 3-4 years.

Last but not the least I would like to thank my family: my parents and my brother for supporting me spiritually throughout the writing of this thesis.

Table of Contents

CHAPTER 1: Introduction

CHAPTER 2: New High-Spin Molecules and SMMs of Manganese Bearing Alkoxido- and/or Oximate-Based Chelating/Bridging Ligands: $\{Mn_{14}\}$, $\{Mn_{16}\}$ and $\{Mn_{15}Na_2\}$

CHAPTER 3: New Classes of Ferromagnetic Materials with Exclusively End-On Azido Bridges: From SMMs to Two-Dimensional Molecule-Based Magnets

CHAPTER 4: Emissive Molecular Nanomagnets: Introducing Optical Properties in Triangular Oximato $\{Mn^{III}_3\}$ SMMs from the Deliberate Replacement of Simple Carboxylate Ligands with their Fluorescent Analogues

CHAPTER 5: Towards the Synthesis of Emissive SMMs from the Use of Naphthalene- and Pyridine-Based Diols in Ln^{III} Cluster Chemistry: $\{Ln_8\}$ and $\{Ln_4\}$ Complexes with Unprecedented "Christmas Star" and Zigzag Topologies

List of Schemes

List of Figures

List of Tables

List of Publications

CHAPTER 2:

D. I. Alexandropoulos, C. Papatriantafyllopoulou, C. Li, L. Cunha-Silva, M. J. Manos, A. J. Tasiopoulos, W. Wernsdorfer, G. Christou, Th. C. Stamatatos. "Approaches to molecular magnetic materials from the use of cyanate groups in higher oxidation state metal cluster chemistry: Mn_{14} and Mn_{16}", European Journal of Inorganic Chemistry, 2286, **2013**.

D. I. Alexandropoulos**,** E. C. Mazarakioti, S. J. Teat, Th. C. Stamatatos. "Rare nuclearities, new structural motifs, and slow magnetization relaxation phenomena in manganese cluster chemistry: A $Mn_{15}Na_2$ cage from the use of triethanolamine/pivalate/azide blend", Polyhedron, *64*, 91, **2013**.

CHAPTER 3:

D. I. Alexandropoulos, L. Cunha-Silva, A. Escuer, Th. C. Stamatatos. "New classes of ferromagnetic materials with exclusively end-on azido bridges: From SMMs to 2-D molecule-based magnets", Chemistry - A European Journal, *20*, 13860, **2014** (inside cover).

CHAPTER 4:

D. I. Alexandropoulos, A. M. Mowson, M. Pilkington, V. Bekiari, G. Christou, Th. C. Stamatatos. "Emissive molecular nanomagnets: Introducing optical properties in triangular oximato $\{Mn^{III}_3\}$ SMMs from the deliberate replacement of simple carboxylate ligands with their fluorescent analogues", Dalton Transactions, *43*, 1965, **2014** (front cover).

CHAPTER 5:

D. I. Alexandropoulos, L. Cunha-Silva, L. Pham, V. Bekiari, G. Christou, Th. C. Stamatatos. "Tetranuclear lanthanide (III) complexes with a zigzag topology from the use of pyridine-2,6-dimethanol: Synthetic, structural, spectroscopic, magnetic and photoluminescence studies", Inorganic Chemistry, *53*, 3220, **2014**.

D. I. Alexandropoulos, A. Fournet, L. Cunha-Silva, A. M. Mowson, V. Bekiari, G. Christou, Th. C. Stamatatos. "Fluorescent naphthalene diols as bridging ligands in Ln^{III} cluster chemistry: Synthetic, structural, magnetic and photophysical characterization of Ln^{III}_8 'Christmas-stars'", Inorganic Chemistry, *53*, 5420, **2014**.

List of Abbreviations

1-D	One-dimensional
2-D	Two-dimensional
3-D	Three-dimensional
A	Absorption
Å	Angstrom
ac	Alternating Current
acacH	Acetylacetone
AF	Antiferromagnetic Interactions
ancaH	9-Anthracenecarboxylic Acid
C	Curie Constant
CH_2Cl_2	Dichloromethane
cm^{-1}	Wavenumbers
D	Axial Zero-Field Splitting Parameter
dapdoH_2	2,6-Diacetylpyridine Dioxime

dc	Direct Current
DMF	Dimethylformamide
$dpkd(OH)_2$	Gem-diol form of Di-2-pyridyl Ketone
E	Transverse Anisotropy
E_c	Coercive Electric Field
EO	End-on Coordination Mode
EPR	Electron Paramagnetic Resonance
ET	Energy Transfer
Et_3N	Triethylamine
EtOH	Ethanol
F	Fluorescence
G	Gauss
g	Gyromagnetic Factor
H	Applied Magnetic Field
hmpH	2-(hydroxymethyl)pyridine
HSAB	Hard Soft Acid Base Principle
Hz	Hertz

IR	Infrared
ISC	Intersystem Crossing
J_1, J_2, …	Magnetic Exchange Coupling Constants
k	Boltzman Constant
K	Kelvin
LH	Ligand
L	Lanthanide-centered Luminescence
L1-H	2-Naphthoic Acid
L2-H	9-Anthracenecarboxylic Acid
L3-H	1-Pyrenecarboxylic Acid
Ln^{3+}	Lanthanide Ions
M	Magnetization
M	Metal Ion
$mdeaH_2$	*N*-methyldiethanolamine
Me-	Methyl Group
Me_3N	Trimethylamine
MeCN	Acetonitrile

MeOH	Methanol
mnt^{2-}	Maleonitriledithiolate Ion
mpkoH	Methyl 2-pyridyl Ketone Oxime
M_S, M_J	Microstates
N_3^-	Azide Ion
n-Bu_3N	Tributylamine
NBu_4^+	Tetrabutylammonium Cation
ndH_2	Naphthalene-2,3-diol
nm	Nanometer
o	Ortho Position
OCN^-	Cyanates
P	Phosphorescence
Pc	Phthalocyanine
$pdmH_2$	Pyridine-2,6-dimethanol
P_r	Polarization
QTM	Quantum Tunneling of Magnetization
RCO_2^-	Carboxylate Anion

RCO_2H	Carboxylic Acid
S	Spin Ground State
$S_{0,1,2}$	Singlet States
Et-saoH_2	2-Hydroxyphenylpropanone Oxime
SCM	Single-Chain Magnets
SMMs	Single-Molecule Magnets
SQUID	Superconducting QUantum Interference Device
T	Tesla
T	Temperature
$T_{1,2,3}$	Triplet States
T_B	Blocking Temperature
teaH_3	Triethanolamine
THF	Tetrahydrofuran
U	Energy Barrier for Magnetization Reversal
UV-Vis	Ultra Violet-Visible Spectroscopy
WOC	Water Oxidizing Complex

ZFS	Zero-Field Splitting
η^1, η^2, η^3	Coordination Modes of Ligands
Θ	Weiss Constant
$\mu, \mu_3, \ldots, \mu_5$	Bridging Modes of Ligands
σ	Conductivity
τ	Relaxation Time
τ_0	Pre-exponential Factor
χ	Magnetic Susceptibility
χ_M	Molar Magnetic Susceptibility
ω	Angular Frequency
μ_B	Bohr Magneton

CHAPTER 1: Introduction

1.1. Polynuclear Metal Complexes – Molecular Nanoscience

The top-down approach has been widely employed for the miniaturization of components. This has been proved to be a very successful approach for the construction of modern devices that cover the needs of our society. Techniques such as photolithography[1] have been used by researchers and experts in the field of engineering in order to manufacture and organize progressively smaller and smaller parts of bulk materials. However, the known techniques that are utilized by the top-down approach can only produce materials with dimensions no smaller than 100 nm or so. For the fabrication of devices with applications in everyday life this size is small, but still very large when targeting the construction of devices at the atomic or molecular scale. Thus, it seems that the top-down approach is reaching its size limits as the need to construct smaller nanoscale materials becomes more and more pronounced. Thus, although Feynman elegantly said that 'there is plenty of room at the bottom', it is quite difficult for the top-down approaches to undertake and accomplish the new technological challenges.[2] New routes are thus necessary to be discovered in order for research to proceed towards further miniaturization.[3,4]

An alternative solution to overcome this problem can be offered by the molecular or bottom-up approach. Thus, a potentially successful way to further miniaturization is

through the construction of large in nuclearity molecules that can be used for the design of the new generation of molecular nanoscale devices and machines. Utilizing the bottom-up approach, instead of breaking down bulk materials to gain insight into the properties of their micro-components, atoms or molecules can be used to fabricate molecule-based devices. To highlight the relationship between two different, but at the same time closely related, areas of science, namely the molecular chemistry and materials science, the bottom-up approach to the nanoscale has been coined the name "Molecular Nanoscience".[3] The resources of this approach are individual elements or small molecules, which are used for the construction of molecular nanostructures with the optimized and targeted properties and applications for the desired goal. A chemical definition of the word 'molecule' seems to be useful at this point: a molecule is a sufficiently stable, discrete and electrically neutral species with a finite-size group of at least two atoms held together by chemical bonds. Molecules are discrete species and different than the multi-dimensional polymers which can be one-dimensional chains, two-dimensional sheets or three-dimensional networks. Also, molecules are composed of neutral atoms and their neutrality differentiates them from 'ionic salts', such as sodium chloride (NaCl) which is composed of Na^+ and Cl^- charged species (ions). However, these strict definitions often become blurred. For example, in biochemistry, DNA, which is strictly speaking a one-dimensional polymer of linked nucleotides and it is not electrically neutral, usually is reported as the 'molecule of life'. DNA and other polymers, such as proteins and carbohydrates, are perhaps best described as 'macromolecules'.[3,4]

Hence, a molecule-based material can be described as the collection of different molecular components that are assembled together to achieve a specific function. In this assembly, each molecular component acts individually performing a single function, while the supramolecular or multi-molecular unit has the ability to carry out more complex actions. These actions are the result of the synergy between the individual molecular components.[5] Molecular devices operate via atomic and electronic rearrangements. To achieve an operation, molecular devices, such as the macroscopic ones, need energy and an appropriate stimulus. Thus, the idea of making molecule-based devices is an appealing target not only for understanding fundamental principles of science but also for the further development of nanoscience and nanotechnology with potential applications in applied research and materials industry.[3,4,6]

In Molecular Nanoscience, the desired molecules are synthesized by using relatively simple and small in size starting materials. Thus, Molecular Nanoscience relies a lot on the ability of synthetic chemists to construct multi-molecular species that shall exhibit the desired properties and potential applications. It therefore becomes apparent that for the synthesis of the appropriate molecule-based devices new synthetic strategies and extended methodologies need to be developed. The bottom-up approach brings to the field of nanoscale materials all the advantages offered by molecular chemistry, as these are summarized below. In the majority of the cases, the synthesis of nanoscale molecular materials is performed at mild conditions and at room temperature, or nearly so. Thus, a high synthetic control can be achieved using these 'low energy' conditions, which provide an enhanced opportunity to make and adjust molecules according to the targeted applications. In particular, the most important molecular advantages are:[3,7] (i)

monodispersity; upon purification and crystallization of the sample, all the molecular species of the material in the crystal are of identical size. By using traditional top-down approaches it is very difficult to achieve such a monodisperse collection of nanosized particles. This is very important because the size of the particle or domain has a great effect on the overall properties of nanoscale materials. Thus, a distribution of nanoparticles size causes an important distribution of properties (i.e., magnetic, conductivity and catalytic). In contrast, in a monodisperse molecular system each molecule is expected to possess identical properties; (ii) the molecules are surrounded by *organic groups* of various types as a result of the low-energy synthetic methods that are used for the synthesis of these materials. Such organic groups are called 'ligands', and typically they possess 'arms' and functional groups which can bind to one or more metal ions. The ability to vary these organic shells at our own will provides a means of adjusting important properties of the molecule, such as solubility, purity and crystallinity; (iii) good *solubility*; molecular systems comprising metal ions and organic groups are typically soluble in a wide variety of organic solvents due to the 'coating' of the metal ions by the organic functionalities. This is a major advantage of molecular species when compared to classical metal nanoparticles of the top-down approach which are insoluble and usually yield colloidal suspensions. Solubility allows for purification, tailoring, tethering, processing (e.g. deposition on electrical and conductive surfaces, removal from surfaces, etc.) and controlled modification; (iv) *crystallinity* via the formation of single-crystals suitable for X-ray diffraction studies. In a single-crystal of a molecular material the constituent molecules are arranged in an orderly repeating pattern that extends in all three-dimensions (Figure 1.1).[8] Thus, all the molecules in the crystal display the same

response to an external stimulus, such as an applied magnetic field, pressure, or light. Crystallization of traditional nanoparticles is extremely difficult to achieve and usually requires excessive amounts of energy (i.e., high temperatures and pressures); (v) the molecules in the crystal are *well-separated* due to the presence of the peripheral organic groups, which prevent close contact of the neighbouring molecules and do not allow significant intermolecular interactions to dominate. This protection provided by the organic shell also minimizes effects commonly observed in traditional nanoparticles, including surface variations, roughness, defects, etc. As a result of all the above advantages, it becomes obvious that there is a continuous need for new molecular materials with nano-sized structures and improved, or even new, properties than the ones seen to date from the bulk and traditional materials of the top-down approach. In the case that the interest is focused on the magnetic properties, and consequently into the area of molecule-based electronics, then the desired nanoscale molecular compounds may be constituted of many paramagnetic metal ions surrounded and linked by flexible and multifunctional bridging ligands. Such high-nuclearity metal species are known as polynuclear metal complexes, and their synthesis and applications have become the focal point of a large number of research groups worldwide.[3,4]

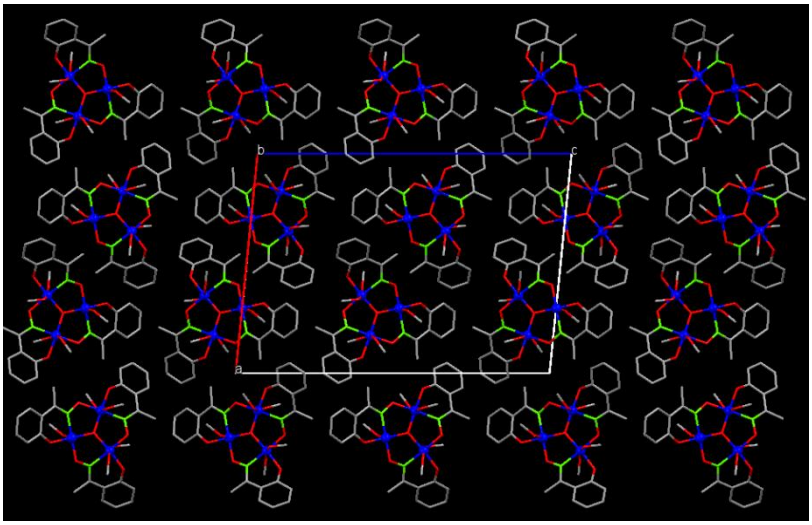

Figure 1.1. A three-dimensional, ordered array of monodisperse, identically oriented molecules within a crystal. Each molecule comprises three manganese atoms (blue) connected by oxygen (red) and nitrogen (green) atoms and surrounded by organic groups (grey). The box defines the repeating unit of the crystal. Reproduced from Ref. 9.

Polynuclear metal complexes or "coordination clusters", or simply "clusters", are molecular species consisting of a large number of metal ions (M^{n+}; "n" varies). For the synthesis of such compounds, synthetic chemists have to use both bridging (L) and terminal (L′) ligands. Polydentate bridging organic ligands are necessary for the aggregation of metal ions into high nuclearity products with unpredictable structures and novel topologies. On the other hand, terminal ligands are employed to block the extensive polymerization in order to isolate zero-dimensional structures and avoid the isolation of multi-dimensional polymers. In most of the cases, the organic molecules can also act as chelating ligands, thus providing thermodynamic stability and crystallinity to the resulting molecular species. A general formula for polynuclear metal complexes is:

$[M_x(L)_y(L')_z]^n$, where "x" is an integer number larger or equal to three, "y" and "z" are also integer numbers, and "*n*" can be any integer number, including zero; if "*n*" is negative, the cluster compound is anionic; if it is positive, then the compound is cationic, and if it is zero the complex is neutral.[10a] In polymetallic, Werner-type complexes, the metal ions are mostly in moderate-to-high oxidation states and they are considered, according to the HSAB (Hard and Soft Acid and Base) principle,[10b] as relatively hard acids. Therefore, they prefer binding to ligands that are moderate-to-hard bases. Hence, such metal cluster compounds are frequently bridged by elements of the *p*-block, such as oxygen bridges, and any type of exchange interactions (magnetic, electronic, etc.) between the spin carriers is propagated through the orbitals of the bridging ligand(s). These compounds are different from the metal-metal bonded complexes,[11] which are also termed "clusters" by many research groups.[3,4]

In order to reach the nanoscale regime, the size of molecular clusters needs to be increased. The size of a metal cluster in molecular chemistry is closely related to its nuclearity, and it increases as the nuclearity increases. To date, the largest molecule-based clusters synthesized by bottom-up strategies are of the same order of magnitude as the smallest classical nanoparticles fabricated by top-down approaches.[12] However, the synthesis and crystallization of such species have been always a challenging task for coordination and structural chemists. Christou, Winpenny, Brechin, and others,[13] have shown that *3d*-metal clusters can indeed reach the size regimes of small nanoparticles, and apart from their architectural beauty, they can also exhibit interesting physicochemical properties.[14] Record nuclearities for homometallic manganese clusters to date are the $\{Mn^{III}_{84}\}$ torus (Figure 1.2),[15] the $\{Mn^{II/III}_{44}\}$ loop-of-loops cage,[16] and the

$\{Mn^{II/III}_{32}\}$ double-decker wheel (Figure 1.3).[17] In homometallic lanthanide(III) coordination chemistry the record in size is held by the structurally impressive $\{Gd_{104}\}$ and $\{Dy_{104}\}$ clusters of Kong[18] and Xue[19] (Figure 1.4, left and right, respectively).

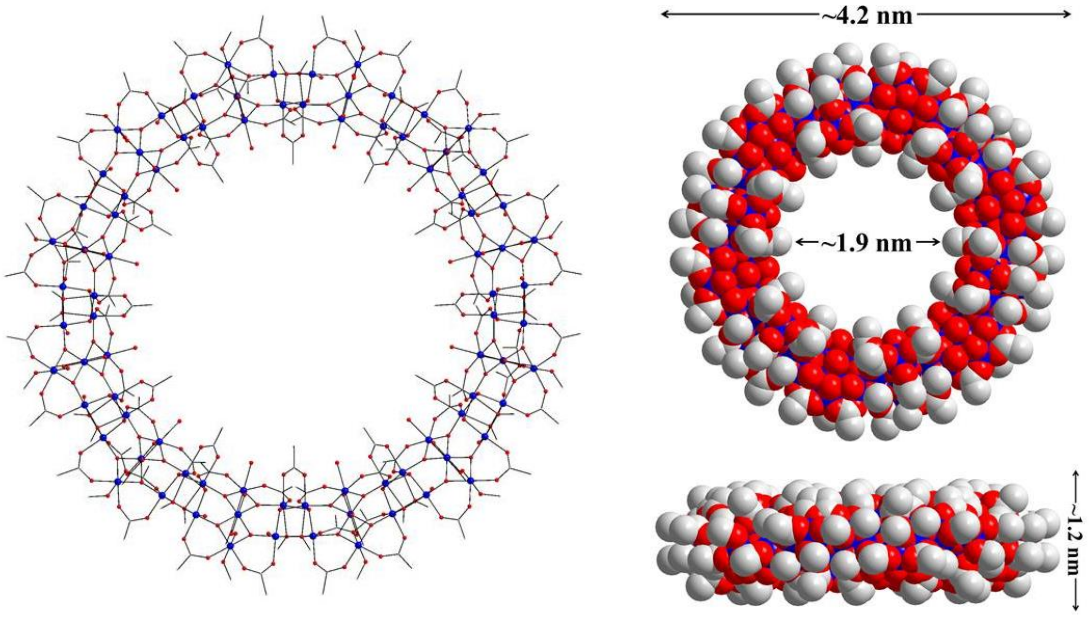

Figure 1.2. (left) Molecular structure of the $\{Mn_{84}\}$ torus-like cluster, excluding hydrogen atoms. (right) Space-filling representations showing that the torus has a diameter of about 4.2 nm and a thickness of about 1.2 nm, with a central hole of diameter 1.9 nm. Color scheme: Mn^{III}, blue; O, red; C, grey. Reproduced from Ref. 15.

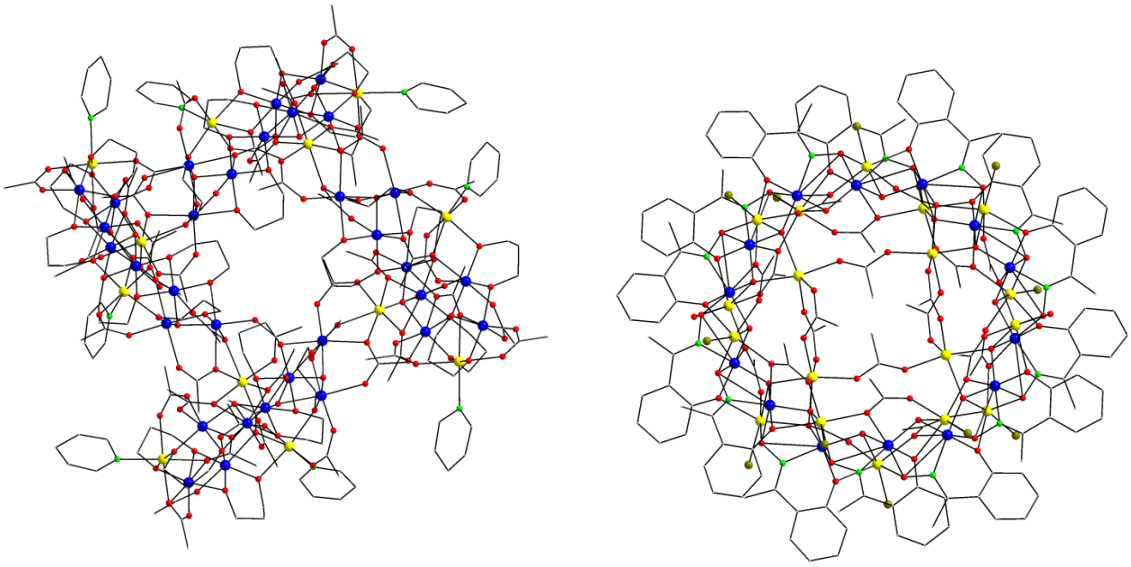

Figure 1.3. (left) Structure of the anion of the $\{Mn^{II/III}_{44}\}$ loop-of-loops cluster. (right) Molecular structure of the anion of the $\{Mn^{II/III}_{32}\}$ double-decker wheel. H atoms are omitted for clarity. Color scheme: Mn^{II}, yellow; Mn^{III}, blue; O, red; N, green; Br, olive green; C, grey. Reproduced from Refs. 16 and 17.

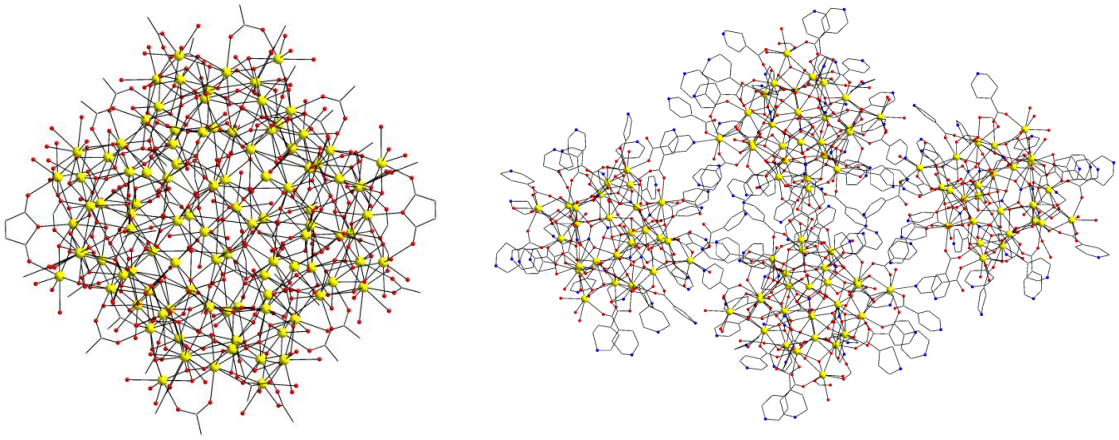

Figure 1.4. (left) Structure of the anion of the $\{Gd_{104}\}$ "keplerate" cluster. (right) Molecular structure of the $\{Dy_{104}\}$ tetramer. H atoms are omitted for clarity. Color scheme: Gd/Dy, yellow; O, red; N, green; C, grey. Reproduced from Refs. 18 and 19.

1.2. Strategies for the Synthesis of Metal Cluster Compounds

The development of new reaction schemes with appropriate organic chelating/bridging ligands or combinations of organic and inorganic ligands will increase the chances of identifying novel types of metal clusters with improved or new properties. One of the great collective achievements of twentieth-century science is the ability of organic chemists to successfully provide methods for preparing large and complicated molecules in a systematic and controlled manner. The attitude of mind involved in such a process has been adopted by all synthetic chemists who are interested in building molecules step-by-step. On the other hand, little progress has been made by inorganic chemists in discovering general approaches for the design of compounds containing large number of metal centers. The main reason was that the obvious biological relevance and commercial applications of large organic molecules and polymers were not matched by the different properties (i.e., magnetic) of polynuclear and polymeric metal complexes.

The lack of control in polynuclear metal chemistry has led to the neologism "self-assembly" or "serendipitous assembly" being coined.[20,21] In such procedures, simple metal salts or preformed small clusters (trinuclear or tetranuclear, mainly containing carboxylate ligands) react with multitopic ligands under a variety of conditions.[3,4,22] To date, serendipitous assembly is a dominant tool and the the vast majority of polymetallic complexes with interesting physical properties have been created by utilizing this route. This is because the accurate prediction of the physical properties of a given structure is

extremely difficult, and designing structures is only possible when working with predictable metal-ligand combinations. The main principle of serendipitous assembly relies on the creation of a mismatch between either the number or type of coordination sites available for a single metal ion, as well as the nature of the donor atoms supplied by the ligand. Polycarboxylic acids,[23] such as nitrilotriacetic acid and its derivatives, have been used by Powell and Heath for the synthesis of new metal complexes. In such ligands the dispositions of the donor atoms make it impossible for all of them to bind to a single metal ion. Thus, the formation of a polymetallic compound is favored. In such polynuclear complexes the metal ions are bridged by the organic ligand. The degree of metal binding can be elegantly controlled through pH adjustment and careful choice of the metal-to-ligand ratio. This approach has yielded very impressive results, including aesthetically pleasing $\{Fe^{III}_{17}\}$, $\{Fe^{III}_{19}\}$ and $\{Cu^{II}_{36}\}$ cages with unprecedented topologies and nanometer sizes.[24] Adopting a similar approach, Zeng and co-workers managed to isolate $\{Eu^{III}_{12}\}$ and $\{Eu^{III}_{15}\}$ clusters through the employment of polydentate α-amino acids, such as tyrosine, in homometallic lanthanide cluster chemistry (Figure 1.5).[25]

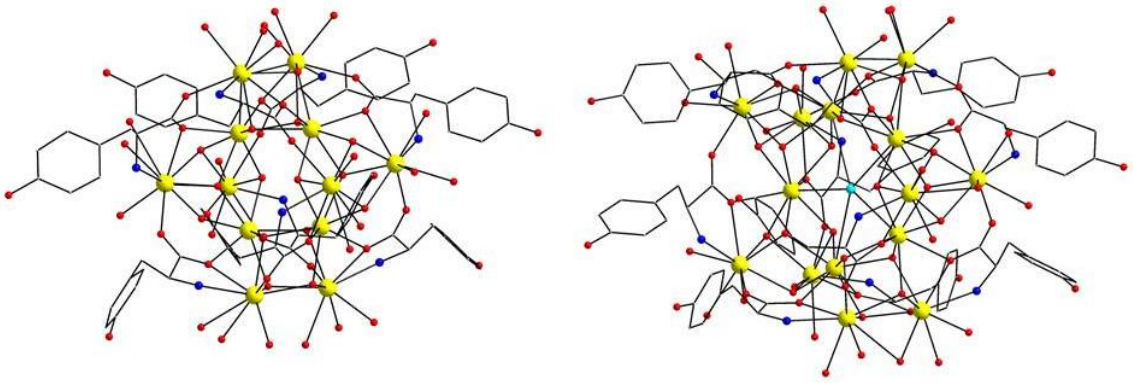

Figure 1.5. Structures of $\{Eu_{12}\}$ (left) and $\{Eu_{15}\}$ (right) clusters. H atoms are omitted for clarity. Color scheme: Eu, yellow; O, red; N, green; Cl, cyan: C, grey. Reproduced from Ref. 25.

The choice of the organic ligand is particularly important since serendipitous assembly generates unpredictable results. Ligands with multiple donor atoms are preferred, while organic ligands that require considerable synthetic effort may be avoided, as it cannot be foreseen whether they will be useful for the construction of new and structurally interesting polynuclear compounds. Secondly, instead of a single organic ligand, a series of related ligands should be ideally explored because minor variations in the ligands' substituents and functionalities may affect the nuclearity, core topology and physicochemical properties of the resulting metal compounds. Lastly, it is important that the organic molecules used as ligands have good solubilities in as many solvents as possible since a range of solvents will need to be examined in order to improve the crystallinity of metal cluster compounds.[4]

On the opposite end, designed assembly employs rigid ligands which have strong preferences for specific bonding modes and metal ions with preferred coordination geometries. Designed assembly has been successfully utilized for the synthesis of metal complexes by several research groups and has indeed led to many beautiful clusters.[26] Approaches based on the designed assembly introduce an element of design into the aggregation process. Thus, the structures of the resulting compounds are moderately predictable, and are based on the preferred coordination geometry of the metal ion, the number of pre-organized donor sites offered by the ligand and the limited flexibility of

the latter. Fujita[27] and Stang[28] have developed an attractive projection of this approach towards the designed synthesis of new coordination clusters which was dubbed 'ligand-directed rational approach'. According to this route, the complexity of the system has to be reduced by combining rigid, multi-branched monodentate ligands and partially coordinatively saturated, labile metal centers with well-defined coordination preferences (Figure 1.6). By avoiding ligands with multiple binding sites and metals with multiple coordination geometries, it becomes much more practical to view a self-assembling system as a "molecular Meccano" (Figure 1.7).[29] It becomes apparent that 'designed assembly' or 'molecular paneling' cannot be easily employed in 4*f*- or 3*d*-metal coordination chemistry since lanthanides and moderate-to-high oxidation 3*d*-metal ions are susceptible in adopting a variety of different coordination geometries and ligand environments. Only metal ions with strict coordination preferences, i.e. Pd^{2+}, Ag^{+} and Pt^{2+}, are usually employed in 'designed assembly'.[4]

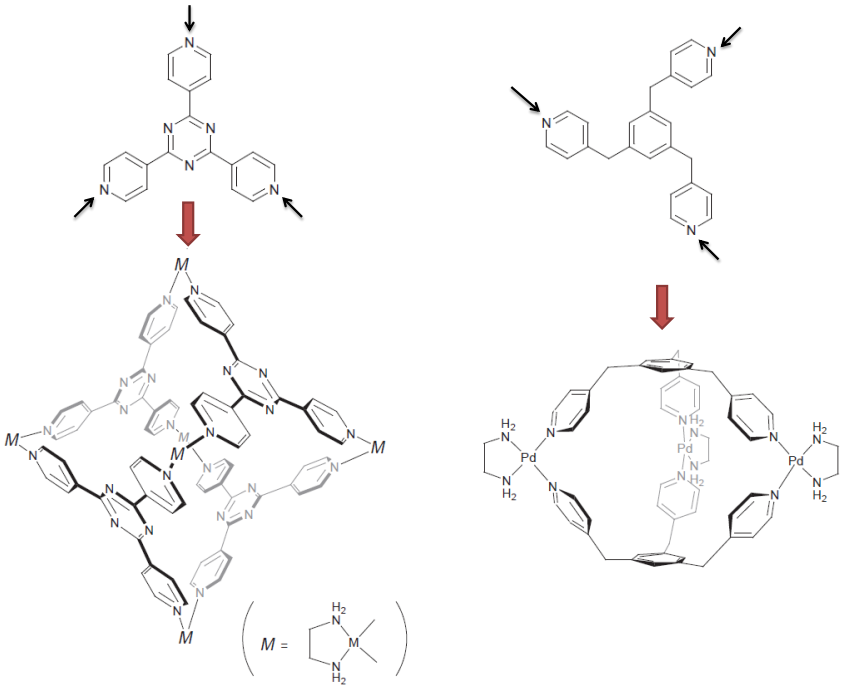

Figure 1.6. (top) Two families of rigid, N-donor polydentate ligands with specific binding sites (indicated with black arrows), and (bottom) their corresponding nanometer-sized metal cluster compounds. "M" denotes to a divalent metal ion in the {M(en)} chelating unit, where "en" is diethanolamine. Reproduced from Ref. 29 with permission from the Royal Society of Chemistry.

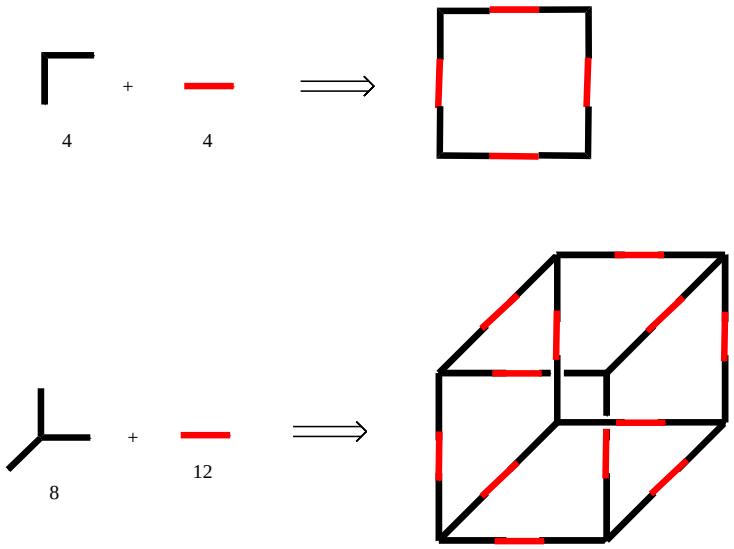

Figure 1.7. A scheme showing the assembly of a square and a cube, which require 2-D and 3-D (black bricks) 90º corner units, respectively, linked by linear spacers (red bricks).[29]

Serendipitous assembly has brought considerable advantages in metal cluster chemistry. Designed assembly in metal cluster chemistry restricts the number of accessible structures, e.g. to Platonic solids, rings and grids because such high-symmetry motifs require similar -if not the same- coordination environments for each metal

center.[30] On the other hand, serendipitous or less-designed assembly vastly increases the range of compounds available for isolation and study. The unusual structures of some of these compounds can lead to novel physicochemical (magnetic, optical and chirality) properties. Although there is little synthetic control with serendipitous assembly, we cannot leave it all to happenstance; there are important synthetic parameters that need to be examined, such as the choice of organic ligand and metal ion(s), as well as the reaction conditions (i.e., ratios of reagents, apparent pH, solvent, temperature, crystallization methods, etc.), for any significant progress to be made.[31] The organic molecules that are frequently used as bridging and/or bridging/chelating ligands in metal cluster chemistry are carboxylates, poly-alcohols, pyridyl-alcohols, pyridyl oximes and aromatic Schiff-bases (Scheme 1.1).[31] In all cases, the deprotonated oxygen atom(s) of these ligands is(are) not coordinatively saturated by binding to one metal, and therefore acts(act) as bridge, leading to the build-up of large in nuclearity metal clusters.[4]

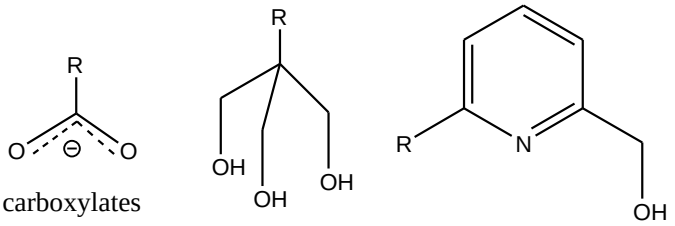

carboxylates triols pyridyl alcohols

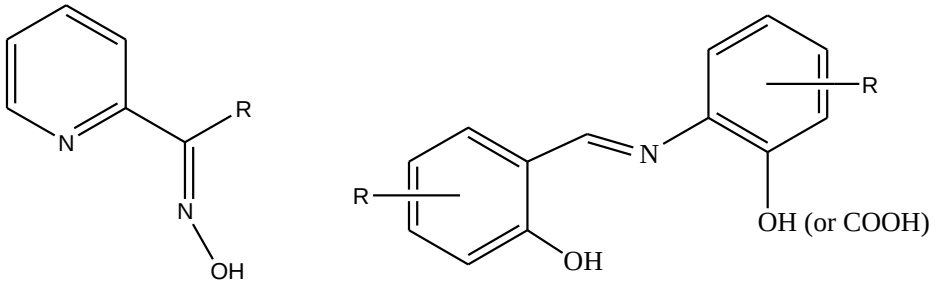

pyridyl oximes Schiff bases

Scheme 1.1. The general classes of organic chelating/bridging ligands discussed in the text (R = various substituents with electron donor or non-donor atoms).

Finally, what is really interesting in these two synthetic approaches is the existence or absence of any dichotomy between the two. Indeed, some new and appealing synthetic endevours are now emerging, where results, originally obtained by serendipity, are further exploited through design, or where careful design has not completely excluded the possibility of a fortunate accident. However, the potential of the bottom-up approach to the nanoscale is immense. Exploiting this potential will require the skills of a synthetic coordination chemist, i.e., a pronounced ability to design and test new procedures, and a capacity to develop new results obtained by serendipitous to maximize our good fortune. It seems meaningless to restrict ourselves to "rational synthesis" when targeting the construction of metal cluster compounds, especially the ones with interesting magnetic properties. Excluding serendipity from our synthetic toolbox is both impossible and undesirable.[4,20]

1.3. Single-Molecule Magnets (SMMs) and Related Phenomena

The spin and orbital motions of electrons cause the phenomenon of magnetism in atoms and/or molecules. An individual atom or molecule can be either diamagnetic due to the absence of unpaired electrons, possessing a net magnetic moment of zero, or,

paramagnetic, possessing a non-zero net magnetic moment due to the presence of one or more unpaired electrons. In a bulk material, the interactions between the spins of the individual paramagnetic atoms give rise to paramagnetism, ferromagnetism, antiferromagnetism, and ferrimagnetism. The best way to determine the magnetic behavior of a species is by measuring its magnetization response to an external magnetic field or its magnetic susceptibility, χ (dimensionless). The volume magnetic susceptibility, χ_v, is given by the Equation 1.1,

$$\chi_v = \frac{M}{H} \tag{1.1}$$

where M is the magnetization of the material and H is the strength of the applied magnetic field. Volume magnetic susceptibility can be converted to mass (χ_g) or molar (χ_M) susceptibility by using the Equations 1.2 and 1.3, respectively, where ρ is the density of the material in $Kg \cdot m^{-3}$ or $g \cdot cm^{-3}$ and M_r is the molar mass in $Kg \cdot mol^{-1}$ or $g \cdot mol^{-1}$.

$$\chi_g = \frac{\chi_v}{\rho} \tag{1.2}$$

$$\chi_M = M_r \cdot \chi_g = M_r \cdot \frac{\chi_v}{\rho} \tag{1.3}$$

Paramagnetic behavior in a bulk solid results from the random orientation of the magnetic moments of the constituent paramagnetic atoms. By the application of an external magnetic field, the spins of the atoms will be attracted by the field and they will align with it, giving rise to a field dependent molar susceptibility, which is also temperature dependent. The dependence of χ_M on the temperature can be described by the Curie law (Equation 1.4),

$$\chi_M = \frac{C}{T}, \qquad C = \frac{N_A \mu_\beta^2 g^2 S(S+1)}{3k_B} \tag{1.4}$$

where C is a constant as derived by N_A (Avogadro's number), g (Landè factor), μ_β (Bohr magneton), k_B (Boltzmann constant), T (temperature), and S (spin quantum number).[32]

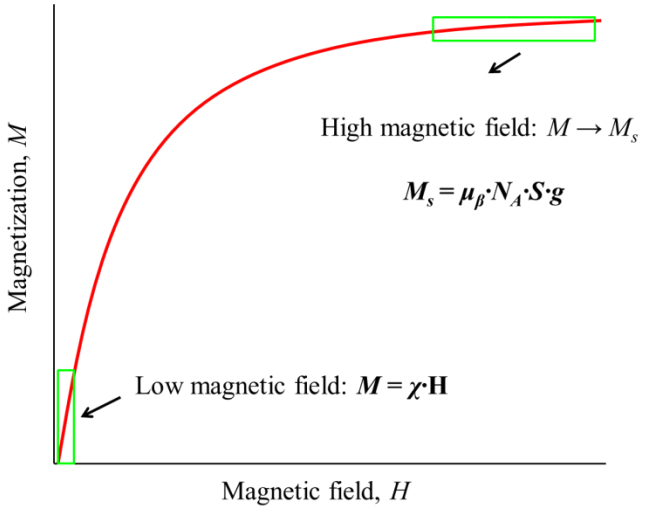

Figure 1.8. Plot of *M vs. H* for a paramagnetic material. Reproduced from Ref. 32.

The field dependence of the magnetization of a paramagnet is illustrated in Figure 1.8. At low fields, the magnetization increases linearly with the field, following the relationship: $M = \chi \cdot H$, while at higher fields, the magnetization rapidly increases and starts approaching a saturation value, M_s, which is calculated by the Equations 1.5 and 1.6.

$$M_s = \mu_\beta \cdot N_A \cdot S \cdot g \tag{1.5} \qquad \rightarrow \qquad \frac{M_s}{\mu_\beta N_A} = S \cdot g = n \tag{1.6}$$

Usually, the plot of reduced magnetization ($\frac{M_S}{\mu_\beta N_A}$) *vs.* field is used to calculate the spin, *S*, of a paramagnetic species from the saturation value and subsequently the number of unpaired electrons, *n*.[32]

Ferromagnetic behavior is observed in a bulk solid when the individual magnetic moments are aligned parallel to each other. Thus, a large net magnetic moment is expected for ferromagnets in the absence of an applied magnetic field. However, ferromagnetic materials are divided into smaller regions called domains. Each domain has a non-zero magnetic moment due to the parallel alignment of the spins within the domain, but the domains are randomly oriented and their spins can be eventually cancelled out. Thus, the material possesses a zero net magnetic moment in the absence of a magnetic field.[32]

When the individual magnetic moments of a material are aligned antiparallel, two different magnetic behaviors can be observed. If the magnetic spins are of the same magnitude they will be cancelled out leading to a zero net magnetic moment, in the absence of an applied magnetic field. This is known as an antiferromagnetic behavior. In the case that the magnetic spins differ in magnitude, even if they will have an antiparallel alignment, the net magnetic moment will be non-zero, in the absence of an applied field. This is known as a ferrimagnetic response. However, ferrimagnetic materials, akin to ferromagnetic ones, exist in domains; thus, a zero net magnetic moment may be observed for a bulk ferrimagnet in the absence of a magnetic field.[32]

Long-range magnetic ordering is a property observed only in ferro-, antiferro- and ferri-magnets below specific temperatures. Above a specific temperature, T_C (Curie

temperature; for ferromagnets) or T_N (Néel temperature; for antiferromagnets), these materials lose their long-range magnetic ordering properties and act as paramagnets, because thermal energy is large enough to overcome the magnetic order present in the solids.[32]

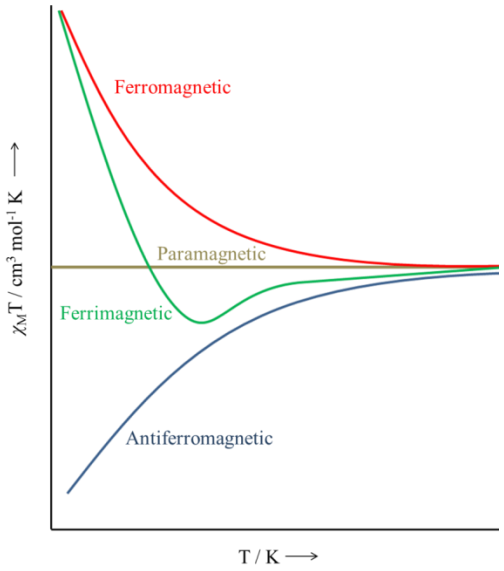

Figure 1.9. Plots of magnetic susceptibility *vs.* temperature, as $\chi_M T$ *vs.* T, for the four main classes of bulk magnetic materials. Reproduced from Ref. 32.

$\chi_M T$ *vs.* T plots can be used to describe the magnetic behavior of bulk materials (Figure 1.9). Paramagnetic materials, as mentioned earlier, obey the Curie law: $\chi_M = \frac{C}{T}$ and, thus, the $\chi_M T$ *vs.* T plot is a straight line, while ferro-, antiferro- and ferri-magnetic materials deviate from this line below T_C or T_N, due to their long-range magnetic ordering. In order to quantify the deviation from the Curie law, the Curie-Weiss law is usually utilized (Equation 1.7),

$$\chi_M = \frac{C}{T-\theta} \tag{1.7}$$

where θ is the Weiss constant. The data are then plotted as inverse susceptibility *vs.* *T*, as shown in Figure 1.10. For paramagnetic materials, a linear relationship between $\frac{1}{\chi_M}$ and *T* is observed, with a slope equal to Curie constant, *C*, and $\theta = 0$. For ferromagnetic and antiferromagnetic materials, deviations from the linearity are observed. Again, the slope of the curve is equal to *C*, while θ is equal to x-axis intercept. For ferromagnetic materials, θ is positive and for antiferromagnetic θ is negative, while the magnitude of θ indicates the strength of the interaction.[32]

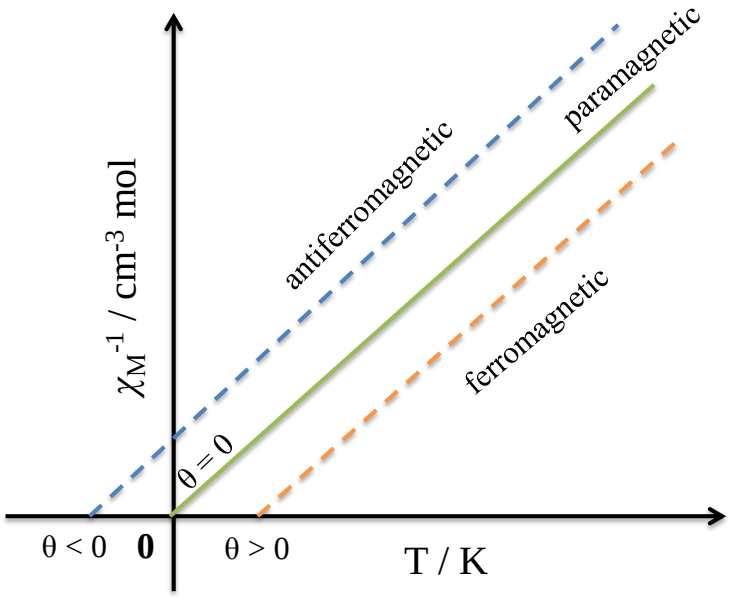

Figure 1.10. Plot of inverse susceptibility, $\frac{1}{\chi_M}$, *vs.* *T* for paramagnetic, ferromagnetic and antiferromagnetic materials. Reproduced from Ref. 32.

The term of molecule-based magnets was introduced by Feynman in 1959[33a] and it was not until 1987 when the first molecule-based magnet was reported.[33b] Molecule-based magnets are materials consisting of isolated spin centers that are magnetically coupled through a molecular orbital and not *via* direct covalent bonds. By definition, any inorganic, organic or hybrid organic/inorganic system with unpaired electrons in *d*- or *f*-orbitals, but also in σ- or π-molecular orbitals, could be a molecular magnet. In early 1990s two new classes of molecule-based magnets were reported; the zero-dimensional single-molecule magnets and the one-dimensional single-chain magnets.[33c-e] In such compounds the magnetic properties have pure molecular origin since the molecules or chains of molecules are well isolated in the crystal. However, intermolecular interactions cannot be ruled out at low temperatures. For every array of molecules with a non-zero spin ground state there is, in principle, a finite T_c (or T_N, Néel temperature) temperature at which long-range magnetic ordering may occur. T_c (or T_N) depends on the type and strength of the intermolecular interactions and can be either very weak (10^{-2} K) in the presence of van der Waals interactions or may reach a few Kelvin in the presence of strong hydrogen bonding interactions. Above the magnetic ordering temperature the spin of each molecule is independent of all the others and the correlation length (ξ), the length along which the spins become correlated with each other, is zero. As the temperature decreases towards T_c, the correlation length increases and it becomes infinite at T_c. The spin carriers are aligned parallel to each other when the interaction is ferromagnetic, while the spins are oriented antiparallel to each other if the interaction is antiferromagnetic. Long-range magnetic ordering can be easily detected by plotting $\chi_M T$ *vs. T*. At temperatures higher than T_c, the correlation length is zero and the compound

obeys the Curie law, with the Curie constant depending on the spin ground state of the molecular system. At lower temperatures, and assuming ferromagnetic intermolecular interactions, the $\chi_M T$ increases since the correlation length increases, while at T_c the correlation length becomes infinite and the material undergoes a transition from paramagnet to superparamagnet.[32]

In molecular magnetism arena, polynuclear complexes of paramagnetic 3*d*- and/or 4*f*-metal ions have received a tremendous attention over the last three decades or so, especially after the discovery that they can function as single-molecule magnets (SMMs).[32,33] Single-molecule magnets are molecular species that, below a certain blocking temperature, retain their magnetization in the absence of an external magnetic field.[33] Thus, SMMs can exhibit the properties of bulk magnets but in the molecular level and they could, in principle, find applications in quantum computing and spintronics. Their molecular characteristics could also offer the potential of high-density memory storage devices with unrivaled speeds.[34] However, the operating temperatures must increase significantly in order for SMMs to find real practical applications.[4]

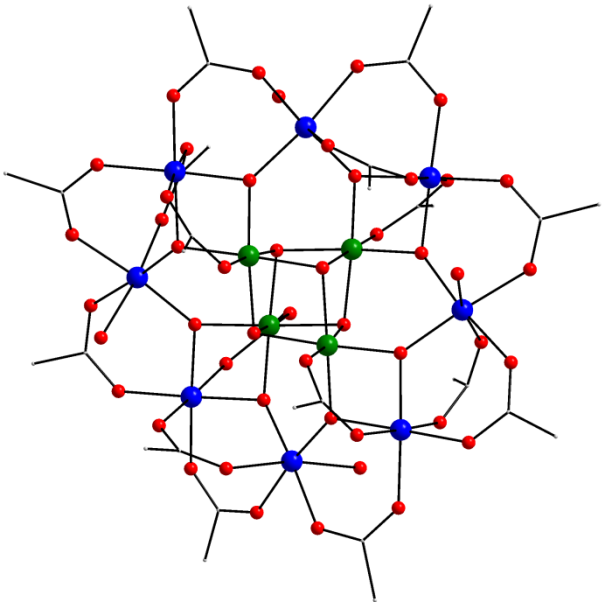

Figure 1.11. Structure of the archetypal Mn_{12}ac SMM. Color scheme: Mn^{III}, blue; Mn^{IV}, olive green; O, red; C, grey. H atoms are not shown for clarity. Reproduced from Ref. 35.

Mn_{12}ac was the first molecule for which it was observed SMM behavior.[33c,35] The mixed-valence compound consists of four central Mn^{IV} ions and eight outer Mn^{III} ions held together by μ_3- and μ_4-O^{2-} ions, while peripheral ligation is provided by bridging acetate groups and terminal water molecules (Figure 1.11).[35] In the following years, and after the initial discovery of Mn_{12}ac SMM, researchers were focused on the synthesis of polynuclear complexes with many different and paramagnetic 3*d*-metal ions.[7,36] Although a large number of complexes displaying SMM behaviors have been prepared with a variety of high-spin, paramagnetic 3*d*-metal ions, SMMs based on highly anisotropic Mn^{3+} ions have been the most frequently observed, and therefore manganese chemistry has become the most fruitful source of SMMs.[37]

In 3*d*-metal SMMs, the blocking temperature is dependent on the magnitude of the energy barrier, *U*, for the magnetization reversal. The magnitude of the energy barrier is proportional to $S^2|D|$ for integer spin systems and $(S^2\text{-}1/4)|D|$ for half-integer spin systems. Thus, in order to observe single-molecule magnetic behavior in a transition metal-based molecular compound it must possess two properties; a large spin ground state (*S*) and a significant magnetic anisotropy of the Ising (or easy-axis) type, the latter being reflected in a large and negative zero-field splitting parameter, *D*.[38] A large spin ground state, *S*, for a polynuclear 3*d*-metal compound results from the ideal situation where all the metals' spin vectors are aligned parallel to each other; such entirely ferromagnetic systems are called high-spin molecules and their synthesis and isolation are among the most difficult tasks in synthetic coordination chemistry. Furthermore, high-spin molecules can also derive when spin frustration effects from the presence in certain metal topologies of competing antiferromagnetic exchange interactions prevent (frustrate) the preferred antiparallel spin alignments that would normally yield low-spin species.[39] Zero-field splitting (ZFS), however, is a parameter that a synthetic chemist cannot really predict its sign and size; it mainly depends on the nature of the paramagnetic metal ion, the single-ion anisotropy of the metal ion of choice, the structural arrangement of the metal ions in the resulting polynuclear compound, and the presence of spin-orbit coupling.[40]

In 3*d*-metal SMMs, there are $[2S + 1]$ M_S microstates, resulting from the different orientation of the total spin, *S*, projections. The presence of zero-field splitting (ZFS) lifts the degeneracy of the microstates, in the absence of an applied magnetic field, and as long as $D < 0$ then $M_S = \pm S$ lies lowest in energy. Because of the anisotropy, the $M_S = -S$

is energetically the most favorable and thus, at low temperatures, the molecule can be magnetized and the magnetization can remain trapped in the M_S = -*S* spin ground state (Figure 1.12). In order for the magnetization to relax or the spins to flip from the M_S = -*S* to the M_S = +*S*, it has to overcome the thermal barrier with transitions through higher energy intermediate states in increments of one and over the barrier until a thermal equilibrium is reached. Instead of the thermal-assisted relaxation mechanism, magnetization can also relax following a different pathway, namely through the barrier, *via* a process known as resonant quantum tunneling of magnetization (QTM), from one side of the double-well to the other (Figure 1.12, right). Quantum tunneling of magnetization (QTM) can be detected and studied via magnetization (*M*) *vs. dc* field experiments, appearing as distinct step-like features in the magnetization hysteresis loops (*vide infra*).[41]

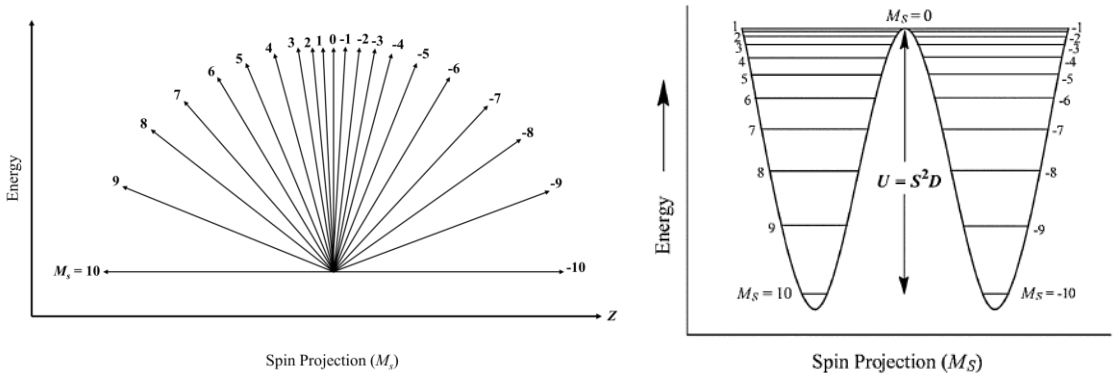

Figure 1.12. (left) Plot showing the allowed, quantized orientations (m_S states) of the spin vector of a molecule such as Mn_{12}ac with S = 10 and D < 0. (right) An alternative figure commonly employed to depict the situation in the left figure, and indicating the barrier (U) to magnetization relaxation as being the energy difference between the M_S = 0 and 10 states. Reproduced from Ref. 35.

For many years the synthetic attempts in the SMM research were focused on increasing substantially the energy barrier, *U*, by maximizing the total spin ground state, *S*, of the high-nuclearity molecules. The most successful route for maximizing *S* has been the design of polynuclear metal complexes with ferromagnetic coupling between the metal ions. Following this strategy, the largest energy barrier to date for a 3*d*-metal based SMM is reported for the ferromagnetic hexametallic compound $[Mn^{III}_6O_2(Et\text{-}sao)_6(O_2CPh(Me)_2)_2(EtOH)_6]$ (Figure 1.13), where Et-saoH_2 is 2-hydroxyphenylpropanone oxime, with a total spin of S = 12, D = -0.43 cm^{-1}, and an overall U = 86.4 K.[42] In this context, large in nuclearity complexes have been reported with record *S* values (currently up to S = 83/2);[43] however, in all cases the lack of anisotropy or the small *D* values made them insufficient SMMs.[44]

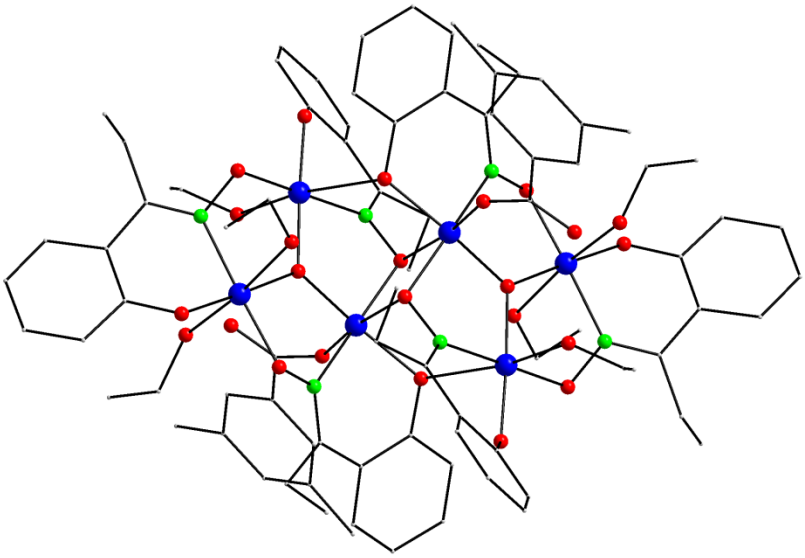

Figure 1.13. Structure of the hexametallic cage $[Mn^{III}_6O_2(Et\text{-}sao)_6(O_2CPh(Me)_2)_2(EtOH)_6]$. Color scheme: Mn^{III}, blue; O, red; N, green; C, grey. H atoms are not shown for clarity. Reproduced from Ref. 42.

In the last decade, there has been a noticeable shift of the interest of SMM community into the effect of single-ion anisotropy on the enhancement of the energy barrier for the magnetization reversal.[45] Since 2003, but more intensively in the last five years, there has been a renewed interest in lanthanides and actinides due to their remarkable single-ion anisotropy when compared with the other metallic elements of the periodic table. SMMs based on lanthanide coordination compounds have been synthesized and magnetically studied, with some of them showing unique properties, responsible for some of the most outstanding late advances in the field of SMMs.[46] The big breakthrough that opened new directions in the field of molecular magnetism resulted from the observation of slow relaxation of magnetization in a sandwich-type, double-decker Tb^{3+} complex with two phthalocyanate (Pc^{-}) ligands, $[NBu_4][TbPc_2]$ (Figure 1.14), which displayed record energy barriers, as high as 584 cm^{-1}, depending on the reaction conditions.[47] The magnetic behavior of the Tb^{3+} complex has pointed out some important conclusions: (i) it was the first time that a coordination complex based on a single metal ion exhibited SMM behavior; (ii) both the anisotropy barrier and the blocking temperature are significantly higher than any previously reported transition metal-based SMMs, and; (iii) the slow magnetization relaxation of the compound was due to its molecular origin rather than the result of any intermolecular interactions and long-range ordering, as it was confirmed by magnetic dilution studies in a diamagnetic lattice of $[NBu_4][YPc_2]$ complexes.

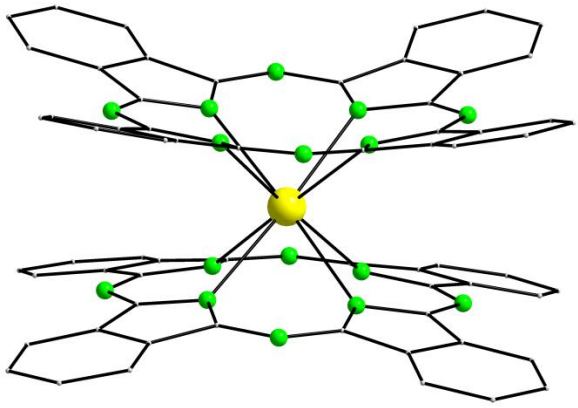

Figure 1.14. Crystal structure of the anion of $[TbPc_2]^-$. Color scheme: Tb, yellow; N, green; C, grey. H atoms are not shown for clarity. Reproduced from Ref. 47.

Larger in nuclearity lanthanide complexes have also been discovered to exhibit the SMM behavior.[48] In particular, dysprosium has played an important role in the synthesis of such compounds due to some unique magnetic features that it possesses (*vide infra*). Dy^{3+}-based SMMs have flourished over the last five years, leading to compounds with groundbreaking energy barriers and large blocking temperatures. Examples of Dy^{3+}-based SMMs with different structural topologies and metal nuclearities ranging from Dy_2 to Dy_{36} are known, but with cage-like complexes of more than eight Dy^{3+} centers the SMM behavior is usually weak. For instance, Powell and coworkers reported discrete $\{Dy_3\}$ triangles[49] and $\{Dy_6\}$ dimer-of-triangles[50] (Figure 1.15) with SMM behaviors and anisotropy barriers as high as $U = 139$ cm^{-1}.

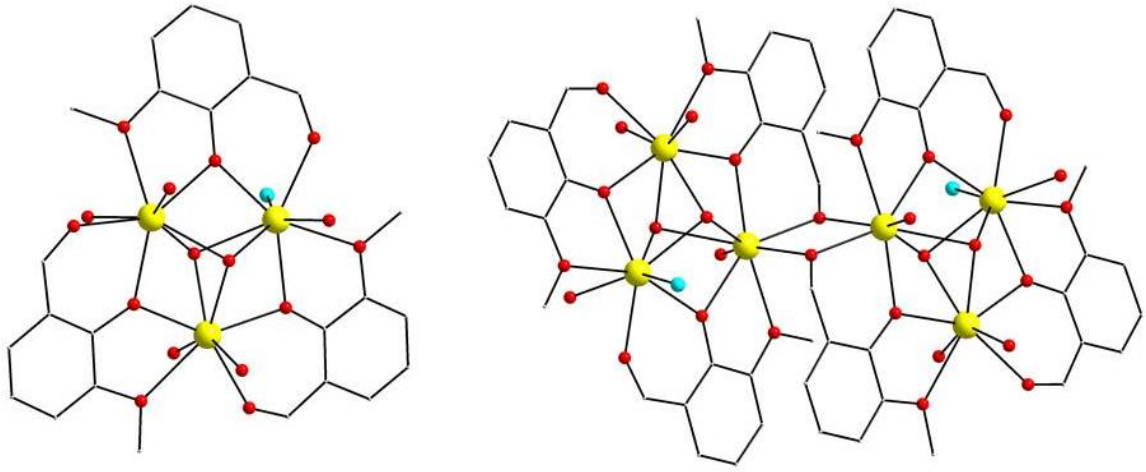

Figure 1.15. (left) Structure of the cation of the $\{Dy_3\}$ triangle. (right) Structure of the cation of the $\{Dy_6\}$ dimer-of-triangles. H atoms are omitted for clarity. Color scheme: Dy, yellow; O, red**;** N, green; Cl, cyan; C, grey. Reproduced from Refs. 49 and 50.

The origin of SMM behavior in lanthanide-based complexes is related to the ground multiplet state of the lanthanide ion. Because in lanthanides the spin-orbit coupling is much stronger than that of transition metals, the Russell-Saunders (RS) coupling scheme can be used in order to describe their electronic states. According to the RS coupling scheme, the spins of the individual electrons are coupled together to give the spin quantum number (S); in a similar way, the orbital angular momenta of the individual electrons are coupled together to give the orbital quantum number (L). The vector sum of S and L leads to a total spin-orbit coupled quantum number, J, and this results in an electronic structure of ${}^{2S+1}L_J$ multiplet states. In order to determine the term symbol of a lanthanide's ground state, Hund's rules need to be considered. Firstly, the ground state must have the largest spin multiplicity ($2S+1$) and, secondly, the largest orbital

multiplicity, *L*. The quantum number *L* can take values of 0, 1, 2, 3, 4, 5, and 6, and the corresponding term symbols are S, P, D, F, G, H, and I. According to the third Hund's rule, the value of *J* is equal to (*L*-*S*) for a shell that is less than half-filled, while for a shell that is more than half-filled the *J* is equal to (*L*+*S*). In a similar way that the *D* value splits the ground state and generates [2*S* + 1] M_S microstates in transition metal ions, in lanthanide chemistry the spin-orbit coupled electronic ground state generates [2*J* + 1] M_J microstates.[51] There are two important requirements for a lanthanide complex to function as an SMM. Firstly, the ground state must be bistable and possess a high $\pm M_J$ value. A singlet ground state would have no magnetic interest in terms of bistability and relaxation of magnetization. The higher the magnitude of the M_J value, the higher the magnetization retained at low temperature will be, where only the ground state is populated. It is important to note that the maximum $\pm M_J$ state of a lanthanide ion is not always the ground state and sometimes M_J states with smaller values may be lower in energy. The second prerequisite is that the doubly-degenerate ground state should be well separated from the first excited state. This separation represents the energy that is necessary to flip the spins from the $-M_J$ to the $+M_J$ state, assuming a thermally-assisted relaxation mechanism over the barrier. If these two needs are fulfilled, a magnetic ground state should be generated and a significant barrier to magnetization relaxation must be observed at temperatures below the corresponding energy that is required to reach the first excited state.

The 4*f*-orbitals of the lanthanide ions do not participate directly in bonding since they are well shielded by the outer $5s^2$ and $5p^6$ orbitals. Because of that, the magnetic coupling between the lanthanide ions, through the orbital(s) of the bridging donor atom(s), is

expected to be very weak to negligible. Consequently, there are not many chances to obtain really large spin values in the ground state, and in the most of the cases the magnetic behavior of polynuclear lanthanide SMMs arises from predominant single-ion effects of the individual metal centers. Modulation of the intramolecular magnetic exchange coupling constants, J_{ij}, using simple spin-Hamiltonians, which has been a useful tool for the study of most transition metal complexes, is usually feasible only for the spin-only (isotropic) gadolinium compounds. In contrast, the presence of a significant spin-orbit coupling in the remaining lanthanide ions does not allow the use of straightforward spin-only Hamiltonians. The J_{ij} values usually obtained for polynuclear Gd^{3+} compounds are in the range 0.1-3 cm^{-1}, which is much smaller than any magnetic coupling that includes 3*d*-metal ions.

A conventional SQUID magnetometer is used in order to record the bulk magnetic properties of a molecular compound and study its possible SMM behavior and magnetic dynamics (i.e., barrier for magnetization reversal, relaxation time, etc.). Usually, the response of the compound to an alternating current (*ac*) magnetic field is monitored using a very small *ac* field of about 1-5 Oe in a temperature range of 5-300 K and in the absence of a direct current (*dc*) field. The driving *ac* field can normally oscillate in the frequency range of 5-1500 Hz. If the compound possesses a non-zero energy barrier to relaxation then the magnetization will not alternate as fast as the phase of the field but it will lag behind the field. In that ideal case, out-of-phase (χ'') susceptibility signals will be observed, suggestive of an SMM behavior for the compound. If the compound is not an SMM, then the magnetization will keep up with the oscillating field and only an in-phase (χ') component of the magnetic susceptibility will be observed and no out-of-phase

signals will be detected. The χ'' *ac* signals of an SMM are both temperature and frequency dependant. For SMMs with a sufficient energy barrier, the χ'' gradually increases as the temperature decreases to reach a peak maximum, and then decays to indicate the completion of the magnetization relaxation, while the position of the χ'' maxima is shifted as the *ac* frequency is altered (Figure 1.16). For a given *ac* frequency, the temperature where the χ'' is accompanied with a peak maximum is called the blocking temperature. In order to quantify the energy barrier to magnetization reversal, the χ'' is plotted as a function of frequency at several different temperatures. From each $\chi''(\nu)$ curve, an average relaxation time (τ) can be calculated, at a given temperature, using $\tau = \frac{1}{2\pi\nu}$, where ν is the frequency that was used to obtain the corresponding χ'' maxima (Figure 1.16). The relationship between τ and T is given by the Arrhenius-type Equation (1.8),

$$\tau = \tau_0 \exp(U_{eff}/kT) \qquad (1.8)$$

where τ_0 is the pre-exponential factor, a coefficient that depends on the environment of the individual molecules, k is the Boltzmann constant, and U_{eff} is the effective energy barrier for the magnetization reversal which can be quoted in either cm^{-1} or K units. Thus, the energy barrier can be accurately determined from the slope of $\ln\tau$ *vs.* T^{-1} plot. When the magnetization relaxes *via* a thermally-assisted pathway, the relaxation time becomes temperature independent and this is associated with a straight line in the $\ln\tau$ *vs.* T^{-1} diagram.

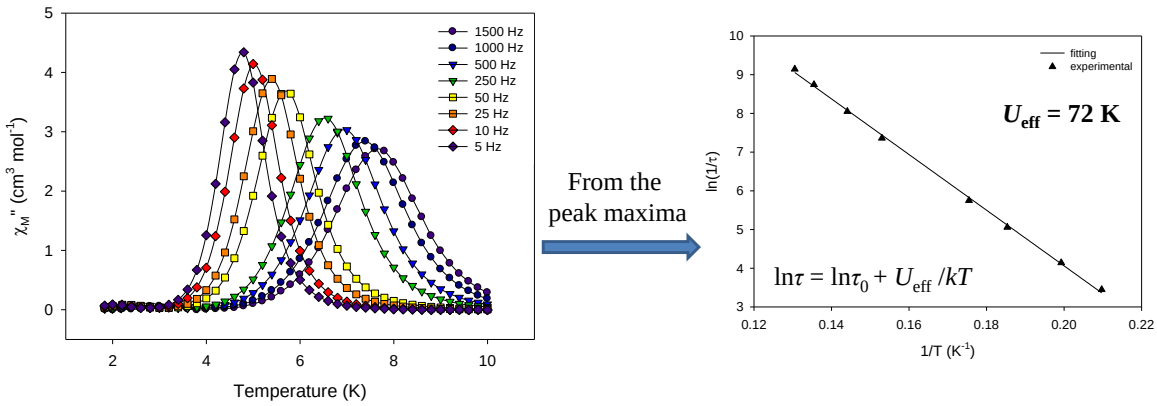

Figure 1.16. (left) Frequency-dependent peaks of the χ_M'' *ac* signals of Mn_{12}ac and (right) the corresponding Arrhenius plot constructed from the peak maxima and their corresponding temperatures. Note that Mn_{12}ac possesses an effective barrier for the magnetization reversal of 72 K, one of the highest yet reported for any transition metal-based SMM. Reproduced from Ref. 35.

Although the appearance of χ'' *ac* signals is a good indicator of the SMM behavior of a compound, it is not enough alone to confirm the SMM property. The observation of steps in the magnetic hysteresis loops (Figure 1.17, left) is the absolute 'fingerprint' of an SMM. In this experiment, the molecular compound is subjected to a reverse magnetic field and the magnetization is monitored. Firstly, the field increases from zero to a large value (+*H*) and then it is shifted from +*H* to -*H* and back to +*H*. If the compound is 'magnetic' then it will display non-zero magnetization (*M*) at zero-field, and thus magnetization hysteresis will be observed in the resulting magnetization (*M*) *vs.* field plot. This phenomenon is mainly temperature dependent; however, other factors, such as the field sweep rate, could determine the temperature range within hysteresis loops is

observed. Very often hysteresis loops are not observed at the operating temperature limits of the commercial SQUID magnetometers (1.8-400 K), and therefore measurements at extremely low-*T* (<1.8 K) need to be conducted using a micro-SQUID apparatus.

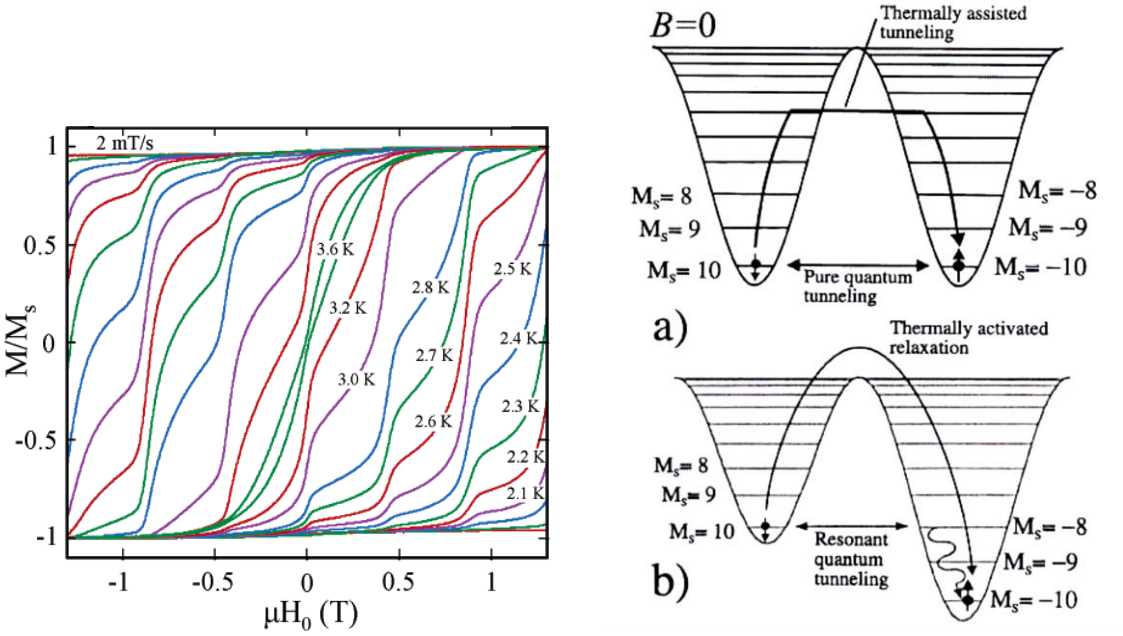

Figure 1.17. (left) Magnetization (*M*) *vs.* field hysteresis loops for a single-crystal of Mn_{12}ac showing the temperature dependence at a fixed sweep rate of 2 mT/s. (right) Possible tunneling mechanisms for *3d*-metal SMMs. Reproduced from Ref. 35 with permission from the Royal Society of Chemistry.

In both transition-metal and lanthanide SMMs, the relaxation of magnetization can follow a thermally-activated mechanism (Figure 1.17) and the data are fit to the Arrhenius law (Equation 1.8) giving linear plots with a positive slope which gives the U_{eff}. At lower temperatures, the lnτ data gradually become temperature-independent, indicating that the magnetization relaxes *via* quantum tunneling. QTM can occur at low

temperatures where the M_s or M_J levels on one side of the double-well are degenerate with the corresponding M_s or M_J levels of the other side. Often, there is a critical temperature where the QTM is found to compete with the thermally-activated mechanism. As the temperature is lowered below that critical temperature, then the contribution of QTM to the overall relaxation mechanism increases. It is obvious that there is a temperature region where the thermal and quantum mechanisms can occur concurrently in a process known as the 'quantum-assisted thermal regime'. To suppress QTM, the *ac* measurements can be performed in the presence of a small external direct-current magnetic field, which alters the relative energies of the M_S or M_J levels (Figure 1.17). In such way, the tunneling rate is lowered and the magnetization relaxes predominantly through the thermal regime, resulting in a shift of the out-of-phase signals to higher temperatures. When the SMM behavior is detected only in the presence of an external *dc* field (for very fast-relaxing SMMs) the compound is described as a 'field-induced' SMM.

1.4. Photoluminescence

Luminescence is the emission of light by a molecule in an electronic excited state. Excitation of a molecule can be caused in a number of ways, including chemical reactions, electrical energy or light. In the latter case, the luminescence is called photoluminescence. During photo-excitation, electrons within the material are promoted to accesible excited states by absorption of photons. Excited states are not stable and

electrons have to return back to the lowest energy state, their ground state. The decay from the excited states to the ground state is accompanied with the release of energy, and it can be radiative, followed by light emission, or non-radiative. Usually, the emitted light appears at longer wavelengths than these of the initially absorbed, and its energy would be equal to the energy difference between the excited and the ground state. Both organic (small dye molecules) and inorganic (metal complexes) materials can, potentially, exhibit photoluminescence properties.[52]

In organic chromophores, the emission in the visible region arises from electronic transitions between π-electrons. Such π-conjugated systems are essentially planar with all atoms linked by σ-bonds and lying in the same plane. Above and below the plane there is a charge cloud formed by the delocalized π-electrons. Thus, π-electrons can fluctuate between the energy levels of that extended network of π-orbitals by absorption and emission of light. A Jablonski diagram[53] (Figure 1.18) is an energy level diagram that illustrates the electronic states of a molecule and the mechanism of radiative and non-radiative transitions that are responsible for the photoluminescence observed in organic molecules. The arrangement of the states is vertical in terms of energy and horizontal in terms of spin multiplicity. The symbol *S* refers to a singlet state, either the ground state (S_0) or the excited states (S_1 and S_2), while the symbol *T* refers to a triplet state. According to the selection rules of electronic spectroscopy only transitions between states of the same spin multiplicity are allowed, while transitions between states of different spin multiplicity are commonly forbidden, although they may occur due to the spin-orbit coupling. Thus, the excitation process always involves a singlet-to-singlet transition. The decay from the excited state back to the ground state may be radiative or non-radiative. In

a Jablonski diagram, radiative and non-radiative decays are represented by solid and dashed arrows, respectively (Figure 1.18).[54]

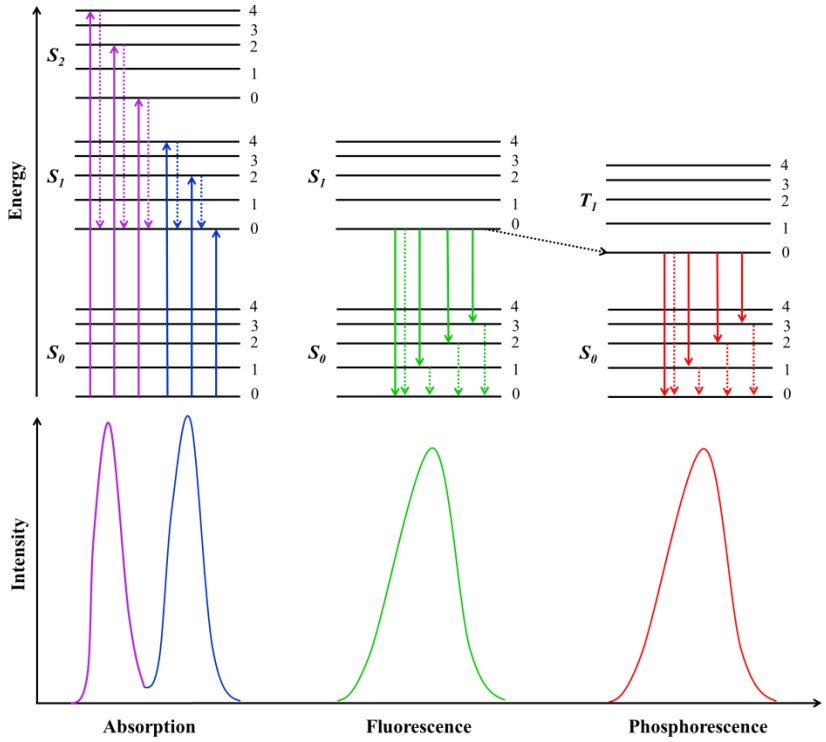

Figure 1.18. Jablonski diagram illustrating electronic energy states, and absorption and emission spectra. Radiative transitions indicating absorption (violet, blue) or emission (green for fluorescence and red for phosphorescence) of light are depicted by solid arrows. Non-radiative transitions (violet, blue, green, and red) are represented by dashed arrows. The internal conversions: $S_{2,4} \rightarrow S_{1,0}$, $S_{2,2} \rightarrow S_{1,0}$, $S_{2,0} \rightarrow S_{1,0}$ and $S_{1,0} \rightarrow S_{0,0}$ and the intersystem crossing $S_{1,0} \rightarrow T_{1,0}$ (*vide infra*) are also indicated in the diagram. Drawings of the corresponding absorption-, fluorescence- and phosphorescence spectra are displayed below the diagram. In notation of the states, the first subscript corresponds to the electronic state and the second to the vibrational level. Reproduced from Ref. 55.

There are several ways for an excited state electron to return back to the ground state; following a non-radiative process including vibrational relaxation, internal conversion and intersystem crossing. Upon excitation, an electron may move to a higher vibrational level of the first excited state. This state is unfavorable and the electron decays rapidly to the lowest level of the first excited state through vibrational relaxation and therefore it looses kinetic energy. This process is described by very short lifetimes (10^{-14} – 10^{-12} s) and usually precedes luminescence. The decay from a second excited singlet state to the first excited singlet state follows the same mechanism albeit this time the process is called internal conversion. Internal conversion can also occur for molecules in triplet states. Lifetimes are again short (10^{-12} s). When a singlet-to-triplet or conversely a triplet-to-singlet electronic transition takes place, that process is known as intersystem crossing. Since intersystem crossing violates the spin multiplicity selection rule, the probability for such transitions to occur is low and they are thus described by longer lifetimes (10^{-8} s) than those detected in internal conversion.[56]

A molecule in an excited state can also decay by undergoing a radiative transition that involves fluorescence and phosphorescence. Fluorescence occurs when an electron from the first excited singlet state relaxes to its ground state by emitting a photon. An electron from an excited singlet can also undergo intersystem crossing to an excited triplet state and from there it can decay to the ground state through phosphorescence emission. Note that fluorescence and phosphorescence emissions are spin-allowed and spin-forbidden decays, respectively. Consequently, fluorescent materials re-emit immediately the photons they absorb and exhibit lifetimes typically < 10^{-6} s. Unlike fluorescence,

phosphorescence is a longer process with lifetimes in the range of microseconds or greater.[56]

Upon excitation, some organic molecules can form excimers. An excimer is a short-lived dimer formed by the interaction between one excited and one ground state monomer.[57] The classical example of polyaromatic hydrocarbons that exhibit excimer formation is pyrene due to its long lived excited states.[58] The formation of pyrene excimers requires a sufficient separation between neighboring pyrene molecules during light absorption in order for the excitation to be localized at one of the molecules. The diffusion of the molecules allows an excited and a ground state pyrene to form an excimer which will be dissociated upon relaxation to the ground state.[59] The excimer emission band is usually observed at ~460 nm and it is concentration dependent. This means that as the concentration of pyrene in solution or in the solid-state increases, the monomeric fluorescence emission peak (~375-405 nm) is quenched and the excimer emission is increased.[60]

Many Ln^{3+} ions exhibit photoluminescence upon ultraviolet excitation, and their emission covers the entire spectrum, from ultraviolet to visible and near-infrared. The emission wavelenght depends on the lanthanide ion but is almost independent of the environment of a given lanthanide ion. For example, Eu^{3+} and Tb^{3+} ions are notable for their red and green photoluminescence, respectively, with other lanthanide ions (i.e., Sm^{3+}, Dy^{3+}, and Tm^{3+}) also known for their emissions in the visible region. Pr^{3+}, Nd^{3+}, Ho^{3+}, Er^{3+}, and Yb^{3+} ions show near-infrared luminescence. Ultraviolet emission can be observed for Gd^{3+} but only in the absence of organic ligands with low-lying singlet and triplet levels. The emission bands of lanthanide ions arise from electronic transitions that

involve the *f*-electrons. Due to the shielding of the 4*f*-orbitals by the 5*s* and 5*p* orbitals, the promotion of an electron into a 4*f*-orbital of higher energy does not perturb much the bonding in the molecules and the internuclear distances remain almost the same in the excited state(s). As a result, the *f-f* emission lines possess sharp and narrow bands with very small Stokes' shifts. This is the main difference between the emission of Ln^{3+} ions and the emission of organic molecules in which excitation leads frequently to a lengthening of the chemical bonds, resulting in broad emission bands with large Stokes' shifts.

Since the molar absorption coefficients of most of the *f-f* transitions of the Ln^{3+} ions are very small, direct excitation in the 4*f*-levels rarely leads to intense photoluminescence. To overcome the problem of weak absorption, an alternative way has been developed which is known as the 'antenna effect'.[61] The emissive Ln^{3+} ion is coordinated to organic ligands which contain chromophore groups. Upon UV irradiation, the organic chromophores absorb much more light than the free Ln^{3+} ion due to their intense absorption bands. Then, the excitation energy is transferred from the organic ligands to the metal ion *via* intramolecular energy transfer. Finally, the characteristic metal-centered photoluminescence can be observed for the lanthanide coordination complex. Note that during the energy migration procedure many excited states of the Ln^{3+} ion may be involved. Another way to sensitize the lanthanide photoluminescence is through charge-transfer. This process only works well in the case of redox-active Ln^{3+} ions, such as Sm^{3+}, Eu^{3+} and Yb^{3+}, which can be easily reduced to their divalent state. During that process, light can be absorbed by an intense ligand-to-metal charge transfer state and from there the excitation energy can be transferred to the 4*f*-states of the Ln^{3+} ion.[62]

Finally, in order to sensitize the photoluminescence of near-infrared emitted lanthanides, such as Nd^{3+}, Er^{3+} and Yb^{3+}, strongly absorbing chromophores containing *d*-block metal ions are used due to their ability to absorb at longer wavelengths (visible region) than the common organic chromophores.[63] This process has been followed for many years in making inorganic phosphors for lighting applications.

Herein, we will focus on the energy transfer mechanism from the organic ligand(s) to the Ln^{3+} ion(s) (Figure 1.19). Upon UV irradiation, the organic ligands absorb light and an electron is promoted to a vibrational level of the first excited singlet state ($S_0 \rightarrow S_1$). This phonon undergoes fast internal conversion to the lowest vibrational level of the first excited singlet state (S_1), from where it can return to the ground state directly, through ligand fluorescence ($S_1 \rightarrow S_0$), or follow a non-radiative intersystem crossing from the excited singlet to a triplet state ($S_1 \rightarrow T_1$). From the triplet state, the phonon can be either deactivated radiatively to the ground state, through the spin forbidden $T_1 \rightarrow S_0$ transition which results in ligand phosphorescence, or, alternatively, undergo a non-radiative intersystem crossing, but this time to a nearby excited state of the lanthanide ion. This energy transfer generates an indirect excitation of the lanthanide ion which can deactivate radiatively to a lower 4*f*-state by characteristic photoluminescence or follow a non-radiative vibronic coupling with the ligand and/or solvent molecules.[64]

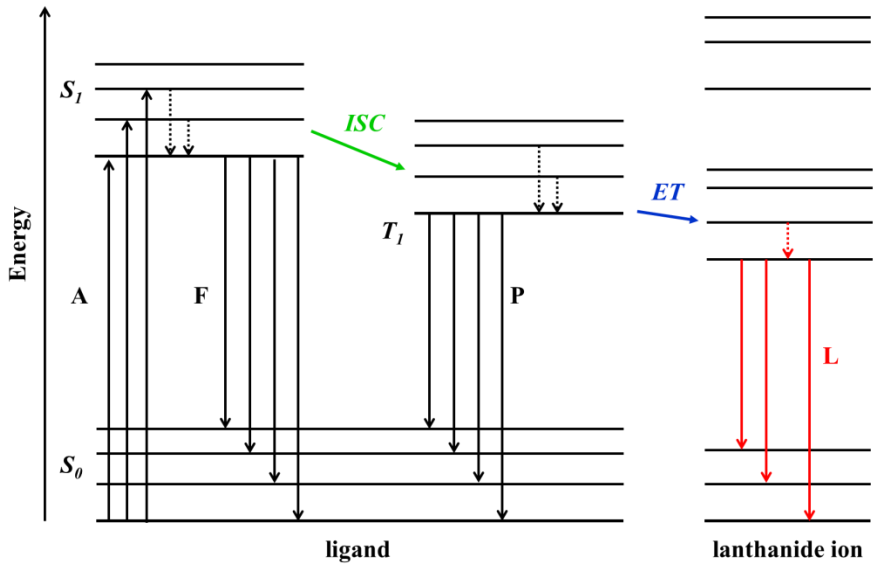

Figure 1.19. Schematic representation of the photophysical processes that could potentially take place in Ln^{3+} coordination complexes ('antenna effect'). Abbreviations: A = absorption; F = fluorescence; P = phosphorescence; L = lanthanide-centered luminescence; ISC = intersystem crossing; ET = energy transfer; S = singlet; T = triplet. Solid vertical lines indicate radiative transitions; dashed vertical lines indicate non-radiative transitions. Reproduced from Ref. 65.

An important factor in the design of efficient photoluminescent lanthanide complexes is the choice of the organic ligand, since this often controls the photoluminescent intensity of the compound through the energy transfer process. In order to achieve this, we have to consider that the emission of the Ln^{3+} ion is only possible from specific states, which are called resonance states. Resonance states are different for each lanthanide ion. During the energy transfer process it is possible for the Ln^{3+} ion to be excited to a non-emitting state. The excitation energy can be deactivated by internal conversion to the resonance state of

the Ln^{3+} ion, from where the metal-centered emission can de observed. In that case it is obvious that there will be a competition between the radiative and non-radiative processes. The basic requirement of an organic ligand to act as an efficient 'antenna' is its triplet state to be located in an energy level almost equal or above the resonance state of the lanthanide ion, but not below.[66] If the triplet state of the ligand is below the resonance state of the Ln^{3+} ion the excitation energy will not be transferred to the Ln^{3+} ion and it can be deactivated by molecular fluorescence or phosphorescence, or by a non-radiative process. Energy can be transferred back from the Ln^{3+} ion to the triplet state of the ligand if the two states are very close in energy. Thus, a close match in energy between the triplet state and the receiving 4*f*-state is not preferable either. Finally, it is occasionally possible to observe a combination of the ligand emission (fluorescence or phosphorescence) and the lanthanide-centered emission. In that case the energy transfer process is described as a not very efficient one.

1.5. Multifunctional Molecular Magnetic Materials

During the last three decades, the field of molecule-based materials has attracted the scientific interest of a large number of research groups worldwide due to their ability to exhibit a variety of technologically important properties such as conductivity, ferroelectricity and ferromagnetism.[67] After these discoveries, the synthesis of multifunctional molecular materials has become one of the most appealing targets for synthetic chemists and material scientists. Traditional multifunctional systems, i.e.,

materials that combine multiple features, usually include various composite or nanocomposite materials in which one of the components plays the role of the matrix and the other components with various tailored properties are integrated into the matrix.[68] The definition of multifunctional molecular materials relies on the combination of two or more physical properties in the same crystal lattice and covers a variety of different compounds.[69] Basically, a coordination or molecular compound can be seen as possessing at least two different physicochemical properties, named A and B. These two properties can be brought by two different moieties within the material as well as by a single entity. Several cases can be identified. The two functions can merely coexist; the material is then defined as "dual acting". Function B can modify function A. The two functions can interact to give rise to a third function. One of the functions can be influenced by an external stimulus. Finally, the external stimulus can influence both functions (Figure 1.20).[70]

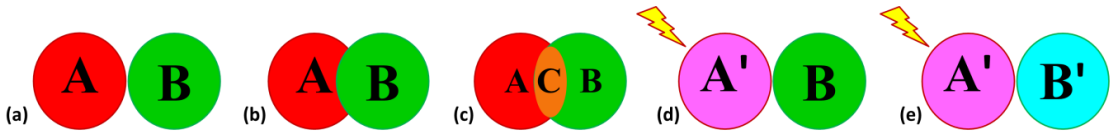

Figure 1.20. Multifunctional materials where (a) the two functions A and B coexist, (b) A is modified by B, (c) A and B give birth to a third function C, (d) A is modified by an external stimulus to yield A′, (e) both A and B are modified by an external stimulus to yield A′ and B′, respectively. Reproduced from Ref. 70.

Designing, synthesizing and studying multifunctional molecular materials is an appealing challenge for both chemists and physicists due to their unique properties and potential applications in disciplinary fields of fundamental and applied science. Among these, the addition of a second physical property to the magnetic one seems to be an attractive direction towards the construction of multifunctional molecular magnetic materials with potential applications in the new generation of molecule-based electronic devices, high-memory storage devices and spintronics. The main goal of this interdisciplinary field of research is to synthesize and explore new classes of coordination compounds that shall exhibit -besides single-molecule magnetism and/or ferromagnetism- another physical property, such as conductivity, photoluminescence and ferroelectricity.[70,71]

Several strategies for the synthesis of conductive single-molecule magnets have been developed, where sulfur-rich organic ligands or related metal complexes were always utilized. These sulfur-rich units may lead to molecular conductivity through interchalcogen atom-to-atom interactions, which are often observed in molecule-based conductors. The continuous research in this area has yielded important materials, such as paramagnetic superconductors,[72] antiferromagnetic superconductors,[73] and ferromagnetic metals.[74]

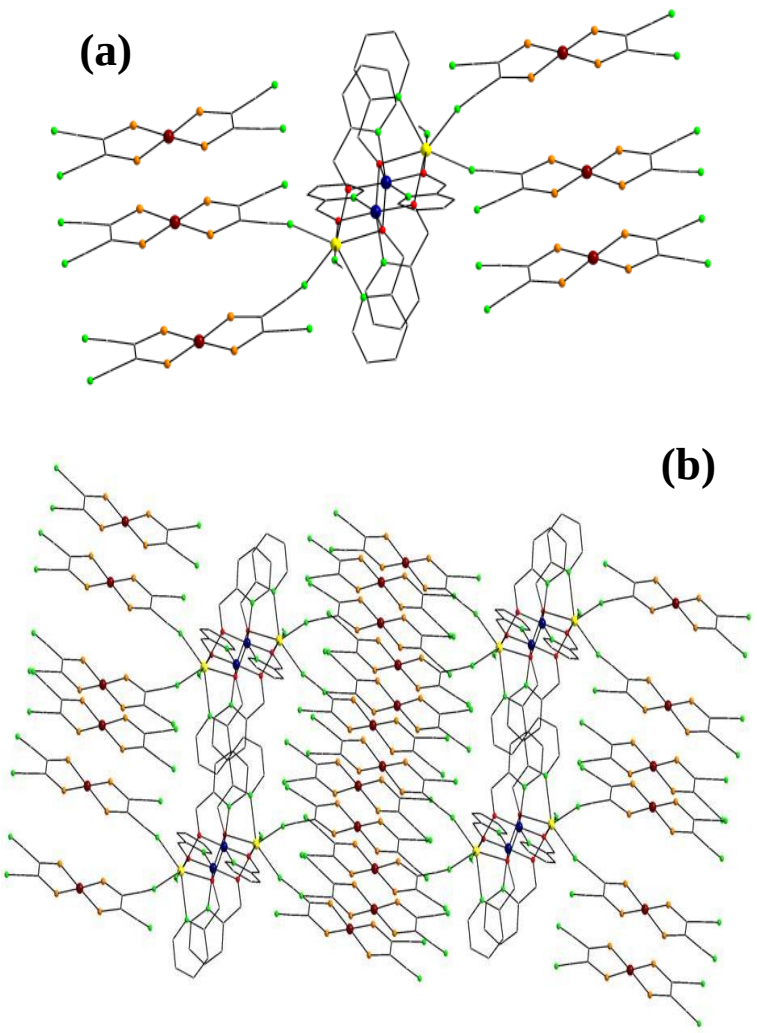

Figure 1.21. (a) Crystal structure of $[\{Mn^{II}_2Mn^{III}_2(hmp)_6(MeCN)_2\}\{Pt(mnt)_2\}_4][Pt(mnt)_2]_2$, and (b) the packing of the compound in the crystal. Color scheme: Mn^{II}, yellow; Mn^{III}, blue; Pt, dark red; N, green; O, red; S, orange; C, grey. H atoms are omitted for clarity. Reproduced from Ref. 78.

In 2007, Yamashita and coworkers reported the first example of a multifunctional molecular material exhibiting both SMM behavior and conductivity.[75] Using the tetranuclear SMM, $[Mn^{II}_2Mn^{III}_2(hmp)_6(MeCN)_2(H_2O)_4](ClO_4)_4$ (hmpH = 2-

hydroxymethylpyridine), and the molecular conductor, $(NBu_4)[Pt^{III}(mnt)_2]$ (mnt^{2-} = maleonitriledithiolate), as starting materials the authors were able to isolate a new $[\{Mn^{II}_2Mn^{III}_2(hmp)_6(MeCN)_2\}\{Pt(mnt)_2\}_4][Pt(mnt)_2]_2$ cluster (Figure 1.21a). The compound consists of a $\{Mn^{II}_2Mn^{III}_2\}$ double-cuboidal unit and six $[Pt(mnt)_2]^{0.66-}$ groups. The two Mn^{II} ions are seven-coordinate with distorted pentagonal-bipyramidal geometries while the two Mn^{III} ions are six-coordinate with distorted octahedral geometries. Among the $[Pt(mnt)_2]^{0.66-}$ groups, four are directly bound to the Mn^{II} ions and the remaining two do not participate in bonding but they occupy instead the void space on the crystal packing. The coordinated and the uncoordinated $[Pt(mnt)_2]^{0.66-}$ units are mutually stacked to form a segregated 1D double column (Figure 1.21b). The Pt ions have an average charge of +3.33, a fact that indicates the delocalization of the electrons in the $[Pt(mnt)_2]^{0.66-}$ network.

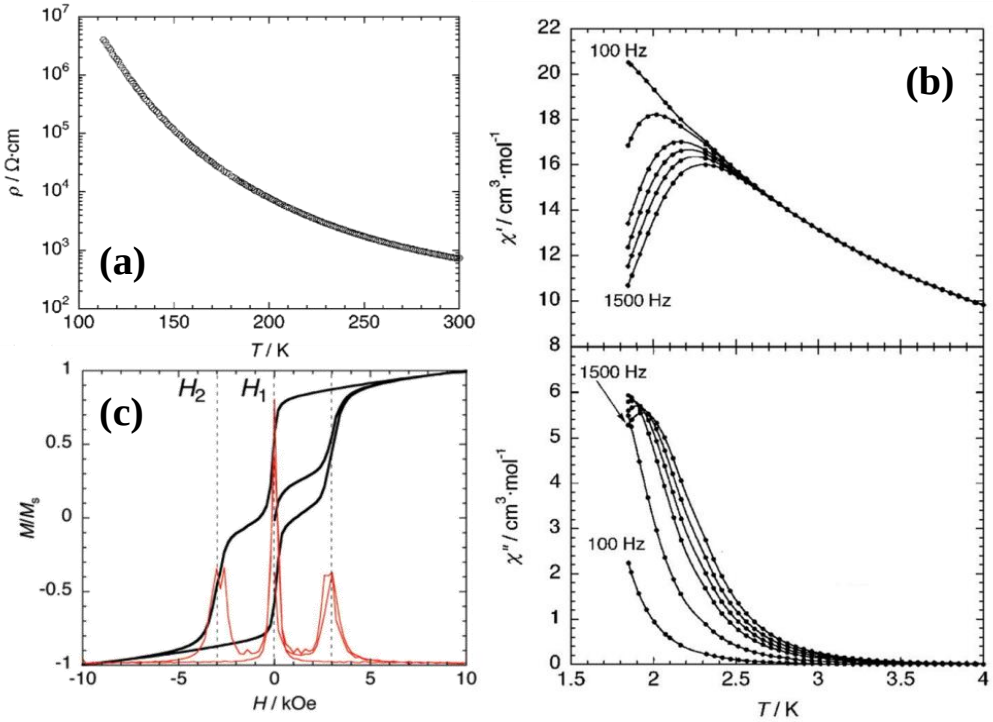

Figure 1.22. (a) Temperature-dependence of resistivity for a single-crystal of $[\{Mn^{II}_2Mn^{III}_2(hmp)_6(MeCN)_2\}\{Pt(mnt)_2\}_4][Pt(mnt)_2]_2$ using four-probe attachment along the $[Pt(mnt)2]^{0.66-}$ network; (b) Temperature-dependence of the *ac* susceptibilities of the compound measured at several frequencies in the range of 100-1500 Hz; and (c) field-dependence of magnetization measured on field-oriented single crystals of the complex at 470 mK and 2 Oe/s. Red lines represent d*M*/d*H* plots (arbitrary scale). Reproduced from Ref. 75 with permission from the American Chemical Society.

The magnetic properties of the compound were almost identical with these of the isolated Mn_4 SMM, and there are no significant intermolecular magnetic interactions between the Mn_4 units. The molecule exhibits frequency-dependent in-phase (χ') and out-of-phase (χ'') signals below 3 K (Figure 1.22b). The fit of the data to the Arrhenius-type equation gave an effective energy barrier U_{eff} = 18.7 K and $\tau_0 = 3.8 \times 10^{-8}$ s. A hysteresis loop with two distinct steps was observed at 0.47 K, which further confirms the SMM behavior of the compound (Figure 1.22c). Conductivity studies were performed in the temperature range of 300 to 5 K. The compound shows transport property when the probes are attached in the direction of the $[Pt(mnt)_2]^{0.66-}$ network. The conductivity at room temperature is σ = 0.22 $S \cdot cm^{-1}$, which decreases gradually with decreasing temperature; the system is no longer conductive at approximately 110 K (Figure 1.22a), as indicated by its semiconducting behavior with an activation energy of 136 meV between a valence band and a conducting band.

In recent years, there is an intense interest for the study of SMMs at the single-molecular level by placing them on conductive surfaces.[76] However, it can often be difficult to determine the exact position or dispersion of species deposited on surfaces. When SMMs with photoluminescent properties are employed, it may be possible to precisely ascertain the positions and concentration of molecules on surfaces. Therefore, the synthesis of such photoluminescent compounds could be valuable for the detection of single molecules, an issue of vital importance in the field of molecular electronics.[77]

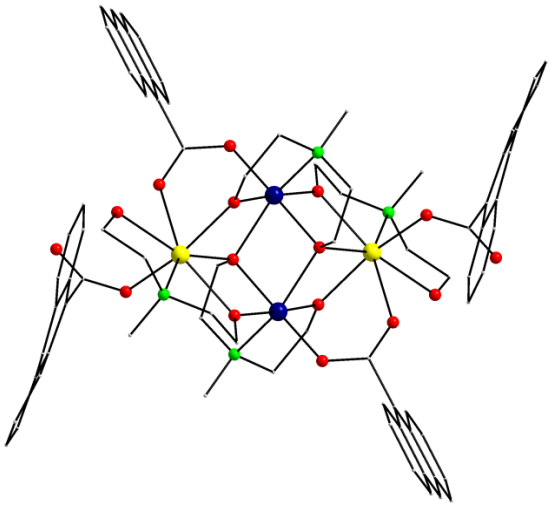

Figure 1.23. Crystal structure of $[Mn_4(anca)_4(Hmdea)_2(mdea)_2]$ cluster. Color scheme: Mn^{II}, yellow; Mn^{III}, blue; N, green; O, red; C, grey. H atoms are omitted for clarity. Reproduced from Ref. 78.

Hendrickson and coworkers synthesized a new $\{Mn_4\}$ emissive single-molecule magnet, $[Mn_4(anca)_4(Hmdea)_2(mdea)_2]$ (ancaH = 9-anthracenecarboxylic acid, $mdeaH_2$ = *N*-methyldiethanolamine), as depicted in Figure 1.23.[78] The complex consists of an alkoxido-bridged $[Mn^{II}_2Mn^{III}_2(OR)_6]^{4+}$ core resembling two face-sharing cubanes that

miss opposite vertices. The divalent Mn ions are seven-coordinate with distorted pentagonal-bipyramidal geometries, while the trivalent Mn ions are six-coordinate with distorted octahedral geometries.

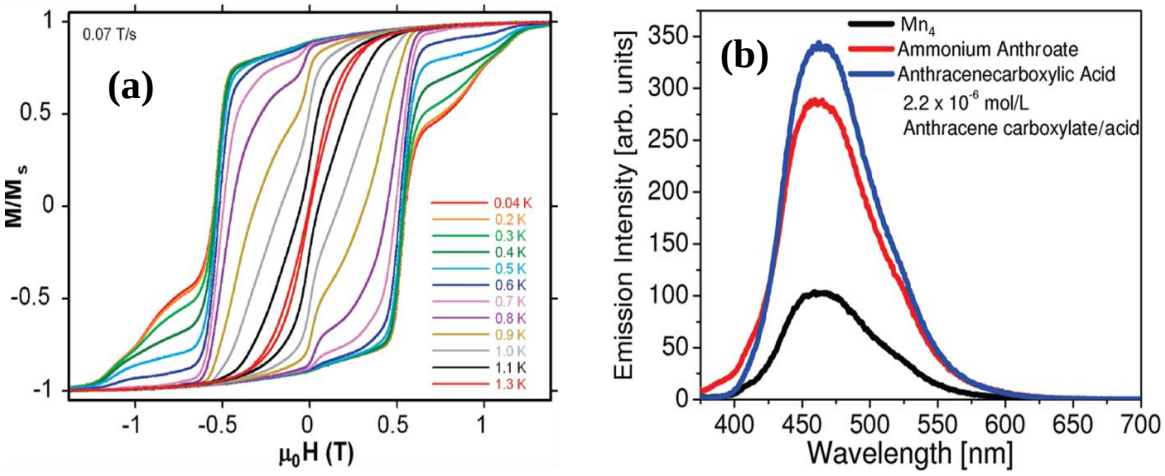

Figure 1.24. (a) Plot of temperature-dependent magnetization *vs.* field hysteresis loops for complex $[Mn_4(anca)_4(Hmdea)_2(mdea)_2]$, and (b) room-temperature fluorescence emission spectra for 9-anthracenecarboxylic acid (blue), ammonium 9-anthroate (red), and $\{Mn_4\}$ complex (black) at 10^{-6} M concentrations in solvent dichloromethane. Reproduced from Ref. 78 with permission from the American Chemical Society.

To determine if the complex is a SMM, single-crystal magnetization *vs.* field hysteresis experiments were performed. The steps in the temperature-dependent (Figure 1.24a) and field sweep-rate-dependent hysteresis loops were indicative of QTM and confirmed the SMM behavior of the compound. In addition, as shown in Figure 1.24b, the emission spectrum of the complex exhibits the same lines shape and peak positions (~460 nm) with

these of free 9-anthracenecarboxylic acid and ammonium 9-anthroate, indicating that the photoluminescent properties resulted from the four coordinated to the metal ions 9-anthracenecarboxylate groups. Compared to the free ligand, a significant quenching of the emission intensity for the compound was also seen, which was most likely due to paramagnetic effects.

Finally, another area where molecular materials can find applications is that of electro-magnetism through the synthesis of chiral-magnetic compounds. Since chirality can be controlled at the molecular level, it can be then delivered to the solid-state by using the appropriate chiral precursors. The control over the chirality of molecular materials has been actually applied mainly in magnetism, with the synthesis of chiral molecular magnets becoming a challenging, albeit very attractive, task due to the discovery of magnetochiral phenomena in various paramagnetic and chiral systems.[79] In particular, reactions of the chiral enantiomers 2-((E)-((R)-2,3-dihydroxypropyl-imino)methyl)-6-methoxyphenol (*R*-LH_3) and 2-((E)-((S)-2,3-dihydroxypropyl-imino)methyl)-6-methoxyphenol (*S*-LH_3) with $MnCl_2$ in the presence of NEt_3 have led to the isolation of the first nanoscale homochiral manganese complexes with both ferroelectric and ferromagnetic properties, namely the $\{[Mn^{II}Mn^{III}_3O(H_2O)_3(R\text{-}L)_3]_4[Mn^{III}_6Cl_4O_4]\}[Mn^{III}_3O(H_2O)_3(R\text{-}L)_3](OH)_4$ (*R*-Mn_{25}) and $\{[Mn^{II}Mn^{III}_3O(H_2O)_3(S\text{-}L)_3]_4[Mn^{III}_6Cl_4O_4]\}[Mn^{III}_3O(H_2O)_3(S\text{-}L)_3](OH)_4$ (*S*-Mn_{25}) clusters, respectively.[80]

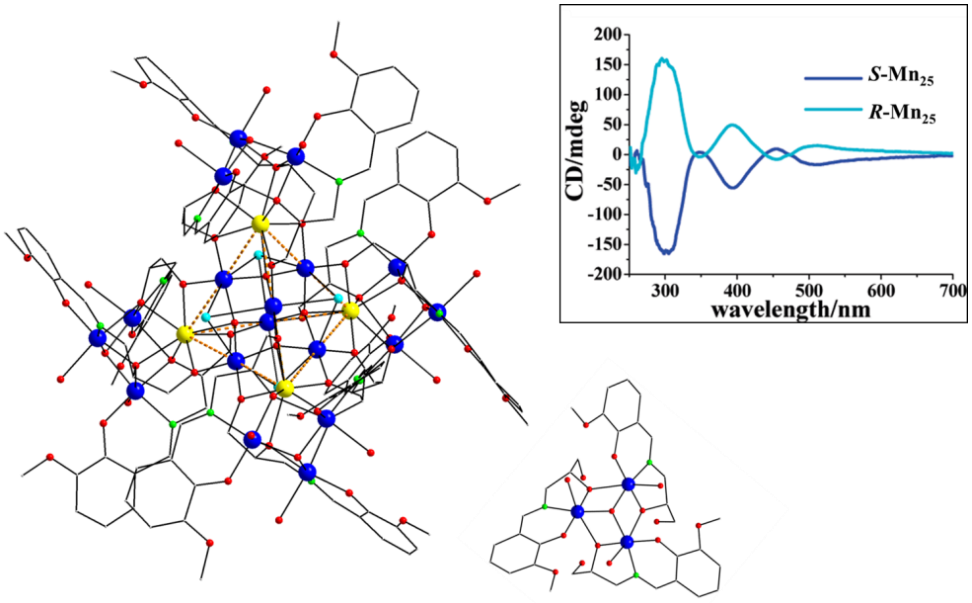

Figure 1.25. Crystal structure of the *R*-Mn_{25} cluster. Color scheme as in Figure 1.23. H atoms are omitted for clarity. Inset: CD spectra of *R*-Mn_{25} and *S*-Mn_{25} at room temperature ($2 \cdot 10^{-5}$ M in MeOH). Reproduced from Ref. 80 with permission from the Royal Society of Chemistry.

Both complexes crystallize in a chiral space group (R3), possessing C_3-symmetric structures composed of a $\{Mn_{22}\}$ cation and a $\{Mn_3\}$ anion (Figure 1.25). The $\{Mn_{22}\}$ cation comprises four $\{Mn^{II}\ Mn^{III}{}_3\}$ distorted cubane subunits that are linked around a $[Mn^{III}{}_6Cl_4O_4]^{6+}$ core *via* oxido bridges, generating a $[Mn^{II}{}_4Mn^{III}{}_6O_4]^{18+}$ supertetrahedron. There are also 15 chiral stereogenic centers from the 15 chiral Schiff-base ligands. Therefore, the *R*-Mn_{25} exhibited a strong positive Cotton effect at 300 nm and a positive dichroic signal centered at 394 nm, while the *S*-Mn_{25} showed Cotton effects of the opposite sign and at the same wavelengths (inset of Figure 1.25).

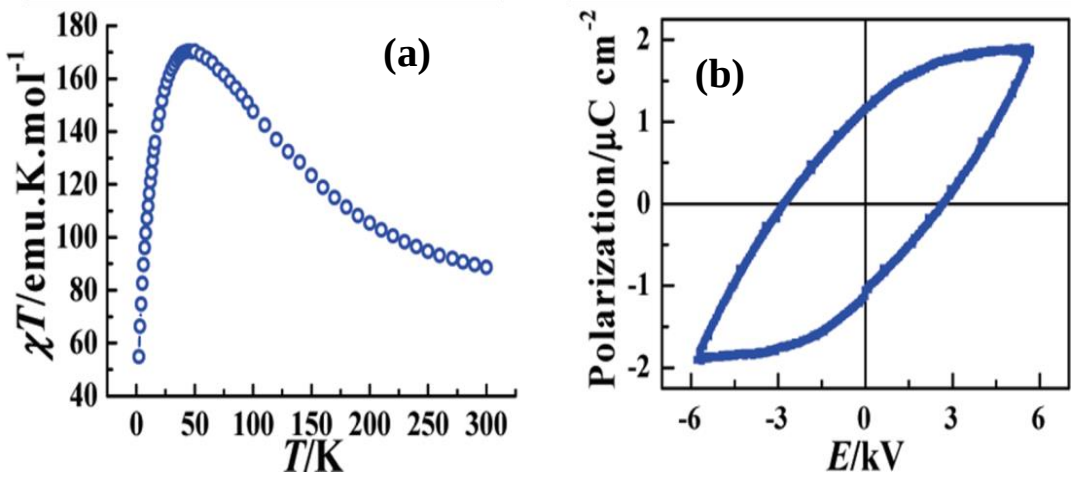

Figure 1.26. (a) Plot of χT *vs.* T for the R-Mn_{25} measured under a field of 1 kOe, and (b) electric hysteresis loop for a single-crystal of R-Mn_{25} at room temperature using a ferroelectric tester. Reproduced from Ref. 80 with permission from the Royal Society of Chemistry.

Magnetic and polarization studies were performed for the R-Mn_{25} compound. The continuous increase of the χT product, upon lowering the T, suggests predominant ferromagnetic interactions between the metal centers and consequently the stabilization of a large ground state spin value, S_T (Figure 1.26a). Above 150 K, the χ^{-1} *vs.* T plot follows the Curie-Weiss law with θ = 71.5 K and C = 71.4 emu K mol^{-1}. The positive θ value confirms the ferromagnetic behavior of the complex. The compound exhibits an electric hysteresis loop (Figure 1.26b), indicative of its ferroelectric behavior, with a remnant polarization (P_r) of 1.16 μC cm^{-2} and a coercive field (E_c) of 2.65 kV cm^{-2}.

In conclusion, the field of multifunctional molecular magnetic materials has experienced a very rapid development since the discovery that a variety of solid-state

properties, such as conductivity and superconductivity, photoluminescence, and ferroelectricity can be combined with magnetism. For the synthesis of such molecular materials, inorganic chemists usually rely on the versatility of the building blocks combined with a rational design that is mainly based on self-assembly rules. In addition, lanthanide ions exhibiting more intense magnetic dynamics than the first-row transition metals have become particularly popular in the synthesis of multifunctional magnetic materials, thereby providing a chance for improvement in the field.

1.6. Long- and Short-Term Research Objectives

The long-term objectives of the present thesis are the synthesis and complete characterization of: (i) new high-spin molecules and/or single-molecule magnets, and (ii) multifunctional molecular magnetic materials based on polynuclear metal complexes. For the accomplishment of the long-term objectives, our research endeavours have been organized into seven short-term research objectives, which are: (i) the synthesis of new, high-nuclearity manganese compounds bearing both pseudohalides and versatile alkoxido- or oximate-based chelating/bridging ligands, (ii) the synthesis of new 3*d*-metal cluster compounds with exclusively azides as bridging ligands, in the absence of any organic chelating/bridging ligand, as a means of obtaining very high-spin and ferromagnetic molecules and SMMs, (iii) the synthesis of emissive molecular nanomagnets based on 3*d*- and/or 4*f*-metal ions, (iv) the growth of single-crystals of all the desired products suitable for X-ray diffraction studies in order to elucidate their

crystal structures; this is a very difficult and demanding process given the fact that large in nuclearity cluster compounds frequently crystallize in irregular shapes and tiny sizes of crystals, (v) the complete spectroscopic and physicochemical characterization of the synthesized compounds in both solid-state and solution, utilizing IR, UV/Vis, electrochemistry, and elemental analyses techniques, (vi) the performance of *dc* and *ac* magnetic susceptibility studies in order to assess the magnetic properties and dynamics of the synthesized paramagnetic complexes, and (vii) the performance of solid-state photoluminescence studies in order to gain any possible access into additional physical properties, such as light emission in the visible part of the electromagnetic spectrum.

We decided to approach the synthesis of emissive molecular nanomagnets, or more simplistically emissive SMMs, from two different directions. The first approach includes the deliberate replacement of non-emissive carboxylato ligands in known 3*d*-metal SMMs with their fluorescent analogues, without perturbing the metal-core structure and SMM properties. The carboxylic acids chosen were all based on naphthalene, anthracene and pyrene (Scheme 1.2), all organic substituents with simple fluorophores but with numerous applications in optics.[81] The second route involves the use of polyalcohol bridging ligands (*vide infra*) as a means of obtaining new polynuclear Ln^{3+} metal clusters with novel topologies, enhanced SMM behaviors, and luminescent properties arising from the increased efficiency of the "antenna" organic group.

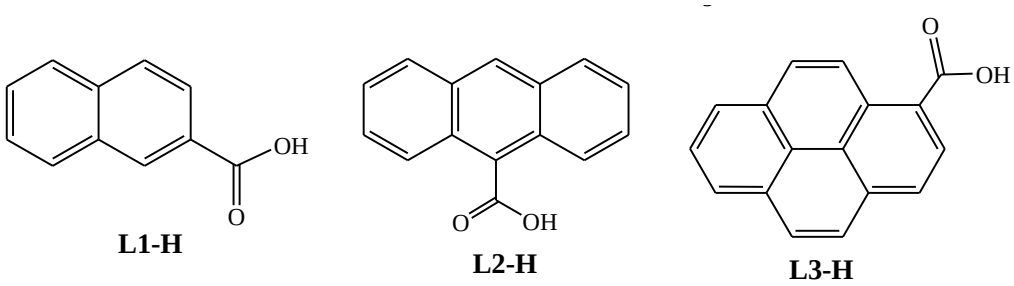

L1-H **L2-H** **L3-H**

Scheme 1.2. Structural formulae and abbreviations of the fluorescent carboxylate ligands used in the present dissertation. L1-H is 2-naphthoic acid; L2-H is 9-anthracenecarboxylic acid; L3-H is 1-pyrenecarboxylic acid.

1.7. Choices of Ligands and Metal Ions

An important factor in the synthesis of new polynuclear metal complexes is the choice of the primary organic chelating/bridging ligands or "ligand blends", since this often dictates not only cluster symmetry, topology and the number of paramagnetic metal ions present, but also the nature of the intramolecular magnetic exchange interactions and, in the case of Ln^{3+} complexes, the intensity of the photoluminescence properties. Polyalcohols (pyridyl and non-pyridyl) belong to one of the most well-known families of ligands in coordination cluster chemistry as a result of their remarkable versatility and bridging capacity.[31] They readily form stable complexes with most of the 3*d*- and/or 4*f*-metals. The idea here is that, upon deprotonation, each oxygen atom can, potentially, bridge up to three metal ions. The latter can be further bridged by O^{2-} and/or OH^{-} ions to form polymetallic complexes with interesting magnetic and/or photoluminescence

properties. The structures of the resulting compounds are expected to rely on: (i) the number of oxygen atoms and the level of deprotonation of the organic ligand(s), i.e., the mono-, di-, or tri-anionic forms, (ii) the presence of other donor atom(s) of the polyalcohol ligand(s), and (iii) the presence of additional ancillary bridging and/or terminal ligands, such as carboxylates and/or pseudohalides (i.e, N_3^-, OCN^-, etc).

Scheme 1.3 illustrates the four polyalcohol ligands used in this thesis. Previous use of these ligands in coordination chemistry has revealed (i) their ability in binding to both transition metal and lanthanide ions, (ii) their ability to bridge many metal centers but prevent polymer formation due to their readily formed chelate rings with the metal ions, and (iii) their dual role in both promoting fairly strong magnetic exchange interactions between the metal centers they bridge and enhancing the photoluminescence intensities of the Ln^{3+} complexes due to the aromatic group(s) they contain. Note that the $dpkdH_2$ ligand does not exist as a free species but only as a ligand in the respective metal complexes.[31] It derives from the metal-assisted hydration of the commercially available di-2-pyridyl ketone (dpk). The carbonyl group makes dpk a special ligand in coordination chemistry because upon coordination of the carbonyl oxygen atom to a metal center, a water molecule -among other nucleophiles- can add to the carbonyl group to form the ligand $dpkdH_2$, which is the *gem*-diol form of dpk. In cluster chemistry, the neutral form of $dpkdH_2$ is not very interesting but, upon single- or double-deprotonation, the corresponding mono- or dianionic forms can lead to a plethora of metal complexes with large nuclearities, nanoscale dimensions and interesting magnetic characteristics.

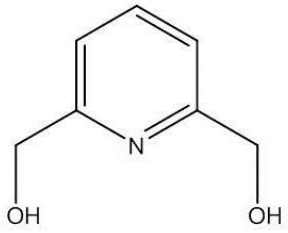

$pdmH_2$

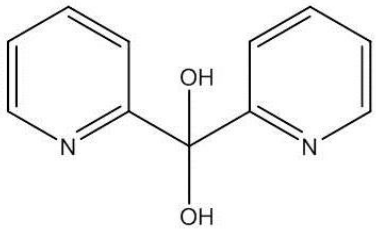

$dpkdH_2$

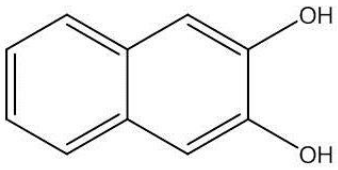

ndH_2

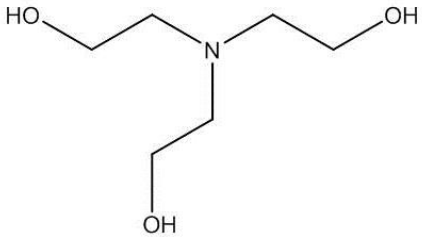

$teaH_3$

Scheme 1.3. Structural formulae and abbreviations of the polyalcohol ligands used in the present dissertation. $pdmH_2$ is pyridine-2,6-dimethanol; $dpkdH_2$ is the *gem*-diol form of di-2-pyridyl ketone; ndH_2 is naphthalene-2,3-diol; $teaH_3$ is triethanolamine.

The second family of organic ligands that we decided to explore in the synthesis of new polynuclear metal complexes with enhanced magnetic properties was that of 2-pyridyl mono- and di-oximes. Both ligands, as shown in Scheme 1.4, are not commercially available but their synthesis is quite straightforward and includes the addition of hydroxylamine to the corresponding aldehydes or ketones.

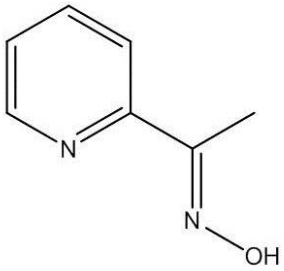

mpkoH

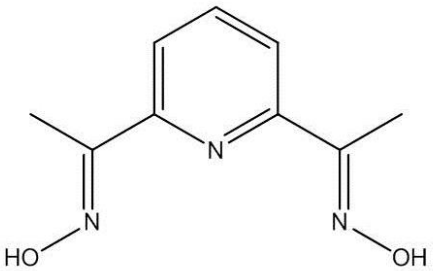

$dapdoH_2$

Scheme 1.4. Structural formulae and abbreviations of the two oxime ligands used in the present dissertation. mpkoH is methyl 2-pyridyl ketone oxime; $dapdoH_2$ is 2,6-diacetylpyridine dioxime.

There is currently a renewed interest in the coordination chemistry of oximes. The research efforts are driven by a number of considerations. These include the solution of pure chemical problems, the desire to make useful bioinorganic models (oximes are considered reasonable models for the biologically important imidazole donor group of the histidine amino acid), and the employment of oximato ligands in the synthesis of homometallic and heterometallic clusters and coordination polymers with interesting magnetic properties, including single-molecule magnetism and single-chain magnetism.

Carboxylates (RCO_2^-; R = various) are widely used in metal cluster chemistry as ancillary ligands since they display a variety of advantages upon coordination to the metal centers. They are bidentate bridging ligands, potentially capable of bridging up to five metal centers and thus fostering the formation of polynuclear metal clusters. They are also flexible and versatile bridging ligands, adopting a variety of different ligation modes (Scheme 1.5).[22b] Furthermore, they often occupy peripheral sites of a coordination

cluster, thus offering some additional thermodynamic and kinetic stability to the resulting crystalline products. Finally, they can also act as bases in solution, facilitating further the deprotonation of OH-containing groups.

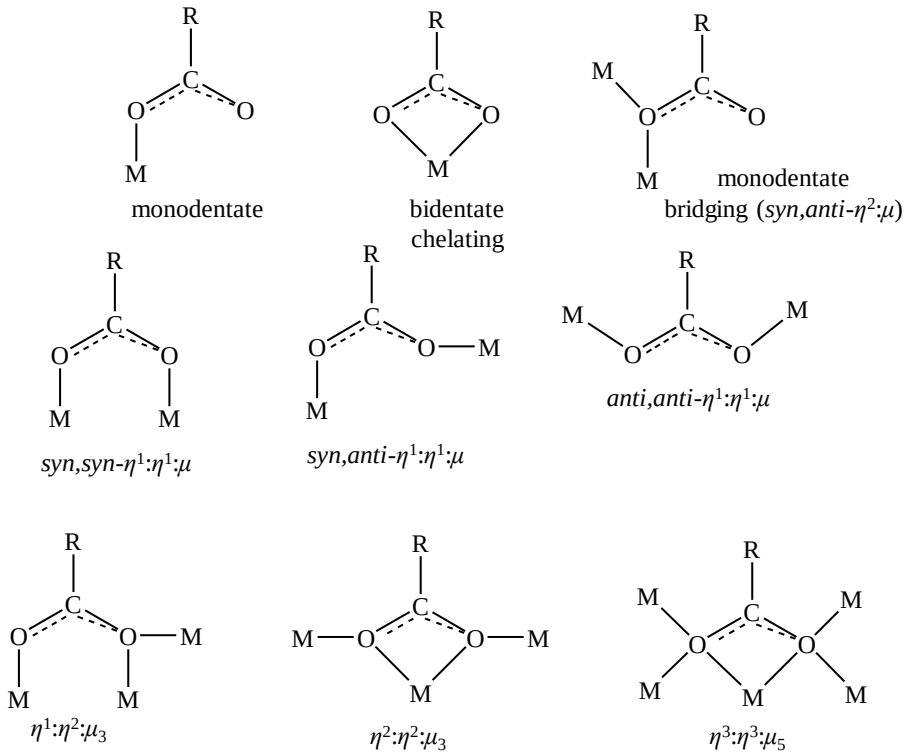

Scheme 1.5. The crystallographically established coordination modes of carboxylate ligands in metal cluster chemistry (R = various; M = metal). Symbols "η" and "μ" denote to the "hapticity" of the donor atoms and the "bridging" fashion of the entire group, respectively.

The wide variety of coordination modes for the RCO_2^- ions arises from the presence of four lone pairs on the two oxygen atoms which are donated to the metal ions for bond formation. Each lone pair is located on the plane of the carboxylate group. Due to steric

and electronic effects it has been proposed that the *syn*-lone pairs are more basic than the ones adopting the *anti*-conformation; this observation has been also confirmed by theoretical calculations.[22b] The preference of 3*d*-metal ions to bind to the *syn*-lone pair(s) of the RCO_2^- moiety is due to their basicity. The *syn*-lone pairs are involved in all frequently observed coordination modes of carboxylates, such as terminally-monodentate, bidentate-chelating, and bidentate-bridging. Most likely due to the lower basicity of the *anti*-lone pairs, coordination modes such as *anti*-(terminal-monodentate), *syn*-*anti*-(bidentate-bridging) and *anti*-*anti*-(bidentate-bridging) are rather scarce. The presence of a monoatomic bridge (Scheme 1.5, top right) is the only one that utilizes both *syn*- and *anti*-lone pairs of a single O atom for the formation of coordination bonds.

The azide ion (N_3^-) is one of the most commonly employed pseudohalide bridging ligands for the preparation of transition metal clusters and coordination polymers with characteristic and tunable physical properties.[82] It also participates as a terminal ligand in many metal complexes. When acting as a monoatomic bridge (end-on coordination mode, EO, Scheme 1.6), the azido ligand can link up to four metal ions; using both terminal nitrogen atoms, it can bridge two metal ions in an end-to-end coordination mode (EE, Scheme 1.6). Combining both the EO and EE modes (EE/EO), azido groups are capable of bridging up to six metal centers. All the crystallographically established bridging modes of the azido ligand in coordination chemistry are shown in Scheme 1.6. Sometimes, azido groups exhibiting two or even three different coordination modes coexist in the same cluster compound. The ability of the N_3^- ion to adopt EO and EE/EO modes makes it an ideal ligand for metal cluster formation. The azide ion is also

extremely versatile, which is reflected in totally unpredictable coordination chemistry with numerous structures, metal topologies and novel supramolecular motifs.

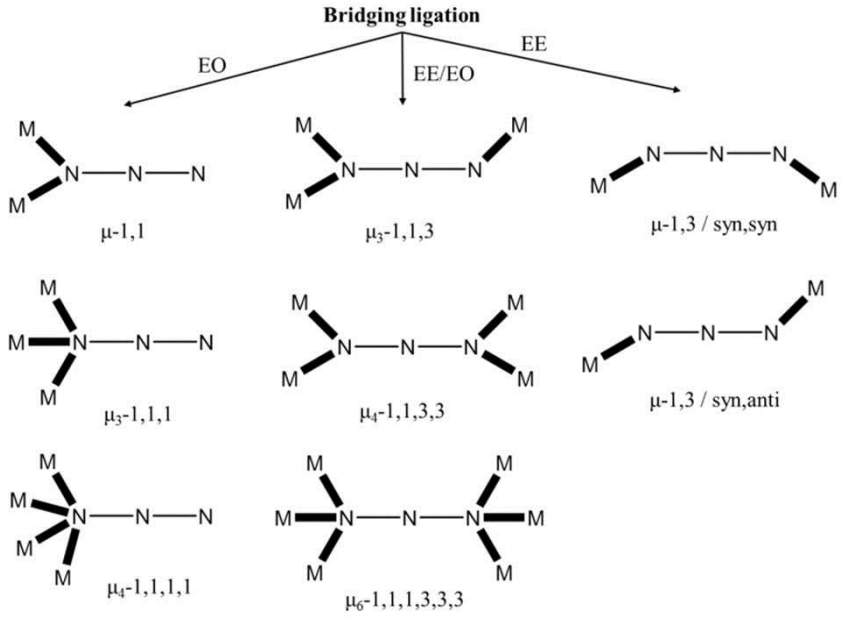

Scheme 1.6. Crystallographically established bridging modes of the azido ligand in coordination chemistry.[82]

The bridging azido ligand is also very popular in the field of Molecular Magnetism. Its different bridging modes and the ability to propagate a variety of magnetic exchange interactions have led to plentiful magnetic behaviors, such as ferromagnetism, antiferromagnetism, ferrimagnetism, canted ferromagnetism, spin-flop, SMM and SCM. In general, EE azido groups propagate antiferromagnetic (AF) interactions, whereas the EO coordination modes are associated with ferromagnetic coupling; exceptions to this general rule have been reported. The coordination mode is not the only factor that affects the magnetic coupling. Parameters such as bridging angles, dihedral angles, bond

distances, and factors such as strict and accidental orthogonality of magnetic orbitals, spin polarization and delocalization of unpaired electrons, including charge transfer, contribute significantly to the strength and sign of the magnetic coupling between the spin carriers.

Cyanate ion (OCN^-) also belongs to the general class of pseudohalides but its use in metal cluster chemistry could not compare to the impact of azides.[83] In contrast to the homoatomic-type azides (N_3^-), cyanates (OCN^-) consist of three heteroatoms and therefore two different types of donor atoms (O- and N-atoms). Thus, in principle, they provide the potential to bind to both lower oxidation state transition metal ions (soft or moderate hard Lewis acids) through their N-atom (soft or moderate hard donor atom) and/or to higher oxidation state metal ions (hard Lewis acids) through their O-atom (hard donor atom). The OCN^- ion has been found to exhibit a wide variety of coordination modes (Scheme 1.7).

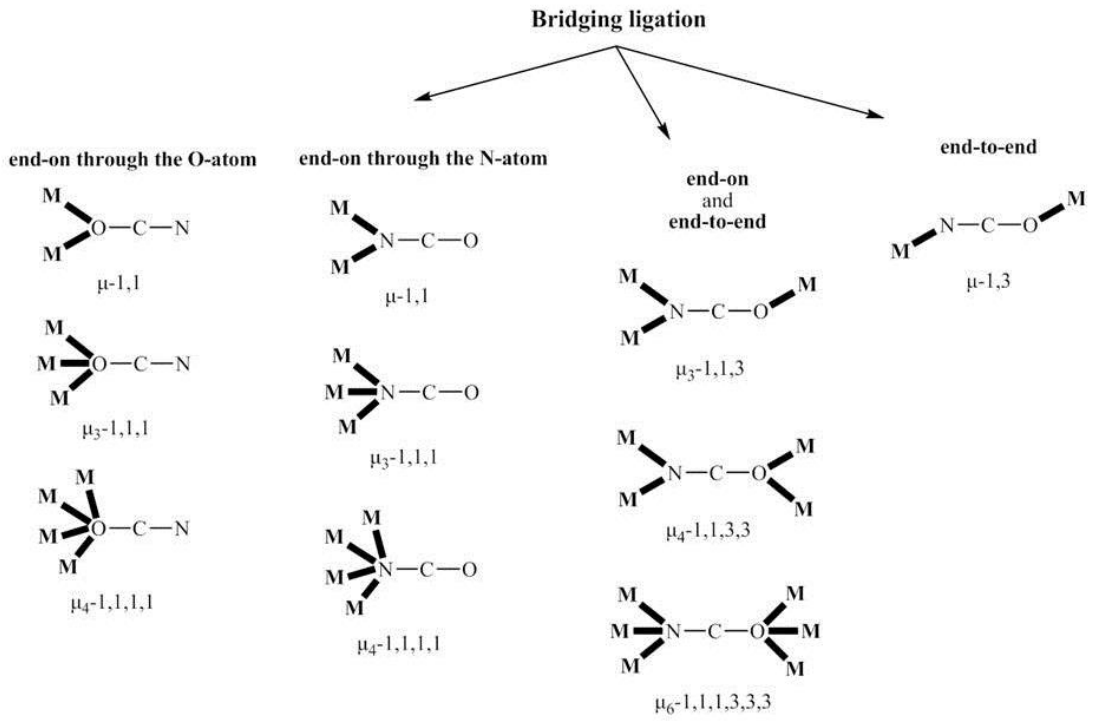

Scheme 1.7. The proposed bridging modes of cyanates in transition metal complexes, some of which have been also crystallographically established in divalent metal chemistry.

From the magnetism perspective, cyanates have been almost always employed in M^{2+}-chemistry (M = metal) mainly for magnetostructural reasons, i.e. for comparison of the strength of the magnetic exchange interactions between structurally similar M^{2+}/N_3^- and M^{2+}/OCN^- complexes. From such comparison studies on several divalent molecular systems, as well as on structurally characterized coordination polymers, it was found that the end-on cyanato ligands (Scheme 1.7) promote stronger ferromagnetic coupling than the analogous end-on azido species. The structurally-characterized cyanato-based 3*d*-metal complexes are much less in number compared to the corresponding azido species,

and in all cases the former products are isostructural with the latter. Thus, the highest nuclearity M^{2+}/OCN^- complex to date is a nonanuclear $\{Fe^{II}_9\}$ cluster which comprises an isomorphous structure with the $\{Co^{II}_9\}$ and $\{Ni^{II}_9\}$ analogues, and is also the only cyanato-bridged SMM discovered to date.[83b]

The choice of the 3*d*-metal ions for the synthesis of nanoscale molecular magnetic compounds is of significant importance because it governs the overall magnetic behavior and chemical reactivity towards the construction of large families of different cluster compounds with dissimilar properties, i.e. high-spin molecules and SMMs. The metal ions of choice need to be paramagnetic ($S \neq 0$) and also possess a non-zero magnetic anisotropy as reflected in an appreciable zero-field splitting parameter, *D*.[35] To that end, the 3*d*-metal ions of choice for the present research were Mn^{n+} (n = 2, 3, or 4), Fe^{n+} (n = 2 or 3) , Co^{2+}, and Ni^{2+}.

Manganese clusters are often characterized by large spin ground states; this characteristic, in combination with the Jahn-Teller distortion of high-spin Mn^{3+} ions (Mn^{3+}: [Ar]3d^4) in near-octahedral geometry which is the source of the single-ion anisotropy, make manganese clusters ideal candidates for SMM behavior. Thus, it is not surprising that the majority of SMMs are Mn^{3+}-containing complexes of various nuclearities and different structural types, as well as mixed-valence Mn^{2+}/Mn^{3+} and Mn^{3+}/Mn^{4+}.[33a,36,38,43] Despite this, there is a continuing need for Mn-SMMs exhibiting new structural types in order to improve our understanding on this exciting phenomenon. The paramagnetic nature of iron in its common oxidation states can often lead to interesting magnetic properties for its polynuclear complexes, such as high ground state spin values and single-molecule magnetism. High-spin Fe^{3+} ions have a relatively large

number of unpaired electrons ([Ar]3d^5, S = 5/2) but they usually interact strongly and in an antiferromagnetic way, thus cancelling their spins out and yielding small ground state spin values.[84] On the other hand, high-spin Fe^{2+} ([Ar]3d^6) is ideally suited for the preparation of SMMs, since it combines a large spin (S = 2) with a significant single-ion magnetic anisotropy; with the appropriate ligands bridging the Fe^{II} centers, ferromagnetic interactions can be also promoted and high-spin molecules may result.[85]

Another good candidate for the construction of new SMMs is Co^{2+} ([Ar]3d^7). In order to explain the complex magnetic behavior of Co^{2+} complexes we have to take into account the presence of spin-orbit coupling effects. The magnetic properties of octahedral (O_h) Co^{2+} ion are highly affected by the local symmetry.[86] Distortions from the O_h geometry lift the degeneracy of the $^4T_{1g}$ ground state and generate two new states, the $^4A_{2g}$ and the ^4E_g (Figure 1.27). For a tetragonal distortion, the $^4A_{2g}$ becomes the new ground state, with the ^4E_g becoming the excited state. The presence of strong spin-orbit coupling upon these levels generates six Kramer's doublets with M = ±1/2 ground state and M = ±3/2 excited state. The separation between the M = ±1/2 ground state and M = ±3/2 excited state of the $^4A_{2g}$ state can be considered as the ZFS (D parameter). Thus, at high temperatures (> 77 K) the magnetic behavior of Co^{2+} would be consistent with an S_i = 3/2 spin state, with the orbital contributions being incorporated into D. At low temperatures, where only the M = ±1/2 ground state will be populated, Co^{2+} possesses an effective spin, S' = 1/2, with the orbital contributions being incorporated into the principal effective g'-values, which are anisotropic.

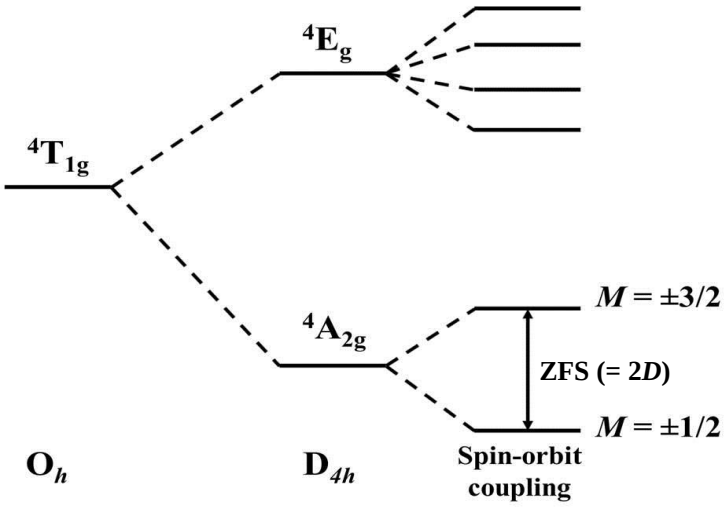

Figure 1.27. The combined effect of a tetragonal distortion and spin-orbit coupling on the energy levels of a high-spin Co^{2+} ion. Reproduced from Ref. 86.

During the last years, Ni^{2+} ions have shown some promise towards the synthesis of SMMs. Ni^{2+} is known to often adopt a distorted octahedral coordination geometry when surrounded by O- and/or N-donor ligands, thus possessing an [Ar]3d^8 electronic configuration with 2 unpaired electrons and an S = 1 spin-only value. Further, mononuclear Ni^{2+} complexes have been shown to possess appreciable |D| values, e.g., >10 cm^{-1},[87] thus allowing us to consider Ni^{2+} as a promising candidate for the delivery of SMM behavior in its corresponding cluster compounds.

Due to the unique electronic properties of lanthanide ions, their coordination complexes can exhibit not only SMM behavior but also photoluminescence properties. In the molecular magnetism field, the basic requirement for the 4*f*-metal ions is to possess a bistable ground m_J state. Also, this ground state should be large in magnitude and well-

separated from the first excited state.[48a] For these reasons, the lanthanide ions used in the present research were mainly the Dy^{3+} and Tb^{3+}. Both Dy^{3+} and Tb^{3+} ions are highly anisotropic but due to different reasons. Dy^{3+} is a Kramer's ion and it has an odd number of electrons, possessing an [Xe]$4f^9$ electronic configuration. For Kramer's ions, the ground state will always be bistable regardless of the ligand-field symmetry (Figure 1.28). For non-Kramer's ions, such as Tb^{3+} ([Xe]$4f^8$), the ground state may be arranged as singlet or doublet, and thus the bistability of the ground state will result from the appropriate ligand-field environment.[88] In order to identify the type and strength of the magnetic interactions between lanthanide ions, Gd^{3+} ([Xe]$4f^7$) complexes, usually isostructural to the Dy^{3+} and Tb^{3+} analagues, shall be synthesized.[89] Gd^{3+} has a half-filled 4*f*-shell with seven electrons and no orbital angular momentum, thus the contributions to its magnetic behavior is only from a pure $S = 7/2$ spin state.

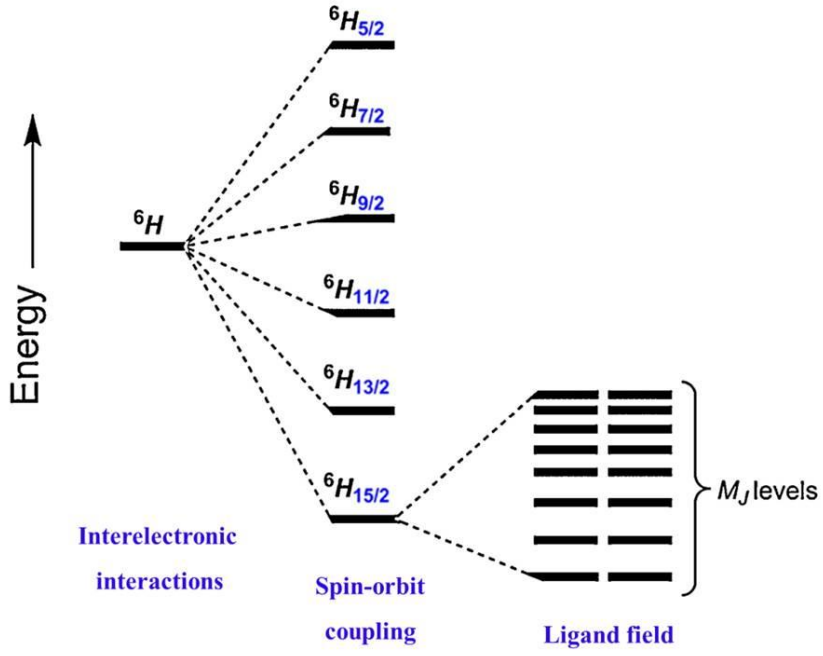

Figure 1.28. The [2J + 1] sublevels with quantum number m_J created by the effect of a ligand-field on the $^6H_{15/2}$ ground state of a Dy^{3+} ion. Not all ^6H_J states of the Dy^{3+} ion are shown. The sixteen m_J sublevels of $^6H_{15/2}$ are arranged into eight Kramer's doublets. Reproduced from Ref. 88.

In the field of photoluminescence, Eu^{3+} and Tb^{3+} complexes are the most studied lanthanide complexes due to their intense and long-lived emissions. Eu^{3+} complexes, which unfortunately are magnetically non-interesting (J = 0), display strong red photoluminescence due to electronic transitions from the lowest in energy emissive state, $^5D_0$, to one of the ^7F_J (J = 0-4) sublevels (Figure 1.29). The most intense peaks are commonly observed for the $^5D_0 \rightarrow {}^7F_1$ and $^7F_2$, while the $^5D_0 \rightarrow {}^7F_4$ emission peak has usually a moderate intensity. The $^5D_0 \rightarrow {}^7F_3$ emission is always weak and the $^5D_0 \rightarrow {}^7F_0$ emission is rarely observed since it is very sensitive to the ligand environment.[90]

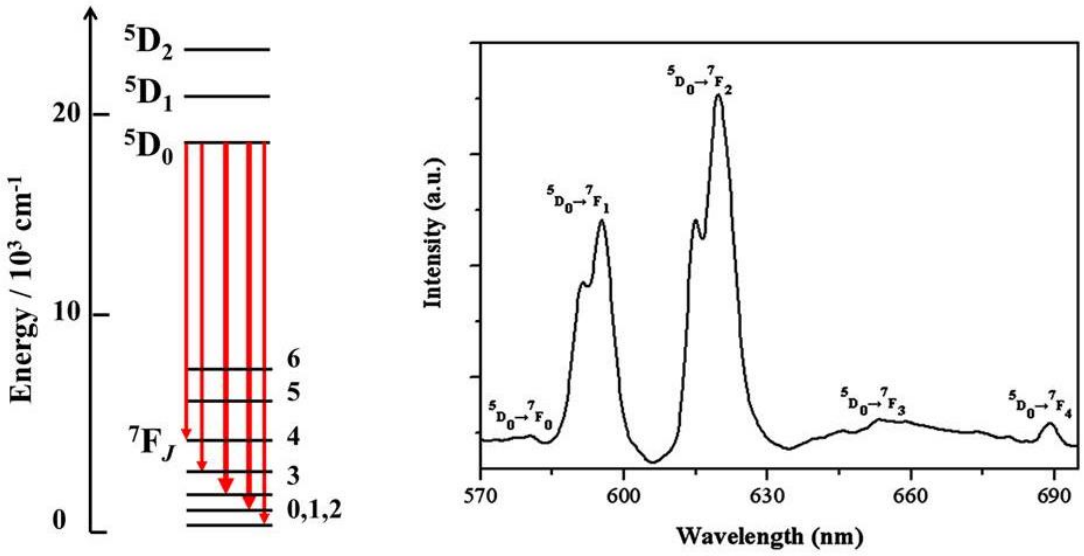

Figure 1.29. The energy levels (left) and emission spectrum (right) of Eu^{3+} ion. Reproduced from Ref. 91 with permission from the American Chemical Society.

For Tb^{3+} complexes, the strong green photoluminescence arises from electronic transitions from the $^5D_4$ state to each of the ^7F_J (J = 0-6) states, with the $^5D_4 \rightarrow {}^7F_5$ transition corresponding to the most intense and sharp peak (Figure 1.30). The $^5D_4 \rightarrow {}^7F_{0,1}$ emissions are rarely observed and they are very weak, while the intensities of the remaining peaks follow the order $^5D_4 \rightarrow {}^7F_6 > {}^7F_4 > {}^7F_3 > {}^7F_2$.[90]

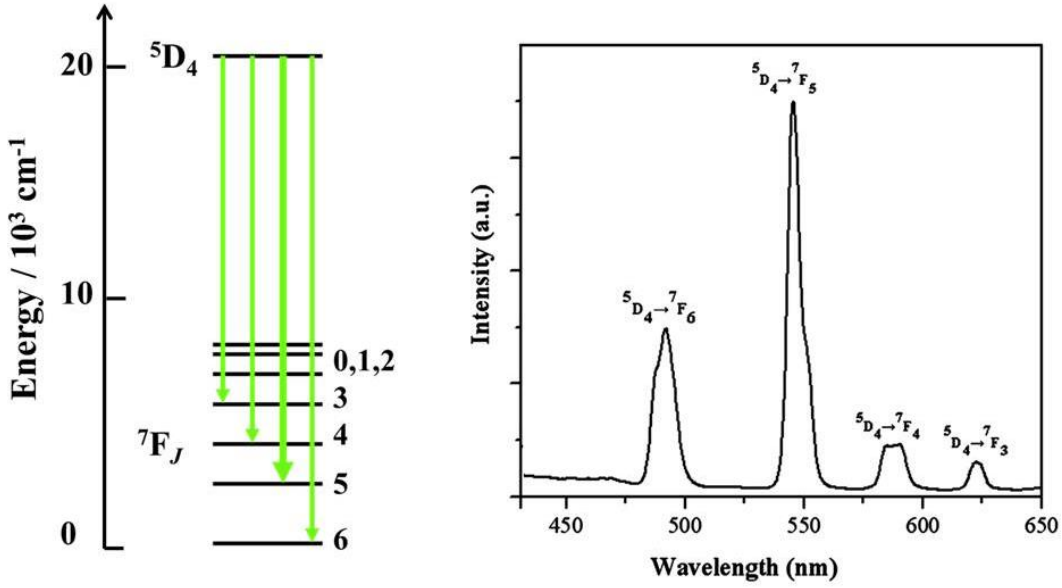

Figure 1.30. The energy levels (left) and emission spectrum (right) of Tb^{3+} ion. Reproduced from Ref. 91 with permission from the American Chemical Society.

CHAPTER 2: New High-Spin Molecules and SMMs of Manganese Bearing Alkoxido- and/or Oximate-Based Chelating/Bridging Ligands: $\{Mn_{14}\}$, $\{Mn_{16}\}$ and $\{Mn_{15}Na_2\}$

2.1. Experimental Section

2.1.1. Physical Measurements

Elemental Analysis: Elemental analyses (C, H, and N) were performed on a Perkin-Elmer 2400 Series II Analyzer.

FT-IR spectroscopy: Infrared (IR) spectra were recorded in the solid state on a Bruker FT-IR spectrometer (ALPHA Platinum ATR single reflection) in the 4000-450 cm^{-1} range. Notation for IR bands: vs, very strong; s, strong; m, medium; mb, medium broad; w, weak; b, broad.

Magnetic susceptibility measurements: Variable-temperature direct current (*dc*) and alternating current (*ac*) magnetic susceptibility data were collected at the University of Florida using a Quantum Design MPMS-XL SQUID susceptometer equipped with a 7 T magnet and operating in the 5-300 K range. The Superconducting QUantum Interference Device (SQUID) allows for the complete *dc* and *ac* study of the magnetic properties of bulk and molecule-based materials at various temperatures and magnetic fields. The *dc* scan mode provides continual plotting and capture of raw magnetic data points at static or

sweeping fields and temperatures. The *ac* susceptibility mode uses an oscillating magnetic field; this measurement uses the MPMS SQUID to measure the *ac* susceptibility of a sample. This is of vital importance for the study of bistability (magnetization relaxation and quantum phenomena) associated with the anisotropic and paramagnetic nature of the materials (both molecule-based and bulk). Many materials display dissipative mechanisms when exposed to an oscillating magnetic field, and their susceptibility is described as having real and imaginary components – the latter being proportional to the energy dissipation in the sample. The key is resolving the component of the sample moment that is out-of-phase with the applied *ac* field. SQUID technology is the measurement system of choice because it offers a signal response that is virtually flat over a broad frequency range (0.1Hz to 1 kHz). In a SQUID system, the output voltage is proportional to the magnetic flux in the pick-up coil instead of its time derivative as in conventional *ac* systems. Herein, the samples were embedded in solid eicosane to prevent torquing. Alternating current magnetic susceptibility measurements were performed in an oscillating *ac* field of 3.5 G and a zero *dc* field. The oscillation frequencies were in the 5-1500 Hz range. Pascal's constants were used to estimate the diamagnetic corrections, which were subtracted from the experimental susceptibilities to give the molar paramagnetic susceptibilities (χ_M).[92] Low-temperature (< 1.8 K) hysteresis studies and *dc* relaxation measurements were performed at Grenoble using an array of micro-SQUIDS.[93] The high sensitivity of this magnetometer allows the study of single crystals of SMMs of the order of 10-500 μm. The field can be applied in any direction by separately driving three orthogonal coils. Crystals were maintained in mother liquor to

avoid degradation and were covered with grease for protection during transfer to the micro-SQUID.

2.1.2. Synthesis

General considerations: All experiments were performed under ambient conditions. All chemicals were purchased from Sigma Aldrich and Alfa Aesar. Chemicals and solvents were used as received without further purification. The ligand dapdoH_2 was synthesized as previously reported.[94]

Safety note: Azide (N_3^-) and perchlorate (ClO_4^-) salts are potentially explosive; such compounds should be synthesized and used in small quantities, and treated with utmost care at all times.

$[Mn_{14}O_4(OH)_2(OCN)_6(O_2CMe)_2(dpkd)_8(DMF)_2(H_2O)_4](OH)_2$ (1): To a stirred, pale yellow solution of dpk (0.18 g, 1.0 mmol) and NEt_3 (0.14 mL, 1.0 mmol) in MeCN/DMF (25 mL, 4:1 v/v) were added solid $NaO_2CMe{\cdot}3H_2O$ (0.27 g, 2.0 mmol) and NaOCN (0.07 g, 1.0 mmol). The obtained solution was stirred for 15 min and then solid $Mn(ClO_4)_2{\cdot}6H_2O$ (0.36 g, 1.0 mmol) was added under vigorous stirring. The resulting orange solution was stirred for 24 h, during which time all the solids dissolved and the color of the solution changed to dark brown. The solution was filtered, and the filtrate was left undisturbed at ambient temperature. After 10 days, X-ray quality dark red plate-like crystals of **1**·*x*DMF·*y*H_2O appeared and were collected by filtration, washed with MeCN (2 × 5 mL) and Et_2O (4 × 5 mL), and dried under vacuum. The yield was 60%.

Elemental analysis (%) calcd for **1**·DMF: C 40.62, H 3.28, N 11.07; found C 40.60, H 3.25, N 11.38. Selected IR data (ATR): ν = 3442 (mb), 2180 (vs), 1656 (s), 1598 (s), 1570 (m), 1474 (w), 1436 (s), 1298 (w), 1214 (m), 1150 (m), 1116 (m), 1076 (m), 1044 (m), 1016 (s), 958 (w), 822 (w), 780 (m), 758 (m), 680 (m), 654 (m), 636 (s), 554 (m), 414 (w).

$[Mn_{16}O_8(OH)_4Cl_2(OCN)_4(L)_2(dapdo)_6(DMF)_4]$ (2): To a stirred, pale yellow solution of $dapdoH_2$ (0.10 g, 0.5 mmol) and NEt_3 (0.14 mL, 1.0 mmol) in MeCN/DMF (25 mL, 4:1 v/v) was added solid NaOCN (0.03 g, 0.5 mmol). The obtained solution was stirred for 15 min and then solid $MnCl_2·4H_2O$ (0.20 g, 1.0 mmol) was added under vigorous stirring. The resulting red solution was stirred for 45 min, during which time all the solids dissolved and the color of the solution changed to dark brown. The solution was filtered, and the filtrate was left undisturbed at ambient temperature. After 3 days, X-ray quality dark brown prismatic crystals of **2**·x(solv) had appeared and were collected by filtration, washed with MeCN (2 × 5 mL) and Et_2O (4 × 5 mL), and dried under vacuum. The yield was 45%. Elemental analysis (%) calcd for the lattice solvent-free **2**: C 33.09, H 3.09, N 14.03; found: C 32.79, H 3.14, N 13.86. Selected IR data (ATR): ν = 3440 (mb), 2182 (vs), 1654 (m), 1594 (s), 1534 (m), 1450 (m), 1390 (s), 1268 (w), 1166 (w), 1128 (m), 1050 (vs), 802 (m), 742 (w), 690 (m), 668 (mb), 624 (m), 564 (m), 484 (m), 425 (w).

$[Mn_{15}Na_2O_8(OH)_2(OMe)(N_3)_2(O_2CH)(O_2CBu^t)_{11}(tea)_4(MeOH)]$ (3): To a stirred, colorless solution of $teaH_3$ (0.13 mL, 1.0 mmol) and NEt_3 (0.14 mL, 1.0 mmol) in MeCN/MeOH (15 mL, 2:1 v/v) were added solid $NaO_2CBu^t·H_2O$ (0.25 g, 2.0 mmol) and NaN_3 (0.13 g, 2.0 mmol). The obtained solution was stirred for 15 min and then solid $Mn(ClO_4)_2·6H_2O$ (0.36 g, 1.0 mmol) was added under vigorous stirring. The resulting red

solution was stirred for 10 h, during which time all the solids dissolved and the color of the solution changed to dark brown. The solution was filtered, and the filtrate was left undisturbed at ambient temperature. After 3 days, X-ray quality brown needle-like crystals of **3** had appeared and were collected by filtration, washed with cold MeCN (2 × 5 mL), and dried under vacuum. Typical yields were in the 40-45% range. Elemental analysis (%) calcd for **3**: C 33.72, H 5.42, N 4.79; found: C 33.51, H 5.28, N 4.96. Selected IR data (ATR): ν = 3450 (mb), 2958 (m), 2870 (w), 2101 (s), 1600 (s), 1556 (vs), 1480 (m), 1409 (vs), 1367 (m), 1223 (m), 1080 (m), 900 (m), 780 (w), 697 (m), 663 (mb), 600 (m), 564 (w), 442 (m).

2.1.3. Single-crystal X-ray Crystallography

Single-crystal X-ray diffraction measurements were carried out on all three complexes **1**-**3**. For complex **1**, data were collected on an Oxford Diffraction Xcalibur-3 diffractometer (equipped with a Sapphire CCD area detector) using a graphite-monochromated Mo Ka radiation (λ = 0.71073 Å). A suitable crystal of **1**·*x*DMF·*y*H_2O was attached to glass fibers using silicone grease and transferred to a goniostat where it was cooled to 100 K for data collection. Data were collected using the ω-scan method (0.75° frame width). Empirical absorption corrections were applied using the CRYSALIS RED software.[95] The structure was solved by direct methods using SHELXS-97,[96] and refined on F^2 using full-matrix least-squares with SHELXL-97.[97] The non-H atoms were treated anisotropically, whereas the H atoms were placed in calculated, ideal positions and refined as riding on their respective C atoms. The programs used were CRYSALIS

CCD[95] for data collection, CRYSALIS RED[95] for cell refinement and data refinement and WINGX[98] for crystallographic calculations.

A single-crystal of complex **2**·*x*(solv) was manually harvested and mounted on a cryoloop using FOMBLIN Y perfluoropolyether vacuum oil (LVAC 25/6).[99] Diffraction data were collected at 150.0(2) K on a Bruker X8 Kappa APEX II Charge-Coupled Device (CCD) area-detector diffractometer controlled by the APEX2 software package[100] (Mo Kα graphite-monochromated radiation, λ = 0.71073 Å), and equipped with an Oxford Cryosystems Series 700 cryostream monitored remotely with the software interface Cryopad.[101] Images were processed with the software SAINT+,[102] and absorption was corrected using the multi-scan semiempirical method implemented in SADABS.[103] The structure was solved by direct methods employed in SHELXS-97,[96] allowing the immediate location of the majority of the heaviest elements. The remaining, non-H-atoms were located from difference Fourier maps, calculated by full-matrix least-squares refinement cycles on F^2 using SHELXL-97,[97] and refined with anisotropic displacement parameters.

Data for a selected crystal of **3** were collected at Station 11.3.1 of the Advanced Light Source at Lawrence Berkeley National Laboratory, using a Bruker Apex II CCD diffractometer (ω_o rotation with narrow frames, synchrotron radiation at 0.7749 Å, silicon 111 monochromator). The structure was solved by direct methods and refined using the SHELX-TL[96] suite of programs. All fully occupied non-H atoms were refined anisotropically. All disordered or partially groups were left isotropic to conserve the data to parameter ratio, as the crystal only diffracted to 0.91 Å. In this case the refinement would require extensive restraints to produce nice looking displacement parameters and

therefore it seemed more sensible just to leave them isotropic. Hydrogen atoms were placed geometrically on the carbon atoms, then constrained and refined using a riding model. The hydroxyl and water hydrogen atoms could not be found in the difference map nor placed and were therefore omitted from the refinement but not from the chemical formula. O14 is fully occupied, however 60% of the time it is part of a methoxide and 40% is a part of a hydroxide interaction with a partial water (O1W).

The voids created by the crystal packing of complexes **1** and **2** contained a considerable electron density, mainly due to disordered lattice solvate molecules (most likely DMF). Several attempts to locate and model such molecules revealed to be unsuccessful as the electron density was highly smeared-out, thus avoiding full convergence upon full-matrix least squares refinement cycles on F^2. The searches for the total potential solvent area using the software package PLATON[104] revealed the existence of a large cavity with a potential solvent accessible void volume of *ca.* 1768 $Å^3$. Subsequently, the original data set was treated using the SQUEEZE[105] subroutines to fully remove the contribution of these highly disordered molecules in the solvent-accessible volume (contribution of *ca.* 988 electrons was effectively removed). The calculated solvent-free reflection list was then used for the final structure refinement.

The programs used for molecular graphics were MERCURY[106] and DIAMOND.[107] Unit cell parameters and structure solution and refinement data for complexes **1**-**3** are listed in Table 2.1.

Table 2.1. Crystallographic data for complexes **1**-**3**

Parameter	**1**·*x*DMF·*y*H_2O	**2**·*x*(solv)	**3**
Formula	$C_{208}H_{162}Mn_{28}N_{48}O_{88}$	$C_{88}H_{98}Mn_{16}N_{32}O_{40}Cl_2$	$C_{81.60}H_{157}Mn_{15}Na_2N_{10}O_{48.40}$
Fw / g mol^{-1}	6280.19	3193.92	2922.84
Crystal type	Dark red plate	Black prism	Brown needle
Crystal size / mm	0.08×0.06×0.04	0.25×0.17×0.08	0.20×0.04×0.03
Crystal system	Triclinic	Monoclinic	Orthorhombic
Space group	*P*-1	$P2_1/c$	$P2_12_12_1$
a / Å	16.1201(8)	14.5921(4)	16.8501(19)
b / Å	20.8879(6)	21.4515(6)	25.427(3)
c / Å	22.0475(1)	23.1946(6)	29.736(3)
α / º	85.219(3)	90	90
β / º	70.039(4)	100.600(2)	90
γ / º	82.447(3)	90	90
V / $Å^3$	6911.3(5)	7136.5(3)	12740(2)
Z	1	2	4
T / K	100.0(2)	150.0(2)	150.0(2)
ρ_{calc} / g cm^{-3}	1.509	1.486	1.524
μ / mm^{-1}	1.315	1.476	1.914
θ range / °	3.38 - 25.00	3.66 - 25.68	2.404 - 25.218
Index ranges	$-19 \le h \le 19$	$-17 \le h \le 17$	$-18 \le h \le 18$
	$-24 \le k \le 24$	$-25 \le k \le 26$	$-27 \le k \le 27$
	$-26 \le l \le 26$	$-28 \le l \le 28$	$-32 \le l \le 32$
Collected reflections	86184	101693	71633
Independent reflections	23965 (R_{int} = 0.1368)	13532 (R_{int} = 0.0427)	17717 (R_{int} = 0.0567)
Final $R^{a,b}$ indices [$I>2\sigma(I)$]	$R1$ = 0.0694	$R1$ = 0.0537	$R1$ = 0.0527

	w$R2$ = 0.1489	w$R2$ = 0.1555	w$R2$ = 0.1368
$(\Delta\rho)_{max,min}$ / e Å^{-3}	1.179, -0.693	0.912, -0.706	0.875, -0.520

^{a}R1 = $\Sigma(||F_o| - |F_c||)/\Sigma|F_o|$. ^{b}wR2 = $[\Sigma[w(F_o^2 - F_c^2)^2]/\Sigma[w(F_o^2)^2]]^{1/2}$, $w = 1/[\sigma^2(F_o^2) + (ap)^2 + bp]$, where $p = [\max(F_o^2, 0) + 2F_c^2]/3$.

2.2. Results and Discussion

2.2.1. Synthetic Comments

Many synthetic methodologies to high-spin molecules have been reported.[7] One strategy that has proven to be very successful is the employment of flexible, ancillary ligands that are known to promote ferromagnetic exchange interactions between the metal ions they bridge, such as pseudohalides, combined with alkoxido- or oximate-based chelates, which can yield high nuclearity products.[108] Azides are the most commonly employed pseudohalides and their previous use in Mn cluster chemistry has led to a large number of new clusters with nuclearities up to $\{Mn_{32}\}$[109] and S_T values as large as 83/2.[43] On the other hand, there has been little use of cyanates in higher oxidation Mn coordination chemistry. The reason for that is most probably the assumption that their use will lead to products that are isomorphous with azide products, with similar magnetic properties. In order to identify if cyanates can act as ferromagnetic couplers in higher oxidation Mn chemistry, we decided to employ them, for the first time, in manganese cluster chemistry, in conjunction with pyridyl diols ($dpkdH_2$) or pyridyl dioximes

(dapdoH_2), in the presence or absence of ancillary carboxylates. We have also used the azide-teaH_3 'ligand blend' in manganese carboxylate chemistry as a means of obtaining new nanoscale molecular magnetic materials with possible large S_T values and SMM behaviors.

A variety of reactions differing in the cyanate amount, the Mn:dpk ratio, the carboxylate groups present, the organic base, and/or the reaction solvent(s) were explored in identifying the following successful system. The one-pot reaction of $Mn(ClO_4)_2 \cdot 6H_2O$, $NaO_2CMe \cdot 3H_2O$, dpk, NEt_3, and NaOCN in a 1:2:1:1:1 molar ratio in MeCN/DMF (4:1, v/v) gave a dark brown solution that, upon filtration and slow evaporation at room temperature, afforded dark red crystals of the tetradecanuclear, mixed-valence(II/III) complex $[Mn_{14}O_4(OH)_2(OCN)_6(O_2CMe)_2(dpkd)_8(DMF)_2(H_2O)_4](OH)_2$ (**1**) in 60% yield. The formation of **1** is summarized in Equation 2.1.

$$14\ Mn^{2+} + 8\ dpk + 18\ NEt_3 + 6\ OCN^- + 2\ MeCO_2^- + 2\ O_2 + 2\ DMF + 14\ H_2O \rightarrow$$

$$[Mn_{14}O_4(OH)_2(OCN)_6(O_2CMe)_2(dpkd)_8(DMF)_2(H_2O)_4]^{2+} + 18\ NHEt_3^+ \qquad (2.1)$$

The synthesis involves Mn oxidation, undoubtedly by O_2 under the prevailing basic conditions, and Equation 2.1 has been balanced accordingly. Note that dpkdH_2 ligand is the *gem*-diol form of dpk (Scheme 2.1) and results from the metal-assisted, nucleophilic attack of H_2O at the carbonyl C atom of dpk.

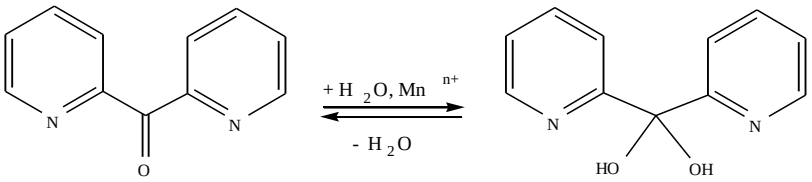

dpk dpkdH$_2$

Scheme 2.1. Structural formulae and abbreviations of dpk and dpkdH$_2$ organic ligands discussed in the text.

The NEt$_3$ is essential to ensure basic conditions and to act as a proton acceptor to facilitate the deprotonation of the dpkdH$_2$ groups. In addition, the presence of NEt$_3$ facilitates the *in situ* generation of OH^- and O^{2-} ions through the deprotonation of the H_2O-containing starting materials and solvents. A similar role could also be carried out by the $MeCO_2^-$ ions; however, in the absence of NEt$_3$ longer reaction times (>24 h) are required to get a significant dark brown coloration, and the yield of isolated **1** is much lower (<10%). Employment of different organic bases, such as NMe$_3$, Bu^n_3N and Me$_4$NOH, did not afford crystalline materials but only oily products that we were not able to characterize further. An increase in the amount of dpk led to yellow or pale-orange solutions indicative of Mn^{II} products. Finally, substitution of $MeCO_2^-$ ions in the NaO_2CMe precursor by other carboxylate groups, such as $EtCO_2^-$ or $Bu^tCO_2^-$, did not lead to any crystalline material under various crystallization techniques and reaction conditions.

In the next step of our synthetic attempts, we decided to employ cyanates in conjunction with oximate-based chelates, such as dapdoH$_2$, in manganese chemistry.

Several reactions of $Mn^{II}/RCO_2^-/OCN^-$ (R = various) with $dapdoH_2$ in MeCN/DMF were performed, but we were unable to isolate any crystalline material. We thus explored systems in the absence of carboxylates and the reaction of $MnCl_2 \cdot 4H_2O$, $dapdoH_2$, NEt_3, and NaOCN in a 2:1:2:1 molar ratio in MeCN/DMF (4:1, v/v) gave a dark brown solution that, upon filtration and slow evaporation at room temperature, afforded dark brown crystals of the hexadecanuclear complex $[Mn_{16}O_8(OH)_4Cl_2(OCN)_4(L)_2(dapdo)_6(DMF)_4]$ (**2**) in 45% yield. The compound is again mixed-valence but this time it consists of eight Mn^{2+}, four Mn^{3+} and four Mn^{4+} ions. The formation of **2** is summarized in Equation 2.2.

$$16\ Mn^{2+} + 8\ dapdoH_2 + 26\ NEt_3 + 4\ OCN^- + 2\ Cl^- + \frac{11}{2}\ O_2 + 4\ DMF + 5\ H_2O \rightarrow$$

$$[Mn_{16}O_8(OH)_4Cl_2(OCN)_4(L)_2(dapdo)_6(DMF)_4] + 26\ NHEt_3^+ \qquad (2.2)$$

The reaction is again an oxidation by atmospheric O_2 under the prevailing basic conditions. Note that the coordinated ligand L^{3-} is the anion of an unprecedented pyridine dioximato acid, most likely derived from the *in situ* metal-assisted, oxidation of the methyl groups of $dapdoH_2$ ligand (Scheme 2.2). Such unexpected organic ligand transformations are with precedent in higher oxidation manganese cluster chemistry.[108]

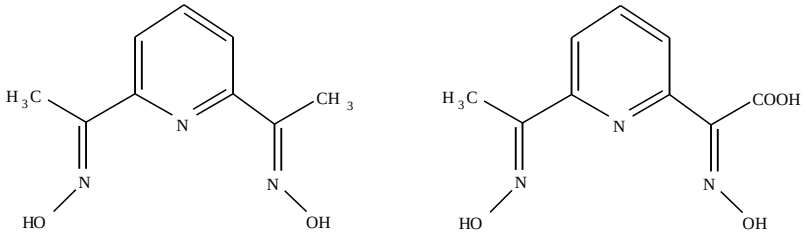

Scheme 2.2. Structural formulae and abbreviations of $dapdoH_2$ and LH_3 organic ligands discussed in the text.

It is obvious that the presence of chlorides is essential for the formation and crystallization of complex **2**, since there are two chlorides coordinated to two Mn^{2+} ions (*vide infra*). Under the context of chemical reactivity of cluster **2**, we decided to use other MnX_2 precursors, such as $Mn(NO_3)_2$ or $Mn(ClO_4)_2$, in order to assess how the nature of inorganic anions would affect the chemical identity of crystalline products. Using $Mn(NO_3)_2$ we were able to isolate crystals of the known, cyanate-free, mixed-valence $[Mn_8O_2(dapdo)_6(NO_3)_2]$ compound.[110] Similarly, the employment of $Mn(ClO_4)_2$ gave the reported compound $[Mn_6O_2(OH)_2(dapdo)_2(dapdoH)_4](ClO_4)_2$ in which no cyanate ions were present.[111]

Trying to further explore the combined cyanate/alkoxido-chelate reaction systems in manganese carboxylate chemistry, we decided to use the tripodal ligand $teaH_3$. Previous use of that ligand has shown that it exhibits impressive coordination versatility with various metal centers;[112] thus, its amalgamation with cyanates would provide an attractive route to new high-nuclearity/high-spin Mn clusters and SMMs.[108] Unfortunately, no crystalline products came out from these reactions but only insoluble amorphous

precipitates that were probably Mn oxides or oxo/hydroxido species. We have then decided to replace cyanates with azides, and the reaction of $Mn(ClO_4)_2 \cdot 6H_2O$, $NaO_2CBu^t \cdot H_2O$, $teaH_3$, NEt_3 and NaN_3 in 1:2:1:1:2 molar ratio in MeCN/MeOH (2:1 v/v) afforded well-formed brown needle-like crystals of the new complex $[Mn_{15}Na_2O_8(OH)_2(OMe)(N_3)_2(O_2CH)(O_2CBu^t)_{11}(tea)_4(MeOH)]$ (**3**) in good yields (40-45%). The new pentadecanuclear complex **3** is again mixed-valence but contains only Mn^{2+} and Mn^{3+} ions, and includes two Na^+ atoms and a coordinating HCO_2^- group (*vide infra*); the latter most likely results from the metal-assisted oxidation of solvent MeOH.[113] The formation of **3** is summarized in Equation 2.3.

$$15\ Mn^{2+} + 2\ Na^+ + 4\ teaH_3 + 19\ NEt_3 + 2\ N_3^- + 11\ Bu^tCO_2^- + \frac{7}{2}\ O_2 + 3\ MeOH + 4\ H_2O \rightarrow$$

$$[Mn_{15}Na_2O_8(OH)_2(OMe)(N_3)_2(O_2CH)(O_2CBu^t)_{11}(tea)_4(MeOH)] + 19\ NHEt_3^+ \qquad (2.3)$$

The synthesis involves Mn oxidation, undoubtedly by O_2 under the prevailing basic conditions, and Equation 2.3 has been balanced accordingly. The NEt_3 is essential to ensure basic conditions and to act as a proton acceptor to facilitate the deprotonation of the $teaH_3$- and H_2O-containing groups. More than one equivalent of NEt_3 gave oily products suggestive of mixtures that we have not been able to further characterize. An increase in the amount of $teaH_3$ led to yellow or pale-orange solutions indicative of Mn^{II} products, likely containing mainly or exclusively the neutral form of the $teaH_3$ ligand.

Finally, the MeCN/MeOH reaction solvent mixture was identified as the one giving the highest product yield and purity, as well as the best quality single-crystals.

2.2.2. Description of Structures

A partially-labeled representation of complex **1** is shown in Figure 2.1. Complex **1** crystallizes in the triclinic space group *P*-1. The cation of **1** consists of a mixed-valence ($Mn^{II}_6Mn^{III}_8$) cluster (Figure 2.1, top). The Mn_{14} unit comprises a $Mn^{II}_4Mn^{III}_4$ rod-like subunit attached on either side to two symmetry-related $[Mn^{II}Mn^{III}_2(\mu\text{-}OR)_3]^{5+}$ trinuclear subunits. The 14 Mn atoms are bridged by a combination of two $\mu_4\text{-}O^{2-}$, two $\mu_3\text{-}O^{2-}$, two $\mu_3\text{-}OH^-$, two $\eta^1{:}\eta^1$ (end-on) OCN^-, and the alkoxido arms of eight $dpkd^{2-}$ ligands. The latter are of four types: $\eta^1{:}\eta^2{:}\eta^2{:}\eta^1{:}\mu_3$, $\eta^1{:}\eta^2{:}\eta^1{:}\eta^1{:}\mu_3$, $\eta^1{:}\eta^2{:}\eta^1{:}\eta^1{:}\mu_3$, and $\eta^1{:}\eta^2{:}\eta^2{:}\eta^1{:}\mu_4$ (Scheme 2.3), emphasizing the bridging flexibility of the $dpkd^{2-}$ group and its ability to stabilize metal ions at different oxidation states (i.e., Mn^{2+} and Mn^{3+}). Complex **1** thus contains an overall $[Mn_{14}(\mu_4\text{-}O)_2(\mu_3\text{-}O)_2(\mu_3\text{-}OH)_2(\mu\text{-}OCN)_2(\mu_3\text{-}OR)_2(\mu\text{-}OR)_{10}]^{12+}$ core (Figure 2.1, bottom), with peripheral ligation provided by two $\eta^1{:}\eta^1{:}\mu$ $MeCO_2^-$ groups, four OCN^-, two DMF, and four H_2O terminal ligands.

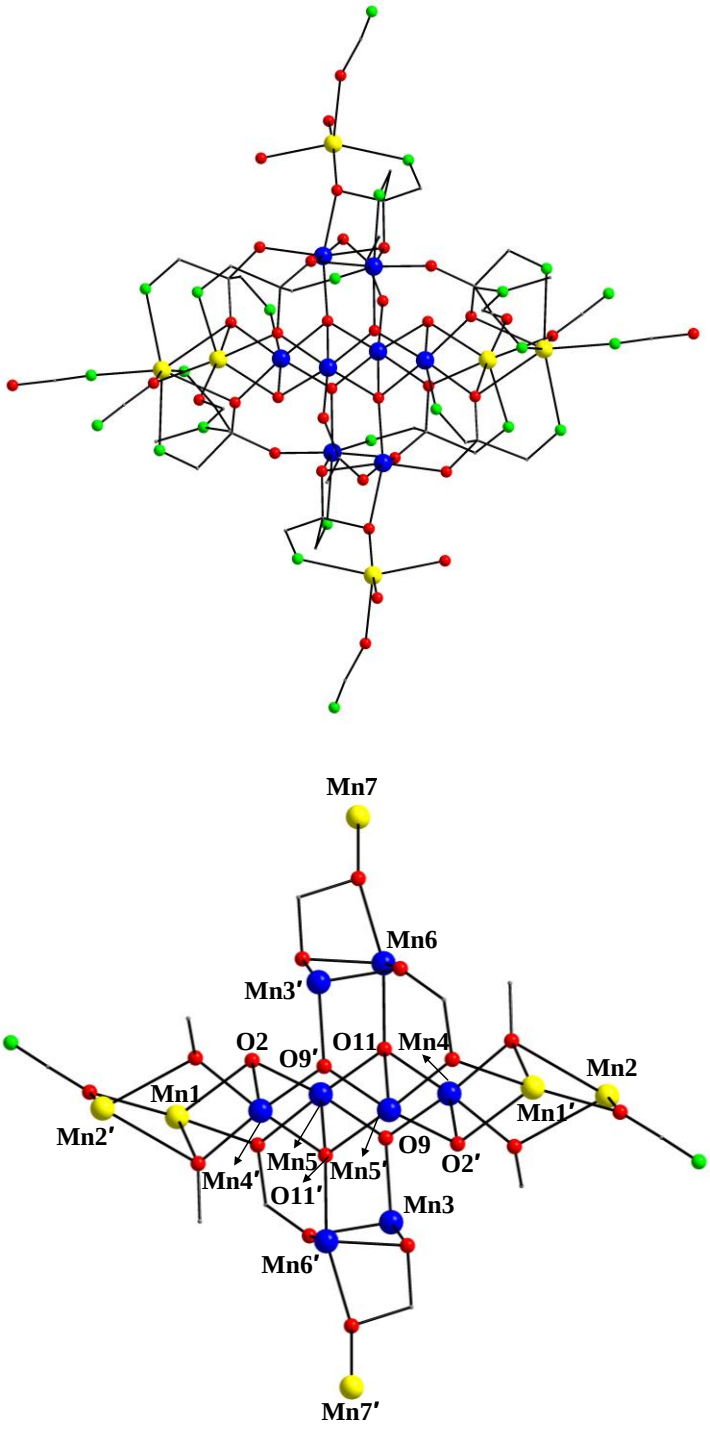

Figure 2.1. The structure of the cation of **1** (top) and its complete core (bottom). Only the *ipso* carbon atoms of the phenyl groups of $dpkd^{2-}$ ligands are shown. Color scheme: Mn^{II},

yellow; Mn^{III}, blue; O, red; N, green; C, grey. H atoms have been omitted for clarity. Symmetry operation for the primed atoms in **1**: *-x, -y, -z*.

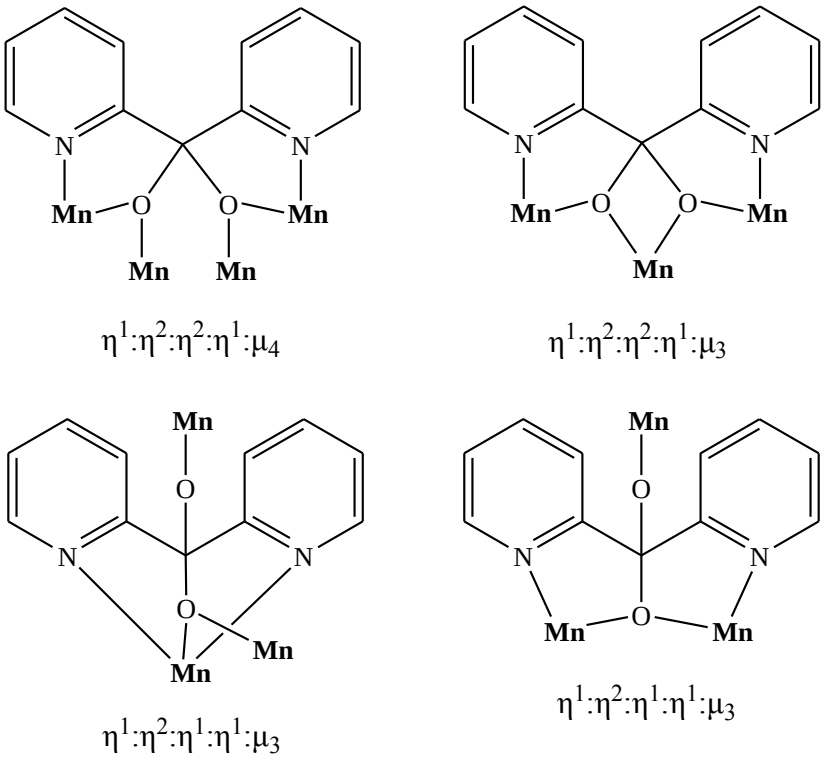

Scheme 2.3. The coordination modes of $dpkd^{2-}$ ligands in complex **1**.

Charge-balance considerations and inspection of the metric parameters indicate a $Mn^{II}_6Mn^{III}_8$ description for **1**. Bond-valence sum (BVS) calculations (Table 2.2)[114] confirm the $Mn^{II}_6Mn^{III}_8$ mixed-valent description for **1**, which identified Mn1, Mn2, Mn7 and their symmetry-related partners as the Mn^{II} atoms, and the remaining as Mn^{III}. All Mn^{III} atoms, Mn(3,3′,4,4′,5,5′,6,6′), are six-coordinate with distorted octahedral geometries and they exhibit Jahn-Teller (JT) axial elongations with the eight JT axes being essentially parallel to each other (Figure 2.2). Mn2 and Mn7 are seven- and five-

coordinate with distorted pentagonal bipyramidal and square pyramidal geometries, respectively (τ = 0.05, where τ is 0 and 1 for perfect square pyramidal and trigonal bipyramidal geometries, respectively).[115] Finally, Mn1 is six-coordinate with a distorted octahedral geometry. Complex **1** does not form any significant intermolecular interactions of any kind. Further, the space-filling representation of compound **1** reveals its large nanometer-sized structure and its almost spherical motif with an average diameter of ~2.1 nm as defined by the longest N···N distance (Figure 2.3).

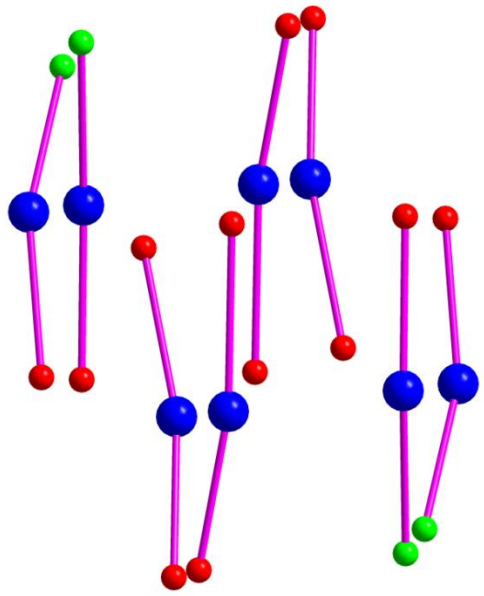

Figure 2.2. The almost parallel arrangement of the eight Mn^{3+} Jahn-Teller (JT) elongation axes in complex **1**.

Table 2.2. Bond valence sum (BVS)[a,b] calculations for Mn and selected O atoms in **1**

Atom	Mn^{II}	Mn^{III}	Mn^{IV}
Mn1	1.98	1.83	1.89

Mn2	1.87	1.78	1.76
Mn3	3.37	3.13	3.20
Mn4	3.32	3.05	3.18
Mn5	3.10	2.84	2.98
Mn6	3.09	2.82	2.96
Mn7	1.75	1.72	1.84

	BVS	assignment
O2	1.04	OH^- (μ_3)
O9	1.93	O^{2-} (μ_3)
O11	2.17	O^{2-} (μ_4)

[a] The underlined value is the one closest to the charge for which it was calculated. The oxidation state is the nearest whole number to the underlined value. [b] An O BVS in the ~1.7-2.0, ~1.0-1.2, and ~0.2-0.4 ranges is indicative of non-, single- and double-protonation, respectively.

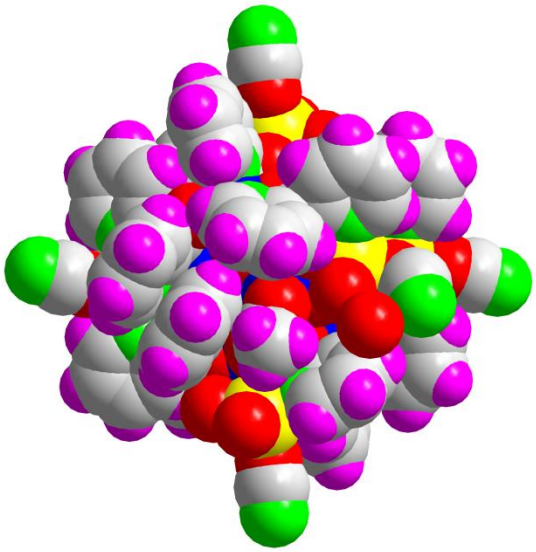

Figure 2.3. Space-filling representation of compound **1**. Color scheme: Mn^{II}, yellow; Mn^{III}, blue; O, red; N, green; C, grey; H, pink.

The structure of **2** consists of a mixed-valence ($Mn^{II}_8Mn^{III}_4Mn^{IV}_4$) cage (Figure 2.4, top, left) with a 'tubular'-like topology. The compound possesses a $[Mn_{16}(\mu_4\text{-}O)_6(\mu_3\text{-}O)_2(\mu_3\text{-}OH)_4(\mu\text{-}OCN)_4(\mu_3\text{-}ON)_{16}]^{4+}$ core (Figure 2.4, bottom), which can be conveniently dissected into 7 layers of four types with an **ABCDCBA** arrangement (Figure 2.4, top, right). The Mn^{II} monomeric layer **A** is the 'lid' (or 'base') of the Mn_{16} 'tube'. Layer **B** is an unusual for its oxidation state $\{Mn^{II}_2Mn^{III}Mn^{IV}(\mu_3\text{-}O)_2(\mu\text{-}ON)_4\}$ 'butterfly' (Mn1, Mn3, Mn6, Mn7, O2, O5). Layers **A** and **B** are connected by O2 which is converted from μ_3 to μ_4. In a similar way, O5 is converted from μ_3 to μ_4 and links layer **B** with **C**. Layer **C** is a 'node'-like Mn^{III} monomer, acting as the connector between layers **AB** and **D**; the latter central layer **D** is again a 'butterfly'-type unit but with a $\{Mn^{II}_2Mn^{IV}_2(\mu_3\text{-}O)_2(\mu\text{-}ON)_4\}$ description (Mn4, Mn8, Mn4′, Mn8′, O3, O3′). Layer **D** is linked on two opposite sites to neighbouring **C** layers through the conversion of μ_3-O3 and O3′ to μ_4. Each layer is additionally linked to neighbouring layers by two $\mu_3\text{-}O^{2-}$, four $\mu_3\text{-}OH^-$, and four $\eta^1\text{:}\eta^1$ (end-on) OCN^-, as well as six $\eta^1\text{:}\eta^1\text{:}\eta^1\text{:}\eta^1\text{:}\mu$ and two $\eta^1\text{:}\eta^1\text{:}\eta^1\text{:}\eta^1\text{:}\eta^1\text{:}\mu$ chelating/bridging $dapdo^{2-}$ and L^{3-} groups, respectively (Scheme 2.4). Peripheral ligation about the core is further provided by two monodentate Cl^- atoms and four terminal DMF molecules.

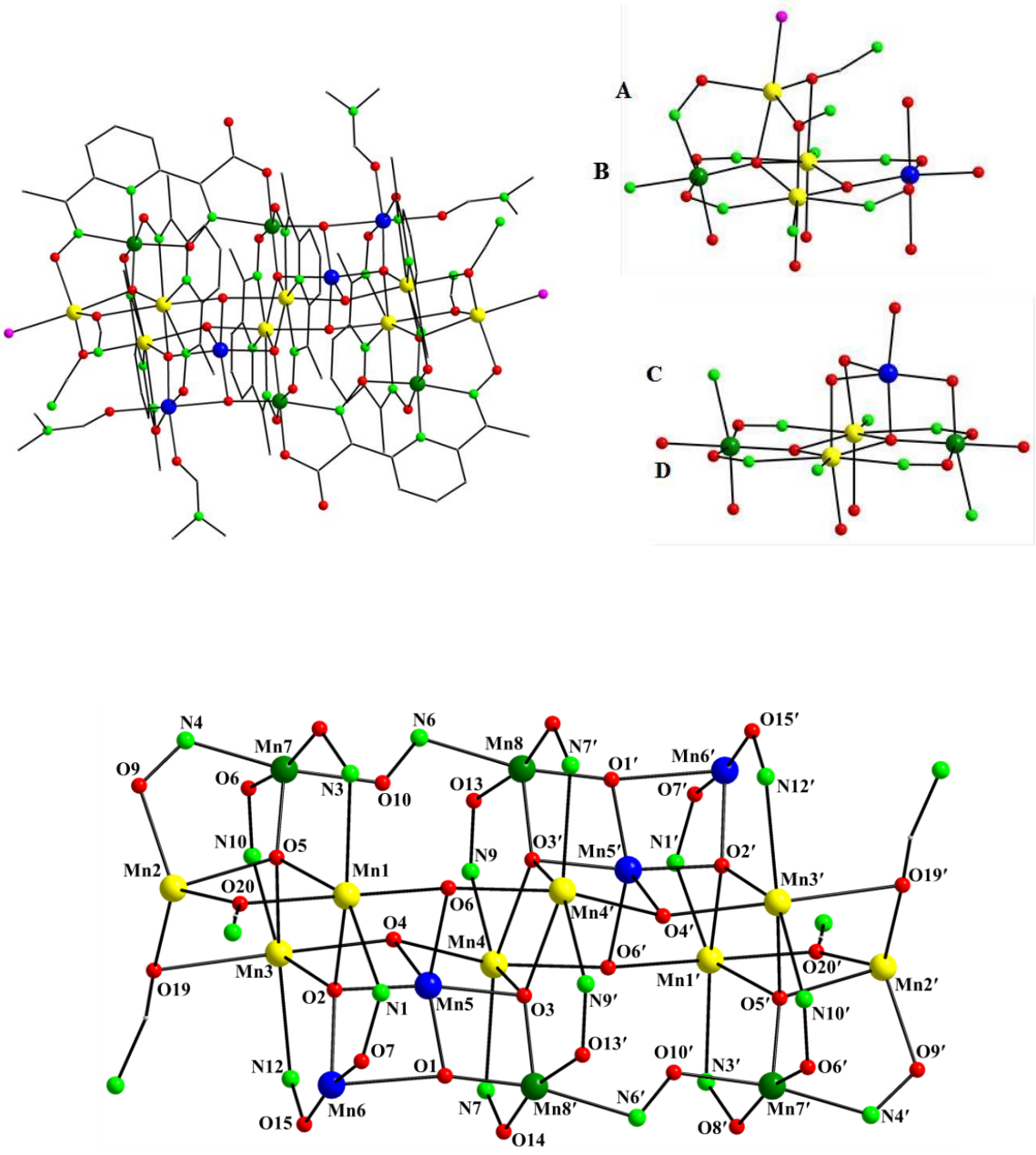

Figure 2.4. Structure of **2** (top, left), the four types of constituent layers of its core (top, right), and the complete core of the compound (bottom). Colour scheme: Mn^{II}, yellow; Mn^{III}, blue; Mn^{IV}, olive green; O, red; N, green; Cl, purple; C, grey. H atoms have been omitted for clarity. Symmetry operation for the primed atoms in **2**: *-x*, *-y*, *-z*.

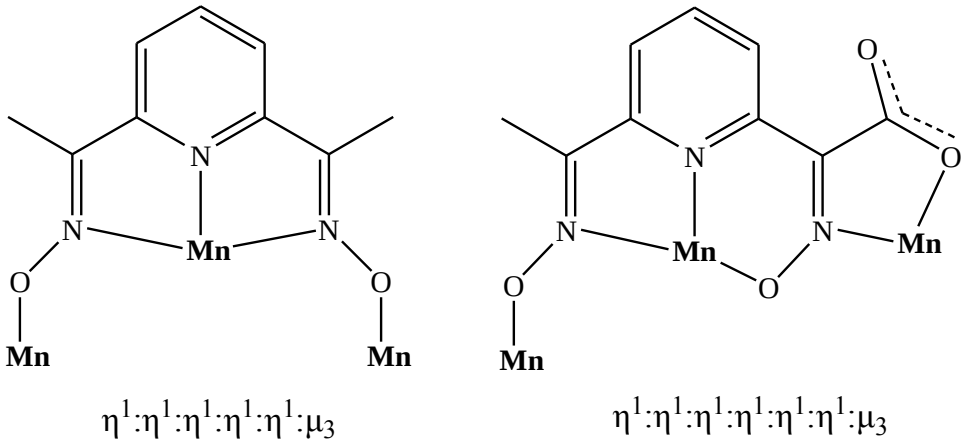

$\eta^1:\eta^1:\eta^1:\eta^1:\eta^1:\mu_3$ $\eta^1:\eta^1:\eta^1:\eta^1:\eta^1:\eta^1:\mu_3$

Scheme 2.4. The coordination modes of $dapdo^{2-}$ and L^{3-} ligands in complex **2**.

Charge-balance considerations and inspection of the metric parameters indicate a $Mn^{II}_8Mn^{III}_4Mn^{IV}_4$ description for **2**. Bond-valence sum (BVS) calculations (Table 2.3) confirm the $Mn^{II}_8Mn^{III}_4Mn^{IV}_4$ mixed-valent description for **2**, which identified Mn1, Mn2, Mn3, and Mn4 as the Mn^{II} atoms, Mn5 and Mn6 as the Mn^{III} atoms, and the others as Mn^{IV}. Mn1, Mn3 and Mn4 atoms are seven-coordinate with distorted pentagonal bipyramidal geometries, while Mn2 is five-coordinate with a distorted trigonal bipyramidal geometry (τ = 0.79).[116] Mn5 and Mn6 are five- and six-coordinate with distorted trigonal bipyramidal (τ = 0.53) and octahedral geometries, respectively. All Mn^{IV} atoms are six-coordinate with distorted octahedral geometries. Complex **2** does not form any significant intermolecular interactions of any kind. Furthermore, the space-filling representation of compound **2** reveals its large nanometer-sized structure and its 'tubular'-like motif with an average diameter of ~2.2 nm as defined by the longest H···H distance (Figure 2.5).

Table 2.3. Bond valence sum (BVS)[a,b] calculations for Mn and selected O atoms in **2**

Atom	Mn^{II}	Mn^{III}	Mn^{IV}
Mn1	<u>1.98</u>	1.86	1.87
Mn2	<u>1.76</u>	1.71	1.85
Mn3	<u>1.80</u>	1.73	1.87
Mn4	<u>2.01</u>	1.89	1.90
Mn5	3.14	<u>2.87</u>	3.01
Mn6	3.24	<u>2.97</u>	3.11
Mn7	4.31	4.01	<u>4.10</u>
Mn8	4.15	3.82	<u>3.97</u>

	BVS	assignment
O1	1.80	O^{2-} (μ_3)
O2	1.81	O^{2-} (μ_4)
O3	1.81	O^{2-} (μ_4)
O4	0.98	OH^- (μ_3)
O5	1.80	O^{2-} (μ_4)
O6	0.96	OH^- (μ_3)

[a] The underlined value is the one closest to the charge for which it was calculated. The oxidation state is the nearest whole number to the underlined value. [b] An O BVS in the ~1.7-2.0, ~1.0-1.2, and ~0.2-0.4 ranges is indicative of non-, single- and double-protonation, respectively.

In both **1** and **2**, the end-on bridging cyanato groups show an obvious preference in binding through their O-atom (hard donor atom), a significantly different ligation than that of the homoatomic-type N_3^-. Indeed, **1** and **2** are the first OCN^--based clusters in which the metal centres are O-bridged, opening a new window in structural 3*d*-metal cluster chemistry.

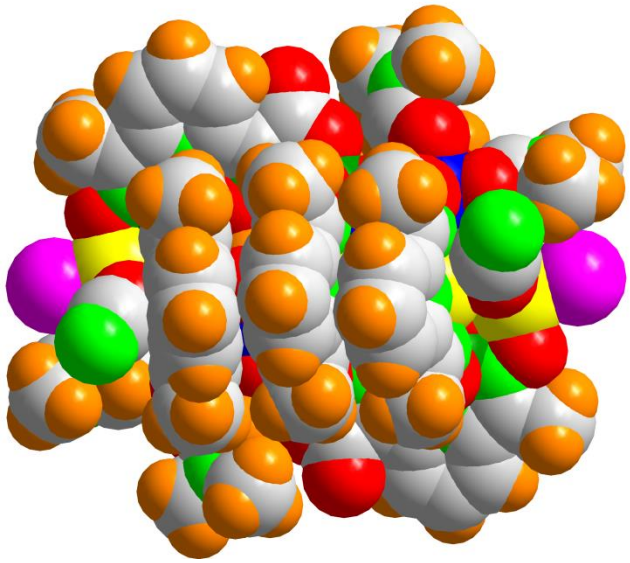

Figure 2.5. Space-filling representation of compound **2**. Colour scheme: Mn^{II}, yellow; Mn^{III}, blue; Mn^{IV}, olive green; O, red; N, green; Cl, purple; C, grey; H, orange.

Complex **3** crystallizes in the orthorhombic space group $P2_12_12_1$ with the $[Mn_{15}Na_2O_8(OH)_2(OMe)(N_3)_2(O_2CH)(O_2CBu^t)_{11}(tea)_4(MeOH)]$ molecule in a general position (Figure 2.6). The cage-like structure of **3** comprises a $[Mn_{15}Na_2(\mu_4\text{-}O)_6(\mu_3\text{-}O)_2(\mu_3\text{-}OH)_2(\mu\text{-}OMe)]^{26+}$ core (Figure 2.7, top), which can be conveniently dissected into four subunits of three types with an **ABCA** arrangement (Figure 2.7, bottom).

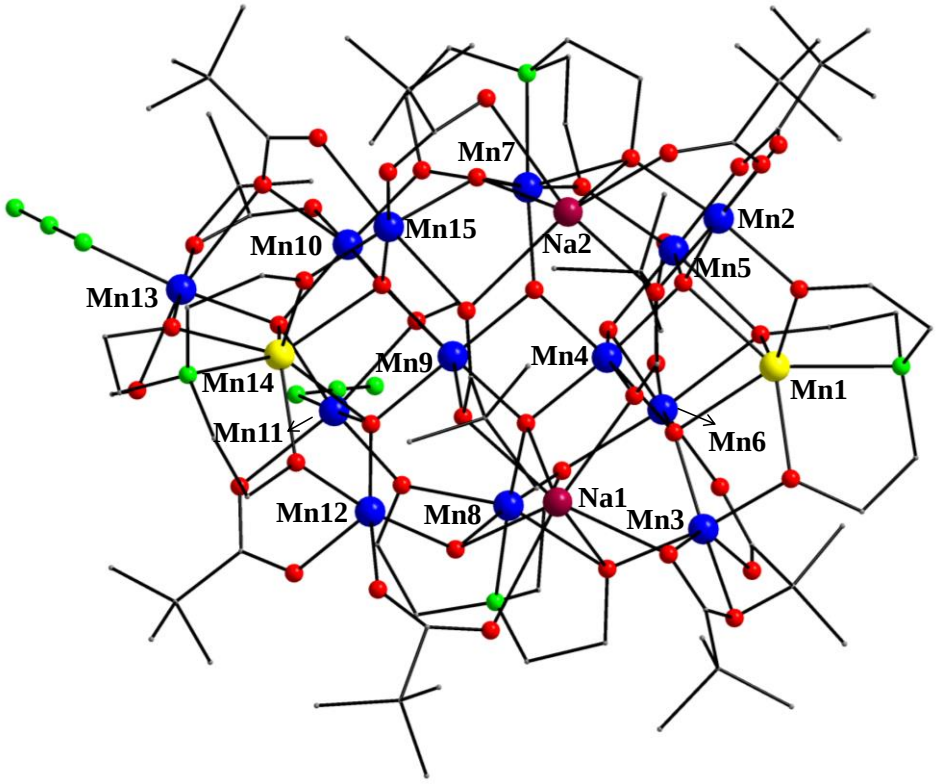

Figure 2.6. Partially-labeled representation of complex **3**. H atoms have been omitted for clarity. Color scheme: Mn^{II}, yellow; Mn^{III}, blue; Na, magenta; O, red; N, green; C, grey.

The two similar subunits **A** occupy the top and bottom sites of the cage, with each of them comprising two Mn^{III} and a Na^{I} atoms (Mn7/Mn15/Na2 and Mn8/Mn12/Na1) in a triangular conformation with a capping μ_3-OH^- ion (O10 and O9). The right-side subunit **B** consists of a $[Mn^{II}Mn^{III}_3(\mu_3\text{-}O)_3(\mu\text{-}OMe)]^{4+}$ cubane (Mn9, Mn10, Mn11, Mn14, O6, O7, O8, O14) with an external Mn^{III} atom (Mn13) attached to oxido atom, O8, making the latter quadruply bridging (μ_4) and yielding a $[Mn_5O_3(OMe)]$ overall subcore. Finally, the left-side subunit **C** comprises a $[Mn^{II}Mn^{III}_3(\mu_3\text{-}O)_3]^{5+}$ defective cubane (cubane missing a vertex; Mn1, Mn4, Mn5, Mn6, O1, O2, O3) which is extended to two opposite sides by binding to two Mn^{III} atoms (Mn2, Mn3) through the 'conversion' of μ_3-O1 and

O2 to μ_4; the overall subcore of **C** is thus $[Mn_6O_3]$. Two oxido groups, namely the μ_3-O4 and μ_4-O5, bring the four subunits together, while additional linkage within the **ABCA** arrangement is provided by the alkoxido arms of the four tea^{3-} groups. The latter are of two types: $\eta^2{:}\eta^1{:}\eta^2{:}\eta^2{:}\mu_4$ and $\eta^2{:}\eta^1{:}\eta^2{:}\eta^3{:}\mu_5$ (Figure 2.8, top), emphasizing the bridging flexibility of the tea^{3-} group and its ability to bridge multiple metal ions at different oxidation states (i.e., Na^+, Mn^{2+}, and Mn^{3+}). Peripheral ligation about the central inorganic core (Figure 2.7, top) is provided by eight $\eta^1{:}\eta^1{:}\mu$, one $\eta^1{:}\eta^2{:}\mu$, one $\eta^1{:}\eta^2{:}\mu_3$, and two $\eta^2{:}\eta^2{:}\mu_4$ $Bu^tCO_2^-/HCO_2^-$ groups (Figure 2.8, bottom), as well as two terminal N_3^- ions (at Mn11 and Mn13) and a terminal MeOH molecule (at Mn13).

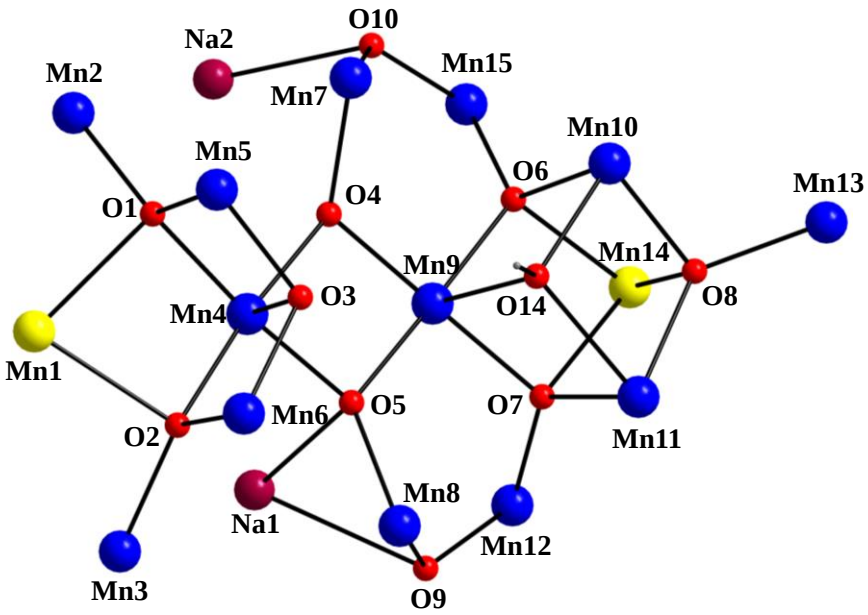

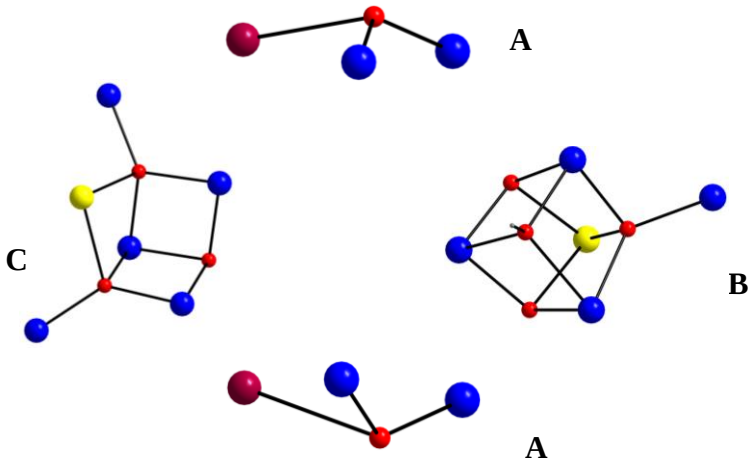

Figure 2.7. Partially-labeled representations of (top) the $[Mn_{15}Na_2(\mu_4\text{-}O)_6(\mu_3\text{-}O)_2(\mu_3\text{-}OH)_2(\mu\text{-}OMe)]^{26+}$ core of **3** and (bottom) the three types of constituent subunits of its core. Color scheme: same as in Figure 2.6.

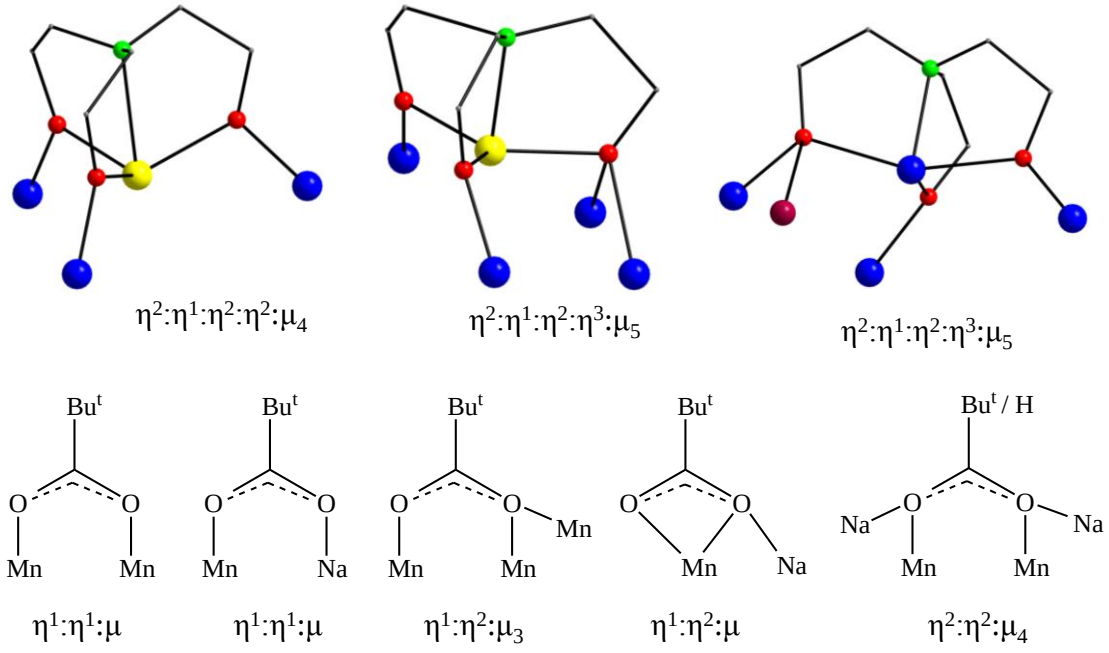

Figure 2.8. The coordination modes of tea^{3-} (top) and carboxylate ($Bu^tCO_2^-$ and HCO_2^-) groups found in complex **3**. Color scheme: same as in Figure 2.6.

Charge-balance considerations and inspection of the metric parameters indicate a $2Mn^{II}$, $13Mn^{III}$ description for **3**. This was confirmed quantitatively by bond valence sum (BVS) calculations (Table 2.4),[114] which identified Mn1 and Mn14 as the Mn^{II} ions, and the others as Mn^{III}. The latter were also consistent with the Jahn-Teller (JT) distortion observed in Mn^{III} ions (Figure 2.9), as expected for high-spin d^4 ions in near-octahedral geometry, taking the form of axial elongation of the two *trans* Mn-$O_{alkoxide}$ (either from the alkoxide arms of tea^{3-} groups or from the terminal MeOH molecule) and Mn-$O_{carboxylate}$ bonds (either from pivalate or formate groups). Thus, as is almost always the case, the JT elongation axes avoid the Mn^{III}-O^{2-} bonds, the shortest and strongest in the molecule.[117] Exceptionally, one of the Mn^{III} atoms (Mn12) is five-coordinate and possesses a square pyramidal geometry (τ = 0.05).[115] The Mn^{II} atom, Mn1, and Na2 are six-coordinate with distorted octahedral geometries, while the Mn^{II} atom, Mn14, and Na1 are seven-coordinate[118] with distorted pentagonal bipyramidal geometries. The protonation level of O^{2-}, OH^-, OMe^-, and MeOH groups was also confirmed by BVS calculations (Table 2.4).

Complex **3** does not form any significant intermolecular interactions of any kind, only a strong intramolecular H-bond between a bridging $Bu^tCO_2^-$ and the terminal MeOH molecule. Furthermore, the space-filling representation of compound **3** reveals its large nanometer-sized structure and its almost spherical motif with an average diameter of ~1.8 nm as defined by the longest H···H distance (Figure 2.10).

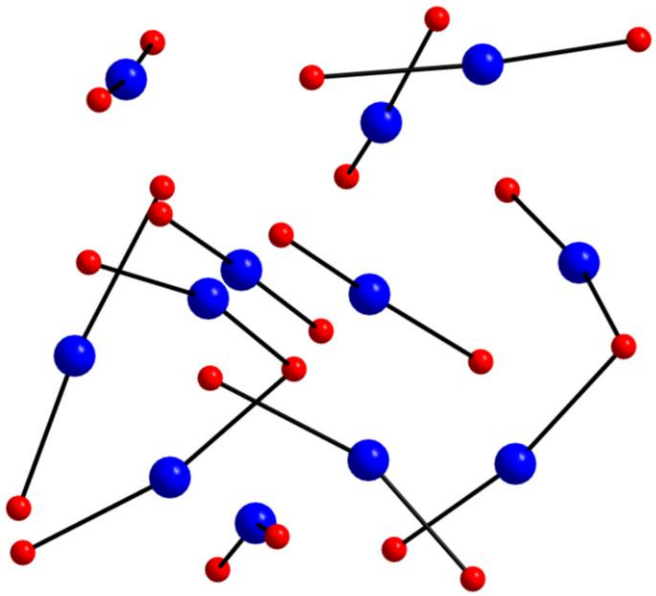

Figure 2.9. The orientations of the Jahn-Teller axial elongations for the twelve, six-coordinate Mn^{III} atoms appeared in complex **3**. The view is along the crystallographic *b*-axis. Color scheme: Mn^{III}, blue; O, red.

Table 2.4. Bond valence sum (BVS)[a,b] calculations for Mn, Na, and selected O atoms in **3**

Atom	Mn^{II}	Mn^{III}	Mn^{IV}
Mn1	<u>2.14</u>	1.98	2.04
Mn2	3.05	<u>2.79</u>	2.92
Mn3	3.07	<u>2.81</u>	2.95
Mn4	3.28	<u>3.08</u>	3.14
Mn5	3.35	<u>3.11</u>	3.19
Mn6	3.19	<u>2.92</u>	3.06

Mn7	3.13	2.90	2.99
Mn8	3.17	2.93	3.03
Mn9	3.26	3.00	3.12
Mn10	3.32	3.07	3.17
Mn11	3.17	2.96	3.02
Mn12	3.10	2.84	2.98
Mn13	3.26	3.02	3.11
Mn14	1.90	1.75	1.82
Mn15	3.29	3.00	3.15

	Mn^{II}	Na^{I}
Na1	0.98	1.09
Na2	0.96	1.05

	BVS	assignment
O1	1.86	O^{2-} (μ_4)
O2	1.83	O^{2-} (μ_4)
O3	1.73	O^{2-} (μ_3)
O4	1.83	O^{2-} (μ_3)
O5	2.00	O^{2-} (μ_4)
O6	1.85	O^{2-} (μ_4)
O7	1.87	O^{2-} (μ_4)
O8	1.83	O^{2-} (μ_4)
O9	1.19	OH^{-} (μ_3)
O10	1.20	OH^{-} (μ_3)

O14	1.81	OMe^- (μ_3)
O191	1.22	MeOH (η^1)

[a] The underlined value is the one closest to the charge for which it was calculated. The oxidation state is the nearest whole number to the underlined value. [b] An O BVS in the ~1.7-2.0, ~1.0-1.2, and ~0.2-0.4 ranges is indicative of non-, single- and double-protonation, respectively.

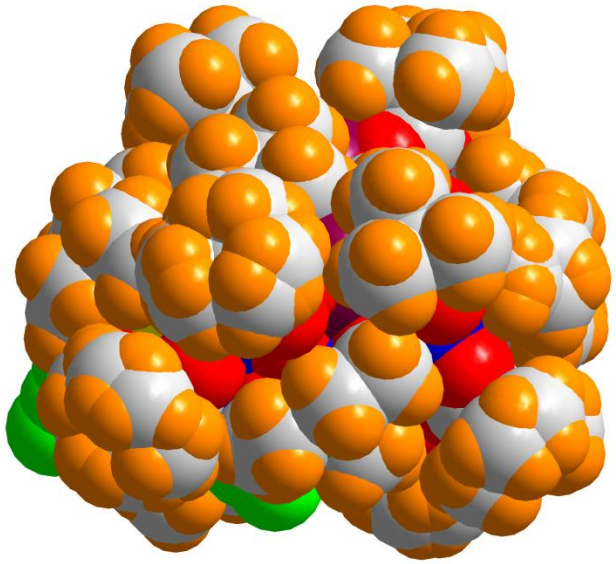

Figure 2.10. Space-filling representation of compound **3**, emphasizing the 'trapped' inorganic metal core by the peripheral organic molecules (RCO_2^- and tea^{3-}). Colour scheme: Mn^{II}, yellow; Mn^{III}, blue; Na, magenta; O, red; N, green; Cl, purple; C, grey; H, orange.

Complex **3** joins only a handful of previous manganese clusters with a nuclearity of 15. Since most of these were reported only relatively recently, we have listed them in Table 2.5 for a convenient comparison of their formulae, oxidation states description, and

pertinent magnetic data such as their ground state spin (*S*) values and the nature of predominant magnetic exchange interactions. The combined examination of Table 2.5 and the previously reported in literature results show that **3** possesses an unprecedented metal core topology; complex **3** is also unique in its given oxidation states' level and exhibits the second largest *S* value among all the other Mn_{15} clusters (*vide infra*). Note that the $Mn^{II}_4Mn^{III}_{11}$ cluster reported by Tong and coworkers[125] is ferromagnetically coupled with a maximum *S* value of 32, but it does not exhibit an SMM behavior due to the particular arrangement of the Mn^{III} JT axes.

Table 2.5. Chemical formulae, oxidation states description, ground-state *S* values, and nature of magnetic exchange interactions for polynuclear Mn complexes with a nuclearity of 15

complex[a,b]	oxidation states	*S*	magnetic interactions	ref
$[Mn_{15}O_{0.5}(OH)_{11.5}(pao)_{18}(EtOH)(H_2O)]^{6+}$	$Mn^{II}_8Mn^{III}_7$	6	AF (SMM)	119
$[Mn_{15}O_6(MePO_3)_2(O_2CMe)_{18}(H_2O)_{12}]^{2+}$	$Mn^{II}_9Mn^{III}_6$	1/2	AF (non-SMM)	120
$[Mn_{15}L_{15}(S)_{15}]$	Mn^{III}_{15}	n.r.	n.r.	121
$[Mn_{15}O_{17}(OMe)_5(O_2CPh)_{12}(MeOH)_4(H_2O)_5]$	$Mn^{III}_9Mn^{IV}_6$	2	AF (non-SMM)	122
$[Mn_{15}O_{17}(OMe)_5(O_2CCh)_{12}(MeOH)_3(H_2O)_6]$	$Mn^{III}_9Mn^{IV}_6$	2	AF (SMM)	122
$[Mn_{15}KO_4(O_2CEt)_{11}(pd)_{12}(py)_2]$	$Mn^{II}_4Mn^{III}_{10}Mn^{IV}$	23/2	F (SMM)	123
$[Mn_{15}O_8(OMe)_6(Bu^tPO_3)_{10}(dmbpy)_2]$	$Mn^{II}_3Mn^{III}_{12}$	n.r.	AF (SMM)	124

$[Mn_{15}Na_2O_8(HL')_{10}(O_2CMe)_2(H_2O)_2(OMe)_{1.5}$ -$(N_3)_{2.5}]^+$	$Mn^{II}_4Mn^{III}_{11}$	32	F (non-SMM)	125
$[Mn_{15}Na_2O_8(OH)_2(OMe)(N_3)_2(O_2CH)$-$(O_2CBu^t)_{11}(tea)_4(MeOH)]$	$Mn^{II}_2Mn^{III}_{13}$	14	F (SMM)	t.w

[a]Counterions and solvate molecules are omitted. [b]Abbreviations: F = ferromagnetic; AF = antiferromagnetic; n.r. = not reported; t.w. = this work; paoH = 2-pyridinealdoxime; LH_3 = *N*-phenylpropiolyl salicylhydrazide; S = DMF or H_2O solvate molecules; $ChCO_2H$ = cyclohexanecarboxylic acid; pdH_2 = 1,3-propanediol; py = pyridine; dmbpy = 4,4′-dimethyl-2,2′-bipyridyl; H_3L' = 2,6-(hydroxymethyl)phenol.

2.2.3. Solid-state Magnetic Susceptibility Studies

Solid-state, variable-temperature magnetic susceptibility measurements were performed on vacuum-dried microcrystalline samples of **1**·DMF, **2**, and **3**, which were suspended in eicosane to prevent torquing. The *dc* (direct current) magnetic susceptibility (χ_M) data were collected in the temperature range of 5.0-300 K, under a 0.1 T magnetic field, and were plotted as $\chi_M T$ *vs.* *T* in Figure 2.11 and 2.15. The data for **1**·DMF and **2** (Figure 2.11) indicate relatively large ground-state spin (*S*) values. $\chi_M T$ for **1**·DMF decreases from 38.71 cm^3Kmol^{-1} at 300 K to 26.65 cm^3Kmol^{-1} at 20.0 K, and then increases to 36.73 cm^3Kmol^{-1} at 5.0 K. For **2**, $\chi_M T$ steadily decreases from 30.94 cm^3Kmol^{-1} at 300 K to a minimum of 22.39 cm^3Kmol^{-1} at 35.0 K, and then increases sharply to 25.61 cm^3Kmol^{-1} at 6.5 K, before slightly dropping to 25.50 cm^3Kmol^{-1} at 5.0 K. The expected, spin-only $\chi_M T$ value for six Mn^{II} and eight Mn^{III} noninteracting ions in complex **1** at room

temperature is 50.25 cm^3Kmol^{-1} (g = 2), while the expected $\chi_M T$ value for eight Mn^{II}, four Mn^{III} and four Mn^{IV} noninteracting ions in complex **2** at 300 K is 54.5 cm^3Kmol^{-1} (g = 2). The overall shape of both $\chi_M T$ *vs. T* curves and the fact that the 300 K values of $\chi_M T$ are much less than the spin-only (g = 2) values are both indicative of predominant antiferromagnetic exchange interactions within **1** and **2**.

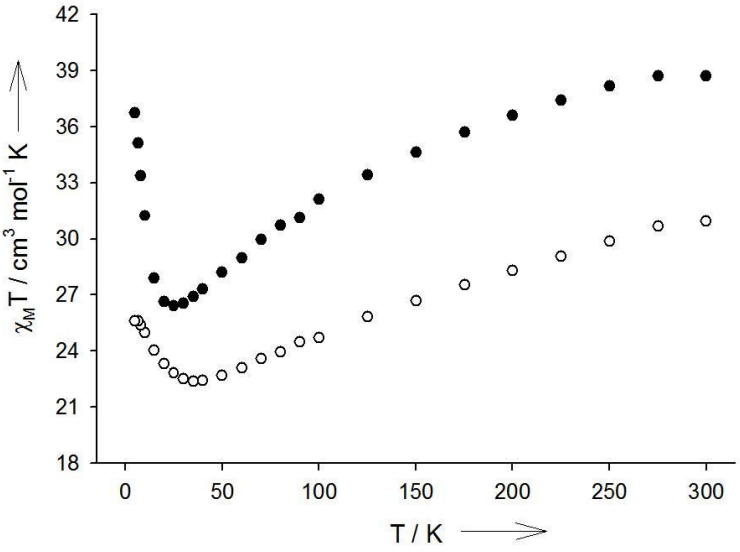

Figure 2.11. $\chi_M T$ *vs. T* plots for complexes **1**·DMF (●) and **2** (○) in a 1 kG field.

Attempted fits of magnetization data collected at various fields and at low temperatures, assuming that only the ground state is populated, were poor, suggesting population of low-lying excited states, as expected for such high-nuclearity complexes. Alternating current (*ac*) studies were also performed in the 1.8-15 K range using a 3.5 G *ac* field oscillating at frequencies in the 5-1500 Hz range. If the magnetization vector can relax fast enough to keep up with the oscillating field, then there is no imaginary (out-of-phase) susceptibility signal (χ''_M), and the real (in-phase) susceptibility (χ'_M) is equal to the *dc*

susceptibility.[126] The $\chi'_M T$ data extrapolated from a temperature high enough to avoid the effects of any weak intermolecular interactions or slow relaxation to 0 K (where only the ground state would be populated) should thus be in agreement with the formula: $\chi'_M T = g^2 S(S + 1)/8$, where S is the ground state of the compound. However, if the barrier to magnetization relaxation is significant compared to the thermal energy (kT), then there is a non-zero χ''_M signal and the in-phase signal decreases. In addition, the χ''_M signal, as well as the $\chi'_M T$ data, will be frequency-dependent. Such frequency-dependent χ''_M signals are a characteristic signature of the superparamagnetic-like properties of an SMM (but by themselves do not prove the SMM behavior).[127]

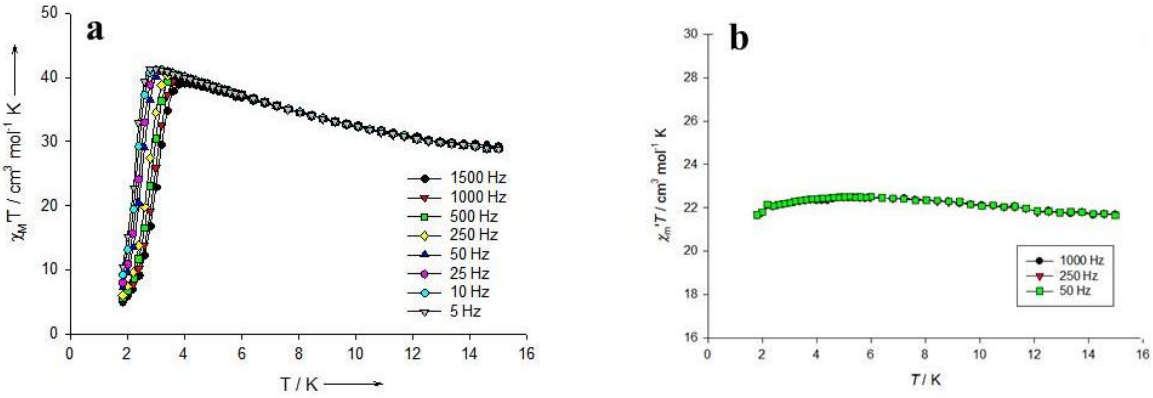

Figure 2.12. Plot of the in-phase (χ'_M) (as $\chi'_M T$) *ac* susceptibility signals of complexes **1**·DMF (a) and **2** (b), measured below 15.0 K in a 3.5 G field oscillating at the indicated frequencies.

For **1**·DMF and **2**, the in-phase (χ_M') *ac* signals, shown as $\chi_M' T$ in Figure 2.12, are temperature-dependent in the 4-15 K region, confirming the conclusion from the *dc* studies of low-lying excited states. Extrapolation of the data above 15 K down to 4 K

gives ~44 and 24 cm^3Kmol^{-1} for **1**·DMF and **2**, which indicates S = 9 and 7 ground states, respectively (with g slightly less than 2). At lower temperatures, only **1**·DMF displays a frequency-dependent decrease in $\chi_M'T$ and concomitant appearance of entirely visible out-of-phase χ_M" signals (Figure 2.13, top and left), a very rare situation for a high-nuclearity $Mn^{II/III}$ cluster and indicative of a significant barrier to magnetization relaxation. Indeed, an Arrhenius plot constructed from the *ac* χ_M'' *vs. T* data (Figure 2.13, top and right) gave the values: U_{eff} = 35(2) K and $\tau_0 = 7.4(2) \times 10^{-12}$ s, where τ_0 is the pre-exponential factor. A U_{eff} of 35 K is one of the highest observed for a $Mn^{II/III}$ mixed-valent complex, but still smaller than the U_{eff} values of the Mn_{12} SMMs.

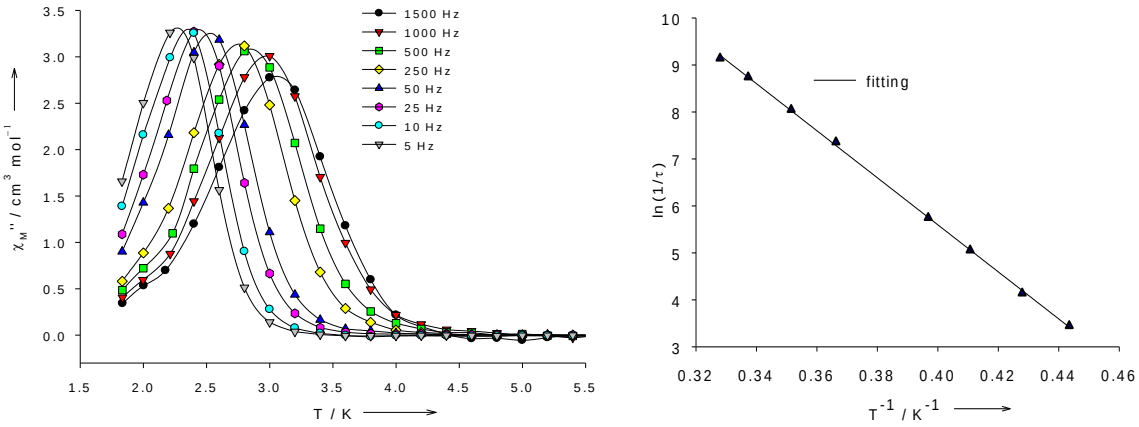

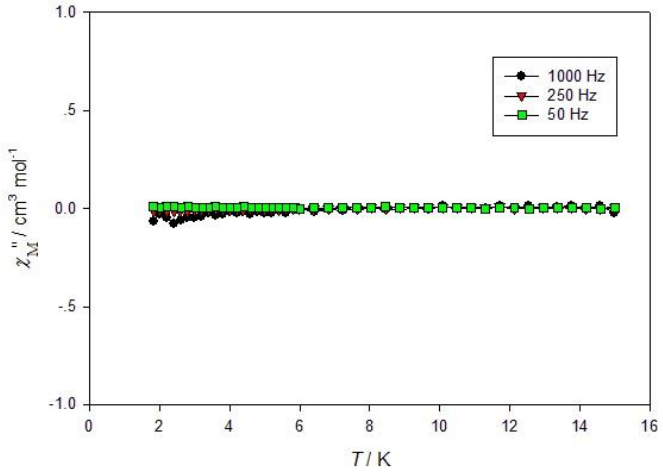

Figure 2.13. Plots of the out-of-phase (χ''_M) *ac* susceptibility signals of complexes **1**·DMF (top, left) and **2** (bottom) at the indicated frequencies. (top, right) Arrhenius plot of maxima observed in χ''_M for complex **1**·DMF; the solid line is the fit of the thermally-activated region to the Arrhenius-type equation.

The confirmation of SMM behavior for **1** was sought by magnetization (*M*) *vs*. *dc* field scans on a single crystal of **1** using an array of micro-SQUIDs. These scans allowed for the observation of magnetization hysteresis loops below 2 K. The loops exhibit coercivities that increase with decreasing temperature (Figure 2.14) and increasing field sweep rate, but do not show the steps characteristic of quantum tunneling of magnetization due to step-broadening effects from low-lying excited states and distributions of local environments owing to solvent disorder effects.[128]

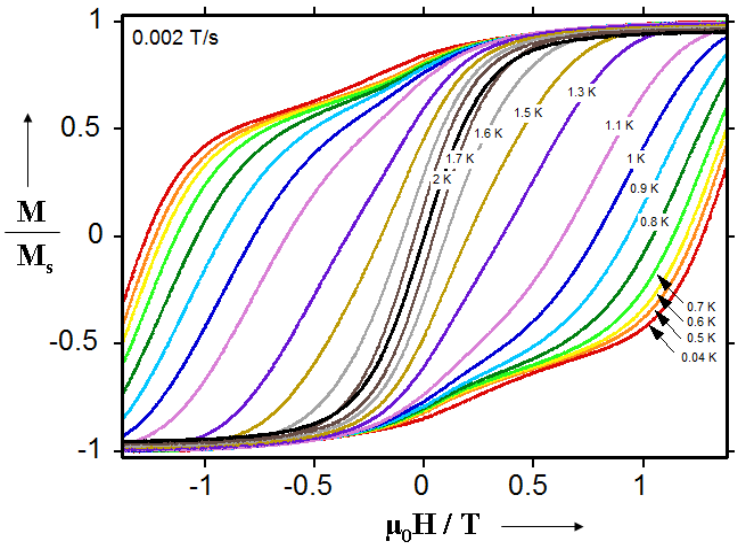

Figure 2.14. Magnetization (*M*) *vs.* applied *dc* field (*H*) hysteresis loops for a single-crystal of **1** at the indicated temperatures. The magnetization is normalized to its saturation value (M_s).

Figure 2.15 shows the thermal evolution of the $\chi_M T$ product for complex **3**. The $\chi_M T$ value at 300 K is 48.24 cm^3Kmol^{-1} and is very close to the spin-only (g = 2) value of 47.75 cm^3Kmol^{-1} expected for a Mn_{15} unit comprising two Mn^{II} and thirteen Mn^{III} non-interacting ions. The $\chi_M T$ value then increases gradually with decreasing temperature to a maximum of 97.84 cm^3Kmol^{-1} at 8 K, before decreasing to 95.98 cm^3Kmol^{-1} at 5.0 K. This behavior is indicative of the presence of predominant ferromagnetic exchange interactions in **3**. In addition, the maximum of 97.84 cm^3Kmol^{-1} at 8 K suggests that **3** possesses a large spin ground state value of S = 13 or 14; the spin-only (g = 2) values for S = 13 and 14 are 91 and 105 cm^3Kmol^{-1}, respectively. The small decrease of $\chi_M T$ at low temperatures (< 8 K) is likely due to zero-field splitting (ZFS), Zeeman effects from the applied field, and/or any weak intermolecular interactions. Given the size and low-symmetry of the Mn_{15} molecule, and the resulting number of inequivalent exchange constants, it is not possible to apply any fitting method to determine the individual pairwise exchange interaction parameters between the Mn ions; direct matrix diagonalization methods are also computationally unfeasible.

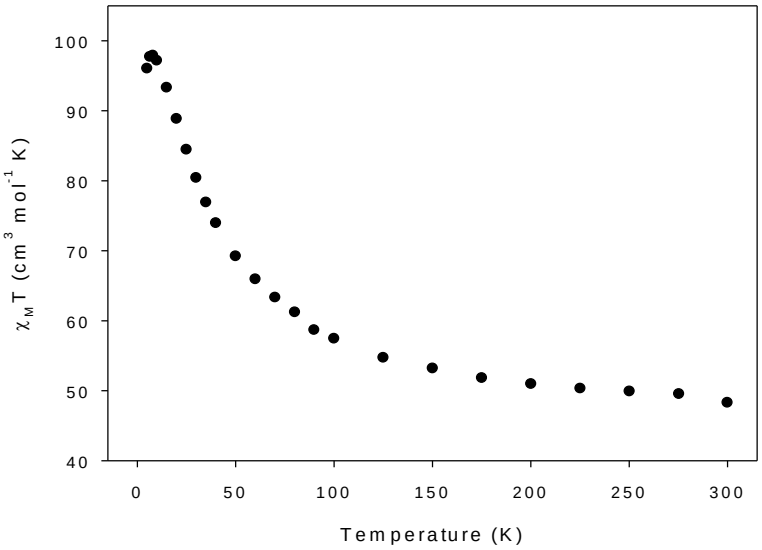

Figure 2.15. Plot of $\chi_M T$ *vs. T* for **3** in a 1 kG field.

To determine the ground state of **3**, magnetization (*M*) *vs. dc* field measurements were performed on a restrained sample of the compound in the magnetic field (*H*) and temperature ranges of 1.0-70.0 kG (0.1-7 T) and 1.8-10.0 K, respectively. The resulting data are shown in Figure 2.16 as a reduced magnetization ($M/N\mu_B$) *vs.* H/T plots, where *N* is Avogadro's number and μ_B is the Bohr magneton. The data were fit using the program MAGNET,[94] which assumes that only the ground state is populated at these temperatures, includes axial zero-field splitting ($D\hat{S}_z^2$) and isotropic Zeeman interactions with the applied field, and carries out a full powder average. The corresponding Hamiltonian is given by Equation 2.4,

$$\mathcal{H} = D\hat{S}_z^2 + g\mu_B\mu_0\hat{S}\cdot H \qquad (2.4)$$

where D is the axial ZFS parameter, $\hat{S}_z$ is the easy-axis spin operator, g is the electronic g factor, μ_0 is the vacuum permeability, and H is the applied field. The last term in Equation 2.4 is the Zeeman energy associated with an applied magnetic field. Unfortunately, we could not get an acceptable fit using data collected over the whole field range, which is a common problem caused by the presence of low-lying excited states or/and intermolecular interactions. As has been described elsewhere on multiple occasions for mixed-valence $Mn^{II/III}$ clusters,[108] a common solution to this problem is to use only data collected at low fields. Indeed, a reasonable fit of the reduced magnetization data could be achieved when data collected in fields only up to 2.0 T were employed. The fit is shown as the solid lines in Figure 2.16 and the fit parameters were: S = 14, D = -0.063(1) cm^{-1} and g = 1.97(1), slightly less than 2.0 as expected for mixed-valence $Mn^{II/III}$ complexes.[108] Attempts were also made to fit the data assuming an S = 13 or 15 spin ground state; however, the resulting fits were of much poorer quality and gave too small (<1.82) or too large (>2.06) for Mn clusters g values, respectively.

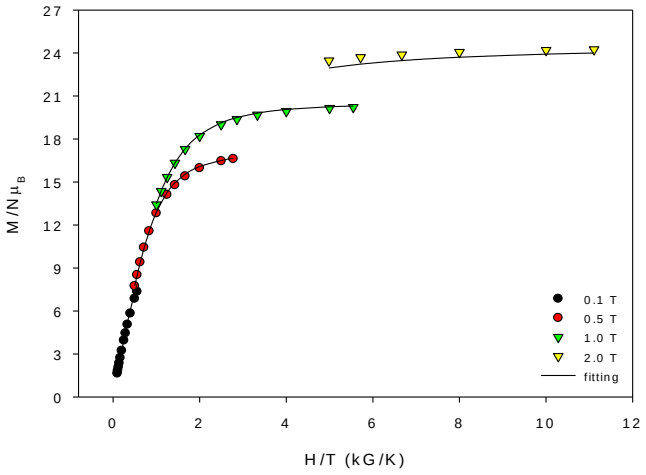

Figure 2.16. Plot of reduced magnetization ($M/N\mu_B$) vs. H/T for complex **3** at applied fields of 0.1–2.0 T and in the 1.8–10.0 K temperature range. The solid lines are the fit of the data.

Alternating current magnetic susceptibility studies were also performed in the 1.8-15 K range using a 3.5 G *ac* field oscillating at frequencies in the 50-1000 Hz range. For complex **3**, the in-phase signal (plotted as $\chi'_M T$ *vs.* T in Figure 2.17, top) increases slightly from ~92 cm^3Kmol^{-1} at 15 K to ~97 cm^3Kmol^{-1} at 8 K, followed by a plateau until ~6 K, and then decreases rapidly at temperatures lower than ~5 K. The small increase of the $\chi'_M T$ values is most likely due to depopulation of excited states with spin S smaller than that of the ground state. The rapid decrease of the $\chi'_M T$ below ~5 K is due to ZFS and any weak intermolecular interactions. In addition, below ~2.5 K there is a frequency-dependent decrease in $\chi'_M T$ and a concomitant appearance of frequency-dependent χ''_M signals (Figure 2.17, bottom). However, only the beginnings of peaks appear above 1.8 K (the operating minimum temperature of any conventional SQUID magnetometer), with the peak maxima clearly lying at lower temperatures. Such tails of signals are an indication of the superparamagnetic-like slow relaxation of an SMM, but one with a rather small relaxation barrier. Further confirmation of the SMM behavior would require single-crystal studies on a micro-SQUID apparatus, but this was not pursued because there are now many SMMs with such small relaxation barriers. Extrapolation to 0 K of $\chi'_M T$ from values above 8 K, to avoid complications from effects such as intermolecular interactions and ZFS at lower temperatures, gives a value of ~104 cm^3Kmol^{-1}, indicative

of a ground spin state of S = 14 with g ~1.99, in satisfying agreement with the results obtained by the *dc* magnetization fits.

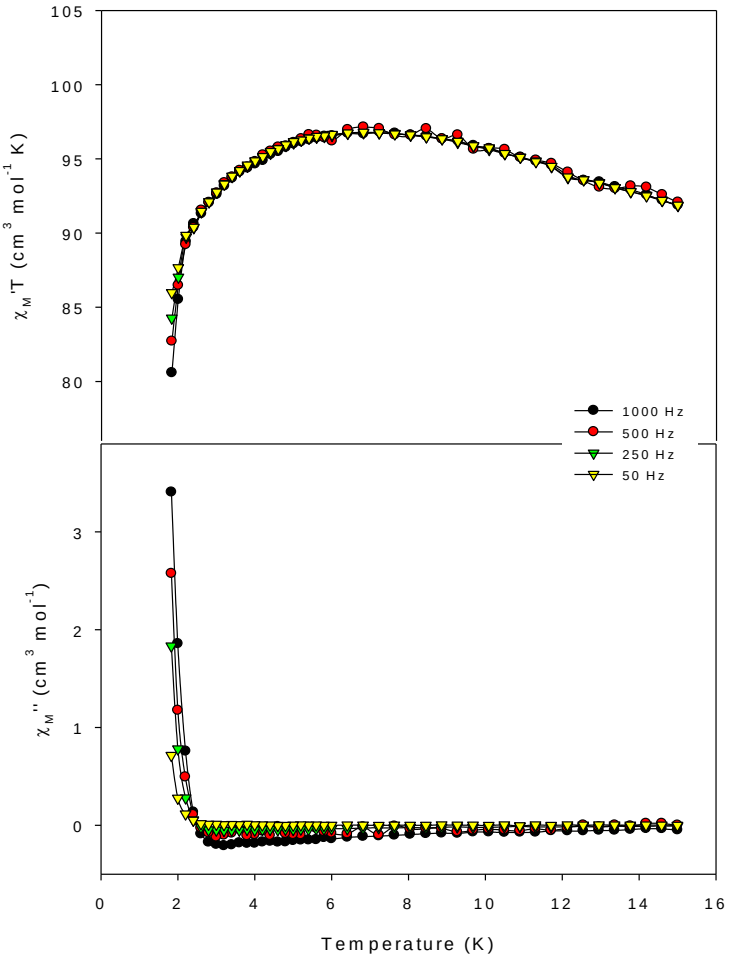

Figure 2.17. Plots of the in-phase (χ_M') as $\chi_M'T$ (top) and out-of-phase (χ_M'') (bottom) *ac* magnetic susceptibilities *vs*. *T* for complex **3** in a 3.5 G field oscillating at the indicated frequencies.

2.3. Conclusions and Perspectives

In this chapter, we have shown for a first time that heteroatomic-type pseudohalides, such as OCN^-, can be employed as structure-directing ligands and ferromagnetic couplers in higher oxidation state Mn cluster chemistry, leading to molecular species with different structural motifs and physical properties than those obtained from the corresponding reactions with N_3^-. Indeed, in past work, Christou and coworkers have shown that azide and the *gem*-diolate form of di-2-pyridylketone in $Mn/MeCO_2^-$ chemistry yields dumbbell-shaped $[Mn_{26}O_8(OH)_4(N_3)_{12}(O_2CMe)_6(dpkd)_{14}(DMF)_4]$ cluster,[117b] while a similar reaction but with the ligand 2,6-diacetylpyridine dioxime ($dapdoH_2$) leads to the $[Mn_8O_4(OH)_6(N_3)_2(dapdo)_2(dapdoH)_2(H_2O)_2]$ compound.[117c] Both $\{Mn_{26}\}$ and $\{Mn_8\}$ azido complexes are structurally and magnetically different than the reported $\{Mn_{14}\}$ and $\{Mn_{16}\}$ cyanato complexes in this chapter. From a magnetic viewpoint, the $\{Mn_{14}\}$ cluster displays entirely visible out-of-phase χ_M" signals below 5 K, as well as large hysteresis loops at temperatures below 2 K, a very rare situation for a high-nuclearity $Mn^{II/III}$ single-molecule magnet. We believe that the combined results will be the prototypes of a rich new area of high-nuclearity/high-spin molecules and SMMs, derived from the amalgamation of cyanato groups and various chelate ligands, surpassing in success the corresponding results obtained from the use of azido ligands.

Furthermore, complex **3** extends the body of results that emphasize the pronounced ability of tea^{3-} anion to stabilize high-nuclearity Mn species when combined with various ancillary groups such as carboxylates and azides. Complex **3** is novel in multiple ways, as described above, but also provides a rare example of a ferromagnetic, high-nuclearity mixed-valence $Mn^{II/III}$ cluster with a large ground-state spin value of $S = 14$. Due to the complexity of the Mn_{15} structure and the multiple fused triangular subunits, textbook

examples of a topology that can give spin frustration effects (competing exchange interactions), any attempts to rationalize the observed *S* value shall fall into inaccuracies. Nevertheless, such magnetostructural complications are of precedence in molecular cluster chemistry, but these have not prevented synthetic chemists from making more and more nanometer-sized compounds with aesthetically-pleasing structures and impressive physical properties.

In conclusion, we believe that this is a new area for scientists to follow and is very promising in leading the scientific community (i.e., inorganic chemists, structural chemists and magnetochemists) to new molecular compounds with interesting physical properties. An obvious future direction for a synthetic inorganic chemist to follow is the exploration of other chemical systems where cyanates would be combined with other alkoxido- and/or oximate-based chelates in higher oxidation state Mn cluster chemistry. We are also working on the chemical reactivity of complex **3** by trying to investigate how the substitution of $Bu^tCO_2^-$ groups by various other carboxylate groups, less employed before in Mn cluster chemistry, may affect the identity of isolated $Mn/teaH_3/N_3^-$ compounds, and to what extent this might prove a route to new cluster types.

CHAPTER 3: New Classes of Ferromagnetic Materials with Exclusively End-On Azido Bridges: From SMMs to Two-Dimensional Molecule-Based Magnets

3.1. Experimental Section

3.1.1. Physical Measurements

Elemental Analysis: Elemental analyses (C, H, and N) were performed on a Perkin-Elmer 2400 Series II Analyzer.

FT-IR spectroscopy: Infrared (IR) spectra were recorded in the solid state on a Bruker FT-IR spectrometer (ALPHA Platinum ATR single reflection) in the 4000-450 cm^{-1} range. Notation for IR bands: vs = very strong; s = strong; m = medium; w = weak; b = broad.

Magnetic susceptibility measurements: Direct current (*dc*) magnetic susceptibility studies were performed at the Chemistry Department of the University of Barcelona on a Quantum Design SQUID magnetometer equipped with a 7 T magnet and operating in the 1.9-300 K range. Samples were embedded in solid eicosane to prevent torquing. Pascal's constants were used to estimate the diamagnetic correction, which was subtracted from the experimental susceptibility to give the molar paramagnetic susceptibility (χ_M).[92]

3.1.2. Synthesis

General considerations: All experiments were performed under ambient conditions. All chemicals were purchased from Sigma Aldrich and Alfa Aesar. Chemicals and solvents were used as received without further purification.

Safety note: Azide (N_3^-) and perchlorate (ClO_4^-) salts are potentially explosive; such compounds should be synthesized and used in small quantities, and treated with utmost care at all times.

$[Co_7(N_3)_{12}(MeCN)_{12}](ClO_4)_2$ (4): To a stirred, pink solution of $Co(ClO_4)_2 \cdot 6H_2O$ (0.07 g, 0.2 mmol) and NEt_3 (0.03 mL, 0.2 mmol) in MeCN (10 mL) was added Me_3SiN_3 (0.11 mL, 0.8 mmol). The resulting deep-pink solution was stirred for 10 min, filtered and carefully layered with Et_2O (20 mL). Next day, large in size, X-ray quality pink plate-like crystals of **4** were collected by filtration, washed with cold MeCN (2 x 2 mL) and dried in air. The yield was 75%. Elemental analysis (%) calcd for **4**: C 17.92, H 2.26, N 41.80; found: C 17.69, H 2.16, N 42.02. Selected IR data (ATR): *v* = 3356 (w), 3002 (w), 2089 (vs), 2063 (vs), 1635 (w), 1412 (w), 1365 (w), 1284 (m), 1229 (w), 1095 (sb), 1031 (m), 933 (w), 673 (w), 623 (m).

$[Ni_7(N_3)_{12}(MeCN)_{12}](ClO_4)_2$ (5): To a stirred, green solution of $Ni(ClO_4)_2 \cdot 6H_2O$ (0.07 g, 0.2 mmol) and NEt_3 (0.03 mL, 0.2 mmol) in MeCN (10 mL) was added Me_3SiN_3 (0.11 mL, 0.8 mmol). The resulting deep-green solution was stirred for 10 min, filtered and carefully layered with Et_2O (20 mL). Next day, large in size, X-ray quality green plate-like crystals of **5** were collected by filtration, washed with cold MeCN (2 x 2 mL) and dried in air. The yield was 78%. Elemental analysis (%) calcd for **5**: C 17.94, H 2.26, N

41.85; found: C 18.05, H 2.32, N 41.68. Selected IR data (ATR): ν = 3356 (w), 3002 (w), 2089 (vs), 2063 (vs), 1635 (w), 1412 (w), 1365 (w), 1284 (m), 1229 (w), 1095 (sb), 1031 (m), 933 (w), 673 (w), 623 (m).

$[Fe_2(N_3)_5(MeCN)_2]_n$ (6): To a stirred, orange solution of $Fe(ClO_4)_2 \cdot xH_2O$ (0.05 g, 0.2 mmol) and NEt_3 (0.03 mL, 0.2 mmol) in MeCN (10 mL) was added Me_3SiN_3 (0.11 mL, 0.8 mmol). The resulting dark orange-red solution was stirred for 10 min, filtered and carefully layered with Et_2O (20 mL). Slow mixing gave after 1 day dark orange-red prismatic crystals of **6**, suitable for X-ray diffraction studies, which were collected by filtration, washed with cold MeCN (2 x 2 mL) and dried in air. The yield was 52%. Elemental analysis (%) calcd for **6**: C 11.90, H 1.50, N 58.95; found: C 11.74, H 1.38, N 59.09. Selected IR data (ATR): ν =3220 (mb), 2062 (vs), 1618 (w), 1341 (w), 921 (w), 645 (wb).

3.1.3. Single-crystal X-ray Crystallography

Crystals of the complexes **4**-**6** were selected and mounted on cryoloops using inert oil. Diffraction data were collected at 150.0(2) K on a Bruker X8 Kappa APEX II Charge-Coupled Device (CCD) area detector diffractometer controlled by the APEX2 software package[100] (Mo Kα graphite-monochromated radiation, λ = 0.71073 Å), and equipped with an Oxford Cryosystems Series 700 cryostream monitored remotely with the software interface Cryopad.[101] Images were processed with the software SAINT+,[102] and absorption effects were corrected with the multiscan method implemented in SADABS.[103] The structures were solved by direct methods employed in SHELXS-97,[96,97]

allowing the immediate location of the metals. The other non-hydrogen atoms of the complexes were located from difference Fourier maps calculated by successive full-matrix least-squares refinement cycles on F^2 using SHELXL-97,[98,99] and effectively refined with anisotropic displacement parameters. Hydrogen atoms of the MeCN molecules were located at their geometrical positions using the HFIX-137 instruction in SHELXL and incorporated in subsequent refinement cycles in riding-motion approximation with isotropic thermal displacements parameters (U_{iso}) fixed at 1.5 × U_{eq}. Information concerning crystallographic data collection and structure refinement details is summarized in Table 3.1.

Table 3.1. Crystallographic data for complexes **4**-**6**

Parameter	**4**	**5**	**6**
Formula	$C_{24}H_{36}Cl_2Co_7N_{48}O_8$	$C_{24}H_{36}Cl_2N_{48}Ni_7O_8$	$C_4H_6Fe_2N_{17}$
Formula weight / g mol^{-1}	1608.42	1606.88	403.96
Crystal type	Pink plates	Green plates	Red prisms
Crystal size / mm^3	0.25 × 0.07 × 0.05	0.30 × 0.07 × 0.05	0.14 × 0.06 × 0.03
Crystal system	Monoclinic	Monoclinic	Monoclinic
Space group	$P2_1/c$	$P2_1/c$	$C2/c$
a / Å	11.932(1)	11.995(1)	8.363(5)
b / Å	23.198(2)	22.730(2)	22.754(2)
c / Å	11.900(1)	11.853(1)	16.385(1)
β / º	92.493(4)	94.232(4)	101.660(3)
Volume / Å^3	3290.8(5)	3222.8(5)	3053.5(5)

Z	2	2	8
D_c / g cm^{-3}	1.623	1.656	1.757
μ(Mo-Kα) / mm^{-1}	1.880	2.162	1.929
θ range	3.76 - 25.68	3.68 - 25.37	3.66 - 26.37
Index ranges	$-14 \le h \le 14$	$-14 \le h \le 14$	$-9 \le h \le 9$
	$-28 \le k \le 28$	$-28 \le k \le 28$	$-28 \le k \le 24$
	$-14 \le l \le 14$	$-14 \le l \le 14$	$-20 \le l \le 18$
Reflections collected	90208	54973	24948
Independent reflections	6238 (R_{int} = 0.0378)	6543 (R_{int} = 0.0284)	3121(R_{int} = 0.0510)
Data completeness	to θ = 25.68º, 99.6%	to θ = 25.37º, 99.4%	to θ = 26.38º, 99.6%
Final R indices [I>2σ(I)][a,b]	$R1$ = 0.0584	$R1$ = 0.0581	$R1$ = 0.0598
	$wR2$ = 0.1402	$wR2$ = 0.1290	$wR2$ = 0.0906
Final R indices (all data)	$R1$ = 0.0682	$R1$ = 0.0700	$R1$ = 0.0742
	$wR2$ = 0.1457	$wR2$ = 0.1383	$wR2$ = 0.0942
$(\Delta\rho)_{max,min}$ / e Å^{-3}	1.072 and −0.808	1.521 and −1.057	1.072 and −0.808

[a] $R1 = \Sigma(||F_o| - |F_c||)/\Sigma|F_o|$. [b] $wR2 = [\Sigma[w(F_o^2 - F_c^2)^2]/ \Sigma[w(F_o^2)^2]]^{1/2}$, $w = 1/[\sigma^2(F_o^2) + [(ap)^2 + bp]$, where $p = [\max(F_o^2, 0) + 2F_c^2]/3$

3.2. Results and Discussion

3.2.1. Synthetic Comments

Azido (N_3^-) ligand has been known for years as one of the most flexible, multitopic and versatile groups in coordination chemistry, capable of bridging many metal centers and yielding beautiful structures with interesting magnetic properties.[82] However, in all previously reported metal cluster compounds and coordination networks, azides have been always employed in conjunction with organic bridging/chelating ligands. Although necessary for the thermodynamic stability and crystallinity of the resulting molecular species, the presence of organic ligands often affects the magnetic properties and magnetization dynamics of the compounds, leading to competing antiferromagnetic interactions, moderate-to-weak magnetic couplings, and low-lying excited states, among others.[82] A potential solution to overcome these problems and construct strongly ferromagnetic systems is the discovery of new synthetic strategies for the assembly of polymetallic-azido structures without the co-presence of organic chelating/bridging ligands. In the present work we decided to follow a new, simpler synthetic route which does not require the co-presence of any organic chelating/bridging ligand but only the azido-ligand precursor Me_3SiN_3. Our initial synthetic scheme included one-pot reactions between various M^{II} (M = Co and Ni) sources and Me_3SiN_3 under basic conditions in different solvent media and crystallization conditions. The idea was that, although the mechanism of cluster formation is difficult to predict, it is likely that the base will raise the pH of the solutions and facilitate the deprotonation of H_2O-containing solvents and

starting materials to OH^- groups; the latter will be then abstracted[129] by Me_3Si^+ groups allowing the isolation of metal/N_3^--rich polynuclear compounds. Therefore, the resulting metal complexes would likely contain only end-on (EO) bridging azides and consequently their magnetic properties would be characterized by high-spin ground state values.

A variety of reactions differing in the $M^{II}(ClO_4)_2$:Me_3SiN_3 ratio (M = Co or Ni), the organic base and/or the reaction solvent(s) were explored in identifying the following successful systems. The reaction of $Co(ClO_4)_2 \cdot 6H_2O$, NEt_3, and Me_3SiN_3 in a 1:1:4 molar ratio in MeCN led to a pink solution which was layered with Et_2O to give next day pink plate-like crystals of $[Co^{II}_7(N_3)_{12}(MeCN)_{12}](ClO_4)_2$ (**4**) in 75% yield. A similar reaction with $Ni(ClO_4)_2 \cdot 6H_2O$ in place of $Co(ClO_4)_2 \cdot 6H_2O$ afforded the isomorphous $[Ni^{II}_7(N_3)_{12}(MeCN)_{12}](ClO_4)_2$ (**5**) compound as green plates in 78% yield. The formation of **4** and **5** can be represented by the balanced Equation 3.1.

$$7\ M^{2+} + 12\ N_3^- + 12\ MeCN \rightarrow [M^{II}_7(N_3)_{12}(MeCN)_{12}]^{2+} \quad (M = Co \text{ or } Ni) \qquad (3.1)$$

An important synthetic factor that is worthy investigating is the effect of the organic base on the structural identity of the complexes. To that end, the successful reaction that led to the isolation of **4** and **5** was repeated, under exactly the same conditions, but in the presence of different organic bases, such as Me_4NOH, Et_4NOH, and $^nBu_4NOH$. However, all these reactions failed to give any crystalline material but only amorphous precipitates that were probably metal oxides or oxo/hydroxide species. No significant reactions were

observed in the absence of organic base NEt_3. Analogous reactions employing NaN_3 or LiN_3, instead of Me_3SiN_3, did not yield any products. All these observations further support our hypothesis that both the presence of base and Me_3Si^+ groups is essential for the formation of the isolated compounds.

After the employment of Me_3SiN_3 in divalent 3*d*-metal chemistry, we attempted to develop this synthetic strategy further, now to more redox-active 3*d*-metals. Thus, the aerobic reaction of $Fe(ClO_4)_2 \cdot xH_2O$, NEt_3, and Me_3SiN_3 in a 1:1:4 molar ratio in MeCN led to dark orange crystals of the mixed-valence compound $[Fe^{II}Fe^{III}(N_3)_5(MeCN)_2]_n$ (**6**) in 52% yield. The formation of **6** can be represented by the balanced Equation 3.2.

$$2n\ Fe^{2+} + 5n\ N_3^- + n\ H^+ + \frac{n}{4} O_2 + 2n\ MeCN \rightarrow$$

$$[Fe^{II}Fe^{III}(N_3)_5(MeCN)_2]_n + \frac{n}{2} H_2O \qquad (3.2)$$

The synthesis involves $Fe^{II} \rightarrow Fe^{III}$ oxidation, undoubtedly by atmospheric O_2, and equation 3.2 has been balanced accordingly. Finally, the MeCN reaction solvent was identified as the one giving the highest product yield and purity, as well as the best quality single crystals.

3.2.2. Description of Structures

Given the structural similarity of clusters **4** and **5** (Figure 3.1), only the structure of the former will be discussed in detail. The centrosymmetric heptanuclear dication of **4** (Figure 3.1, left) contains an almost ideal, planar hexagon of alternating Co^{II} atoms surrounding a central, seventh Co^{II} atom. The Co_7 disk-like unit is held together by 12 N atoms of six 3.30 (or μ_3-1,1,1) and six 2.20 (or μ-1,1) end-on bridging azido ligands. The former type of N_3^- groups bridge the Co_6 hexagon with the central Co atom and the latter bridge the Co_2 pairs of the hexagon. Peripheral ligation is completed by 12 terminal MeCN solvate molecules, two on each of the external Co^{II} atoms. All Co^{II} ions are six-coordinate with near-octahedral geometries. The $[Co_7(\mu_3\text{-}N_3)_6(\mu\text{-}N_3)_6]^{2+}$ inorganic core of **4** (Figure 3.1, right) can alternatively be described as consisting of six $\{Co_3(N_3)_4\}$ partial-cubane units, each double face-sharing, and all six vertex-sharing at the central Co^{II} atom. Complex **4** has a layered structure, with layers of N atoms from azides above and below the Co_7 plane (Figure 3.1, right). The Co_7 dication has virtual or imposed C_3 symmetry. The Co···Co separations and Co-(μ-N_3)-Co angles span the range 3.228-3.279 Å and 95.0-103.0°, respectively. The packing of the Co_7 clusters shows large intermetallic separations between Co^{II} atoms of neighboring molecules, with the closest intermolecular Co···Co distance being 8.13 Å.

Complex **4** belongs to a family of structurally known disk-like Co_7 clusters albeit is the first solely bridged by μ- and μ_3-EO azido groups.[130] Of significant importance is the fact that **4** (and **5**) consists of 1.7:1 N_3^-/metal ratio, the highest yet reported for any polynuclear metal system with a nuclearity larger than four, which renders these species potentially attractive for high energy density materials study.[131] Furthermore, **4** and **5** are

the first metal clusters in moderate oxidation states which are exclusively bridged by azido groups and stabilized without the co-presence of any additional organic N,O-bridging/chelating ligand.

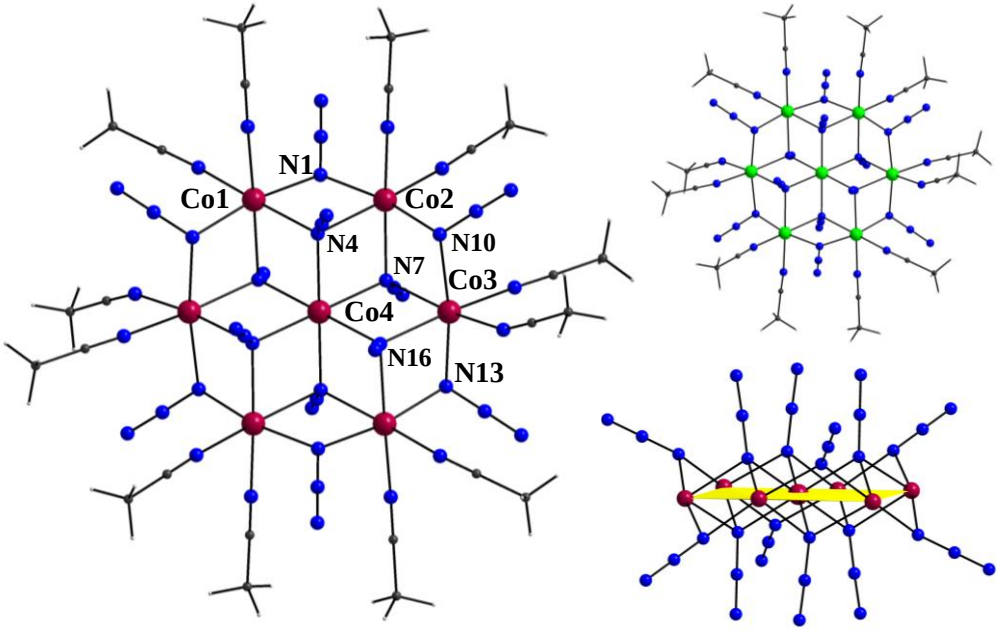

Figure 3.1. Partially-labeled representations of the dications of complexes **4** (left) and **5** (top, right), and a side view of the $[Co_7(\mu_3\text{-}N_3)_6(\mu\text{-}N_3)_6]^{2+}$ core (bottom, right). Color scheme: Co^{II}, maroon; Ni^{II}, green; N, blue; C, dark grey; H, light grey.

Complex **6** is a neutral 2-D coordination polymer (Figure 3.2) with the asymmetric unit consisting of two iron centers bridged by five 2.20 (or μ-1,1) end-on azido ligands; peripheral ligation is provided by two terminal MeCN molecules. Due to the crystallographic *C*2/*c* point group symmetry, Fe1 and Fe3 are half-occupied while Fe2 is

fully-occupied in the asymmetric unit. The metal ions oxidation states were assigned based on metric parameters and BVS calculations.[114] As a result, Fe1 and Fe3 atoms are +2 and Fe2 is +3, confirming the mixed-valence description for **6**; all metal atoms are high-spin and six-coordinate with distorted FeN_6 octahedral geometries.

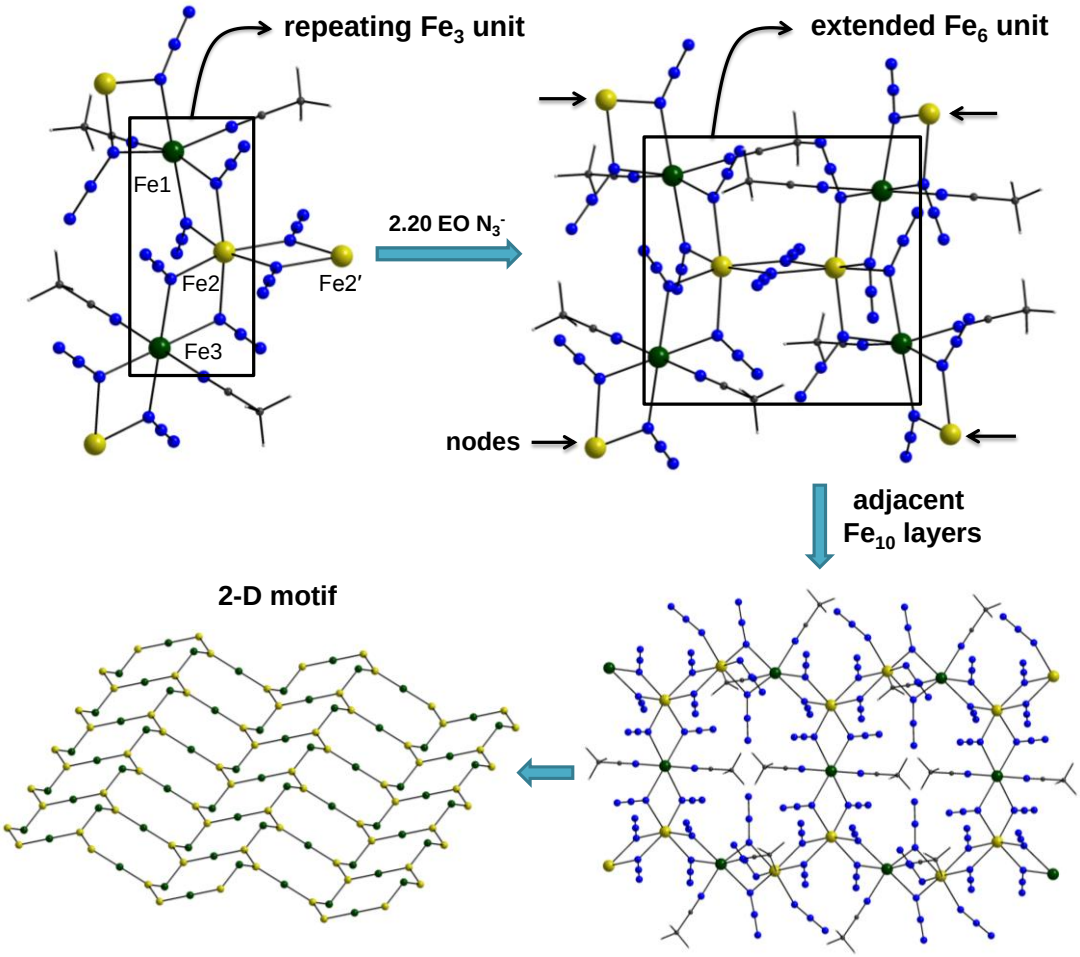

Figure 3.2. 'Building up' the 2-D polymer **6** from simpler fragments. Color scheme: Fe^{II}, dark green; Fe^{III}, yellow; N, blue; C, dark grey; H, light grey.

The repeating $\{Fe^{II}_2Fe^{III}(N_3)_7(MeCN)_2\}$ unit is not linear but bent, with an Fe1···Fe2···Fe3 angle of 119.1°. Two N_3^- groups, bound to the central Fe2 atom, become

2.20 EO, serving to bridge the $\{Fe^{II}_2Fe^{III}(N_3)_7(MeCN)_2\}$ unit with an adjacent one. The Fe2-($\mu_{1,1}$-N_3)$_2$-Fe2′ subunit is strictly planar. The resulting $\{Fe^{II}_4Fe^{III}_2(N_3)_{14}(MeCN)_4\}$ moieties are further linked by 2.20 EO-N_3^- groups (bound to the 'nodal' Fe1 and Fe3 atoms) to finally form aesthetically pleasing $[Fe^{II}_4Fe^{III}_6(N_3)_{26}(MeCN)_8]_\infty$ cyclic units which create an extended 2-D network of ladder-like hexagonal layers. The Fe···Fe intralayer separations and Fe-($\mu_{1,1}$-N_3)-Fe angles span the range 3.331-3.393 Å and 102.5-106.7°, respectively. The shortest interlayer distance is 9.47 Å. Complex **6** is, to our knowledge, the first 2-D coordination polymer containing solely EO-N_3^- groups. It is by far the compound with the highest N_3^-/metal ratio (2.5/1) and a unique member of a new, emerging class of azido-rich/ligand-free multidimensional coordination polymers.

3.2.3. Solid-state Magnetic Susceptibility Studies

To elucidate the static and dynamic magnetic properties of the heptanuclear compounds, solid-state *dc* (direct current) and *ac* (alternating current) magnetic susceptibility studies were performed on freshly crystalline samples of **4** and **5** in the 1.8-300 K range. Under a *dc* field of 1 kG (0.1 T), the value of $\chi_M T$ for **4** at 300 K is 25.10 $cm^3mol^{-1}K$, which is much higher than the spin-only value of seven high-spin, S = 3/2, Co^{II} ions (13.13 $cm^3mol^{-1}K$), indicating significant orbital contributions of the distorted octahedral Co^{II} ions. Upon cooling, the $\chi_M T$ product rapidly increases to a maximum of 74.53 $cm^3mol^{-1}K$ at 14 K and then decreases sharply to a value of 46.79 $cm^3mol^{-1}K$ at 2 K (Figure 3.3, top, left). The data above 150 K obey the Curie-Weiss law with C = 21.06

$cm^3mol^{-1}K$ and θ = +48.7 K, clearly suggesting an overall ferromagnetic coupling between the seven Co^{II} centers (Figure 3.3, bottom).

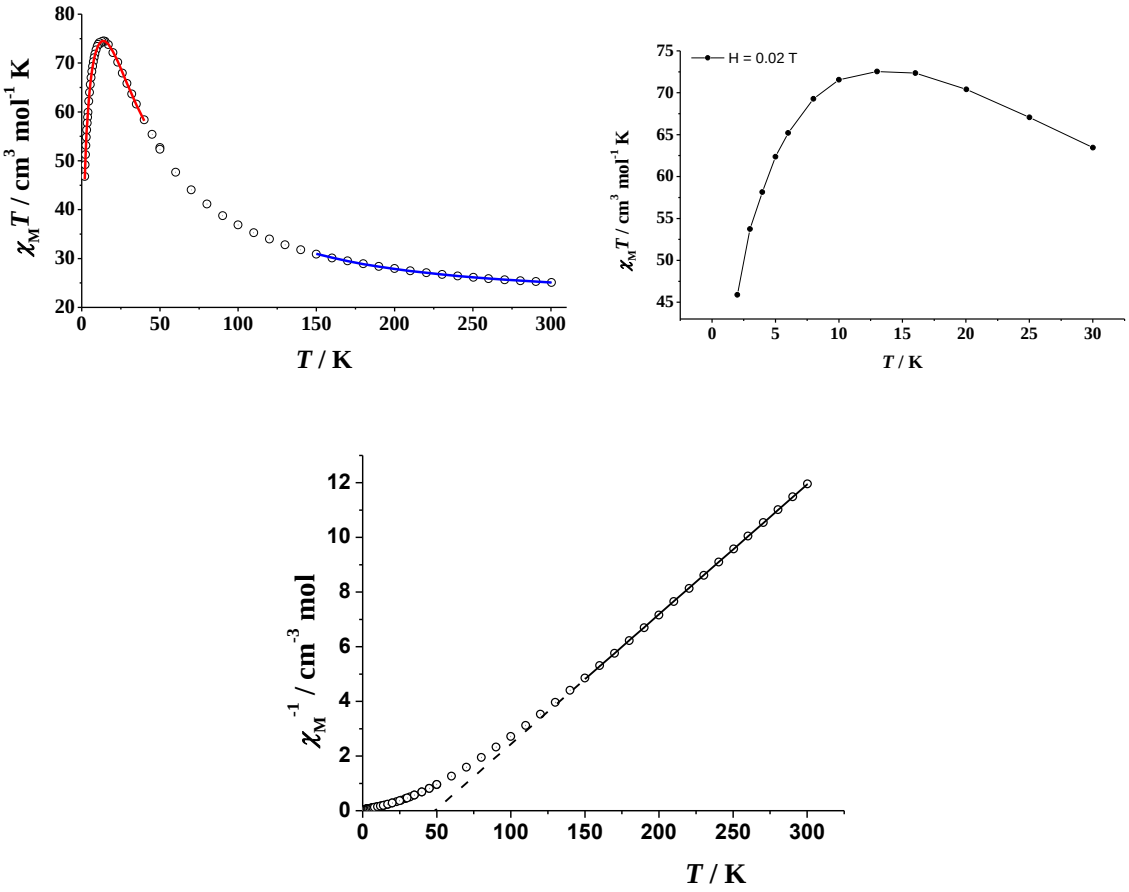

Figure 3.3. (top, left) $\chi_M T$ *vs.* T plot for **4** in a 1 kG field. The solid lines are the fits of the data (see below). (top, right) The low-temperature region of $\chi_M T$ *vs.* T plot for **4** under a 0.02 T *dc* field, showing a similar behavior with the corresponding data under 0.1 T, to exclude any field saturation effects. (bottom) χ_M^{-1} *vs.* T plot for **4**. The thick line represents the fitting of the data to the Curie-Weiss law.

Considering the bridging ligation within the Co_7 core of **4**, we attempted to simulate the magnetic data using the fitting models previously employed by Gao and coworkers for the structurally similar $[Co^{II}_7(N_3)_9(OMe)_3(bzp)_6]^{2+}$ (bzp = 2-benzoyl pyridine) with an approximate S_6 symmetry.[132] The program used for fitting all the magnetic data was PHI,[133] and all J values are referred to the general spin-Hamiltonian, $\hat{H} = -J\hat{S}_a\hat{S}_b$. The fitting of the high-T (>150 K) regime (blue line in Figure 3.3) gave an average J_{av} = +9.34 cm^{-1} with each S_{Co} = 3/2 and g = 2.50. An alternative fit with a 2-J coupling constant scheme (one J between the peripheral Co ions and another J for the interactions between the peripheral and central Co ions) tended to give very similar J parameters. For the low-T region (2-40 K) we considered an effective spin S'_{Co} = 1/2 system; an excellent fit (red line in Figure 3.3) was obtained with J_{av} = +29.4 cm^{-1}, zJ' = -0.11 cm^{-1} and g = 6.63, where zJ' is a term which accounts for the weak intermolecular interactions. This further confirms the strong intracluster ferromagnetic interactions in **4** which lead to an effective spin ground state of S = 7/2. The field-dependent magnetization studies were also performed at the temperature range 1.8-6.8 K with the isofield lines being far from superposition, indicating significant magnetoanisotropy. An excellent fit of the reduced magnetization data was obtained assuming a well-isolated, S = 7/2 ground state with D = -5.55 cm^{-1} and g = 6.56 (Figure 3.4).

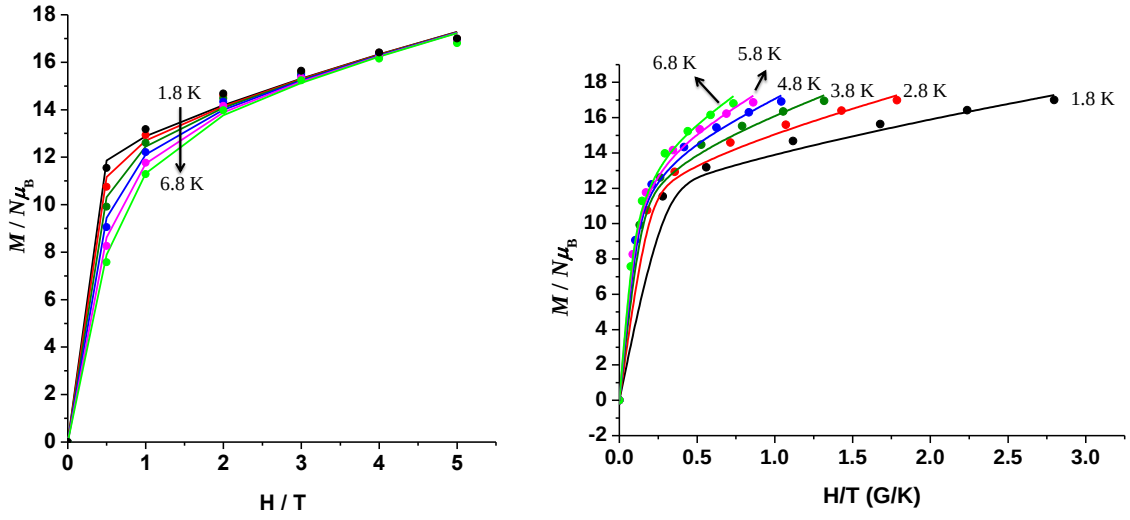

Figure 3.4. Plots of magnetization (*M*) *vs.* field (*H*) (left) and reduced magnetization (right) for complex **4** at different low temperatures and applied fields. The solid lines are the fit of the data (see the text for the fit parameters).

Another evidence for the possible SMM behavior of **4** is the observation of strong and frequency-dependent out-of-phase (χ_M'') *ac* signals below 6 K in zero applied *dc* field, although no peak maxima were observed for the majority of frequencies down to 1.8 K (Figure 3.5). It is now well-established that the effective energy barrier, U_{eff}, for the magnetization reversal of an SMM can be tuned by the application of a small external *dc* field which suppresses the fast tunneling usually seen for almost all Co^{II} SMMs.[86] That was also the case for **4**; application of a 0.1 T *dc* field resulted in an appreciable shift of the in-phase (χ_M') and out-of-phase (χ_M'') *ac* signals at higher-*T* (Figure 3.6), and thus the peak maxima were now clearly observed for all high- and low-*ac* frequencies (Figure 3.7). An Arrhenius plot constructed from the ac χ_M'' *vs. T* data of Figure 3.8 gave $\Delta E/k_B$ = 28.1 K (= 19.6 cm^{-1}) and $\tau_0 = 8.0 \times 10^{-8}$ s, where τ_0 is the pre-exponential factor.

Compared with all the previously reported Co^{II}_7 disks, complex **4** (i) is a stronger ferromagnetic system due to the presence of 2.20 and 3.30 EO azides, (ii) has a very well isolated ground state spin value as evidenced by the similar EPR spectra at 4 and 23 K (Figure 3.9), and (iii) is a better field-induced SMM with an energy barrier amongst the highest yet reported for any polynuclear Co^{II} SMM.[86,134]

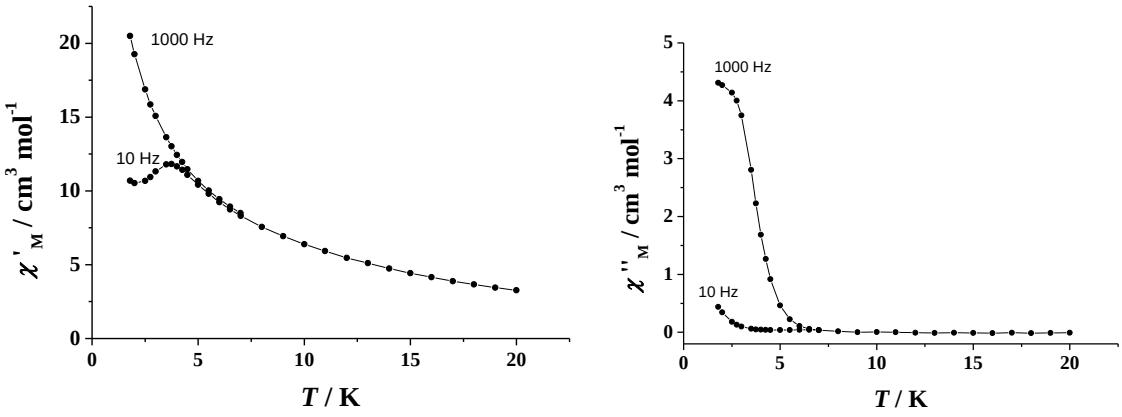

Figure 3.5. Plots of the in-phase (χ'_M, left) and out-of-phase (χ''_M, right) *ac* susceptibility signals of complex **4**, measured below 20.0 K in a 4.0 G *ac* field (and zero *dc* static field) oscillating at the indicated frequencies.

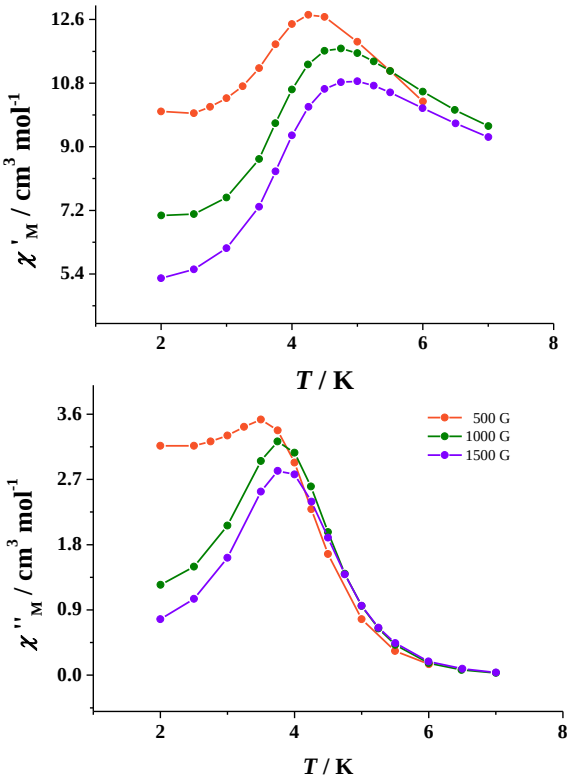

Figure 3.6. Temperature-dependence of the real (top) and imaginary (bottom) components of the *ac* susceptibility of **4** in three different applied *dc* fields (0.05, 0.10 and 0.15 T) with an oscillating *ac* field of 4.0 G.

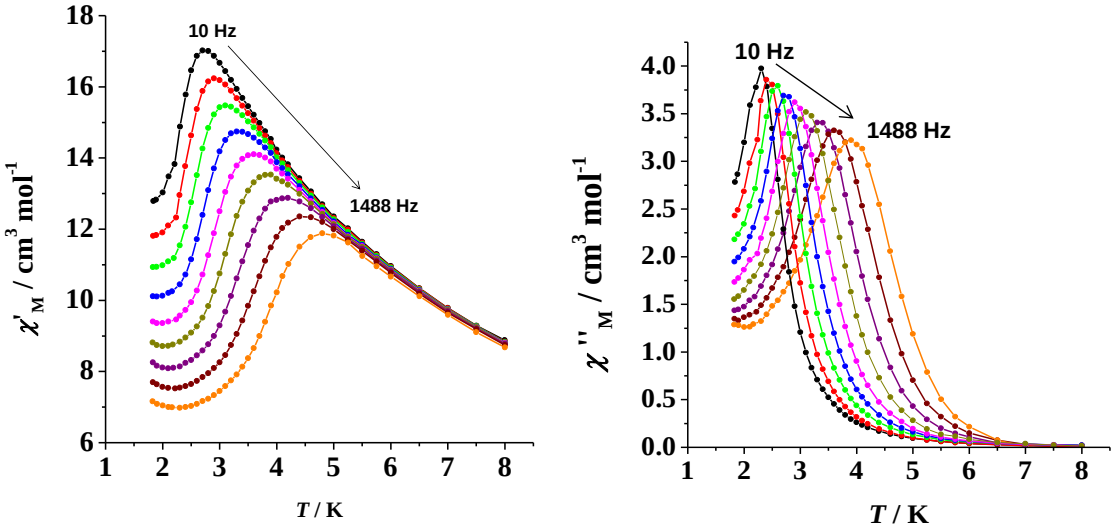

Figure 3.7. (left) Plot of the in-phase (χ'_M) *ac* susceptibility signals of **4** under a 0.1 T static *dc* field, with a 4.0 G *ac* field oscillating at various frequencies (10, 19, 35, 65, 122, 228, 426, 795 and 1488 Hz). (right) Out-of-phase (χ''_M) *vs. T ac* susceptibility signals for **4** under a 0.1 T static *dc* field, with a 4.0 G *ac* field oscillating at various frequencies.

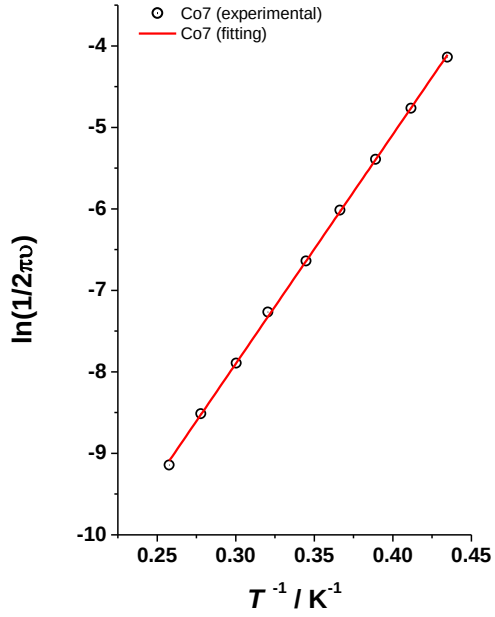

Figure 3.8. Arrhenius plot constructed from the peak maxima observed in Figure 3.7 (right). The red line is the fit of the data to the Arrhenius-type equation; see the text for the fit parameters.

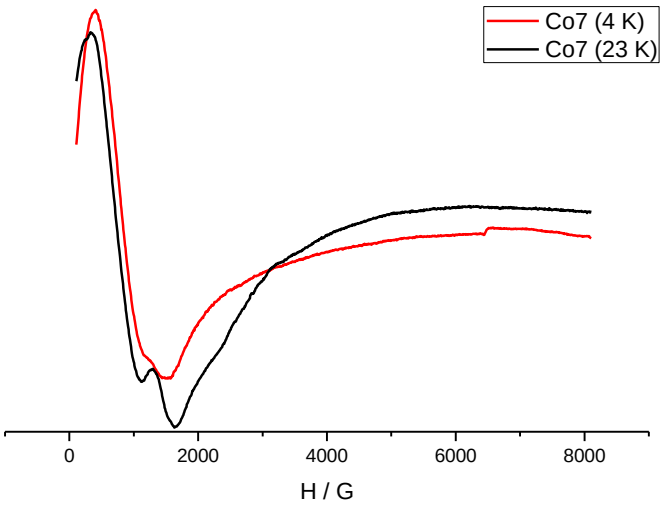

Figure 3.9. X-Band EPR spectra of a microcrystalline sample of **4** at 23 and 4 K. The practically similar EPR spectra at different low-temperatures support the lack of low-lying excited states close in energy with the ground state. The corresponding *g* values at 23 and 4 K are 8.85/4.64 and 7.80, respectively.

The $\chi_M T$ product of complex **5** steadily increases with decreasing *T* to reach a maximum value of 33.7 $cm^3mol^{-1}K$ at 20 K before dropping to a value of 21.0 $cm^3mol^{-1}K$ at 2 K (Figure 3.10). This is indicative of an overall ferromagnetically-coupled system with an $S = 7$ ground state spin value. The low-*T* decrease of $\chi_M T$ is attributed to ZFS within the ground state and/or weak antiferromagnetic (zJ') intermolecular interactions.

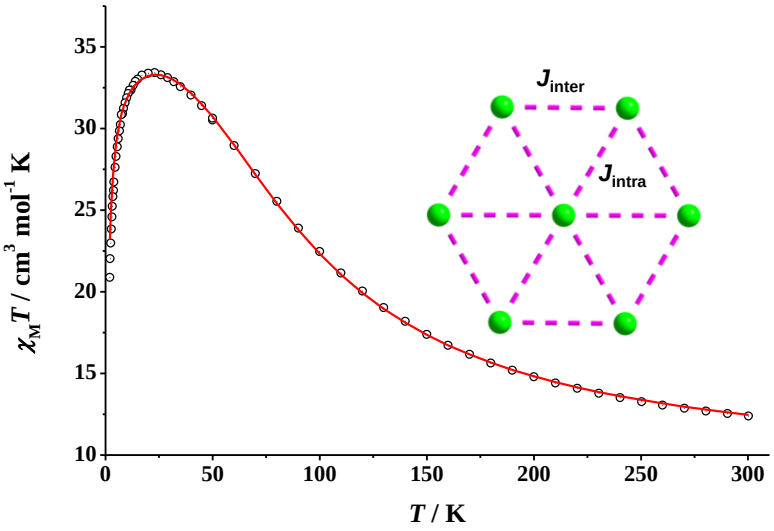

Figure 3.10. $\chi_M T$ *vs.* *T* plot for **5** in a 1 kG field. The red solid line is the fit of the data. (inset) 2-*J* coupling scheme for **5**.

The fitting (-*J* Hamiltonian) of the data using the program PHI over the entire *T* range (Figure 3.10) gave: J_{intra} = +33.4 cm^{-1}, J_{inter} = +20.0 cm^{-1}, zJ' = -0.02 cm^{-1} and g = 2.23, suggesting strong intramolecular ferromagnetic interactions. The two *J* parameters were close in value, consistent with the presence of double EO-N_3^- bridges between all Ni···Ni pairs. The Ni···Ni separations and Ni-(μ-N_3)-Ni angles span the range 3.182-3.225 Å and 96.0-102.0° ranges, respectively.

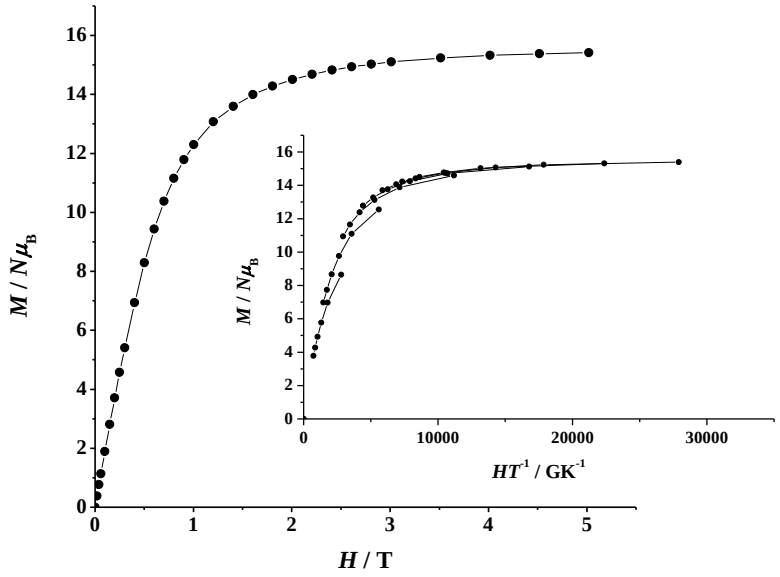

Figure 3.11. Plots of magnetization (*M*) *vs.* field (*H*) and reduced magnetization (inset) for complex **5** at different low temperatures and applied fields.

The magnetization of the system reaches a saturated value close to 15 $M/N\mu_B$ under an external field of 5 T, which is consistent with an $S = 7$ ground state (with $g \sim 2.15$) and a negligible magnetoanisotropy (Figure 3.11). As a result, complex **5** does not exhibit an out-of-phase *ac* signal down to 1.8 K, either in the absence or the presence of an external *dc* field. Although few heptanuclear alkoxido-bridged Ni^{II} complexes have been reported to date,[135] complex **5** is the first azido-bridged Ni^{II}_7 cluster with a disc-like topology. More importantly, **5** is the only entirely ferromagnetic Ni_7 system ever reported, with a very well isolated spin ground state (as also confirmed by EPR studies, see Figure 3.12) and an $S = 6$ first excited state lying ~60 cm^{-1} above the $S = 7$. This is clearly due to the exclusive presence of EO bridging azido groups which promote strong ferromagnetic

interactions without diminishing their "ferro-coupling potency", as is usually the case when azides co-exist in bridging with other organic chelates.

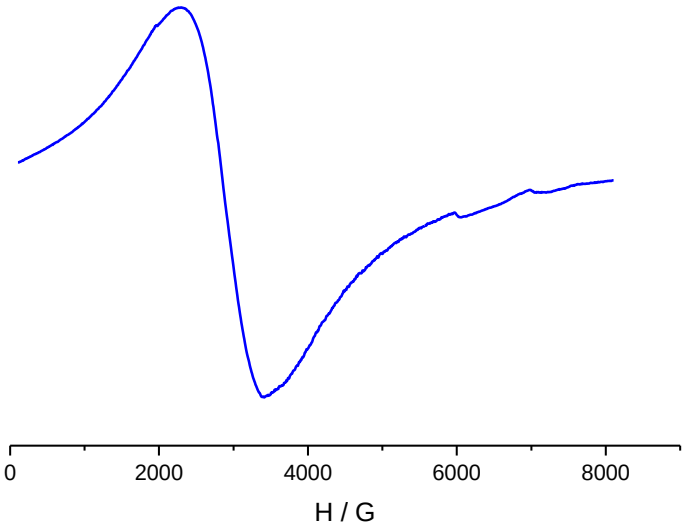

Figure 3.12. X-band EPR spectrum of a microcrystalline sample of **5** at 4 K. The spectrum clearly shows an isotropic absorption centered at g = 2.34 which is also quite broad (linewidth = 1100 G). The corresponding EPR spectra of **5** at 20 and 70 K show the same features.

Dc magnetic susceptibility studies on a polycrystalline sample of **6** were also performed (Figure 3.13, left) and the data at the high-T region (300-80 K) were consistent with ferromagnetic interactions between the $Fe^{II/III}$ centers through the EO-N_3^- bridges, as reflected in a continuous increase of the $\chi_M T$ product from a value of 9.0 $cm^3mol^{-1}K$ at 300 K to 21.5 $cm^3mol^{-1}K$ at 80 K. The data above 120 K follow the Curie-Weiss law with C = 7.25 $cm^3mol^{-1}K$ and θ = +61.0 K, confirming the strong ferromagnetic coupling between the Fe centers (Figure 3.13, right). Below 80 K, the $\chi_M T$ product steeply rises,

reaching a maximum value at T ~ 34 K; such behavior is attributed to a long-range ferromagnetic ordering of the spins.[136] Unfortunately, the magnetic data could not be fitted to a reasonable model due to the complex structure and multidimensionality of **6**.

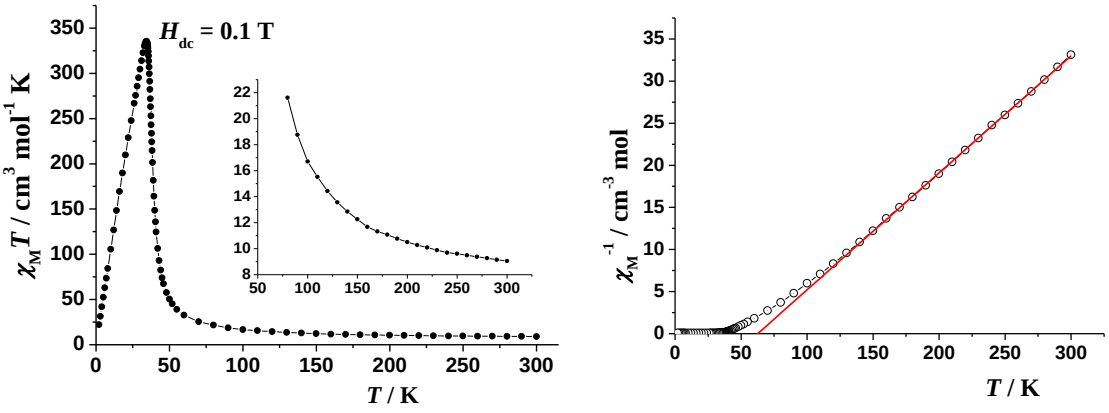

Figure 3.13. (left) $\chi_M T$ *vs.* T plot of **6** in a 1 kG field; the solid line is a guide for the eye. (right) χ_M^{-1} *vs.* T plot for **6**. The red thick line represents the fitting of the data to the Curie-Weiss law.

To characterize the interesting low-T behavior of **6**, field-cooled magnetization measurements were performed under different fields (0.1-0.3 T). The χ_M and $\chi_M T$ products are strongly field dependent showing an increase of their values as the field decreases, reaching a $\chi_M T$ value of 335.4 cm^{3}mol^{-1}K at 35 K (under a field of 0.1 T) and thus confirming the ordered phase (Figure 3.14).

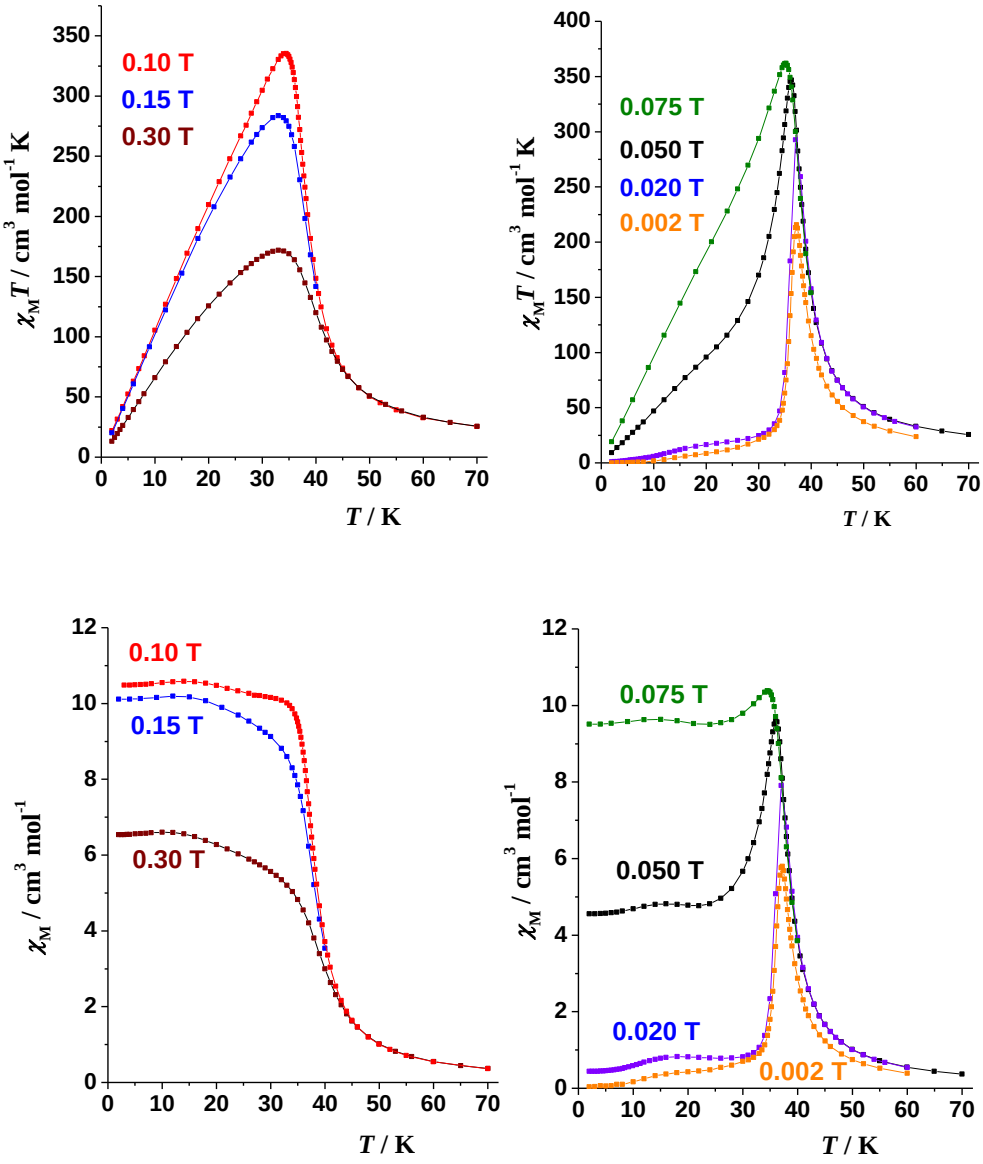

Figure 3.14. $\chi_M T$ (top) and χ_M (bottom) field-cooled susceptibilities for **6**. The different colored lines are guides for the eye.

As is shown in Figure 3.14, all curves join at $T \sim 45$ K. In the 50-300 K region all plots follow exactly the same trend which corresponds to the simple paramagnetic phase of the system. In order to assess the effect of any possible interlayer interactions on the

magnetic properties of **6**, weaker fields (0.002-0.075 T) were employed. The system retains the same ordering peak albeit the susceptibility seems to be vanished on cooling when the field is smaller than 0.002 T. Such behavior is indicative of interlayer interactions and the field to overcome such effects has been estimated to ~0.1 T. Toward that end, magnetization *vs.* field studies were also carried out, and it is clear that under a small field of 0.02 T the system practically does not get magnetized, indicating that the magnetization is not spontaneous (Figure 3.15). For intermediate fields, the system is partially magnetized and keeps the same magnetization value down to 2 K, suggesting that interlayer interactions are not effective.

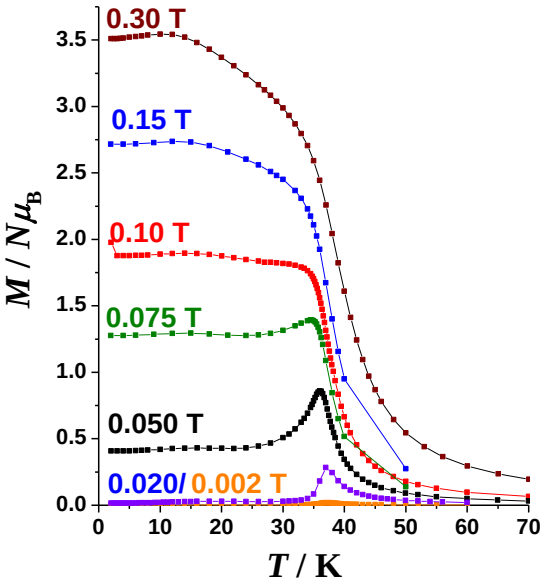

Figure 3.15. Field-cooled magnetization plots for the 2-D coordination polymer **6**.

The thermal dependence of the *ac* susceptibility of **6** was also recorded at various frequencies. Under an *ac* field of 4 G, the system does not show any out-of-phase signal, consistent with the lack of remnant magnetization. However, under static fields of 0.05 and 0.1 T, the χ_M'' component (Figure 3.16, top, right) exhibits nice peaks that correspond to an ordered system. Under larger fields (i.e., 0.3 T), the system remains blocked and the *ac* signals are diminished. It should be noted that the χ_M' (Figure 3.16, top, left) and χ_M'' peaks are slightly unsymmetrical in shape, with the low-*T* part showing some frequency dependence. This is indicative of some complicated dynamic relaxation process, tentatively attributed to the restricted movement of domain walls upon approaching T_c.[137] Finally, the ferromagnetically ordered 2-D system shows magnetization hysteresis loops, still observable at ~20 K, with a remnant magnetization corresponding to 3.3 electrons and a coercive field of ~0.25 T at 2 K (Figure 3.16, bottom).

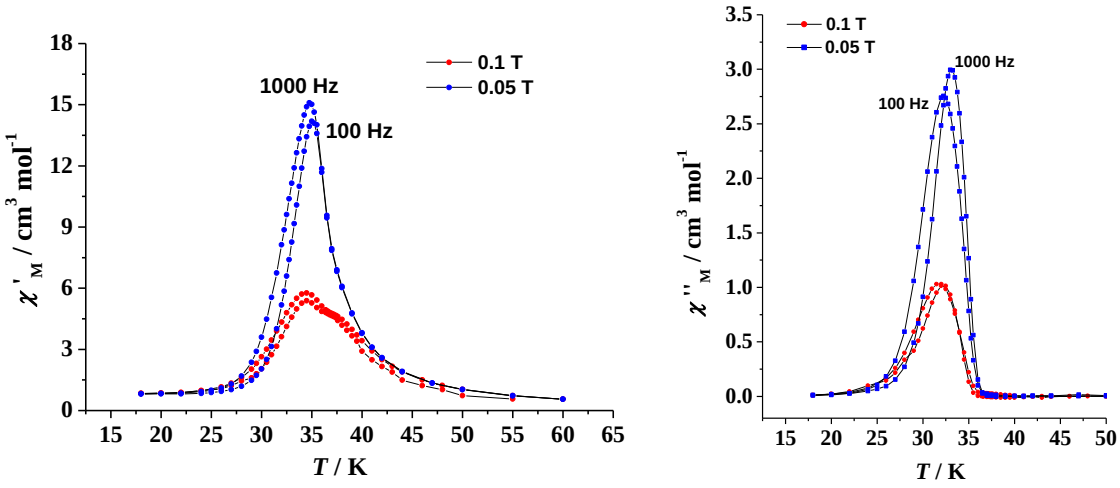

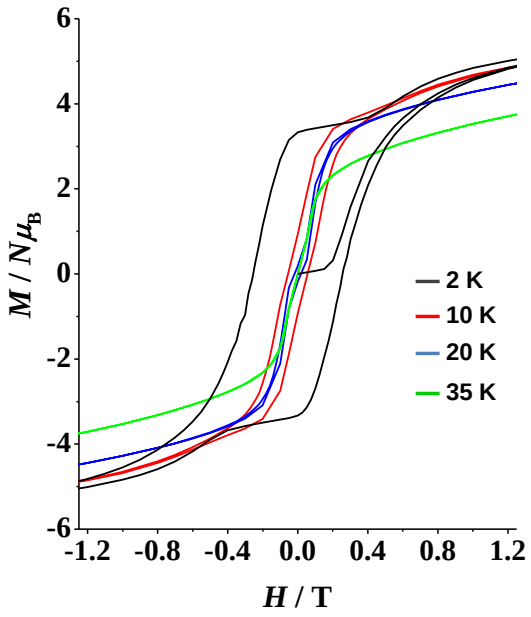

Figure 3.16. (top) Plot of the χ'_M (left) and the χ''_M (right) product of **6** under the indicated static *dc* fields and *ac* frequencies. No signals were detected without static field or larger fields (i.e., 0.3 T). (bottom) Isothermal magnetazation plots at different temperatures.

3.3. Conclusions and Perspectives

In conclusion, we have investigated a new, flexible synthetic route for the isolation of ferromagnetic polynuclear 3*d*-metal complexes and coordination polymers without requiring the simultaneous presence of any organic chelating/bridging ligand. The pioneer employment of Me_3SiN_3 precursor under the reported aerobic and basic conditions seems to be the key for unveiling a new class of exclusively end-on azido-bridged inorganic materials with beautiful structural motifs and fascinating magnetic properties. Complexes **4** and **5** are structurally similar and they possess a

centrosymmetric heptanuclear core consisting of an almost planar hexagon of alternating metals surrounding a central, seventh metal ion. The strong ferromagnetic behavior of both complexes is due to the presence of end-on bridging azido ligands. Magnetic studies revealed that complex **4** is a field-induced SMM with an energy barrier $\Delta E/k_B$ = 28.1 K, one of the highest yet reported for any polynuclear Co^{II} SMM. Complex **5** is the only entirely ferromagnetic Ni_7 system to date with a well-isolated S = 7 spin ground state. On the other hand, the employment of the reported synthetic stateregy to the more redox active Fe^{II} ions led to the isolation of the mixed-valence compound **6**, which is a 2-D coordination polymer instead of an isomorphous heptanuclear metal compound (similar to Co and Ni). The compound exhibits long- range ferromagnetic ordering properties due to the strong ferromagnetic coupling between the Fe centers. In addition to the interesting magnetic properties, the described compounds could potentially show a variety of other applications, e.g., in the fields of high-energy materials and catalysis. Such studies, together with the further development of this chemistry in other 3*d*-, 4*f*- and 3*d*/4*f*-metals, are in progress.

CHAPTER 4: Emissive Molecular Nanomagnets: Introducing Optical Properties in Triangular Oximato $\{Mn^{III}_3\}$ SMMs from the Deliberate Replacement of Simple Carboxylate Ligands with their Fluorescent Analogues

4.1. Experimental Section

4.1.1. Physical Measurements

Elemental Analysis: Elemental analyses (C, H, and N) were performed on a Perkin-Elmer 2400 Series II Analyzer.

FT-IR spectroscopy: Infrared (IR) spectra were recorded in the solid state on a Bruker's FT-IR spectrometer (ALPHA's Platinum ATR single reflection) in the 4000-450 cm^{-1} range. Notation for IR bands: vs, very strong; s, strong; m, medium; mb, medium broad; w, weak; b, broad.

UV-Visible spectra: UV-Visible (UV-Vis) spectra were recorded in MeCN solution at concentrations ~10^{-5} M on a Beckman Coulter DU Series 700 dual beam spectrophotometer.

Electrochemical studies: Electrochemical studies were performed under argon using a BASi EC-epsilon Autoanalyzer and a standard three-electrode assembly (glassy carbon

working, Pt wire auxiliary, and $Ag/AgNO_3$ reference) with 0.1 M $NBu^n_4PF_6$ as supporting electrolyte. Quoted potentials are versus the ferrocene/ferrocenium couple, used as an internal standard. The scan rates for cyclic voltammetry were 100 mV/s. Distilled solvents were employed and the concentrations of the complexes were approximately 1 mM.

Photoluminescence studies: Solid state photoluminescence spectra were recorded using a Cary Eclipse spectrophotometer. Photoluminescence was excited by a 150W xenon lamp.

Magnetic susceptibility measurements: Direct current (*dc*) magnetic susceptibility studies were performed at the University of Florida Chemistry Department on a Quantum Design MPMS-XL SQUID susceptometer equipped with a 7 T magnet and operating in the 5.0-300 K range. Samples were embedded in solid eicosane to prevent torquing. Pascal's constants were used to estimate the diamagnetic correction, which was subtracted from the experimental susceptibility to give the molar paramagnetic susceptibility (χ_M).[92]

4.1.2. Synthesis

General considerations: All experiments were performed under ambient conditions. All chemicals were purchased from Sigma Aldrich and Alfa Aesar. Chemicals and solvents were used as received without further purification. The triangular precursor

$[Mn_3O(O_2CMe)_3(mpko)_3](ClO_4)$ was prepared in yields as high as 95% following the reported procedure.[138]

$[Mn_3O(L1)_3(mpko)_3](ClO_4)$ (7): To a stirred, brown solution of $[Mn_3O(O_2CMe)_3(mpko)_3](ClO_4)$ (0.09 g, 0.1 mmol) in CH_2Cl_2 (20 mL) was added solid L1-H (0.10 g, 0.6 mmol). The mixture was stirred for 30 min, and the solvent was then removed *in vacuo*. Toluene (20 mL) was added to the dark brown residue, and the solution was again evaporated to dryness. The addition and removal of toluene was repeated two more times. The resulting dark brown solid was redissolved in THF/MeOH (20 mL, 10:1 v/v) and the solution was layered with Et_2O (40 mL). After 5 days, X-ray quality dark purple single-crystals of **7**·*x*MeOH·*y*CH_2Cl_2 were collected by filtration, washed with cold MeOH (2 x 2 mL), and dried under vacuum; the yield was 95%. Elemental analysis (%) calcd for **7**: C 54.08, H 3.53, N 7.01; found: C 54.37, H 3.62, N 6.76. Selected IR data (ATR): ν = 3421 (mb), 3060 (m), 2967 (m), 1596 (s), 1558 (s), 1471 (m), 1396 (m), 1373 (vs), 1355 (s), 1238 (w), 1189 (m), 1089 (vs), 940 (w), 784 (m), 700 (m), 611 (mb), 462(w).

$[Mn_3O(L2)_3(mpko)_3](ClO_4)$ (8): To a stirred, brown solution of $[Mn_3O(O_2CMe)_3(mpko)_3](ClO_4)$ (0.09 g, 0.1 mmol) in THF/CH_2Cl_2 (20 mL, 1:1 v/v) was added solid L2-H (0.13 g, 0.6 mmol). The mixture was stirred for 45 min, and the solvent was then removed *in vacuo*. Toluene (20 mL) was added to the dark brown residue, and the solution was again evaporated to dryness. The addition and removal of toluene was repeated two more times. The resulting dark brown solid was redissolved in THF/CH_2Cl_2 (20 mL, 20:1 v/v) and the solution was layered with Et_2O/MeOH (40 mL, 30:1 v/v). After 6 days, X-ray quality dark brown single-crystals of **8**·*x*MeOH·*y*CH_2Cl_2 were collected by

filtration, washed with cold MeOH (2 x 2 mL), and dried under vacuum. The yield was 83%. Elemental analysis (%) calcd for **8**: C 58.75, H 3.59, N 6.23; found: C 58.82, H 3.71, N 6.02. Selected IR data (ATR): ν = 3429 (mb), 3051 (m), 1601 (s), 1575 (vs), 1477 (m), 1443 (m), 1419 (m), 1379 (vs), 1315 (vs), 1274 (s), 1180 (m), 1161 (m), 1108 (vs), 1088 (s), 891 (m), 776 (m), 737 (s), 700 (m), 664 (m), 622 (mb), 563 (w), 495 (w), 439 (w).

$[Mn_3O(L3)_3(mpko)_3](ClO_4)$ (9): To a stirred, brown solution of $[Mn_3O(O_2CMe)_3(mpko)_3](ClO_4)$ (0.09 g, 0.1 mmol) in THF/CH_2Cl_2 (30 mL, 1:1 v/v) was added solid L3-H (0.15 g, 0.6 mmol). The mixture was stirred for 45 min, and the solvent was then removed *in vacuo*. Toluene (20 mL) was added to the dark brown residue, and the solution was again evaporated to dryness. The addition and removal of toluene was repeated two more times. The resulting dark brown solid was redissolved in THF/CH_2Cl_2 (20 mL, 20:1 v/v) and the solution was layered with Et_2O (40 mL). After 10 days, dark brown, very thin, needle-like crystals of **9**, which were bad X-ray diffractors, were collected by filtration, washed with THF (2 x 2 mL), and dried under vacuum. The yield was 92%. The identity of the product was confirmed by (i) a unit cell determination and comparison with the unit cell of compound **8**, (ii) IR spectral comparison with complexes **7** and **8**, and (iii) CHN elemental analysis. Elemental analysis (%) calcd for **9**: C 60.58, H 3.81, N 5.89; found: C 60.95, H 3.47, N 5.85. Selected IR data (ATR): ν = 3430 (mb), 3051 (m), 1601 (s), 1573 (vs), 1478 (m), 1442 (m), 1419 (m), 1379 (vs), 1315 (vs), 1273 (s), 1181 (m), 1107 (sb), 1086 (s), 892 (m), 776 (m), 738 (s), 700 (m), 664 (m), 622 (mb), 561 (w), 496 (w), 441 (w).

4.1.3. Single-crystal X-ray Crystallography

Crystals of the complexes **7** and **8** were selected and mounted on cryoloops using inert oil.[99] Diffraction data were collected at 150.0(2) K on a Bruker X8 Kappa APEX II Charge-Coupled Device (CCD) area detector diffractometer controlled by the APEX2 software package[100] (Mo Kα graphite-monochromated radiation, λ = 0.71073 Å), and equipped with an Oxford Cryosystems Series 700 cryostream monitored remotely with the software interface Cryopad. Images were processed with the software SAINT+,[102] and absorption effects corrected with the multiscan method implemented in SADABS.[103] The structures were solved by direct methods employed in SHELXS-97,[96,97] allowing the immediate location of the metals. The other non-hydrogen atoms of the complexes were located from difference Fourier maps calculated by successive full-matrix least-squares refinement cycles on F^2 using SHELXL-97,[96,97] and effectively refined with anisotropic displacement parameters.

All attempts to refine lattice solvate molecules were less than acceptable, leading to large and distorted ellipsoids, poor bond lengths, and significant residual electron density peaks nearby. Various models were examined with different amounts of modelled solvent, and squeeze applied to each one. The best result was achieved from 'Squeezing' all the solvents. This provided a final R-factor at least 1% lower than any other model tried and therefore this was chosen as the best model. As the solvents were not well-resolved crystallographically the exact nature of the solvent (and there may be several types based on the crystallization method employed) was uncertain. However, that did not affect any of our physical studies since all reported compounds, upon vacuum drying,

were analyzed as lattice solvent-free. Information concerning crystallographic data collection and structure refinement details is summarized in Table 4.1.

Table 4.1. Crystallographic data for complexes **7** and **8**

Parameter	**7**·*x*MeOH·*y*CH_2Cl_2	**8**·*x*MeOH·*y*CH_2Cl_2
Formula	$C_{54}H_{42}Mn_3N_6O_{14}Cl$	$C_{66}H_{39}Mn_3N_6O_{14}Cl$
Fw / g mol^{-1}	1199.20	1349.42
Crystal type	Purple block	Red plates
Crystal size / mm	0.42×0.18×0.10	0.17×0.33×0.38
Crystal system	Monoclinic	Trigonal
Space group	$P2_1/c$	$P\text{-}3c1$
a / Å	20.223(5)	18.4788(10)
b / Å	18.555(5)	18.4788(10)
c / Å	19.641(5)	28.5885(16)
α / º	90	90
β / º	118.303(1)	90
γ / º	90	120
V / $Å^3$	6489(3)	8454.1(10)
Z	4	2
T / K	150.0(2)	150.0(2)
ρ_{calc} / g cm^{-3}	1.227	1.092
μ / mm^{-1}	0.655	0.544

θ range / °	2.19 - 25.00	1.910 - 22.499
Index ranges	$-24 \le h \le 24$	$-19 \le h \le 19$
	$-17 \le k \le 22$	$-17 \le k \le 19$
	$-23 \le l \le 22$	$-30 \le l \le 30$
Collected reflections	60049	36399
Independent reflections	11384 (R_{int} = 0.0652)	3691 (R_{int} = 0.0481)
Final $R^{a,b}$ indices [$I>2\sigma(I)$]	$R1$ = 0.0738	$R1$ = 0.0926
	w$R2$ = 0.1675	w$R2$ = 0.2748
$(\Delta\rho)_{max,min}$ / e Å^{-3}	0.990, -0.489	0.117, -1.045

[a] $R1 = \Sigma(||F_o| - |F_c||)/\Sigma|F_o|$. [b] $wR2 = [\Sigma[w(F_o^2 - F_c^2)^2]/ \Sigma[w(F_o^2)^2]]^{1/2}$, $w = 1/[\sigma^2(F_o^2) + [(ap)^2 + bp]$, where $p = [\max(F_o^2, 0) + 2F_c^2]/3$.

4.2. Results and Discussion

4.2.1. Synthetic Comments

Our target was the synthesis of emissive SMMs, compounds that could exhibit both photoluminescence properties and SMM behaviors, based on anisotropic 3*d*-metal ions. The self-assembly synthesis of such emissive SMMs has been limited to the use of lanthanide ions in complexes with various organic bridging ligands.[139] The only previous example of a photoluminescence SMM based on 3*d*-metal ions was reported by Hendrickson and coworkers.[78] The authors have synthesized a $\{Mn^{II}_2Mn^{III}_2\}$ cluster from

the self-assembly reaction of the optically inactive *N*-methyldiethanolamine and anthracenecarboxylic acid.[78]

In the absence of any previous studies on the designed synthesis of emissive, transition metal-based SMMs we decided to begin a program aiming at the deliberate replacement of non-emissive organic ligands in known SMMs with their fluorescent analogues, without affecting the metal-core structure and SMM properties. Undoubtedly, that was a difficult task considering that the new fluorescence ligands could potentially alter the nuclearity of the compound, change the spin ground state of the system and/or 'switch-off' the SMM property. Furthermore, the resulting photoluminescence induced by the fluorescence ligands could be quenched by the highly paramagnetic nature of the targeted complexes,[140] thus leading to species with eventually no emitting behavior.

Taking all these possible obstacles into account, we undertook the challenge of performing carboxylate substitution reactions in the known, ferromagnetic triangular $[Mn^{III}_3O(O_2CMe)_3(mpko)_3](ClO_4)$ ($mpko^-$ is the anion of methyl 2-pyridyl ketone oxime) compound, which is a good SMM with an $S = 6$ ground state and large magnetoanisotropy.[138] Carboxylate substitution reactions have been previously used in the family of Mn_{12} SMMs as a means of obtaining isostructural compounds with different peripheral carboxylate ligation and improved SMM properties, such as higher energy barriers, blocking temperatures and different tunneling rates.[141] The carboxylic acids chosen for our research objectives were based on naphthalene, anthracene and pyrene, all organic substituents with simple fluorophores but with numerous applications in optics and sensoring.[81] Thus, the reaction of $[Mn^{III}_3O(O_2CMe)_3(mpko)_3](ClO_4)$ with an excess of 2-naphthoic acid (L1-H) in CH_2Cl_2 afforded a dark brown solution. The solvent was

removed *in vacuo*, toluene was added to the residue, and the solution was again evaporated to dryness. The addition and removal of toluene was repeated two more times. The remaining solid was redissolved in MeOH/THF and the resulting solution was layered with Et_2O to afford dark purple crystals of $[Mn^{III}_3O(L1)_3(mpko)_3](ClO_4)$ (**7**) in 95% yield. The formation of **7** is summarized in Equation 4.1.

$$[Mn^{III}_3O(O_2CMe)_3(mpko)_3]^+ + 3\ L1\text{-}H \rightarrow [Mn^{III}_3O(L1)_3(mpko)_3]^+ + 3\ MeCO_2H \qquad (4.1)$$

It is obvious that in order to shift the equilibrium to the right a stronger acid than $MeCO_2H$ should be employed. The reaction proceeded well for 2-naphthoic acid since it has a pK_a value of 4.17, smaller than that of the $MeCO_2H$ (pK_a = 4.76). The complete removal of $MeCO_2H$ as its toluene azeotrope is essential for driving the equilibrium to the right and it guarantees the purity and high yield synthesis of the new products.[142] Finally, the MeOH/THF and THF/CH_2Cl_2 reaction solvent mixtures were identified as the ones giving the highest products' yields and purities, as well as the best crystalline material for all new complexes **7**-**9**. Further, the low pK_a values of 9-anthracenecarboxylic acid (pK_a = 3.65) and 1-pyrenecarboxylic acid (pK_a = 4.00) allowed us to perform similar reactions and obtain the desired isostructural compounds $[Mn^{III}_3O(L2)_3(mpko)_3](ClO_4)$ (**8**) and $[Mn^{III}_3O(L3)_3(mpko)_3](ClO_4)$ (**9**) in 83 and 92% yields, respectively.

4.2.2. Description of Structures

The structures of the crystallographically-established cations of **7** and **8** (Figure 4.1, bottom) are very similar to that of the SMM precursor $[Mn^{III}_3O(O_2CMe)_3(mpko)_3](ClO_4)$ (Figure 4.1, top), and thus only the structure of representative complex **7** will be briefly described. The $[Mn_3O(L1)_3(mpko)_3]^+$ cation of **7** consists of three Mn^{III} atoms in a triangular arrangement bridged by a central μ_3-oxido atom O1. Each edge of the Mn_3 triangle is bridged by an $\eta^1:\eta^1:\mu$-$L1^-$ ion and an $\eta^1:\eta^1:\eta^1:\mu$-$mpko^-$ ligand, with the pyridyl and oximate N atoms chelating a Mn^{III} atom, forming a five-membered chelate ring. The Mn···Mn separations are almost equal (3.218-3.226 Å); the triangle is thus almost equilateral within the usual 3σ criterion.

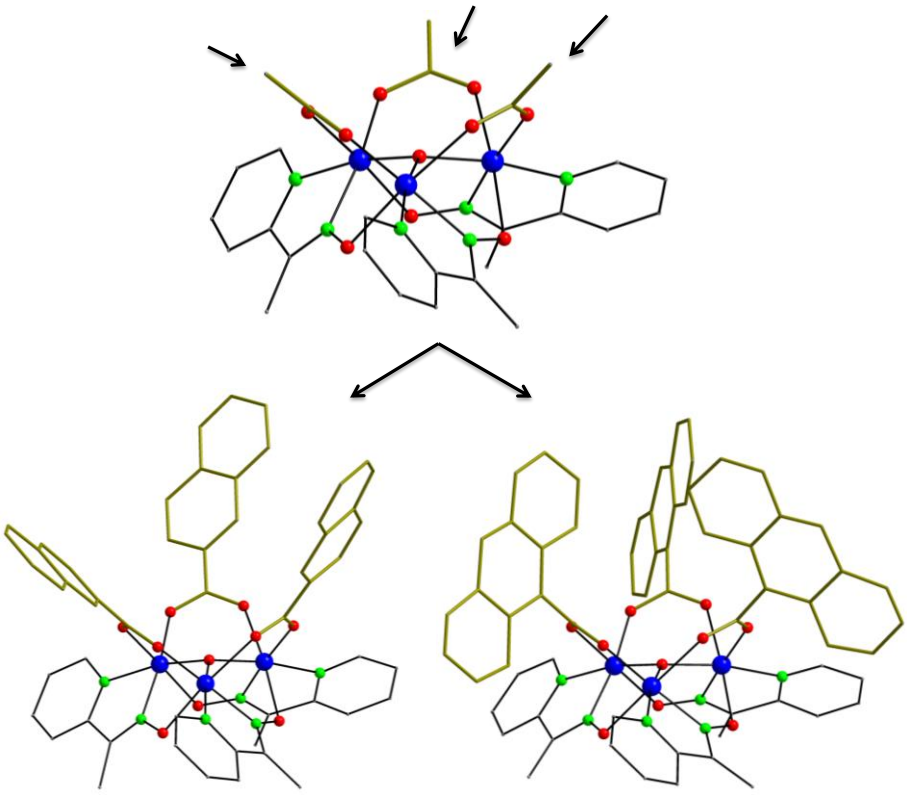

Figure 4.1. Molecular structures of $[Mn^{III}_3O(O_2CMe)_3(mpko)_3]^+$ (top), and the cations present in complexes **7** (bottom, left) and **8** (bottom, right), with the gold thick bonds emphasizing the different carboxylate moieties. Color scheme: Mn^{III}, blue; O, red; N, green; C, grey. H-atoms are omitted for clarity.

Table 4.2. Bond valence sum[a,b] calculations for Mn and selected O atoms in complexes **7** and **8**

		Complex **7**	
Atom	Mn^{II}	Mn^{III}	Mn^{IV}
Mn1	3.21	<u>3.00</u>	3.05
Mn2	3.12	<u>2.92</u>	2.96
Mn3	3.21	<u>3.00</u>	3.05
	BVS	assignment	
O1	1.88	O^{2-}	

		Complex **8**	
Atom	Mn^{II}	Mn^{III}	Mn^{IV}
Mn1	3.25	<u>3.04</u>	3.08
	BVS	assignment	
O4	1.94	O^{2-}	

[a] The underlined value is the one closest to the charge for which it was calculated. The oxidation state is the nearest whole number to the underlined value. [b] An O BVS in the ~1.8-2.0, ~1.0-1.2, and ~0.2-0.4 ranges is indicative of non-, single- and double-protonation, respectively, but can be altered somewhat by hydrogen bonding.

The oxidation states of all Mn atoms were established as +3 by charge-balance considerations and bond valence sum (BVS) calculations (Table 4.2). The three $L1^-$ groups lie on one side of the Mn_3 plane, and the three oximate groups on the other. The Mn atoms are near-octahedral, and the Mn^{III} centers exhibit a Jahn-Teller (JT) distortion, as expected for a high-spin d^4 ion in an octahedral geometry. The JT axes in both **7** and **8** involve the carboxylate and oximate O atoms, and are pointed outwards from the Mn_3 'hard'-plane, thus contributing to the appearance of significant molecular magnetic anisotropy of the easy-axis.[138] The central oxido atoms in **7** and **8** are 0.316 and 0.282 Å above the Mn_3 plane, respectively, on the same side as the carboxylate groups. These values are within the same range reported for $[Mn^{III}_3O(O_2CMe)_3(mpko)_3](ClO_4)$, and other similar triangles.[138] The average Mn-N-O-Mn torsion angles in **7** and **8** are 12.7 and 12.0°, respectively, slightly larger than that of 11.2° for the original triangle with acetates. Finally, as was expected from the presence of many aromatic rings in the carboxylate moieties of **7** and **8**, there are significant intermolecular π-π stacking interactions which serve to link neighboring Mn_3 clusters in the crystal (Figure 4.2).

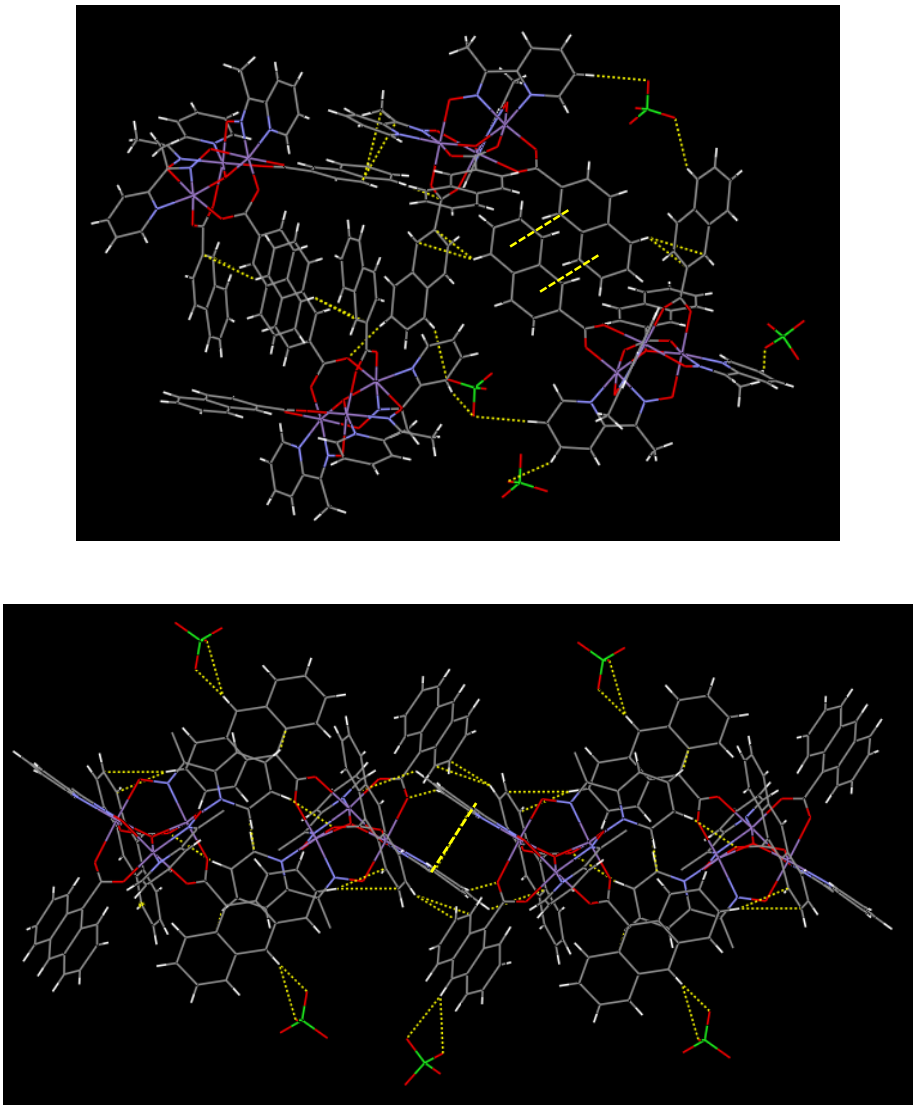

Figure 4.2. A small portion of the supramolecular architectures of complexes **7** (top) and **8** (bottom), emphasizing with yellow dashed lines the intermolecular interactions which serve to link neighboring Mn_3 clusters in the crystal.

4.2.3. Electronic Spectra

UV/Vis studies were performed in order to probe the structural integrity of complexes **7-9** in solution and elucidate any potential for further photophysical studies. The electronic absorption spectra of isostructural complexes **7**, **8**, and **9** were recorded in MeCN solutions of concentrations ~10^{-5} M (Figure 4.3).

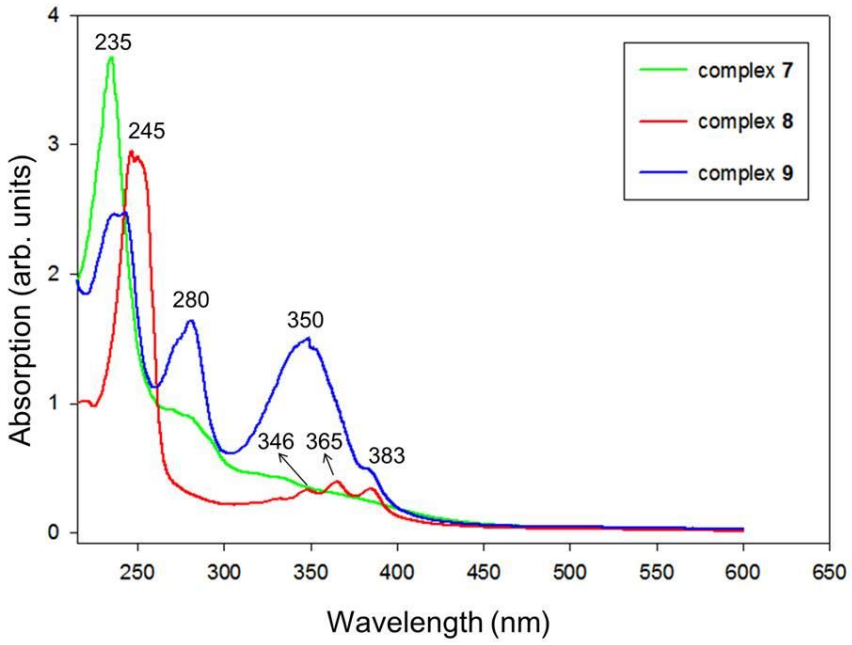

Figure 4.3. Absorption spectra of complexes **7**, **8**, and **9** in MeCN (~10^{-5} M).

All three compounds show the characteristic bands (shoulders and/or sharp peaks) of naphthalene-, anthracene-, and pyrene-functional groups slightly shifted to higher wavenumbers, consistent with coordination of the fluorescence carboxylate ligands to the metal centers.[143] The high intensity absorption bands in the 235-350 nm region are assigned to π-π* transitions within the aromatic organic ligands while the less intense

bands at ~380 nm are possibly due to LMCT effects.[144] Note that the absorption bands of neutral mpkoH ligand (218, 241, and 269 nm) appear to overlap with the bands of polyaromatic carboxylate ligands upon coordination with the metal centers. Hence, the conclusions from the UV/Vis studies were very promising in compounds **7**-**9** retaining their solid-state {Mn_3} structures in solution.

4.2.4. Electrochemistry

The redox activity of electrochemically prominent metal complexes can be assessed by cyclic voltammetry. This technique is of significant importance in the field of molecular magnetism. For example, in molecular magnetism arena, electrochemical studies on various $[Mn^{III}_8Mn^{IV}_4O_{12}(O_2CR)_{16}(H_2O)_4]$ compounds have revealed a rich redox chemistry involving several quasi-reversible oxidation and reduction processes.[145] Four different oxidation levels of this family of clusters have been isolated and the corresponding 1-, 2-, 3-, and 4-electron reduced species were characterized in the solid-state and demonstrated their distinct single-molecule magnetism properties compared to the parent [Mn_{12}] complex.[35]

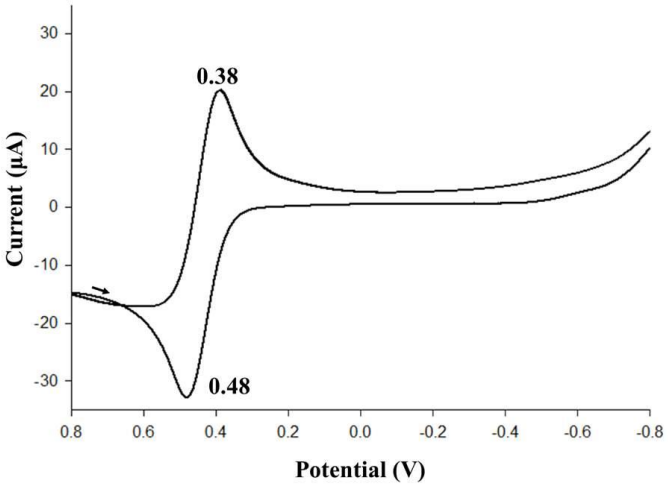
0.38
0.48
Current (µA)
Potential (V)

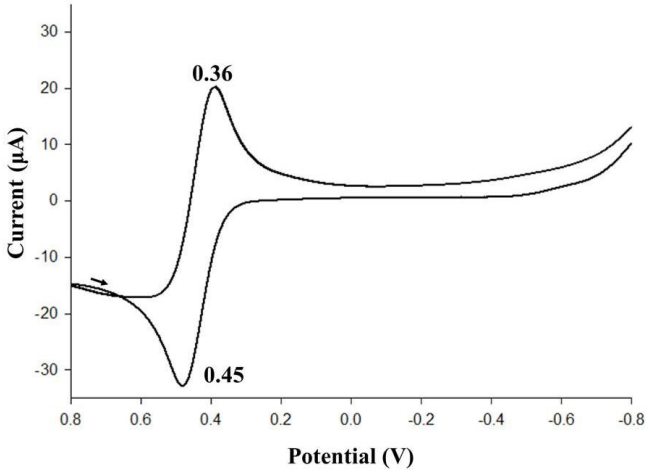
0.36
0.45
Current (µA)
Potential (V)

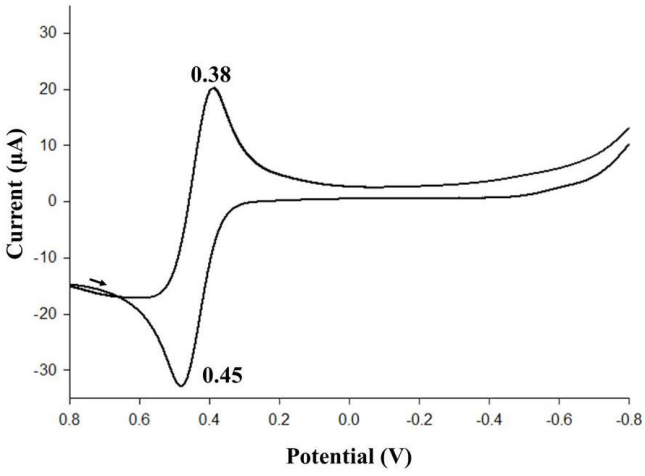
0.38
0.45
Current (µA)
Potential (V)

Figure 4.4. Cyclic voltammograms at 100 mV s^{-1} for complexes **7** (top), **8** (middle), and **9** (bottom) in MeCN containing 0.1 M $NBu^n_4PF_6$ as supporting electrolyte. The indicated potentials are *vs* Fc/Fc^+.

To that end, the electrochemical properties of complexes **7**, **8**, and **9** were studied in MeCN and all showed that they exhibit very similar redox processes. The cyclic voltammogram (CV) of complex **7** is shown in Figure 4.4 (top). It displays a well-defined reversible oxidation at ~0.43 V. The CV spectra of the anthracene-analogue, **8** (Figure 4.4, middle), and the pyrene-substituted, **9** (Figure 4.4, bottom), show very similar patterns of well-defined reversible oxidations at ~0.41 and ~0.42 V, respectively. For the reversible oxidation couple of all three studied compounds, the forward and reverse waves are well formed with a peak separation of 100 (**7**), 90 (**8**), and 70 (**9**) mV comparable to that of ferrocene under the same conditions; this is indicative of an one-electron process.[146] In summary, all complexes exhibited a similar oxidation and the electrochemical results may be illustrated as: $[Mn_3]^+ \leftrightarrow [Mn_3]^{2+}$. Synthetic efforts to isolate and structurally characterize the dicationic form of the $[Mn_3]^+$ precursor are future objectives.

4.2.5. Solid-state Magnetic Susceptibility Studies

With respect to the magnetostructural correlations in the family of $[Mn^{III}_3O(O_2CR)_3(mpko)_3]^+$ (R = various) triangles, it is now established that both the

displacement of the central μ_3-O^{2-} out of the Mn_3 plane and the 'twisting' of the Mn-N-O-Mn units (as reflected in the corresponding torsion angles) contribute to the weakening of the antiferromagnetic contribution and thus the observation of an overall ferromagnetic behavior.[138] This also turned out to be the case for the three new triangles **7**-**9**. For the sake of brevity, the magnetic properties of representative complexes **7** and **8** will be discussed in detail.

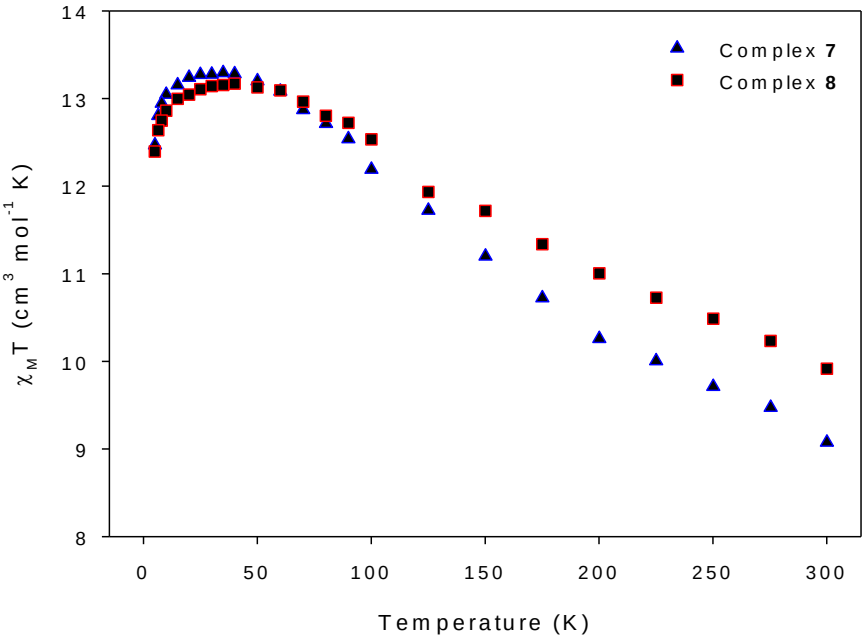

Figure 4.5. $\chi_M T$ *vs.* T plots of **7** and **8** in a 1 kG field.

Variable-temperature *dc* magnetic susceptibility measurements were performed on dried samples of **7** and **8** in the temperature range 5.0-300 K in an applied field of 1 kG (0.1 T). The data are shown as $\chi_M T$ *vs.* T plots in Figure 4.5. The $\chi_M T$ product for **7** increases from 9.08 $cm^3mol^{-1}K$ at 300 K to a maximum of 13.29 $cm^3mol^{-1}K$ at 35.0 K and then decreases to 12.47 $cm^3mol^{-1}K$ at 5.0 K. Complex **8** exhibits similar behavior,

with $\chi_M T$ increasing from 9.91 $cm^3mol^{-1}K$ at 300 K to a maximum of 13.17 $cm^3mol^{-1}K$ at 40.0 K, and then decreases to 12.39 $cm^3mol^{-1}K$ at 5.0 K. The 300 K values for **7** and **8** are slightly larger than the spin-only (g = 2) value of 9 $cm^3mol^{-1}K$ for three non-interacting Mn^{III} ions. The shape of the curves indicates dominant ferromagnetic exchange interactions between the 3 Mn^{III} atoms and a subsequent S = 6 spin ground state. However, the $\chi_M T$ maxima of the two complexes, which are located at high temperatures, are much below the spin-only value expected for a compound with a well-isolated S = 6 ground state (21.00 $cm^3mol^{-1}K$, g = 2). This, combined with the observed decrease of the $\chi_M T$ values at high temperatures (>35 K), is likely attributed to the strong intermolecular antiferromagnetic exchange interactions between the complexes (see Figure 4.2) and the thermal population of excited states with S < 6. Attempts were made to fit the data to the theoretical expression for a 3 Mn^{III} isosceles triangle, but this approach was unfeasible due to the combined presence of strong intermolecular interactions, low-lying excited states (a direct result of the weak magnetic coupling), and crystal structure disorders.[147] The latter are also the reason for the unsuccessful fitting of the magnetization *vs.* field data at low temperature, assuming that the ground state is solely populated.

Ac magnetic susceptibility studies were also performed on **7** and **8**, in a 3.5 G *ac* field oscillating at various frequencies and T < 15 K. Below 3 K, the appearance of a frequency-dependent decrease in the in-phase signal (Figure 4.6, top) and a concomitant increase in the out-of-phase (χ''_M) signal (Figure 4.6, bottom) were suggestive of the superparamagnet-like slow relaxation of a SMM. The χ''_M peak maxima for both compounds clearly lie at T < 1.8 K, the operating limit of the SQUID magnetometer, and are located at the same T range and have the same strength with the original

$[Mn^{III}_3O(O_2CR)_3(mpko)_3]^+$ precursor.[138] Thus, this new family of Mn_3 triangles with oximato and polyaromatic carboxylate groups were proved to retain the SMM behavior and the overall ferromagnetic response.

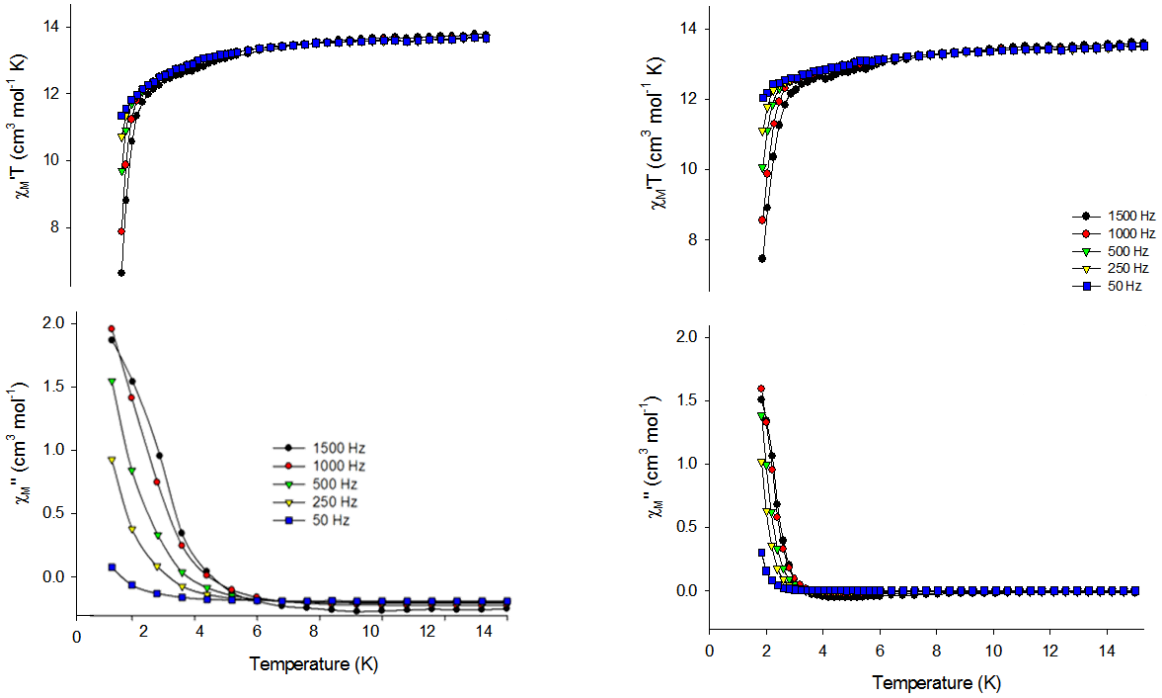

Figure 4.6. Plots of the in-phase (χ'_M) (as $\chi'_M T$) and out-of-phase (χ''_M) *ac* susceptibility signals of complexes **7** (left) and **8** (right) in a 3.5 G field oscillating at the indicated frequencies.

4.2.6. Photoluminescence Studies

The photoluminescence properties of $[Mn^{III}_3O(O_2CMe)_3(mpko)_3](ClO_4)$ precursor and complexes **7-9** were studied in the solid-state and at room temperature. Solid-state

techniques were selected for consistency purposes with the SMM studies. The free mpkoH ligand shows emission at 450 nm upon maximum excitation at 360 nm (Figure 4.7). However, the $[Mn^{III}_3O(O_2CMe)_3(mpko)_3](ClO_4)$ SMM shows no emission in the entire visible region. This is most likely due to a significant quenching of the emission intensity due to paramagnetic effects from the metal centers.

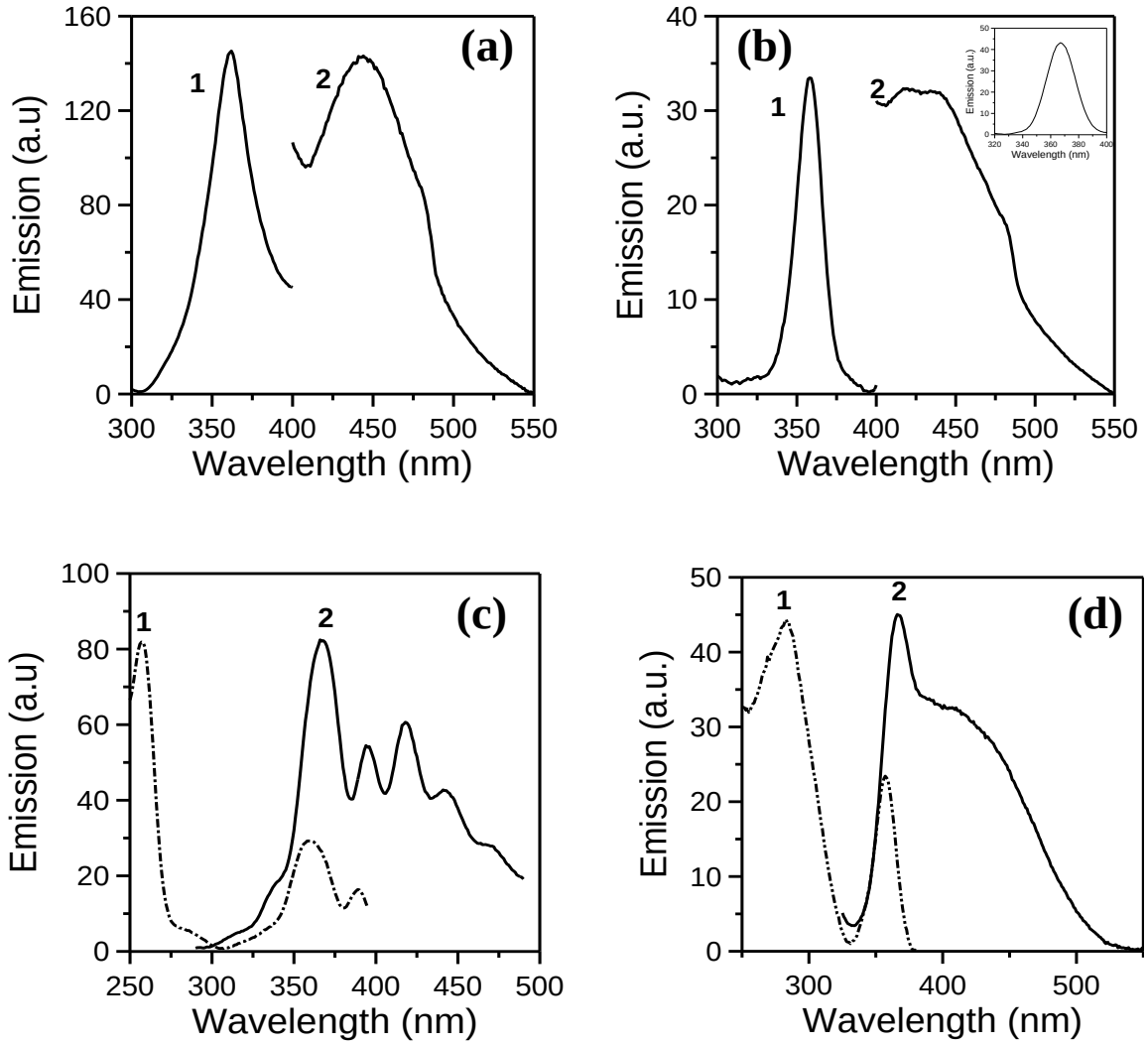

Figure 4.7. Excitation (1) and emission (2) spectra of solid: (a) mpkoH ligand, and complexes (b) **7**, (c) **8**, and (d) **9** at room temperature. Inset: The additional emission peak at 367 nm upon excitation at 270 nm for complex **7**.

In contrast, complexes **7**-**9** exhibit photoluminescence emission at room temperature (Figure 4.7). In the case of complex **7**, two different characteristic areas of emission are detected. The first band appears upon maximum excitation at 360 nm, and is obviously due to the mpkoH ligand, while the second -with a maximum at 367 nm (upon UV excitation)- is located in the same area where the naphthalene ligand emits.[148] Complexes **8** and **9** show blue emissions upon excitation at the UV-region, exhibiting the characteristic peaks of anthracene- and pyrene-units, respectively.[148] Interestingly, for complex **9** we observe both the monomer (peak at 370 nm) and the excimer (peak at 430 nm) emission of pyrene.[148]

4.3. Conclusions and Perspectives

In conclusion, we have shown that it is indeed feasible to synthesize 'hybrid' molecular materials, and particularly emissive SMMs, through the deliberate replacement of non-emissive carboxylate groups with various fluorescence analogues without perturbing the structural core and the SMM property. The combined results demonstrate the beauty of molecular chemistry and the ability to manipulate physical properties in a targeted way, thus contributing to the development of advanced materials with implications in the field

of molecular electronics. Future work in this project may include: (i) the extension of this targeted synthetic route to many other emissive SMMs based on 3*d*-metals, including the famous Mn_{12} and Mn_6 SMMs, (ii) the performance of low-temperature photomagnetic studies in order to 'communicate' the photoluminescence with the SMM property, (iii) the acquisition of single-crystal magnetic hysteresis studies in the presence of light, and (iv) the deposition of the reported compounds on a variety of conducting surfaces and the subsequent evaluation of their dual properties.

CHAPTER 5: Towards the Synthesis of Emissive SMMs from the Use of Naphthalene- and Pyridine-Based Diols in Ln^{III} Cluster Chemistry: $\{Ln_8\}$ and $\{Ln_4\}$ Complexes with Unprecedented "Christmas Star" and Zigzag Topologies

5.1. Experimental Section

5.1.1. Physical Measurements

Elemental Analysis: Elemental analyses (C, H, and N) were performed on a Perkin-Elmer 2400 Series II Analyzer.

FT-IR spectroscopy: Infrared (IR) spectra were recorded in the solid state on a Bruker's FT-IR spectrometer (ALPHA's Platinum ATR single reflection) in the 4000-450 cm^{-1} range. Notation for IR bands: vs, very strong; s, strong; m, medium; mb, medium broad; w, weak; b, broad.

UV-Visible spectra: UV-Visible (UV-Vis) spectra were recorded in MeCN solution at concentrations ~10^{-5} M on a Beckman Coulter DU Series 700 dual beam spectrophotometer.

Photoluminescence studies: Solid-state photoluminescence spectra were recorded using a Cary Eclipse spectrophotometer. Photoluminescence was excited by a 150W xenon lamp.

Magnetic susceptibility measurements: Variable-temperature direct current (*dc*) and alternating current (*ac*) magnetic susceptibility data were collected at the Chemistry Department of the University of Florida using a Quantum Design MPMS-XL SQUID susceptometer equipped with a 7 T magnet and operating in the 1.8-300 K range. Samples were embedded in solid eicosane to prevent torquing.

5.1.2. Synthesis

General considerations: All experiments were performed under ambient conditions. All chemicals were purchased from Sigma Aldrich and Alfa Aesar. Chemicals and solvents were used as received without further purification.

$(Et_4N)_4[Eu_8O(nd)_8(NO_3)_{10}(H_2O)_2]$ (10): To a stirred, colorless solution of ndH_2 (0.05 g, 0.3 mmol) and Et_4NOH (40% w/w, 0.22 mL, 0.6 mmol) in MeCN (20 mL) was added solid $Eu(NO_3)_3{\cdot}6H_2O$ (0.25 g, 0.6 mmol). The resulting pale yellow solution was kept under stirring at room temperature for about 10 min, filtered, and the filtrate was diffused with Et_2O (40 mL). Slow mixing gave after 4 days yellowish prismatic crystals of **10**, which were not of sufficient quality to allow for the acquisition of a complete X-ray diffraction data set. The crystals were collected by filtration, washed with cold MeCN (2 x 2 mL) and Et_2O (2 x 2 mL), and dried under vacuum. The yield was 45%. The identity

of the product was confirmed by (i) unit cell determination and comparison with the unit cell of compound **12**·2MeCN, (ii) IR spectroscopic comparison with all isostructural Ln_8 complexes, and (iii) elemental analysis. The vacuum-dried solid was analyzed as solvent-free **10**: C 36.61, H 3.62, N 5.34 %. Found: C 36.48, H 3.56, N 5.18 %. Selected IR data (ATR): ν = 3460 (mb), 3150 (m), 3045 (m), 1621 (m), 1592 (m), 1564 (m), 1506 (vs), 1460 (vs), 1383 (vs), 1276 (s), 1232 (m), 1163 (s), 1104 (m), 1018 (m), 941 (w), 867 (s), 809 (m), 754 (s), 719 (m), 623 (m), 545 (w), 480 (m).

$(Et_4N)_4[Gd_8O(nd)_8(NO_3)_{10}(H_2O)_2]$ (11): This complex was prepared in the same manner as complex **10** but using $Gd(NO_3)_3·6H_2O$ (0.27 g, 0.6 mmol) as the Ln salt. Due to the small size of the yellowish crystals formed after 3 days, and consequently the weak overall diffraction, we were not able to collect a complete X-ray data set. The crystals were collected by filtration, washed with MeCN (2 x 2 mL) and Et_2O (2 x 2 mL), and dried under vacuum. The yield was 55%. The identity of the product was confirmed by (i) unit cell determination and comparison with the unit cell of compound **12**·2MeCN, (ii) IR spectroscopic comparison with all isostructural Ln_8 complexes, and (iii) elemental analysis. The vacuum-dried solid was analyzed as solvent-free **11**: C, 36.20; H, 3.58; N, 5.28 %. Found: C, 36.28; H, 3.43; N, 5.03 %. Selected IR data (ATR): ν = 3462 (mb), 3152 (m), 3048 (m), 1622 (m), 1596 (m), 1562 (m), 1502 (vs), 1464 (vs), 1385 (vs), 1272 (s), 1235 (m), 1164 (s), 1106 (m), 1020 (m), 942 (w), 862 (s), 814 (m), 750 (s), 720 (m), 621 (m), 540 (w), 482 (m).

$(Et_4N)_4[Tb_8O(nd)_8(NO_3)_{10}(H_2O)_2]$ (12): This complex was prepared in the same manner as complex **10** but using $Tb(NO_3)_3·6H_2O$ (0.27 g, 0.6 mmol) as the Ln salt. After 4 days, X-ray quality yellowish prismatic crystals of **12** had appeared and were collected

by filtration, washed with cold MeCN (2 x 2 mL) and Et_2O (2 x 2 mL), and dried under vacuum. The yield was 55%. The vacuum-dried solid was analyzed as solvent-free **12**: C 36.07, H 3.57, N 5.26 %. Found: C 36.39, H 3.76, N 5.07 %. Selected IR data (ATR): *v* =3465 (mb), 3156 (m), 3050 (m), 1621 (m), 1594 (m), 1569 (m), 1500 (vs), 1467 (vs), 1384 (vs), 1270 (s), 1238 (m), 1166 (s), 1110 (m), 1022 (m), 944 (w), 865 (s), 811 (m), 752 (s), 723 (m), 619 (m), 539 (w), 484 (m).

$(Et_4N)_4[Dy_8O(nd)_8(NO_3)_{10}(H_2O)_2]$ (13): This complex was prepared in the same manner as complex **10** but using $Dy(NO_3)_3{\cdot}6H_2O$ (0.27 g, 0.6 mmol) as the Ln salt. Due to the small size of the yellowish crystals formed after 4 days, and consequently the weak overall diffraction, we were not able to collect a complete X-ray data set. The crystals were collected by filtration, washed with MeCN (2 x 2 mL) and Et_2O (2 x 2 mL), and dried under vacuum. The yield was 60%. The identity of the product was confirmed by (i) unit cell determination and comparison with the unit cell of compound **12**·2MeCN, (ii) IR spectroscopic comparison with all isostructural Ln_8 complexes, and (iii) elemental analysis. The vacuum-dried solid was analyzed as solvent-free **13**: C, 35.79; H, 3.54; N, 5.22 %. Found: C, 35.68; H, 3.38; N, 5.34 %. Selected IR data (ATR): *v* = 3460 (mb), 3154 (m), 3042 (m), 1620 (m), 1592 (m), 1567 (m), 1500 (vs), 1460 (vs), 1387 (vs), 1274 (s), 1237 (m), 1162 (s), 1100 (m), 1022 (m), 946 (w), 866 (s), 810 (m), 752 (s), 718 (m), 624 (m), 536 (w), 480 (m).

$[Eu_4(NO_3)_2(pdmH)_6(pdmH_2)_2](NO_3)_4$ (14): To a stirred, colorless solution of $pdmH_2$ (0.14 g, 1.0 mmol) and NEt_3 (0.14 mL, 1.0 mmol) in MeOH (20 mL) was added solid $Eu(NO_3)_3{\cdot}5H_2O$ (0.21 g, 0.5 mmol). The resulting pale yellow solution was kept under stirring at room temperature for about 20 min, filtered, and the filtrate was layered with

Et_2O (40 mL). Slow mixing gave after 2 days colorless prismatic crystals of **14**, which were not of sufficient quality to allow for the acquisition of a complete X-ray diffraction data set. The crystals were collected by filtration, washed with cold MeOH (2 x 2 mL) and Et_2O (2 x 3 mL), and dried in air. The yield was 60%. The identity of the product was confirmed by (i) unit cell determination and comparison with the unit cell of compound **16**·2MeOH, (ii) IR spectroscopic comparison with all isostructural Ln_4 complexes, and (iii) elemental analysis. The air-dried solid was analyzed as solvent-free **14**: C, 32.23; H, 3.19; N, 9.40 %. Found: C, 32.04; H, 3.05; N, 9.56 %. Selected IR data (ATR): ν = 3445 (wb), 3050 (m), 2925 (w), 1579 (s), 1519 (vs), 1480 (m), 1420 (m), 1384 (s), 1317 (s), 1276 (w), 1226 (w), 1072 (w), 1010 (m), 880 (w), 850 (w), 730 (m), 670 (m), 625 (m), 500 (w), 450 (w).

$[Gd_4(NO_3)_2(pdmH)_6(pdmH_2)_2](NO_3)_4$ (15): This complex was prepared in the same manner as complex **14** but using $Gd(NO_3)_3·6H_2O$ (0.23 g, 0.5 mmol) as the Ln salt. Due to the small size of the colorless crystals formed after 3 days, and consequently the weak overall diffraction, we were not able to collect a complete X-ray data set. The crystals were collected by filtration, washed with cold MeOH (2 x 2 mL) and Et_2O (2 x 3 mL), and dried in air. The yield was 50%. The identity of the product was confirmed by using the same techniques as for complex **14**. The air-dried solid was analyzed as **15**·2MeOH: C, 32.07; H, 3.43; N, 9.03 %. Found: C, 32.16; H, 3.53; N, 8.75 %. Selected IR data (ATR): ν = 3446 (wb), 3050 (m), 2925 (w), 1577 (s), 1519 (vs), 1483 (m), 1423 (m), 1384 (s), 1317 (s), 1274 (w), 1226 (w), 1200 (w), 1072 (w), 1016 (w), 887 (w), 851 (w), 730 (m), 669 (m), 624 (m), 501 (w), 449 (w).

$[Tb_4(NO_3)_2(pdmH)_6(pdmH_2)_2](NO_3)_4$ (16): This complex was prepared in the same manner as complex **14** but using $Tb(NO_3)_3{\cdot}6H_2O$ (0.23 g, 0.5 mmol) as the Ln salt. After 3 days, X-ray quality colorless crystals of **6**·2MeOH had appeared and were collected by filtration, washed with cold MeOH (2 x 2 mL) and Et_2O (2 x 3 mL), and dried in air. The yield was 60%. The air-dried solid was analyzed as **16**·2MeOH: C, 31.97; H, 3.42; N, 9.00 %. Found: C, 32.26; H, 3.52; N, 8.79 %. Selected IR data (ATR): *v* = 3450 (wb), 3050 (m), 2923 (w), 1579 (s), 1519 (vs), 1479 (m), 1423 (m), 1388 (s), 1340 (w), 1321 (s), 1276 (m), 1224 (w), 1200 (w), 1074 (w), 1014 (w), 943 (w), 887 (w), 846 (w), 730 (m), 674 (m), 622 (m), 574 (w), 501 (w), 451 (w).

$[Dy_4(NO_3)_2(pdmH)_6(pdmH_2)_2](NO_3)_4$ (17): This complex was prepared in the same manner as complex **14** but using $Dy(NO_3)_3{\cdot}6H_2O$ (0.23 g, 0.5 mmol) as the Ln salt. Colorless prismatic crystals of **17** had appeared after 4 days, and were collected by filtration, washed with cold MeOH (2 x 2 mL) and Et_2O (2 x 3 mL), and dried in air. The yield was 70%. Due to the small size and phase homogeneity issues (i.e., twinning) of the crystals, we were not able to collect an accurate, complete X-ray data set. However, the identity of the product was confirmed by (i) unit cell determination and comparison with the unit cell of compound **18**·2MeOH, (ii) IR spectroscopic comparison with all isostructural Ln_4 complexes, and (iii) elemental analysis. The air-dried solid was analyzed as solvent-free **17**: C, 31.59; H, 3.12; N, 9.21 %. Found: C, 31.73; H, 3.15; N, 9.01 %. Selected IR data (ATR): *v* = 3450 (wb), 3050 (m), 2925 (w), 1579 (s), 1519 (vs), 1481 (m), 1423 (m), 1386 (s), 1319 (s), 1276 (m), 1224 (w), 1074 (w), 1014 (m), 887 (w), 846 (w), 763 (w), 730 (m), 673 (m), 622 (m), 574 (w), 499 (w), 449 (w).

$[Ho_4(NO_3)_2(pdmH)_6(pdmH_2)_2](NO_3)_4$ (18): This complex was prepared in the same manner as complex **14** but using $Ho(NO_3)_3{\cdot}5H_2O$ (0.22 g, 0.5 mmol) as the Ln salt. After 2 days, X-ray quality colorless crystals of **18**·2MeOH had appeared and were collected by filtration, washed with cold MeOH (2 x 2 mL) and Et_2O (2 x 3 mL), and dried in air. The yield was 65%. The air-dried solid was analyzed as solvent-free **18**: C, 31.45; H, 3.11; N, 9.17 %. Found: C, 31.08; H, 2.91; N, 9.43 %. Selected IR data (ATR): *v* = 3444 (wb), 3050 (m), 2925 (w), 1579 (s), 1519 (vs), 1481 (m), 1423 (m), 1384 (s), 1317 (s), 1276 (m), 1223 (w), 1203 (w), 1072 (w), 1014 (w), 940 (w), 887 (w), 850 (w), 730 (m), 669 (m), 624 (m), 573 (w), 500 (w), 449 (w).

$[Er_4(NO_3)_2(pdmH)_6(pdmH_2)_2](NO_3)_4$ (19): This complex was prepared in the same manner as complex **14** but using $Er(NO_3)_3{\cdot}5H_2O$ (0.22 g, 0.5 mmol) as the Ln salt. After 4 days, X-ray quality colorless crystals of **19**·2MeOH had appeared and were collected by filtration, washed with cold MeOH (2 x 2 mL) and Et_2O (2 x 3 mL), and dried in air. The yield was 55%. The air-dried solid was analyzed as solvent-free **19**: C, 31.31; H, 3.10; N, 9.13 %. Found: C, 31.14; H, 2.95; N, 9.26 %. Selected IR data (ATR): *v* = 3444 (wb), 3050 (m), 2925 (w), 1579 (s), 1519 (vs), 1481 (m), 1423 (m), 1384 (s), 1317 (s), 1276 (m), 1226 (w), 1201 (w), 1072 (w), 1014 (w), 941 (w), 887 (w), 848 (w), 730 (m), 669 (m), 624 (m), 571 (w), 501 (w), 449 (w).

$[Yb_4(NO_3)_2(pdmH)_6(pdmH_2)_2](NO_3)_4$ (20): This complex was prepared in the same manner as complex **14** but using $Yb(NO_3)_3{\cdot}5H_2O$ (0.23 g, 0.5 mmol) as the Ln salt. After 3 days, X-ray quality colorless crystals of **20**·2MeOH had appeared and were collected by filtration, washed with cold MeOH (2 x 2 mL) and Et_2O (2 x 3 mL), and dried in air. The yield was 75%. The air-dried solid was analyzed as solvent-free **20**: C, 30.98; H, 3.06; N,

9.03 %. Found: C, 31.21; H, 3.19; N, 8.95 %. Selected IR data (ATR): ν = 3450 (wb), 3050 (m), 2923 (w), 1579 (s), 1519 (vs), 1479 (m), 1423 (m), 1388 (s), 1321 (s), 1276 (m), 1224 (w), 1201 (w), 1074 (w), 1014 (w), 943 (w), 887 (w), 846 (w), 730 (m), 674 (m), 622 (m), 574 (w), 501 (w), 451 (w).

5.1.3. Single-crystal X-ray Crystallography

Crystals of all compounds **10**-**20** were selected and mounted on cryoloops using an adequate oil.[99] Complete diffraction data have been collected only for compounds **12, 16, 18, 19,** and **20** at 150.0(2) K on a Bruker X8 Kappa APEX II Charge-Coupled Device (CCD) area-detector diffractometer controlled by the APEX2 software package[100] (Mo K_α graphite-monochromated radiation, λ = 0.71073 Å), and equipped with an Oxford Cryosystems Series 700 cryostream monitored remotely with the software interface Cryopad.[101]

For all crystallographically established structures, the images were processed with the software SAINT+,[102] and absorption effects were corrected by the multi-scan semi-empirical method implemented in SADABS.[103] The structures were solved by the direct methods employed in SHELXS-97,[96] allowing the immediate location of most of the heaviest elements. Remaining non-hydrogen atoms were located from difference Fourier maps calculated by successive full-matrix least-squares refinement cycles on F^2 using SHELXL-97.[97] All non-hydrogen atoms of the anionic Tb_8 cluster complex were successfully refined with anisotropic displacement parameters, while those of the cations and MeCN were only refined with isotropic parameters. The hydrogen atoms of the

organic ligands were placed at their geometrical positions and included in subsequent refinement cycles. The hydrogen atoms of the water molecules, cations and MeCN were not added to the structure, but were considered for the final molecular formula. A considerable electron density was found in the Tb_8 cluster complex, probably due to additional disordered solvent molecules. Several attempts to locate and model remaining solvent molecules revealed to be unsuccessful, and searches for the total potential solvent area using the software package *PLATON*[104] confirmed the existence of cavities with potential solvent accessible void volume. Consequently, the original data set was treated using the SQUEEZE[105] subroutines to fully remove the contribution of these highly disordered molecules in the solvent-accessible volume. The small size and apparently the weak diffraction of many crystals of **10**, **11** and **13** that we mounted in the X-ray diffractometer rendered the acquisition of a complete X-ray data set impossible.

In the structures of tetranuclear complexes **16**, **18**, **19**, and **20**, the H-atoms bound to the C-atoms of the $pdmH^-$/$pdmH_2$ ligands and MeOH solvate molecules were placed at their geometrical positions using *HFIX* instructions in SHELXL[97] (*43* for the aromatic, *23* for the CH_2 and *137* for the terminal CH_3 groups) and included in subsequent refinement cycles in riding-motion approximation with isotropic thermal displacements parameters (U_{iso}) fixed at 1.2 or 1.5 × U_{eq} of the C-atom to which they are attached. The H-atoms of the hydroxyl groups of $pdmH^-$/$pdmH_2$ ligands were found in difference Fourier maps and placed in the structural model with the O-H distances restrained to 0.85(1) Å or included in their idealized positions. The programs used for molecular graphics were MERCURY[106] and DIAMOND.[107]

Unit cell parameters and structure solution and refinement data for complexes **10**-**13** and **14**-**20** are listed in Table 5.1 and Table 5.2, respectively.

Table 5.1. Crystallographic data for the octanuclear complexes **10-13**

Parameter	**10**	**11**	**12**	**13**
Formula	$C_{116}H_{138}N_{16}O_{49}Eu_8$	$C_{116}H_{138}N_{16}O_{49}Gd_8$	$C_{116}H_{138}N_{16}O_{49}Tb_8$	$C_{116}H_{138}N_{16}O_{49}Dy_8$
Fw / g mol^{-1}	3756.13	3798.45	3811.78	3840.45
Crystal type	Colorless block	Colorless block	Colorless prism	Colorless block
Crystal size / mm	0.06×0.04×0.02	0.05×0.05×0.03	0.17×0.10×0.08	0.06×0.03×0.03
Crystal system	Triclinic	Triclinic	Triclinic	Triclinic
Space group	Bravais Lattice *P*	Bravais Lattice *P*	P-1	Bravais Lattice *P*
a / Å	14.864(2)	14.853(5)	14.8224(12)	14.802(3)
b / Å	17.555(3)	17.503(6)	17.4520(15)	17.449(4)
c / Å	28.898(2)	28.836(5)	28.926(2)	28.873(3)
α / º	88.95(2)	88.91(3)	88.889(4)	88.89(4)
β / º	82.78(2)	82.89(3)	82.758(3)	82.69(5)
γ / º	80.99(3)	80.72(4)	80.613(3)	80.59(4)
Volume / Å^3	7388.5(4)	7341.6(6)	7323.5(10)	7297.2(7)
Z	-	-	2	-
ρ_{calc} / g cm^{-3}	-	-	1.729	-
μ / mm^{-1}	-	-	3.892	-
θ range / °	-	-	3.65 – 26.73	-
Index ranges	-	-	$-18 \le h \le 18$	-
			$-22 \le k \le 22$	
			$-36 \le l \le 36$	
Collected reflections	-	-	186223	-
Independent reflections	-	-	30815 [R(int) = 0.0321]	-
Final $a^{a,b}$ indices [$I>2\sigma(I)$]	-	-	$R1$ = 0.0392 w$R2$ = 0.0956	-

Final *R* indices (all data)	-	-	*R*1 = 0.0462 w*R*2 = 0.0992	-
$(\Delta\rho)_{max,min}$ / e Å^{-3}	-	-	3.321 and -1.692	-

[a] R1 = $\Sigma(||F_o| - |F_c||)/\Sigma|F_o|$. [b] wR2 = $[\Sigma[w(F_o^2 - F_c^2)^2]/\Sigma[w(F_o^2)^2]]^{1/2}$, $w = 1/[\sigma^2(F_o^2) + (ap)^2 + bp]$, where $p = [\max(F_o^2, 0) + 2F_c^2]/3$.

Table 5.2. Crystallographic data for the tetranuclear complexes **14-20**

Parameter	**14**·2MeOH	**15**·2MeOH	**16**·2MeOH
Formula	$C_{58}H_{74}Eu_4N_{14}O_{36}$	$C_{58}H_{74}Gd_4N_{14}O_{36}$	$C_{58}H_{74}Tb_4N_{14}O_{36}$
Fw[a] / g mol^{-1}	2151.15	2172.28	2178.99
Crystal type	Colorless plate	Colorless plate	Colorless prism
Crystal size / mm	0.07×0.04×0.01	0.08×0.05×0.01	0.17×0.08×0.08
Crystal system	Monoclinic	Monoclinic	Monoclinic
Space group			$P2_1/n$
a / Å	15.484(2)	15.461(2)	15.2655(18)
b / Å	14.941(2)	14.892(2)	14.9732(16)
c / Å	15.953(2)	15.998(2)	16.0103(19)
α / º	90	90	90
β / º	92.561(6)	92.679(7)	92.407(6)
γ / º	90	90	90
Volume / Å^3	3694.7(9)	3683.5(9)	3656.3(7)
Z			2
ρ_{calc} / g cm^{-3}			1.979
μ / mm^{-1}			3.925
θ range / °			3.73 - 28.28
Index ranges			$-20 \le h \le 20$ $-19 \le k \le 19$ $-21 \le l \le 21$
Collected reflections			150416
Independent reflections			9057 (R_{int} = 0.0441)
Final [a,b] indices [$I>2\sigma(I)$]			$R1$ = 0.0442 w$R2$ = 0.0779
Final *R* indices (all data)			$R1$ = 0.0475 w$R2$ = 0.0797
$(\Delta\rho)_{max,min}$ / e Å^{-3}			1.309, −1.195

Table 5.3. Contd…

17·2MeOH	**18**·2MeOH	**19**·2MeOH	**20**·2MeOH
$C_{58}H_{74}Dy_4N_{14}O_{36}$	$C_{58}H_{74}Ho_4N_{14}O_{36}$	$C_{58}H_{74}Er_4N_{14}O_{36}$	$C_{58}H_{74}Yb_4N_{14}O_{36}$
2193.28	2203.03	2212.35	2235.47
Colorless plate	Colorless plate	Colorless plate	Colorless plate
0.06×0.04×0.02	0.08×0.05×0.02	0.04×0.02×0.01	0.07×0.04×0.02
Monoclinic	Monoclinic	Monoclinic	Monoclinic
	$P2_1/n$	$P2_1/n$	$P2_1/n$
15.375(2)	15.2459(19)	15.5716(18)	15.287(2)
14.858 (2)	14.8786(18)	14.0309(15)	14.773(2)
15.943(2)	15.983(2)	16.5856(19)	15.954(2)
90	90	90	90
93.095(7)	92.423(6)	95.035(6)	93.095(7)
90	90	90	90
3642.7(9)	3622.3(8)	3609.7(7)	3597.6(9)
	2	2	2
	2.020	2.035	2.064
	4.426	4.707	5.257
	3.74 - 26.37	3.70 - 25.68	3.76 - 26.37
	$-19 \le h \le 19$ $-18 \le k \le 18$ $-19 \le l \le 19$	$-18 \le h \le 18$ $-16 \le k \le 17$ $-20 \le l \le 20$	$-19 \le h \le 19$ $-18 \le k \le 18$ $-19 \le l \le 19$
	166714	57169	141226
	7388 (R_{int} = 0.0527)	13561 (R_{int} = 0.0502)	7227 (R_{int} = 0.0745)
	$R1$ = 0.0490 w$R2$ = 0.0894	$R1$ = 0.0588 w$R2$ = 0.1266	$R1$ = 0.1030 w$R2$ = 0.1186
	$R1$ = 0.0523 w$R2$ = 0.0904	$R1$ = 0.0761 w$R2$ = 0.1366	$R1$ = 0.1219 w$R2$ = 0.1322
	1.823, −1.713	3.274, −1.108	1.974, −2.435

[a] $R1 = \Sigma(||F_o| - |F_c||)/\Sigma|F_o|$. [b] $wR2 = [\Sigma[w(F_o^2 - F_c^2)^2]/\Sigma[w(F_o^2)^2]]^{1/2}$, $w = 1/[\sigma^2(F_o^2) + (ap)^2 + bp]$, where $p = [\max(F_o^2, 0) + 2F_c^2]/3$.

5.2. Results and Discussion

5.2.1. Synthetic Comments

We have recently started working on the synthesis of polynuclear metal complexes exhibiting dual physical properties, such as magnetism and photoluminescence. We decided to approach this challenge from two different directions. Firstly, by the deliberate replacement of non-emissive carboxylato ligands in known SMMs with their fluorescent analogues, without perturbing the metal-core structure and SMM properties; this approach has led us to the synthesis of triangular, emissive Mn^{III}_3 SMMs (Chapter 4). The second route, which was followed in the present study, involves the use of naphthalene or pyridine-based polyalcohol bridging ligands as a means of obtaining new polynuclear Ln^{III} metal clusters with novel topologies, SMM behaviors and luminescent properties arising from the increased efficiency of the "antenna" organic group.

Many synthetic procedures to polynuclear 4*f*-metal complexes rely on the reactions of simple LnX_3 starting materials (X^- = various) with a potentially chelating/bridging organic ligand.[47,173] The nature of both the X^- group and the organic ligand is of significant synthetic importance. When the X^- belongs to the carboxylate or β-diketonate groups, additional bridging ligation from these groups could be provided resulting in the

formation of higher nuclearity metal species. Occasionally, their strong basic nature fosters the deprotonation of the organic chelating/bridging ligand without requiring the use of an external base. On the other hand, when the choice of X^- is one of the halides, NO_3^-, ClO_4^- or $CF_3SO_3^-$, all with limited bridging affinity, the employment of an external organic base which would carry the role of proton acceptor seems necessary to facilitate deprotonation of the organic chelating/bridging ligand and therefore increase the chances of metal cluster formation. The latter route was followed in the present study, using as organic chelating/bridging ligand the unexplored in lanthanide metal cluster chemistry naphthalene-2,3-diol (ndH_2). The naphthalene diol ligand ndH_2 contains two -OH groups which upon deprotonation can potentially bridge up to five metal centers.

A variety of reactions differing in the metal:ndH_2 ratio, the inorganic ions present, the organic base, and/or the reaction solvent(s) were explored in identifying the following successful system. Reactions of $Ln(NO_3)_3{\cdot}xH_2O$ (x = 5 or 6) with ndH_2 in a 1:2 molar ratio in MeCN in the presence of 2 equivalents of Et_4NOH gave pale yellow solutions that, upon filtration and slow diffusion with Et_2O, afforded yellowish crystals of a family of isostructural octanuclear $(Et_4N)_4[Ln_8O(nd)_8(NO_3)_{10}(H_2O)_2]$ [Ln = Eu (**10**); Gd (**11**); Tb (**12**); Dy (**13**)] complexes in good yields (45-60%). The general formation of **12**, as a representative example, is summarized in Equation 5.1.

$$8\ Tb(NO_3)_3{\cdot}6H_2O + 8\ ndH_2 + 18\ Et_4NOH \rightarrow$$

$$(Et_4N)_4[Tb_8O(nd)_8(NO_3)_{10}(H_2O)_2] + 14\ (Et_4N)(NO_3) + 63\ H_2O \qquad (5.1)$$

The MeCN reaction solvent was found to be of critical importance for the crystallization of all reported compounds **10**-**13**; various other reactions in more polar or non-polar solvent media gave either very soluble compounds that was impossible to grow single-crystals from the corresponding solutions or non-crystalline precipitates that were probably mixtures of different products. The base Et_4NOH has the role of proton acceptor to facilitate the deprotonation of the ndH_2. The base also provides in solution the Et_4N^+ cations, which seem to be necessary for the stabilization and crystallization of **10**-**13** (*vide infra*). Employment of different organic bases, such as NMe_3, *n*-Bu_3N and Me_4NOH, did not afford crystalline materials but only yellowish precipitates that were characterized with IR spectroscopy and confirmed their same structural identity as for **10**-**13**. Finally, the replacement of NO_3^- ions in the LnX_3 precursors by other inorganic ions, such as Cl^- or ClO_4^-, did not lead us to any crystalline material under various crystallization techniques and reaction conditions.

In the next step of our synthetic attempts, we decided to employ the relatively unexplored in lanthanide metal cluster chemistry pyridine-2,6-dimethanol ($pdmH_2$) chelate.[149] Previous use of $pdmH_2$ in 4*f*-metal cluster chemistry has been limited to the two isostructural carboxylate complexes $[Yb_4(O_2CPh)_2(pdm)_4(pdmH)_2(HO_2CPh)_2(H_2O)_2]$[149b] and $[Dy_4(O_2CPh)_2(pdm)_4(pdmH)_2(HO_2CPh)_4]$,[149a] both with a zigzag topology. Performing the same reaction that led to the $\{Ln^{III}_8\}$-nd^{2-} family of clusters but instead with $pdmH_2$ we have been unable to obtain any crystalline material. The employment of MeOH as the reaction solvent instead of MeCN gave white precipitates that we were unable to further

characterize. Finally, the change of the organic base from Et_4NOH to NEt_3 led us to the following successful system.

The reactions of $Ln(NO_3)_3{\cdot}xH_2O$ (x = 5 or 6) with $pdmH_2$ in a 1:2 molar ratio in MeOH in the presence of 2 equivalents of NEt_3 gave colorless solutions that, upon filtration and layering with Et_2O, afforded colorless crystals of a family of isostructural tetranuclear $[Ln_4(NO_3)_2(pdmH)_6(pdmH_2)_2](NO_3)_4$ [Ln = Eu (**14**); Gd (**15**); Tb (**16**); Dy (**17**); Ho (**18**); Er (**19**); Yb (**20**)] complexes in very good yields (50-75%). The general formation of **14-20** is summarized in Equation 5.2.

$$4\ Ln(NO_3)_3{\cdot}xH_2O + 8\ pdmH_2 + 6\ NEt_3 \rightarrow [Ln_4(NO_3)_2(pdmH)_6(pdmH_2)_2](NO_3)_4 + 6\ (NHEt_3)(NO_3) + 4\ H_2O \quad (5.2)$$

Ln = Eu (**14**); Gd (**15**); Tb (**16**); Dy (**17**); Ho (**18**); Er (**19**); Yb (**20**); x = 5 or 6

In an attempt to obtain higher nuclearity Ln^{III} products, several reactions were performed with higher Ln^{III}:$pdmH_2$ ratios, up to 4:1. However, the tetranuclear complexes **14-20** were still the only isolable products, in comparable (from 1:1 or 2:1 ratios) or lower (from 3:1 or 4:1 ratios) yields. Complexes **14-20** were also obtained when the reactions were performed in EtOH (confirmation from IR spectroscopic studies) or mixture of MeCN/MeOH (2:1, v/v), but in much lower yields (~10-20%), whereas no significant reactions were observed when the solvent was CH_2Cl_2 or $CHCl_3$. An increase in the NEt_3:$pdmH_2$ ratio up to 3:1 gave comparable (or slightly decreased) yields of

complexes **14**-**20** instead of higher nuclearity products which could have resulted from the complete deprotonation of $pdmH^-/pdmH_2$ groups. Further increase in the amount of NEt_3 gave oily products suggestive of mixtures that we have not been able to characterize, or insoluble amorphous precipitates that were probably Ln oxides or oxo/hydroxide species. Replacement of NEt_3 by other organic bases, i.e. Me_4NOH, also led to isolation of **14**-**20** but the crystalline solids were contaminated with $(Me_4N)(NO_3)$ salt, requiring copious washing with MeOH to obtain analytically pure samples. Finally, the substitution of NO_3^- ions in the LnX_3 precursors by other inorganic ions, such as Cl^- or ClO_4^-, did not lead us to any crystalline material under various crystallization techniques and reaction conditions. It therefore seems that the presence of nitrates is essential for the stabilization and crystallization of the reported tetranuclear compounds.

5.2.2. Description of Structures

The partially labeled structure of the $[Tb_8O(nd)_8(NO_3)_{10}(H_2O)_2]^{4-}$ anion of **12** is shown in Figure 5.1 (left). The anion of **12** has crystallographic C_1 but virtual S_4 symmetry, and consists of a central $[Tb_4(\mu_4\text{-}O^{2-})]$ tetrahedron (Tb1, Tb2, Tb3, Tb4) whose four edges are each fused with the edge of a $[Tb_3(\mu_3\text{-}OR^-)_2(\mu\text{-}OR^-)_2]$ triangle (RO^- = alkoxido arms of nd^{2-}). The resulting $[Tb_8(\mu_4\text{-}O)(\mu_3\text{-}OR)_8(\mu\text{-}OR)_8]^{6+}$ core has a "Christmas-star" topology (Figure 5.1, right), which is unprecedented in 4*f*-metal cluster chemistry. Similar metal cores have been previously seen only in Fe_8 cluster chemistry albeit with the central subcore possessing a square-planar geometry.[150]

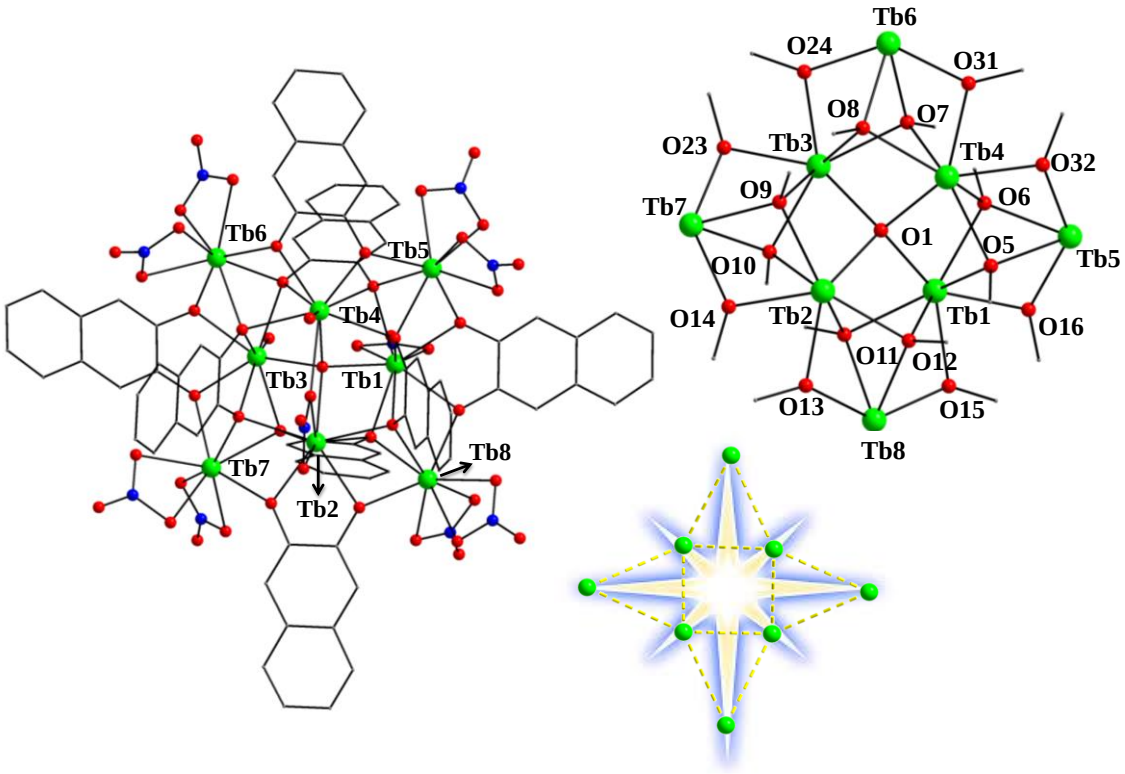

Figure 5.1. (left) The structure of the anion of **12**. (right) The $[Tb_8O(OR)_{16}]^{6+}$ core of **12** emphasizing the "Christmas-star" topology. Color scheme: Tb^{III}, green; O, red; N, blue; C, grey. H atoms are omitted for clarity.

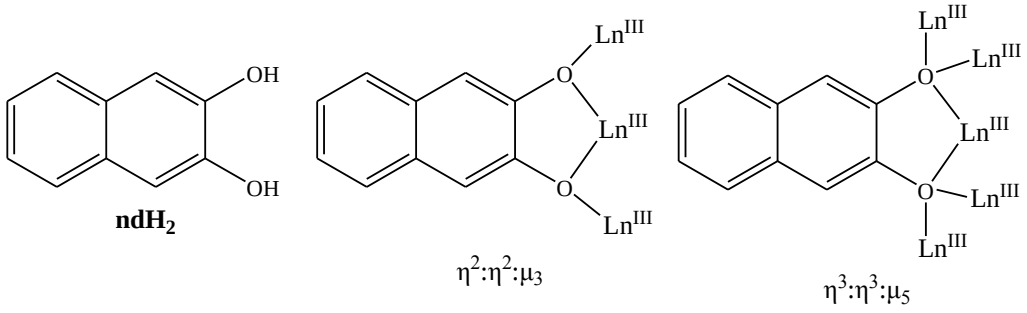

Scheme 5.1. Structural formula and abbreviation of the ligand naphthalene-2,3-diol (ndH_2), and the crystallographically established coordination modes of its dianion (nd^{2-}) in complexes **10**-**13**.

In complex **12**, the central μ_4-O^{2-} (O1), whose protonation level was confirmed by oxygen BVS calculations (BVS = 2.05), is distorted tetrahedral [Tb-O-Tb angles = 99.2(1)-134.7(2)°], and the $[Tb_3(\mu_3\text{-}OR)_2(\mu\text{-}OR)_2]^{5+}$ triangular units are essentially isosceles, the short separations [3.475(6)-3.523(6) Å] being the four (oxido)-bis(μ_3-alkoxido)-bridged edges fused with the central tetrahedron. One of the remaining two edges of the central Tb_4 tetrahedron (Tb2···Tb4) is additionally bridged by a μ-O^- atom (O2) from an η^1:η^2:μ NO_3^- group. In addition, each Tb^{III} of the tetrahedron is linked to two peripheral Tb^{III} atoms by two μ_3- and two μ-O^- atoms from four η^2:η^2:μ_3 and four η^3:η^3:μ_5 nd^{2-} ligands (Scheme 5.1). The ligands possess C-O and C-C bond distances in the ranges 1.34-1.37 and 1.33-1.44 Å, respectively, which are characteristic for catecholato-type ligands rather than semiquinonato or quinonato.[151] Peripheral ligation is provided by nine bidentate chelating NO_3^- groups, two on each of the external Tb^{III} atoms and the remaining on Tb1, and two H_2O molecules terminally bound to the inner Tb3 and Tb4. The internal Tb^{III} atoms are nine-coordinate, except Tb3 which is eight-coordinate; the latter coordination environment is also assigned to all external Tb^{III} atoms.

To estimate the closer coordination polyhedra defined by the donor atoms around all Tb atoms in **12**, we used the program SHAPE.[152] Following the proposal by Avnir and co-workers[153] to consider symmetry and polyhedral shape as continuous properties that can

be quantified from structural data, Alvarez and co-workers have applied these concepts and the associated methodology to the stereochemical analysis of very large sets of molecular structures, including systems with 8- and 9-vertex polyhedra.[154] The so-called Continuous Shape Measures (CShM) approach essentially allows one to numerically evaluate by how much a particular structure deviates from an ideal shape. Values of CShM between 0.1 and 3 usually correspond to a not negligible but still small distortion from ideal geometry, while values larger than 3 refer to very distorted coordination environments. The best fit was obtained for the muffin (Tb1), spherical capped square antiprismatic (Tb2, Tb4), square antiprismatic (Tb3, Tb5) and triangular dodecahedral (Tb6, Tb7, Tb8) geometries (Figure 5.2); the obtained CShM values were 1.06, 1.18/0.88, 1.87/3.69 and 3.85/4.00/4.05, respectively. Finally, the voids between the Tb_8 anions are occupied by countercations and lattice solvate molecules; the crystal structure is stabilized by H-bonds and interanionic π-π interactions. The shortest Tb···Tb intermolecular distance is 9.1 Å.

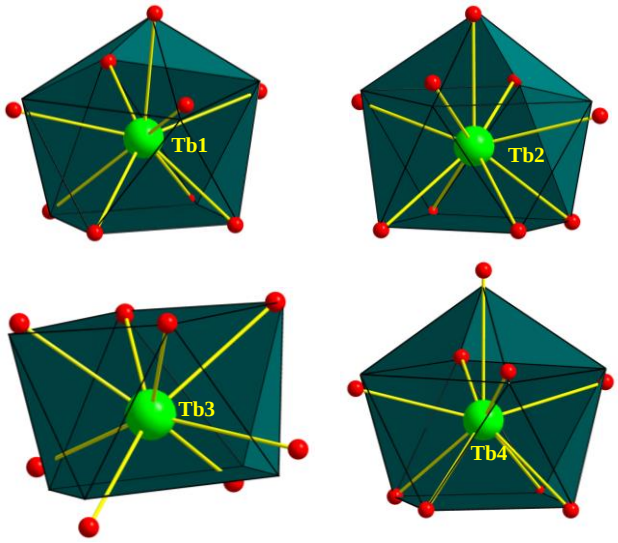

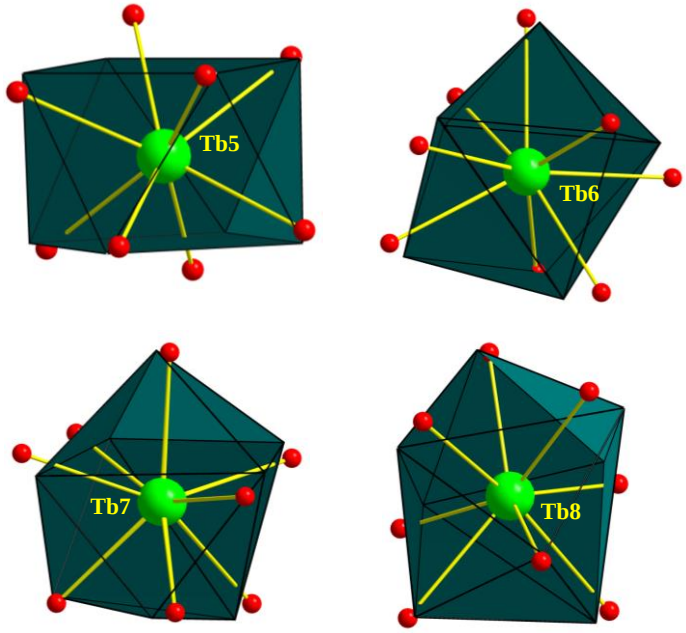

Figure 5.2. Muffin (Tb1), spherical capped square antiprismatic (Tb2, Tb4), square antiprismatic (Tb3, Tb5) and triangular dodecahedral (Tb6, Tb7, Tb8) geometries of the terbium atoms in the structure of **12**. The points connected by the black lines define the vertices of the ideal polyhedron.

The structures of complexes **14**-**20** are very similar, and thus, only the structure of representative complex **16** will be described in detail. The crystal structure of **16** consists of a $[Tb_4(NO_3)_2(pdmH)_6(pdmH_2)_2]^{4+}$ cation (Figure 5.3), four NO_3^- anions, and lattice MeOH molecules; the latter two will not be further discussed. Complex **16**·2MeOH crystallizes in the monoclinic space group $P2_1/n$ with the Tb_4 cation lying on an inversion center.

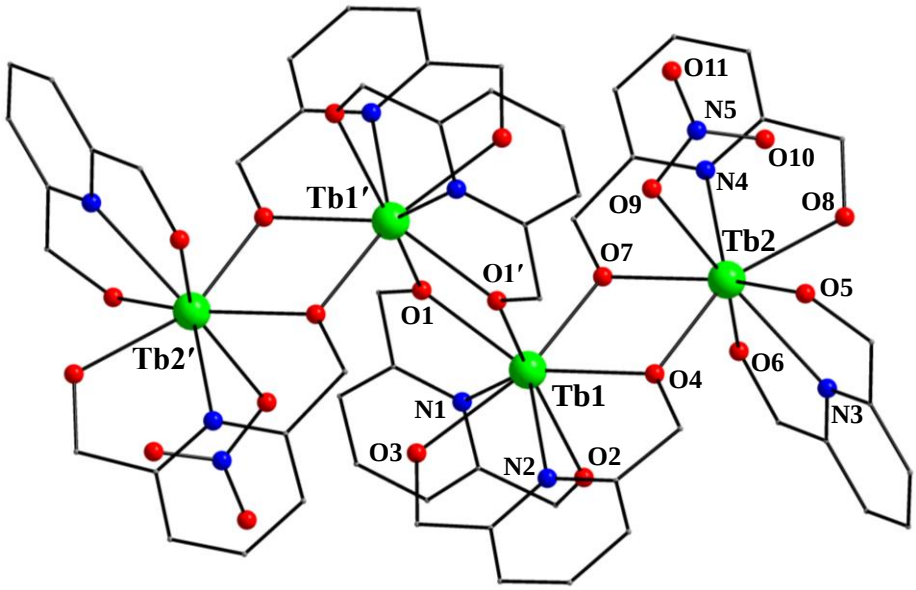

Figure 5.3. Partially labeled representation of the structure of the cation of **16**, with H atoms omitted for clarity. Primes are used for symmetry-related atoms. Color code: Tb^{III}, green; O, red; N, blue; C, grey.

The cation comprises a non-linear, zigzag array of four Tb^{III} atoms (Tb2-Tb1-Tb1′ = 107.56º) with each Tb_2 pair bridged by the deprotonated alkoxido arms of two chelating/bridging $pdmH^-$ groups resulting in an overall $[Tb_4(\mu\text{-}OR)_6]^{6+}$ core (Figure 5.4). There is thus a total of six $\eta^1{:}\eta^1{:}\eta^2{:}\mu$ $pdmH^-$ groups, and peripheral ligation is completed by two neutral, tridentate (N,O,O) chelating $pdmH_2$ ligands and two monodentate NO_3^- groups, one each on the two extrinsic Tb^{III} atoms, Tb2 and Tb2′. The central Tb(1)-O(1)-Tb(1′)-O(1′) rhombus is strictly planar as a result of the inversion center, and the other two rhombs are nearly so, with the Tb(1)-O(4)-Tb(2)-O(7) torsion angle being only 0.8º. The Tb^{III} atoms are all eight-coordinate with distorted geometries.

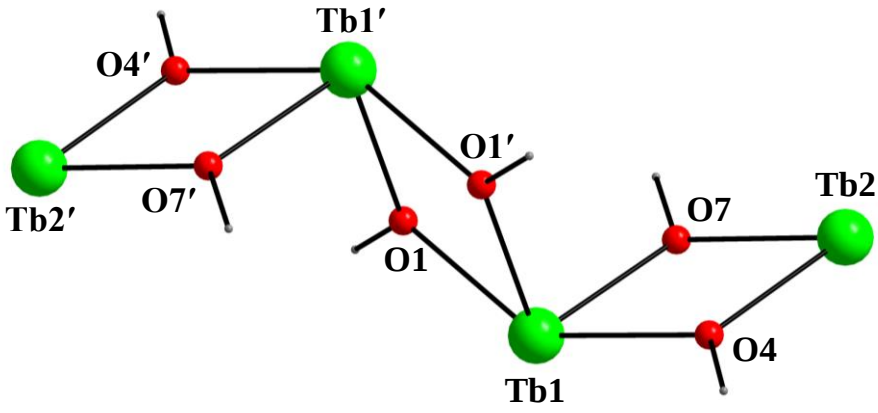

Figure 5.4. Labeled representation of the complete $[Tb_4(\mu\text{-}OR)_6]^{6+}$ core of **16**. Color scheme as in Figure 5.3.

To estimate the closer coordination polyhedra defined by the donor atoms around Tb1 and Tb2 in the asymmetric unit of **16**, a comparison of the experimental structural data with the theoretical data for the most common polyhedral structures with 8 vertices was performed by means of the program SHAPE.[155] There are many polyhedra with eight vertices such as Platonic solids (cube), Archimedean or Catalan (triakis tetrahedron) solids and others such as triangular dodecahedra. In addition, prisms (biaugmented trigonal) or antiprisms (square antiprism) can be made with eight vertices as well as many semi-regular three-dimensional figures. The most common of these, which will be considered here, are the octagon, the heptagonal pyramid, the hexagonal bipyramid, the triangular dodecahedron, and the four Johnson polyhedra (gyrobifastigium, elongated triangular bipyramid, biaugmented trigonal prism and snub tetrahedron). The best fit (Table 5.4) was obtained for the triangular dodecahedron (Tb1; Figure 5.5, left) and

biaugmented trigonal prism (Tb2; Figure 5.5, right) with CShM values of 1.96 and 1.50, respectively.

Table 5.4. Shape measures of the 8-coordinate Tb1 and Tb2 coordination polyhedra in **16**[a,b]

Polyhedron[b]	Tb1	Tb2
OP-8	33.40	28.99
HPY-8	24.47	23.51
HBPY-8	13.65	14.56
CU-8	11.29	10.98
SAPR-8	3.93	2.68
TDD-8	**1.96**	2.25
JGBF-8	10.60	11.74
JETBPY-8	27.05	26.15
JBTPR-8	3.73	2.39
BTPR-8	3.23	**1.50**
JSD-8	3.12	3.49
TT-8	11.58	11.66
ETBPY-8	22.94	22.32

[a] See Figure 5.5; [b] Abbreviations: OP-8, octagon; HPY-8, heptagonal pyramid; HBPY-8, hexagonal bipyramid; CU-8, cube; SAPR-8, square antiprism; TDD-8, triangular dodecahedron; JGBF-8, Johnson gyrobifastigium; JETBPY-8, Johnson elongated triangular bipyramid; JBTPR-8, Johnson biaugmented trigonal prism; BTPR-8, biaugmented trigonal prism; JSD-8, Johnson snub diphenoid; TT-8, triakis tetrahedron; ETBPY-8, elongated trigonal bipyramid. The values in boldface indicate the closest polyhedron according to the Continuous Shape Measures.

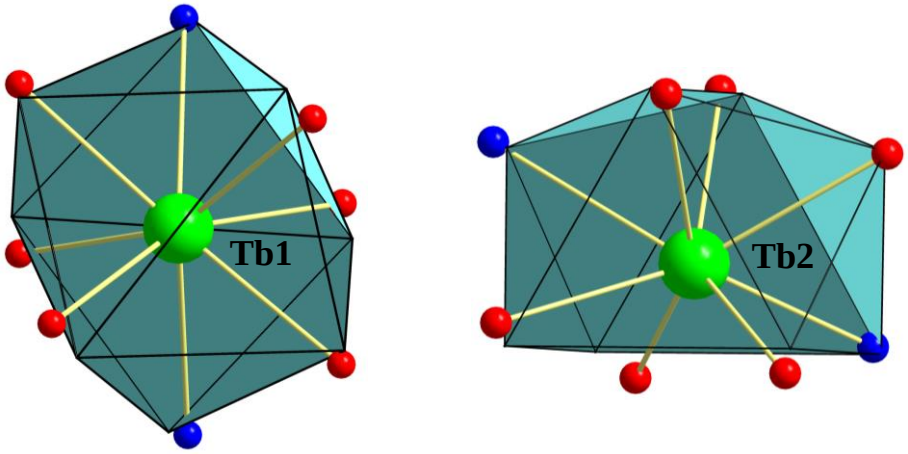

Figure 5.5. Triangular dodecahedron coordination sphere of Tb1 (left) and biaugmented trigonal prismatic geometry of Tb2 (right) in the structure of **16**. The points connected by the black lines define the vertices of the ideal polyhedron.

Four distinct, and eight in total (including the symmetry related atoms), strong intramolecular hydrogen bonds are present in **16**·2MeOH. These include the protonated OH-groups of the $pdmH_2$/$pdmH^-$ ligands, which act as donors, and an O atom from each monodentate or non-coordinated (counteranion) NO_3^- group or the lattice solvate MeOH molecules as acceptors; their dimensions are: O(3)···O(9′) 2.737(7) Å, H(3A)···O(9′) 1.918 Å, O(3)-H(3A)···O(9′) 161.9°; O(6)···O(12) 2.712(7) Å, H(6A)···O(12) 1.868 Å, O(6)-H(6A)···O(12) 175.2°; O(8)···O(15) 2.762(7) Å, H(8A)···O(15) 2.044 Å, O(8)-H(8A)···O(15) 142.2°; O(2)···O(18) 2.635(7) Å, H(2A)···O(18) 1.790 Å, O(2)-H(2A)···O(18) 175.4°. There are no significant intermolecular interactions, only weak contacts which serve to hold the molecules together in the crystal.

The Ln-N and Ln-O bond distances in **14-20** fall into the expected range for similar compounds and take shorter values as we move from **14** to **20**, which are consistent with the lanthanide contraction effect. There have been a large number of Ln_4 complexes reported in the literature, and these possess a wide variety of metal topologies such as linear,[156] rectangles,[157] squares and grids,[158] rhombs and butterflies,[159] cubanes,[160] and dimers-of-dimers.[161] However, complexes **14-20** join only a handful of previous Ln_4 compounds with a similar kind of extended, chain-like topology and an $[Ln_4(\mu\text{-}OR)_6]^{6+}$ core.[162]

5.2.3. Electronic Spectra

The electronic absorption spectra of the free ligand ndH_2 and the isostructural Ln^{III}_8 complexes **10-13** were recorded in MeCN solutions of concentrations ~10^{-5} M. The free ligand (Figure 5.6) shows three absorption bands at 220, 272 and 324 nm which could be assigned to singlet $\pi \rightarrow \pi^*$ electronic transitions of the naphthalene group.[163]

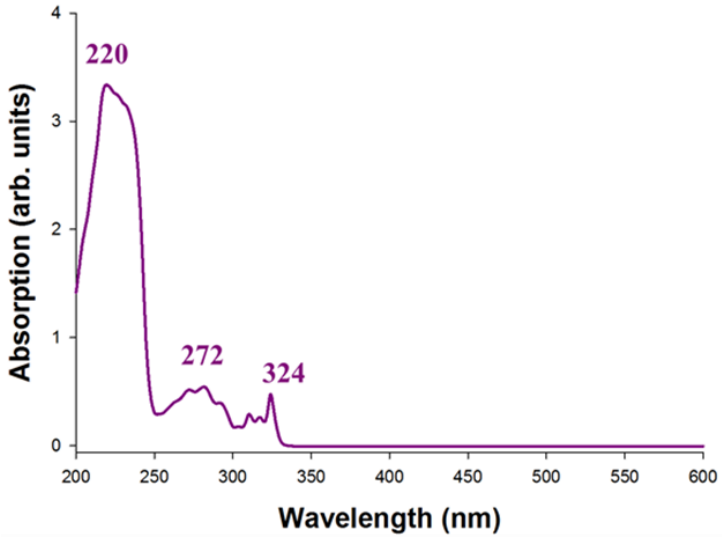

Figure 5.6. Absorption spectrum of the free ndH_2 ligand in MeCN (~10^{-5} M).

All complexes (Figure 5.7) show two absorption bands, one at 252 nm and the second at 346 nm. Both bands are characteristic of the doubly deprotonated ligand (nd^{2-}),[164] and the shift of these bands to higher wavelengths is indicative of the complexation of the ligand with the lanthanide ions.

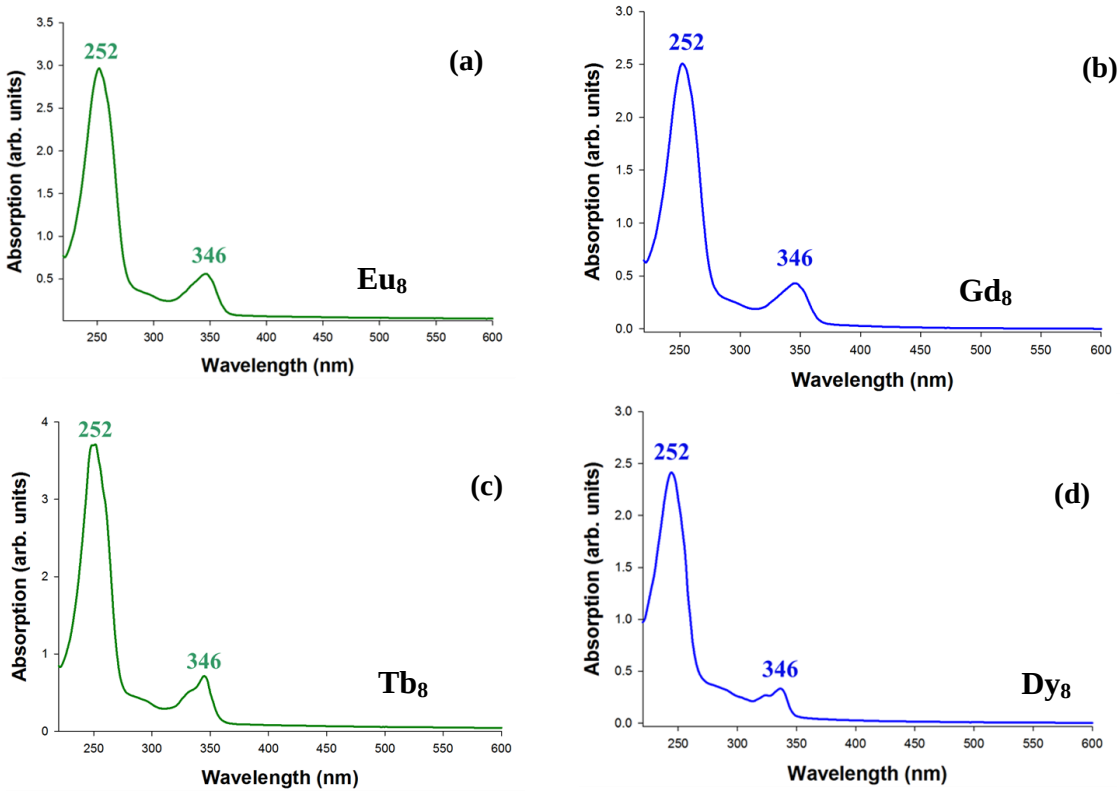

Figure 5.7. Absorption spectra of complexes **10** (a), **11** (b), **12** (c), and **13** (d) in MeCN (~10^{-5} M).

The electronic absorption spectra of the free ligand $pdmH_2$ and the isostructural Ln^{III}_4 complexes **14-20** were also recorded in MeCN solutions of concentrations ~10^{-5} M. The

free ligand (Figure 5.8, left) possesses two absorption bands at 218 and 265 nm, which could be assigned to singlet $\pi \rightarrow \pi^*$ electronic transitions of the pyridyl group.[165] All tetranuclear complexes **14**-**20** show the same characteristic bands of pyridyl group (Figure 5.8, right), slightly shifted to higher wavenumbers, which is consistent with coordination of the $pdmH_2$ ligand to the metal centers. Hence, the results from the UV/Vis studies were consistent with the integrity of the solid-state structures of all complexes in solution.

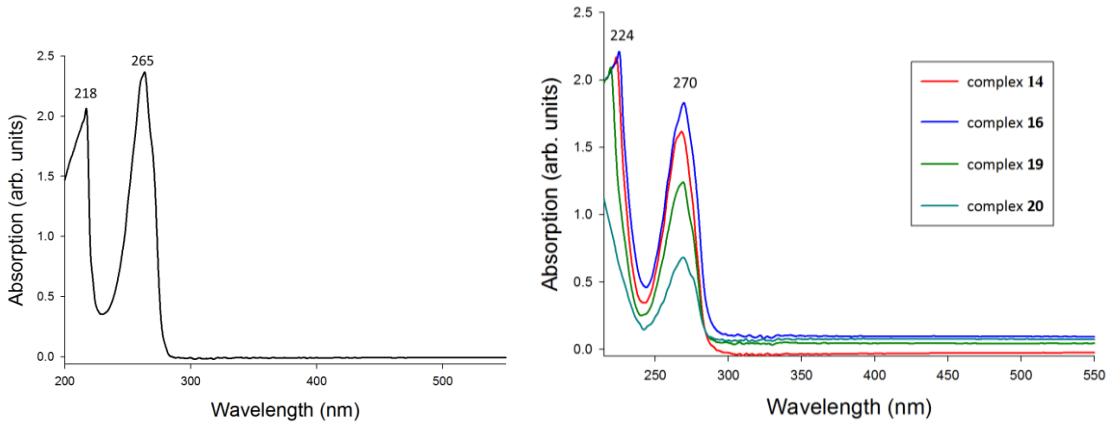

Figure 5.8. Absorption spectra of the free ligand $pdmH_2$ (left) and representative complexes **14**, **16**, **19**, and **20** (right).

5.2.4. Solid-state Magnetic Susceptibility Studies

Variable-temperature direct-current (*dc*) magnetic susceptibility studies were carried out on freshly prepared, crystalline samples of complexes **10**-**13** in the temperature range 5.0-300 K under an applied field of 0.1 T. The obtained data for all studied compounds are shown as $\chi_M T$ *vs.* T plots in Figure 5.9.

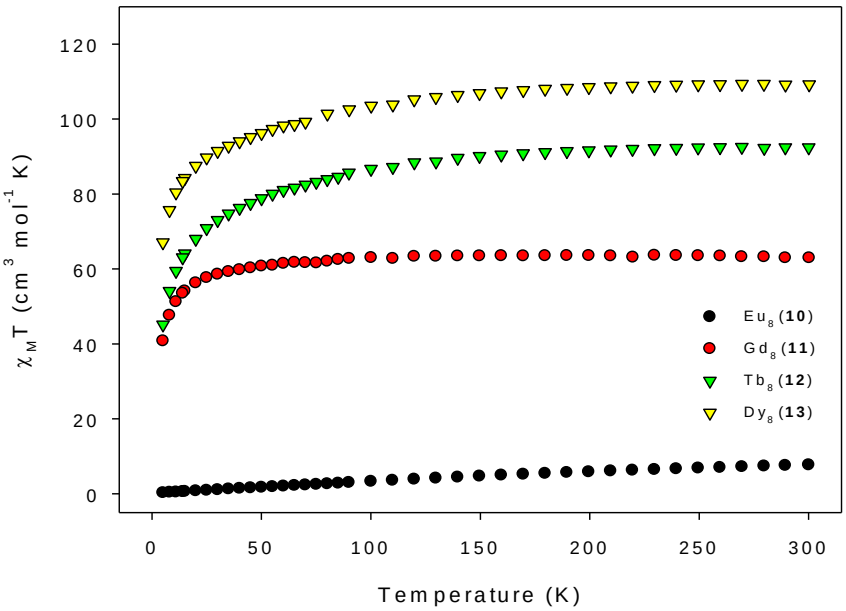

Figure 5.9. Plots of $\chi_M T$ *vs.* *T* for complexes **10**-**13**.

The experimental $\chi_M T$ values at room temperature are in excellent agreement with the theoretical ones (63 cm^3Kmol^{-1} for **11**; 94.56 cm^3Kmol^{-1} for **12**; 113.36 cm^3Kmol^{-1} for **13**) for eight non-interacting Gd^{III} ($^8S_{7/2}$, $S = 7/2$, $L = 0$, $g = 2$), Tb^{III} ($^7F_6$, $S = 3$, $L = 3$, $g = 3/2$), and Dy^{III} ($^6H_{15/2}$, $S = 5/2$, $L = 5$, $g = 4/3$) ions. For the isotropic Gd^{III}_8 complex **11**, the $\chi_M T$ product remains almost constant at a value of ~60 cm^3Kmol^{-1} from 300 K to ~80 K and then steadily decreases to a minimum value of 40.74 cm^3Kmol^{-1} at 5.0 K indicating the presence of intramolecular antiferromagnetic exchange interactions between the eight Gd^{III} centers and/or zero-field splitting. The temperature independent behavior (300-80 K) suggests that the coupling between the Gd^{III} ions is very weak as has been seen in many polynuclear Gd^{III} complexes. For the anisotropic Tb^{III}_8 (**12**) and Dy^{III}_8 (**13**) complexes, the thermal evolution of the magnetic susceptibility is very similar, in

which the $\chi_M T$ product remains essentially constant at a value of ~92 and ~109 cm^3Kmol^{-1} from 300 K to ~150 K and then rapidly decreases to a minimum value of 45.13 and 67.09 cm^3Kmol^{-1} at 5.0 K, respectively. Such low-T decrease of the $\chi_M T$ product is mainly due to depopulation of the excited M_J states of the Tb^{III} and Dy^{III} ions and the weak antiferromagnetic interactions between the metal centers.[46a,48a,48c]

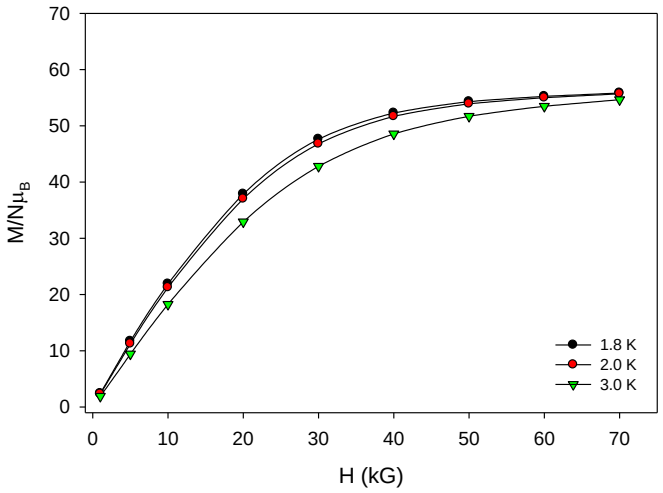

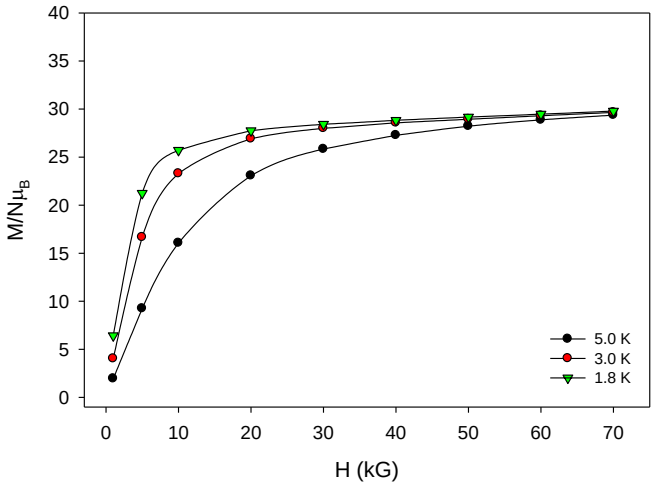

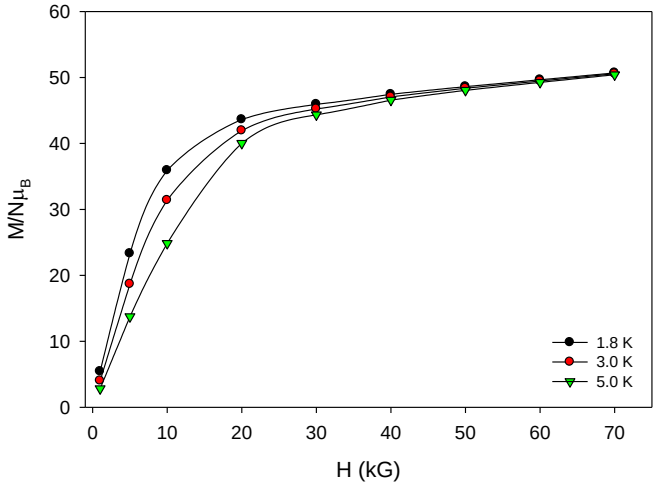

Figure 5.10. Plots of magnetization (*M*) *vs.* field (*H*) for complexes **11** (top), **12** (middle), and **13** (bottom) at different low temperatures.

The lack of true saturation in magnetization of complexes **12** and **13** (Figure 5.10, middle and bottom, respectively) indicates the presence of magnetic anisotropy and/or population of low-lying excited states. In the case of isotropic Gd_8 (**11**), the magnetization almost reaches a saturation at 55.8 μ_B at the highest fields (Figure 5.10, top), which is in good agreement with the expected value of 56 μ_B for eight non-coupled Gd^{III} ions (M_{sat} = 8 x 7 e^- = 56 μ_B). This further supports the weak nature of the magnetic exchange interactions between the Gd^{III} ions so that the antiferromagnetic interactions are easily overcome by the external *dc* field. The slight deviation of *M vs*. *H* for **11** at low temperatures and small magnetic fields is due to the population of low-lying excited states with *S* larger than the ground state. This is also supported by the continuous decrease of the in-phase, $\chi'_M T$, product as the temperature decreases down to 1.8 K (Figure 5.11).

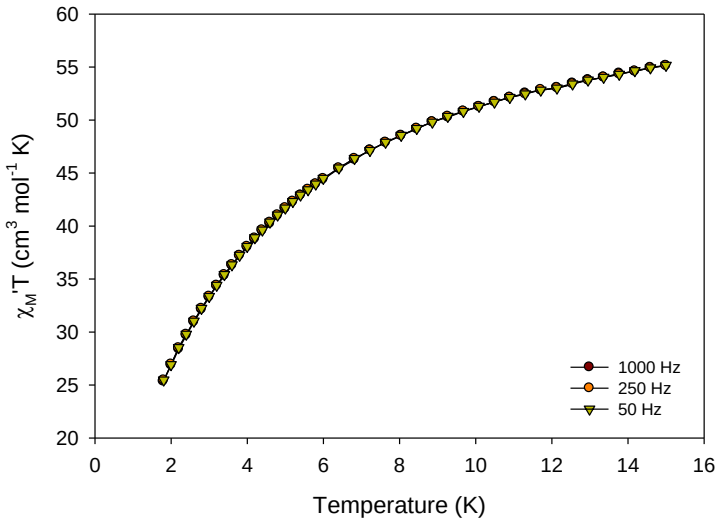

Figure 5.11. The in-phase (χ'_M) (as $\chi'_M T$) *vs. T ac* susceptibility signals for **11** in a 3.5 G field oscillating at the indicated frequencies.

Alternating current (*ac*) magnetic susceptibility studies have been also carried out in order to investigate the magnetization dynamics of the anisotropic Tb^{III}_8 (Figure 5.12, top) and Dy^{III}_8 (Figure 5.12, bottom) clusters under a zero *dc* magnetic field. Complex **13** is the only member of this family of clusters which shows frequency-dependent out-of-phase χ''_M tails of signals at temperatures below ~9 K, indicative of the slow magnetization relaxation of an SMM with a small energy barrier for magnetization reversal. Such behavior most likely arises from predominant single-ion effects of the individual Dy^{III} Kramer ions within **13**.[48a,48c] *Ac* studies were initially performed in the 1.8-30 K range using a 3.5 G *ac* field oscillating at a frequency of 1000 Hz; such primary measurement has been carried out in order to determine any possible second relaxation

process which is usually observed at T > 10 K. However, that turned out not to be the case and we have thus concentrated our *ac* studies at T < 10 K and frequencies in the 5-1500 Hz range. For fast relaxing SMMs and/or SMMs with large quantum tunneling rates, which is usually the case for high-nuclearity Dy^{III} molecular nanomagnets, an entirely visible peak of the χ''_M signal is not often observed even at the lowest possible temperature (~1.8 K) of any commercial SQUID magnetometer; only the tails of peak maxima can thus be detected. The application of an external *dc* field to surpass the tunelling has not induced any significant shift of the out-of-phase signals at higher temperatures.

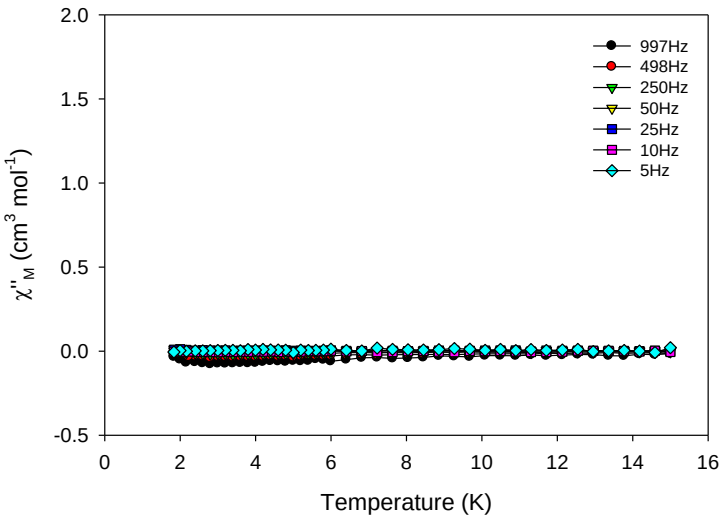

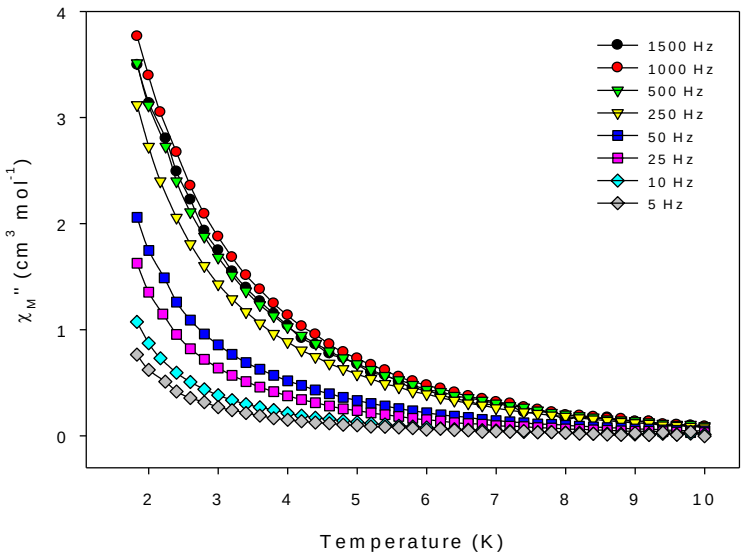

Figure 5.12. The out-of-phase (χ''_M) *vs. T ac* susceptibility signals for **12** (top) and **13** (bottom) in a 3.5 G field oscillating at the indicated frequencies.

Given the lack of χ'' peak maxima, the energy barrier and relaxation time for **13** were approximated using a method employed by Bartolomé et al.,[166] based on the equation: $\ln(\chi''/\chi') = \ln(\omega\tau_0) + E_a/k_BT$, where E_a is the activation energy akin to the energy barrier for magnetization reversal. Considering a single relaxation process, the least-squares fits of the experimental data (Figure 5.13) gave an energy barrier of ~1.9(2) cm^{-1} (~2.8(2) K) and a relaxation time of 7.2(3) × 10^{-6} s, consistent with the expected τ_0 values for a fast-relaxing SMM.[46,47,48]

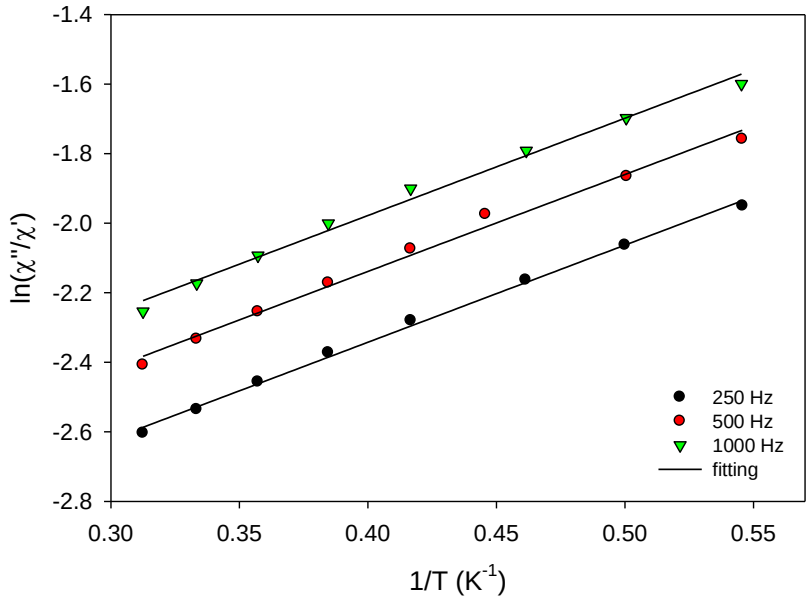

Figure 5.13. Plots of ln(χ″/χ′) *vs.* 1/*T* for **13** at different frequencies of the 3.5 G oscillating *ac* field. The solid lines are the best-fit curves; see the text for the fit parameters.

Variable-temperature direct-current (*dc*) magnetic susceptibility studies were carried out on freshly prepared, crystalline samples of the potentially most interesting -from a magnetism viewpoint- complexes **15**·2MeOH, **16**·2MeOH, **17**, **18** and **20**, in the temperature range 5.0-300 K under an applied field of 0.1 T. Theoretically, the Eu^{III}_4-analogue (**14**), as well as the previously reported Eu^{III}_8 cluster, should not exhibit any magnetic moment, since Eu^{III} has an $^7F_0$ with $J = 0$, although some contribution from thermally accessible levels such as $^7F_1$ and $^7F_2$ may appear.[173b] The obtained data for all studied compounds are shown as $\chi_M T$ *vs.* *T* plots in Figure 5.14 and Figure 5.15. The experimental $\chi_M T$ values at room temperature in all cases are in very good agreement with the theoretical ones (31.50 cm^3Kmol^{-1} for **15**; 47.28 cm^3Kmol^{-1} for **16**; 56.68

cm^3Kmol^{-1} for **17**; 56.28 cm^3Kmol^{-1} for **18**; 10.28 cm^3Kmol^{-1} for **20**) for four non-interacting Gd^{III} ($^8S_{7/2}$, $S = 7/2$, $L = 0$, $g = 2$), Tb^{III} ($^7F_6$, $S = 3$, $L = 3$, $g = 3/2$), Dy^{III} ($^6H_{15/2}$, $S = 5/2$, $L = 5$, $g = 4/3$), Ho^{III} ($^5I_8$, $S = 2$, $L = 6$, $g = 5/4$), and Yb^{III} ($^2F_{7/2}$, $S = 1/2$, $L = 3$, $g = 8/7$) ions.[167]

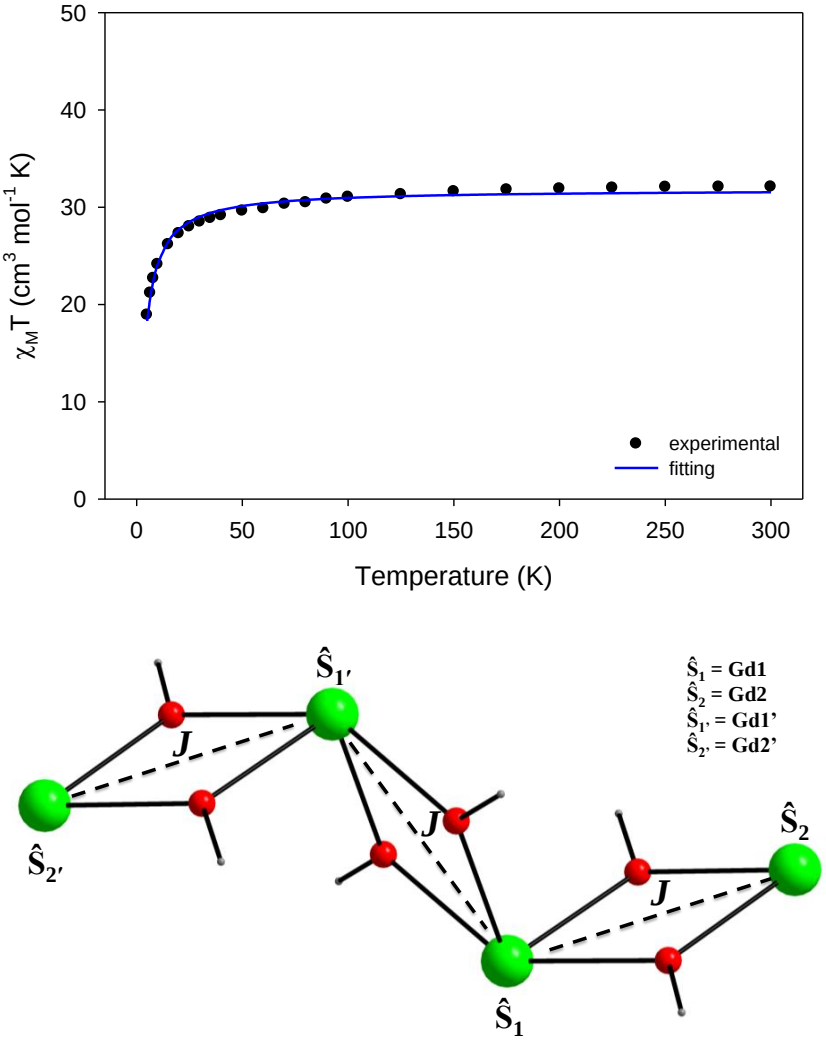

Figure 5.14. (top) Temperature dependence of the $\chi_M T$ for **15**·2MeOH. The blue solid line is the fit of the data; see the text for the fit parameters. (bottom) The fitting model used to simulate the experimental magnetic data.

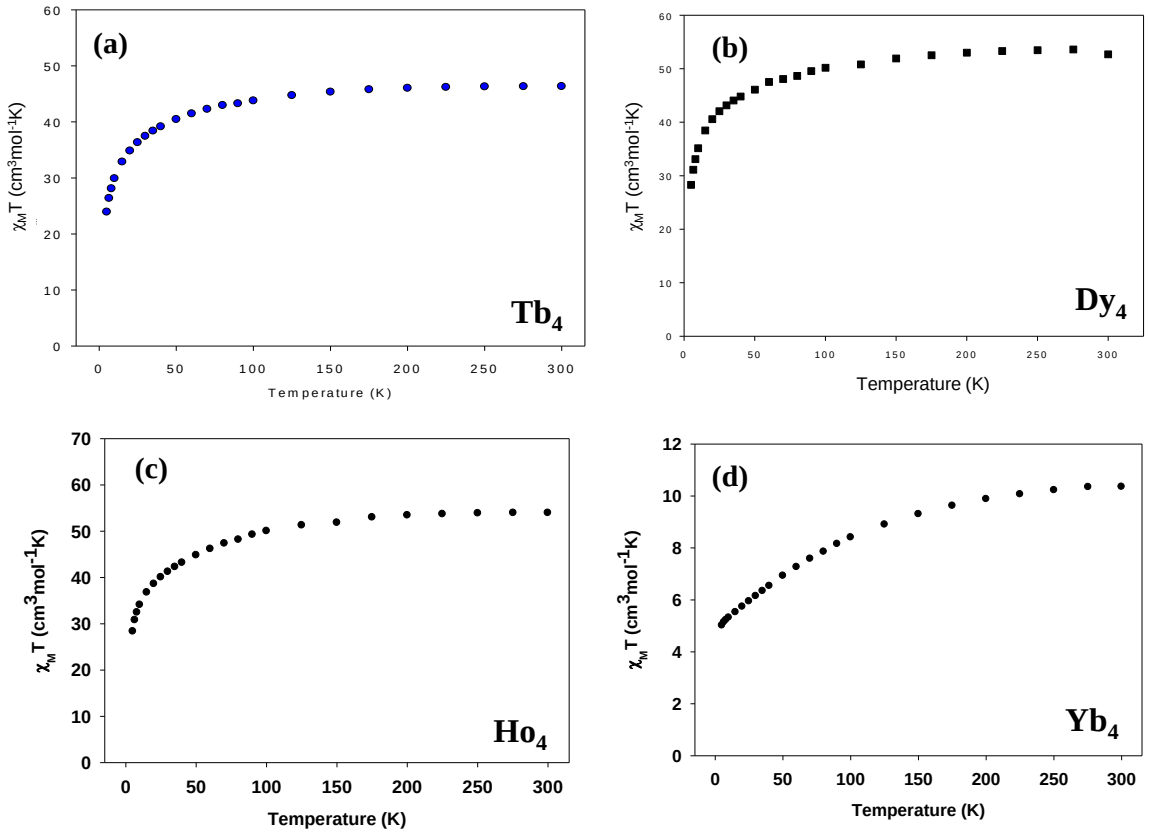

Figure 5.15. Plots of $\chi_M T$ *vs. T* for complexes **16**·2MeOH (a), **17** (b), **18** (c), and **20** (d).

For the isotropic Gd^{III}_4 (**15**·2MeOH) complex, the $\chi_M T$ product remains almost constant at a value of ~31.4 cm^3Kmol^{-1} from 300 K to ~100 K and then steadily decreases to a minimum value of 18.31 cm^3Kmol^{-1} at 5.0 K (Figure 5.14). This is indicative of the presence of intramolecular antiferromagnetic exchange interactions between the four Gd^{III} centers and/or zero-field splitting effects.[159,160] The temperature independent behavior (300-100 K) suggests that the coupling between the Gd^{III} ions is very weak as has been seen in many polynuclear Gd^{III} complexes.[156-161] Given the lack of any first order orbital momentum for the Gd^{III} ions, we undertook the challenge to quantify the

strength of the intramolecular magnetic exchange interactions in **15**·2MeOH. The tetranuclear compound was modeled with the spin Hamiltonian shown in Equation 5.3, according to the structural model of Figure 5.14 (bottom).

$$\mathcal{H} = -2J(\hat{S}_1 \cdot \hat{S}_2 + \hat{S}_1 \cdot \hat{S}_{1'} + \hat{S}_{1'} \cdot \hat{S}_{2'}) \quad (5.3)$$

The data were fit using the program MAGMUN[168] by applying a simple 1-*J* model. The fit (solid blue line in Figure 5.14, top) gave fit parameter values of J = -0.09(1) cm^{-1} and g = 2.00(1), in excellent agreement with the J values reported for antiferromagnetically coupled Gd^{III}_4 clusters of similar or slightly different metal topologies.[158-160] A fit of the data to a 2-*J* model ($J_{11'} \neq J_{12}$ with $J_{12} = J_{1'2'}$ due to the molecular symmetry) gave results of comparable quality but these might lead to overparametarization problems and have thus been ignored.

For the anisotropic Tb^{III}_4 (**16**·2MeOH), Dy^{III}_4 (**17**) and Ho^{III}_4 (**18**) complexes, the thermal evolution of the magnetic susceptibility is very similar (Figure 5.15), in which the $\chi_M T$ product remains constant at a value of ~46.3 (**16**), ~53.5 (**17**) and ~53.0 (**18**) cm^3Kmol^{-1} from 300 K to ~150 K and then steadily decreases to a minimum value of 23.88 (**16**), 28.75 (**17**) and 28.33 (**18**) cm^3Kmol^{-1} at 5.0 K. Such low temperature decrease of the $\chi_M T$ product is mainly due to the depopulation of the excited Stark sublevels of the Ln^{III} ions and the probable weak antiferromagnetic interactions between the metal centers which unfortunately cannot be quantified due to the strong orbital momentum of these Ln^{III} ions. For the Yb^{III}_4 (**20**) complex, the $\chi_M T$ product starts to decrease steadily from a

value of 10.35 cm^3Kmol^{-1} at 300 K to a minimum value of 5.01 cm^3Kmol^{-1} at 5.0 K (Figure 5.15d). Such gradual decrease upon cooling can be ascribed to the thermal depopulation of the ligand field levels.[46] These ligand field levels result from the crystal field created in the first approximation by point charges in the coordination sphere of the lanthanide and constitute linear combinations of M_J's components of the total kinetic moment and depend on the site symmetry.[46,85]

The field dependence of magnetization studies at low temperatures does not show any irregular features for all complexes other than the expected ones for polynuclear, weakly coupled lanthanide(III) clusters. Briefly, the lack of true saturation in magnetization of complexes **16**, **17**, **18**, and **20** indicates the presence of some magnetic anisotropy and/or population of low-lying excited states.[156-161] In the case of isotropic complex **15**, the magnetization almost reaches a saturation of 28.0 μ_B at the highest fields, which is in good agreement with the expected value for four non-coupled Gd^{III} ions (7.0 μ_B per Gd^{III}). This further supports the weak nature of the magnetic exchange interactions between the Gd^{III} centers so that the antiferromagnetic interactions are easily overcome by the external field.[174] The slight deviation of *M vs. H*/*T* for **15** at different low temperatures (<10 K) and small magnetic fields (0.1-1.0 T) is due to the population of low-lying excited states with *S* larger than the ground state (Figure 5.16, top). This is also supported by the continuous decrease of the in-phase, $\chi'_M T$, product as the temperature decreases down to 1.8 K (Figure 5.16, bottom).

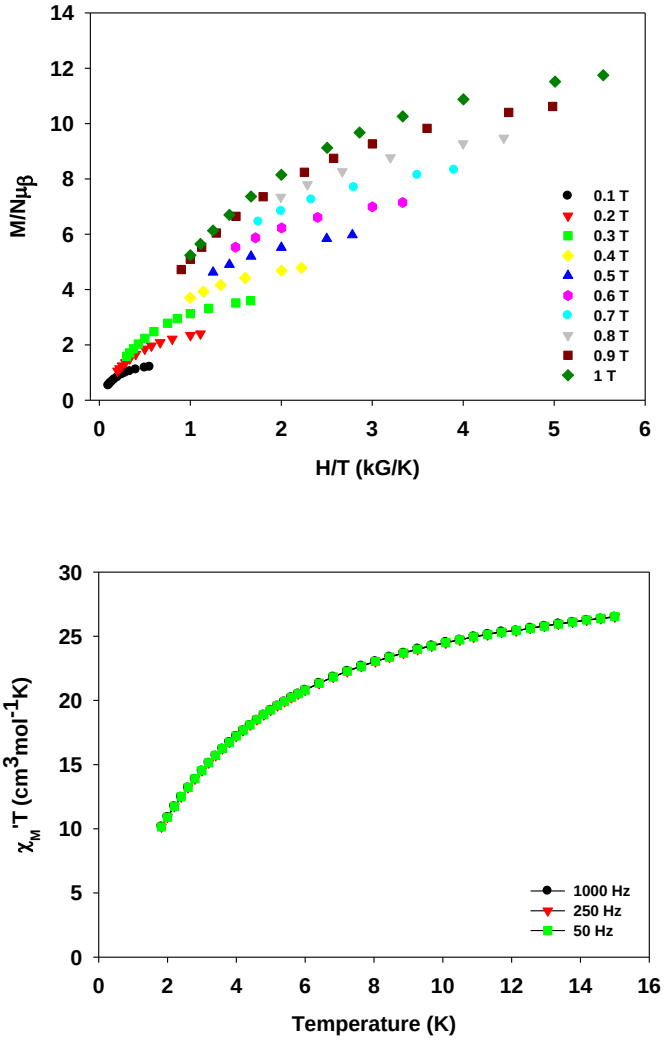

Figure 5.16. (top) Plot of reduced magnetization ($M/N\mu_B$) *vs.* H/T for complex **15** at different low fields and temperatures. (bottom) The in-phase (χ'_M) (as $\chi'_M T$) *vs.* T *ac* susceptibility signals for **15** in a 3.5 G field oscillating at the indicated frequencies.

In the light of the conclusions deduced by the static magnetic measurements on all Ln^{III}_4 compounds, alternating current (*ac*) magnetic susceptibility studies have been also carried out in order to investigate the magnetization dynamics of the anisotropic Tb^{III}_4 (**16**), Dy^{III}_4 (**17**), Ho^{III}_4 (**18**) and Yb^{III}_4 (**20**) clusters under a zero *dc* magnetic field. *Ac*

studies were performed in the 1.8-15 K range using a 3.5 G *ac* field oscillating at frequencies in the 50-1000 Hz range. If the barrier to magnetization relaxation is significant compared to thermal energy (*kT*), then there is a non-zero χ''_M signal which will be also frequency-dependent. Such frequency-dependent χ''_M signals are indicative of the superparamagnetic-like properties of a SMM (but they do not prove the presence of a SMM[169]). For fast relaxing SMMs only the tails of peak maxima can be detected; this is usually the case for high-nuclearity lanthanide SMMs.

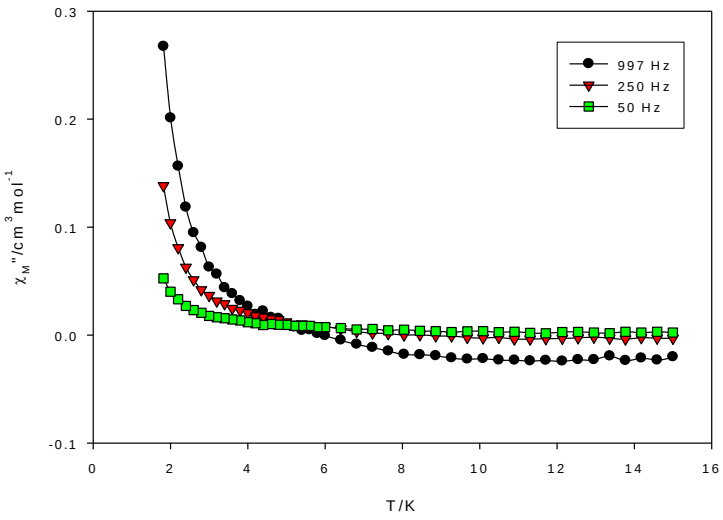

Figure 5.17. The out-of-phase (χ''_M) *vs T ac* susceptibility signals for **17** in a 3.5 G field oscillating at the indicated frequencies. The decrease in the χ''_M signal in the 6-15 K range at 997 Hz is an instrumentation artifact.[169]

Complex **17** is the only member of this family of tetranuclear clusters which shows frequency-dependent out-of-phase χ''_M tails of signals at temperatures below ~5 K

(Figure 5.17), indicative of the slow magnetization relaxation of an SMM with a small energy barrier for magnetization reversal. Such behavior most likely arises from predominant single-ion effects of the individual Dy^{III} centers within **17**.[156-161] There were no out-of-phase *ac* signals down to 1.8 K for the remaining compounds (Figure 5.18). Thus, it can be tentatively seen that while **17** shows slow magnetization relaxation, the isostructural complex **16** does not. This difference most likely originates from the fact that Dy^{III} is a Kramer's ion, and irrespective of the ligand field it is expected to possess a bistable ground state. On the other hand, Tb^{III} is a non-Kramer's ion and so its complexes will have a bistable ground state only if it has an axially-symmetric ligand field.[161d] Efforts to obtain more relaxation data and observe maxima by applying an external *dc* field led only to a slight enhancement of the out-of-phase signal without improving the chances to calculate an effective energy barrier.

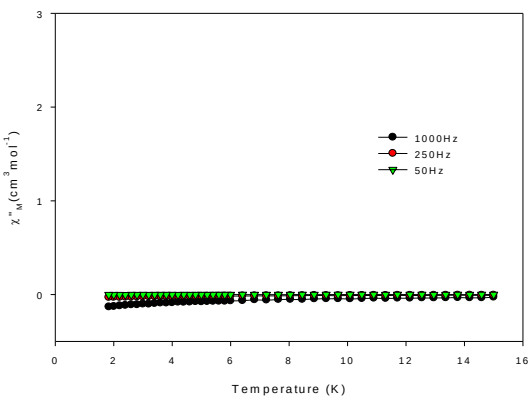

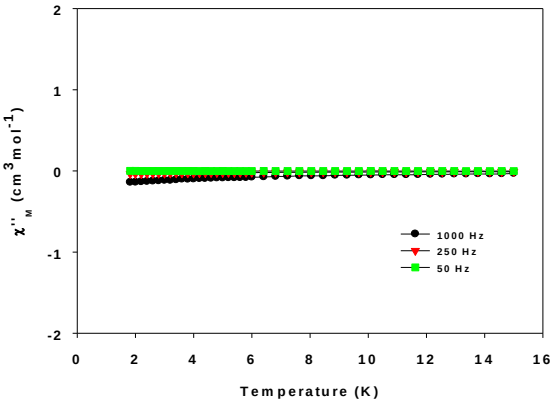

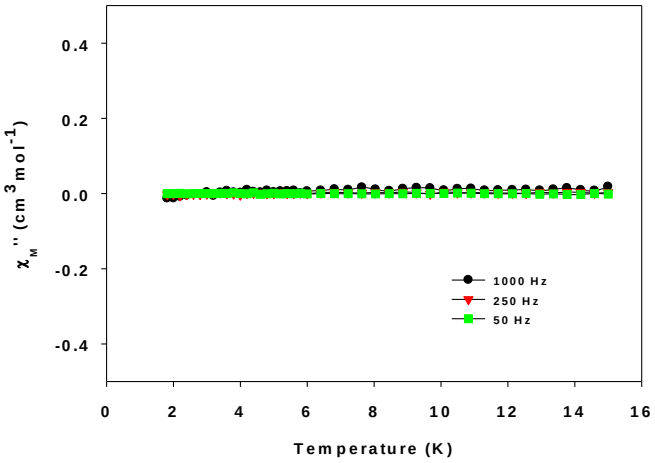

Figure 5.18. The out-of-phase (χ''_M) *vs. T ac* susceptibility signals for **16** (top, left), **18** (top, right), and **20** (bottom) in a 3.5 G field oscillating at the indicated frequencies.

5.2.5. Photoluminescence Studies

In order to gain any possible access into additional physical properties for these families of Ln_8 and Ln_4 complexes, we decided to perform PL studies on all analogues in the solid-state and at room temperature. Ln^{3+} metal complexes have shown to exhibit very characteristic sharp, intense, and narrow bands in their metal-centred emission spectra due to an efficient energy-transfer 'sensitization' of the metal's excited levels from the organic ligand's triplet (or occasionally singlet) state.[170] In contrast, quenching of Ln emission is relatively rare, resulting in the observation of either no emission at all or rarely a ligand-centred emission which is broad and weak. Reasons for such quenching vary and include structural parameters, such as the coordination of aqua ligands and the presence of lattice solvents and counterions in the crystal,[170] the temperature, as well as the location of the lowest triplet state of the ligand.[170]

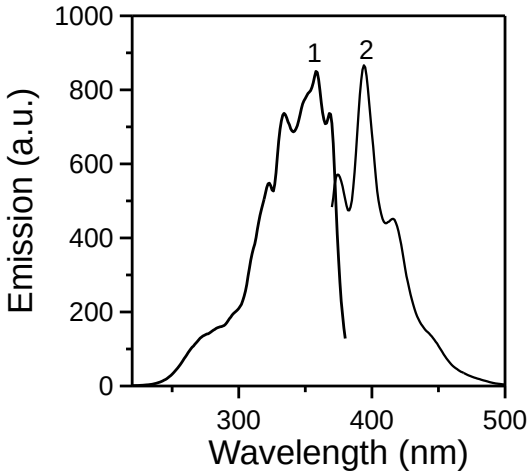
Emission (a.u.)
Wavelength (nm)
1
2

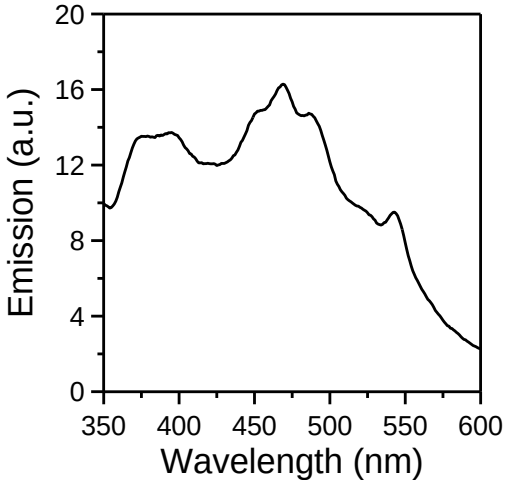
Emission (a.u.)
Wavelength (nm)

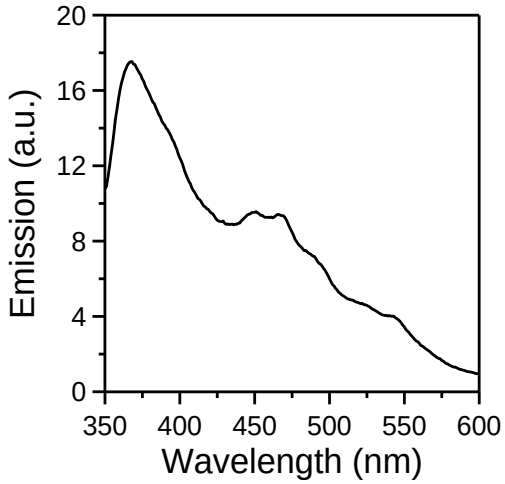
Emission (a.u.)
Wavelength (nm)

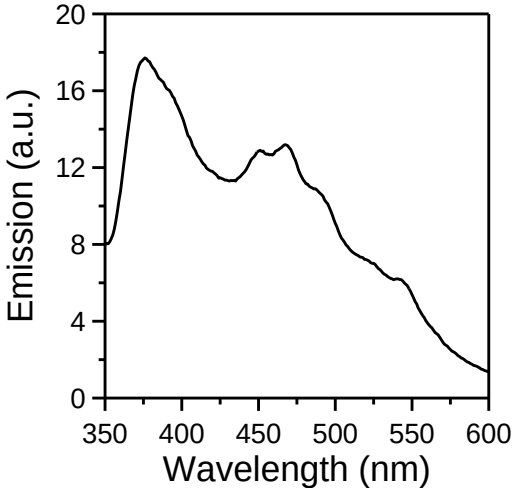
Emission (a.u.)
Wavelength (nm)

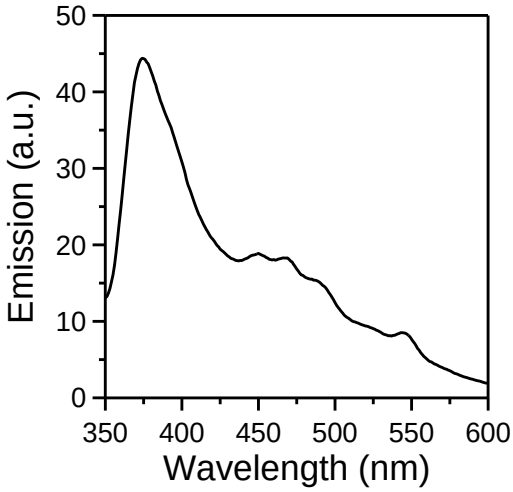
Emission (a.u.)
Wavelength (nm)

Figure 5.19. Excitation (1) and emission (2) spectra of solid ndH_2 (top), and emission spectra of complexes **10** (middle, left), **11** (middle, right), **12** (bottom, left), and **13** (bottom, right) at room temperature.

Undoubtedly, the free ligand ndH_2 is a promising 'antenna' group; upon maximum excitation at 355 nm it shows a strong emission in the 380-450 nm range with a near-UV maximum at 394 nm (Figure 5.19, top), characteristic of the naphthalene functional group.[171] Such behavior offers a strong potential for successful energy transfer to the lanthanide's excited states and consequently to a strong metal-based luminescence with small Stokes' shifts. However, none of the Ln_8 complexes **10**-**13** showed the characteristic Ln emissions but instead similar broad and weak emissions in the range 350-600 nm (Figure 5.19, middle and bottom), upon excitation at 320 nm. Such Ln^{3+}-independent luminescence is most likely attributed to a ligand-centered emission occurring through an Ln^{3+}-to-nd^{2-} back energy transfer process. There is no doubt that quenching effects from the coordinated H_2O molecules, the presence of Et_4N^+ counterions and lattice solvents within **10**-**13**, might contribute to the diminishing of the Ln^{3+} emission.

In our following efforts, we decided to perform photoluminescence studies on the Eu^{III}_4 (**14**), Tb^{III}_4 (**16**·2MeOH), and Dy^{III}_4 (**17**) analogues in the solid-state and at room temperature (Figure 5.20). The free ligand $pdmH_2$ does not emit in the solid state or in solution.[172] However, it has been shown[172] that $pdmH_2$ could potentially act as a good "antenna" ligand for the enhancement of luminescence in a Zn^{II}_6 cluster. The origin of

emission in that Zn^{II}_6 compound is still uncertain due to the co-presence of aromatic benzoate bridging ligands which also affect the resulting optical response.

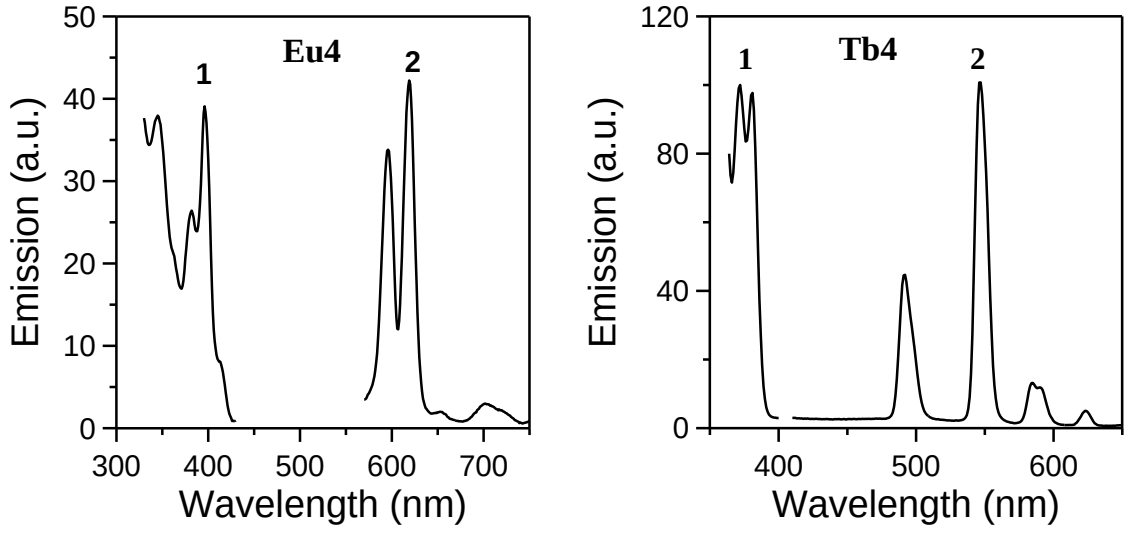

Figure 5.20. Excitation (1) and emission (2) spectra of solid complexes **14** (left) and **16** (right) at room temperature.

The Eu^{III}_4 and Tb^{III}_4 complexes show sharp and narrow emission bands arising from the characteristic $4f \rightarrow 4f$ transitions.[173] However, the Dy^{III}_4 analogue does not display the expected spectrum for a Dy^{III} emission, with the characteristic peaks located at ~480 nm ($^4F_{9/2} \rightarrow {}^6H_{15/2}$) and ~575 nm ($^4F_{9/2} \rightarrow {}^6H_{13/2}$). This is likely due to a significant quenching of the emission intensity for **17** due to paramagnetic effects.[174] Upon maximum excitation at 396 nm, the solid-state emission spectrum of **14** displays relatively strong red photoluminescence, assigned to the characteristic $^5D_0 \rightarrow {}^7F_J$ (J = 0-4) transitions of Eu^{3+}. Specific assignments are as follows: $^5D_0 \rightarrow {}^7F_{0,1}$ (596 nm), $^5D_0 \rightarrow {}^7F_2$ (619 nm), $^5D_0 \rightarrow {}^7F_3$ (655 nm) and $^5D_0 \rightarrow {}^7F_4$ (702 nm).[175] For complex **3**, upon excitation at 380 nm, a

strong green luminescence emission has been obtained which can be ascribed to the characteristic $^5D_4 \rightarrow {}^7F_J$ (J = 3; 623 nm, J = 4; 585 nm, J = 5; 547 nm, J = 6; 492 nm) transitions of Tb^{3+}.[175] In the cases of **14** and **16**, the emission results demonstrate the ability of $pdmH_2$ ligand to act as an efficient "antenna" group by transferring energy to the Ln^{3+} emission states and preventing back-transfer processes from the 4*f*-metal ions, which would otherwise quench or vanish the obtained emission.

5.3. Conclusions and Perspectives

In conclusion, we have tried to bring together molecular magnetism and optics *via* the employment of naphthalene- and pyridine-based diols, ndH_2 and $pdmH_2$, in homometallic lanthanide(III) cluster chemistry. In particular, we were able to isolate a four-member family of octanuclear $(Et_4N)_4[Ln^{III}_8O(nd)_8(NO_3)_{10}(H_2O)_2]$ compounds possessing a "Christmas-star" topology, which is unprecedented in 4*f*-metal cluster chemistry. The Dy^{III}_8 analogue shows slow relaxation of magnetization at low temperatures, whereas all complexes are optically-active with unusual ligand-centered emissions. We are currently trying to improve both the magnetic and optical responses of the reported compounds by combining the Ln^{III}_8 clusters with either paramagnetic and anisotropic 3*d*-metal ions or with efficient for energy-transfer metal ions (i.e., Zn^{II}), respectively.

In addition, we have also reported a seven-membered family of tetranuclear $[Ln^{III}_4(NO_3)_2(pdmH)_6(pdmH_2)_2](NO_3)_4$ complexes with different 4*f*-metal ions and a rare zigzag topology. The Dy^{III}_4 analogue shows slow relaxation of magnetization at low temperatures, whereas the Eu^{III}_4 and Tb^{III}_4 compounds exhibit intense red and green

photoluminescence in the visible region, respectively. The magnetic susceptibility studies of the isotropic Gd^{III}_4 analogue allowed us to quantitatively determine the nature and strength of the magnetic exchange interactions between the four spin carriers, which were found to be antiferromagnetic and very weak (J = -0.09 cm^{-1} for Gd^{III}_4), as is almost always the case in Ln^{3+} complexes due to the radially contracted nature of 4*f* orbitals.[167] We are currently pursuing higher nuclearity 4*f*-metal complexes with the doubly deprotonated form of the $pdmH_2$ ligand and in the presence of various ancillary inorganic groups with bridging affinity, such as N_3^-, NCO^- and CO_3^{2-}. Finally, it is that specific non well-behaved nature of the polyalkoxide ligands which makes (in general) metal cluster chemistry totally unpredictable and one of the most appealing areas of modern coordination chemistry.

5.4. Final Conclusions

In conclusion, we have shown in this thesis that the employment of cyanates in metal cluster chemistry can provide us with compounds structurally and magnetically different than the ones previously reported with the related azides. Very high-nuclearity compounds with large spin ground state values and SMM behaviors can be indeed synthesized when OCN^- groups are utilized in conjunction with various organic chelating/bridging ligands. In addition, we have been able to prove that access to purely inorganic-bridged cluster compounds is indeed possible by utilizing the Me_3SiN_3 precursor under basic conditions. The resulting compounds are all end-on bridged by the azido groups which results in ferromagnetic coupling between the paramagnetic metal

centers and consequently large *S* values and SMM behaviors. This is one of the simplest and most attractive synthetic routes yet in 3*d*-metal cluster chemistry which leads to compounds with an extremely large N_3^--to-metal ratio rendering them suitable candidates for high-energy materials applications. Finally, this thesis provides the reader with some new synthetic directions towards the preparation of hybrid molecular magnetic materials, where the SMM property can be combined with an optical efficiency. Scientists can definitely work with optically inactive transition metal-based SMMs and substitute the non-emissive groups with their fluorescence analogues without preturbing the core structure and magnetization dynamics but instead enhancing the resulting emissions. The type of the targeted emission can also direct our synthetic efforts in terms of metals of choice. Aromatic and polyaromatic organic chelates, such as pyridine alcohols and naphthalene diols, can act as efficient ‘antennas‘ to transfer energy to the emissive states of various lanthanide ions. As a result, and due to the highly paramagnetic and anisotropic nature of many lanthanide ions, new compounds with SMM behaviors and sharp and narrow emissions in the visible region of the electromagnetic spectrum can be made. Based on all these findings, the present thesis may have served to open some new directions in metal cluster chemistry, molecular magnetism and optics.

6. APPENDIX

6.1. Bond Distances and Bond Angles

Table 6.1. Selected interatomic distances and angles for complex **1**

Complex **1**·*x*DMF·*y*H_2O			
Bond lengths			
Mn(1)-O(1)	2.151(6)	Mn(4)-O(9)	1.860(6)
Mn(1)-O(2)	2.176(6)	Mn(4)-O(10)	1.912(6)
Mn(1)-O(4)	2.132(7)	Mn(4)-O(11)	1.959(6)
Mn(1)-O(5)	2.178(8)	Mn(4)-N(10)	2.227(7)
Mn(1)-O(6)	2.306(6)	Mn(5)-O(1)	1.928(6)
Mn(1)-N(1)	2.219(7)	Mn(5)-O(2)	1.958(6)
Mn(2)-O(5')	2.222(8)	Mn(5)-O(9)	1.875(6)
Mn(2)-O(6')	2.634(7)	Mn(5)-O(11)	1.941(6)
Mn(2)-O(10)	2.326(6)	Mn(5)-O(11')	2.468(6)
Mn(2)-N(6)	2.345(8)	Mn(5)-O(12)	2.155(6)
Mn(2)-N(7)	2.149(8)	Mn(6)-O(3')	2.402(6)
Mn(2)-N(8)	2.250(7)	Mn(6)-O(7')	1.887(6)
Mn(2)-N(9)	2.411(7)	Mn(6)-O(11)	1.906(6)

Mn(3)-O(3)	1.911(6)	Mn(6)-O(13)	2.205(6)
Mn(3)-O(8)	1.857(6)	Mn(6)-O(14)	1.946(6)
Mn(3)-O(9)	1.896(6)	Mn(6)-O(15)	1.969(6)
Mn(3)-O(15')	2.214(6)	Mn(7)-O(14)	2.183(6)
Mn(3)-N(2)	2.215(8)	Mn(7)-O(16)	2.147(7)
Mn(3)-N(5)	2.076(7)	Mn(7)-O(17)	2.350(1)
Mn(4)-O(2')	2.280(5)	Mn(7)-O(18)	2.227(1)
Mn(4)-O(6')	1.913(6)	Mn(7)-N(11)	2.239(8)
Bond angles			
Mn(1)-O(1)-Mn(5)	103.8(3)	Mn(4)-O(11)-Mn(5)	92.9(2)
Mn(1)-O(2)-Mn(4')	93.6(2)	Mn(4)-O(11)-Mn(5')	95.4(2)
Mn(1)-O(2)-Mn(5)	101.8(2)	Mn(4)-O(11)-Mn(6)	124.6(3)
Mn(1)-O(5)-Mn(2')	103.8(4)	Mn(5)-O(2)-Mn(4')	101.6(3)
Mn(1)-O(6)-Mn(4')	100.3(2)	Mn(5)-O(11)-Mn(5')	98.5(2)
Mn(2)-O(10)-Mn(4)	110.5(2)	Mn(5)-O(11)-Mn(6)	124.6(3)
Mn(3)-O(3)-Mn(6')	99.3(2)	Mn(6)-O(11)-Mn(5')	114.3(2)
Mn(3)-O(9)-Mn(4)	123.3(3)	Mn(6)-O(14)-Mn(7)	122.4(3)
Mn(3)-O(9)-Mn(5)	129.3(3)	Mn(6)-O(15)-Mn(3')	104.2(3)
Mn(4)-O(9)-Mn(5)	98.4(3)		

Table 6.2. Selected interatomic distances and angles for complex **2**

Complex **2**·*x*(solv)			
Bond lengths			
Mn(1)-O(2)	2.233(3)	Mn(4)-N(7)	2.353(4)
Mn(1)-O(5)	2.294(3)	Mn(5)-O(1)	1.854(3)
Mn(1)-O(6)	2.240(3)	Mn(5)-O(2)	1.883(3)
Mn(1)-O(20)	2.222(4)	Mn(5)-O(3)	1.909(3)
Mn(1)-N(1)	2.324(4)	Mn(5)-O(4)	2.026(3)
Mn(1)-N(2)	2.293(4)	Mn(5)-O(6)	2.059(3)
Mn(1)-N(3)	2.283(4)	Mn(6)-O(1)	2.211(3)
Mn(2)-O(5)	2.256(3)	Mn(6)-O(2)	1.884(3)
Mn(2)-O(9)	2.096(4)	Mn(6)-O(7)	1.901(3)
Mn(2)-O(19)	2.267(3)	Mn(6)-O(15)	1.906(4)
Mn(2)-O(20)	2.134(4)	Mn(6)-O(17)	2.013(4)
Mn(2)-Cl(1)	2.423(0)	Mn(6)-O(18)	2.174(4)
Mn(3)-O(2)	2.211(3)	Mn(7)-O(5)	1.755(3)
Mn(3)-O(4)	2.234(3)	Mn(7)-O(8)	1.904(3)
Mn(3)-O(5)	2.293(3)	Mn(7)-O(10)	1.951(3)
Mn(3)-O(19)	2.495(3)	Mn(7)-O(16)	1.895(3)
Mn(3)-N(10)	2.314(4)	Mn(7)-N(4)	1.999(4)
Mn(3)-N(11)	2.285(4)	Mn(7)-N(5)	2.028(4)
Mn(3)-N(12)	2.367(4)	Mn(8)-O(1)	1.809(3)
Mn(4)-O(3)	2.289(3)	Mn(8)-O(3)	1.836(3)

Mn(4)-O(3')	2.337(3)	Mn(8)-O(11')	1.948(3)
Mn(4)-O(4)	2.205(3)	Mn(8)-O(13')	1.910(3)
Mn(4)-O(6')	2.176(3)	Mn(8)-O(14)	1.916(3)
Mn(4)-N(8)	2.210(4)	Mn(8)-N(6')	2.117(4)
Mn(4)-N(9)	2.313(4)		
Bond angles			
Mn(1)-O(2)-Mn(5)	95.9(2)	Mn(3)-O(2)-Mn(6)	123.6(6)
Mn(1)-O(2)-Mn(6)	122.6(0)	Mn(3)-O(5)-Mn(7)	120.4(8)
Mn(1)-O(5)-Mn(3)	103.1(3)	Mn(4)-O(3)-Mn(4')	107.0(2)
Mn(1)-O(5)-Mn(7)	120.6(2)	Mn(4)-O(3)-Mn(5)	93.2(9)
Mn(1)-O(6)-Mn(4')	159.5(0)	Mn(4)-O(3)-Mn(8)	127.2(4)
Mn(1)-O(6)-Mn(5)	90.8(9)	Mn(5)-O(2)-Mn(6)	101.0(1)
Mn(1)-O(20)-Mn(2)	98.8(3)	Mn(5)-O(3)-Mn(4')	92.9(5)
Mn(2)-O(5)-Mn(3)	95.9(1)	Mn(5)-O(3)-Mn(8)	93.7(0)
Mn(2)-O(5)-Mn(7)	117.7(1)	Mn(5)-O(6)-Mn(4')	93.8(2)
Mn(2)-O(19)-Mn(3)	90.2(6)	Mn(8)-O(3)-Mn(4')	124.7(4)
Mn(3)-O(2)-Mn(5)	96.5(6)		
Torsion angles			
Mn(1)-N(1)-O(7)-Mn(6)	20.4(4)	Mn(4)-N(7)-O(14)-Mn(8)	3.5(4)
Mn(1-N(3)-O(8)-Mn(7)	9.5(4)	Mn(4)-N(9)-O(13)-Mn(8')	15.5(4)
Mn(3)-N(10)-O(16)-Mn(7)	12.1(4)	Mn(7)-N(4)-O(9)-Mn(2)	11.0(5)
Mn(3)-N(12)-O(15)-Mn(6)	11.1(4)	Mn(8)-N(6)-O(10)-Mn(7)	5.7(2)

Table 6.3. Selected interatomic distances and angles for complex **3**

Complex **3**			
Bond lengths			
Mn(1)-O(1)	2.252(8)	Mn(9)-O(14)	2.274(8)
Mn(1)-O(2)	2.268(8)	Mn(9)-O(141)	2.293(8)
Mn(1)-O(11)	2.091(11)	Mn(10)-O(6)	2.112(7)
Mn(1)-O(12)	2.107(10)	Mn(10)-O(8)	1.920(7)
Mn(1)-O(13)	2.169(10)	Mn(10)-O(14)	1.992(8)
Mn(1)-N(11)	2.31(3)	Mn(10)-O(23)	1.902(7)
Mn(2)-O(1)	1.909(8)	Mn(10)-O(162)	2.042(8)
Mn(2)-O(11)	1.943(11)	Mn(10)-O(171)	2.119(8)
Mn(2)-O(21)	1.933(9)	Mn(11)-O(7)	1.943(7)
Mn(2)-O(81)	1.934(10)	Mn(11)-O(8)	1.987(7)
Mn(2)-O(91)	2.152(11)	Mn(11)-O(14)	2.211(8)
Mn(2)-O(202)	2.35(2)	Mn(11)-O(33)	1.921(7)
Mn(3)-O(2)	1.919(8)	Mn(11)-O(181)	2.237(8)
Mn(3)-O(12)	1.901(10)	Mn(11)-N(61)	1.973(10)
Mn(3)-O(31)	1.917(8)	Mn(12)-O(7)	1.877(7)
Mn(3)-O(102)	2.126(9)	Mn(12)-O(9)	1.936(7)
Mn(3)-O(111)	1.971(9)	Mn(12)-O(41)	1.906(8)
Mn(3)-O(112)	2.511(10)	Mn(12)-O(132)	1.941(8)
Mn(4)-O(1)	1.936(8)	Mn(12)-O(182)	2.114(8)
Mn(4)-O(2)	1.970(7)	Mn(13)-O(8)	1.892(7)

Mn(4)-O(3)	2.060(9)	Mn(13)-O(42)	1.876(8)
Mn(4)-O(4)	1.889(7)	Mn(13)-O(162)	2.58(3)
Mn(4)-O(5)	1.891(7)	Mn(13)-O(172)	1.921(8)
Mn(4)-O(201)	2.113(11)	Mn(13)-O(191)	2.163(8)
Mn(5)-O(1)	1.988(8)	Mn(13)-N(71)	1.975(10)
Mn(5)-O(3)	1.868(8)	Mn(14)-O(6)	2.297(7)
Mn(5)-O(13)	2.212(9)	Mn(14)-O(7)	2.428(7)
Mn(5)-O(22)	2.097(8)	Mn(14)-O(8)	2.403(7)
Mn(5)-O(92)	1.930(10)	Mn(14)-O(41)	2.120(8)
Mn(5)-O(121)	1.979(9)	Mn(14)-O(42)	2.156(8)
Mn(6)-O(2)	1.951(8)	Mn(14)-O(43)	2.123(7)
Mn(6)-O(3)	1.860(8)	Mn(14)-N(41)	2.452(9)
Mn(6)-O(13)	2.281(9)	Mn(15)-O(6)	1.864(7)
Mn(6)-O(32)	2.135(8)	Mn(15)-O(10)	1.938(7)
Mn(6)-O(101)	1.941(9)	Mn(15)-O(43)	1.886(8)
Mn(6)-O(122)	1.977(9)	Mn(15)-O(142)	2.325(9)
Mn(7)-O(4)	1.884(7)	Mn(15)-O(151)	1.922(7)
Mn(7)-O(10)	1.924(7)	Mn(15)-O(161)	2.224(8)
Mn(7)-O(21)	2.243(8)	Na(1)-O(5)	2.508(9)
Mn(7)-O(22)	1.910(8)	Na(1)-O(9)	2.571(9)
Mn(7)-O(23)	2.213(7)	Na(1)-O(31)	2.84(3)
Mn(7)-N(21)	2.087(9)	Na(1)-O(112)	2.25(3)
Mn(8)-O(5)	1.883(7)	Na(1)-O(131)	2.669(9)

Mn(8)-O(9)	1.958(8)	Na(1)-O(141)	2.397(3)
Mn(8)-O(31)	2.231(8)	Na(1)-O(201)	2.381(3)
Mn(8)-O(32)	1.901(8)	Na(2)-O(10)	2.296(3)
Mn(8)-O(33)	2.195(8)	Na(2)-O(15B)	2.631(3)
Mn(8)-N(31)	2.068(9)	Na(2)-O(21)	2.527(3)
Mn(9)-O(4)	1.912(7)	Na(2)-O(82)	2.297(3)
Mn(9)-O(5)	1.901(7)	Na(2)-O(142)	2.577(3)
Mn(9)-O(6)	1.898(7)	Na(2)-O(202)	2.21(3)
Mn(9)-O(7)	1.945(7)		

Bond angles

Mn(1)-O(1)-Mn(2)	101.7(3)	Mn(8)-O(9)-Mn(12)	128.6(4)
Mn(1)-O(1)-Mn(4)	93.1(3)	Mn(9)-O(5)-Na(1)	92.5(3)
Mn(1)-O(1)-Mn(5)	102.1(3)	Mn(9)-O(6)-Mn(10)	100.9(3)
Mn(1)-O(2)-Mn(3)	100.1(3)	Mn(9)-O(6)-Mn(14)	103.0(3)
Mn(1)-O(2)-Mn(4)	91.7(3)	Mn(9)-O(6)-Mn(15)	124.5(4)
Mn(1)-O(2)-Mn(6)	103.9(3)	Mn(9)-O(7)-Mn(11)	108.1(3)
Mn(2)-O(1)-Mn(4)	131.8(4)	Mn(9)-O(7)-Mn(12)	117.8(4)
Mn(2)-O(1)-Mn(5)	122.0(4)	Mn(9)-O(7)-Mn(14)	97.1(3)
Mn(3)-O(2)-Mn(4)	133.4(4)	Mn(9)-O(14)-Mn(10)	92.8(2)
Mn(3)-O(2)-Mn(6)	120.8(4)	Mn(9)-O(14)-Mn(11)	89.1(3)
Mn(4)-O(1)-Mn(5)	98.5(3)	Mn(10)-O(6)-Mn(14)	97.7(3)
Mn(4)-O(2)-Mn(6)	99.1(4)	Mn(10)-O(6)-Mn(15)	124.0(4)
Mn(4)-O(3)-Mn(5)	98.3(4)	Mn(10)-O(8)-Mn(11)	105.3(3)

Mn(4)-O(3)-Mn(6)	99.0(4)	Mn(10)-O(8)-Mn(13)	110.6(3)
Mn(4)-O(4)-Mn(7)	129.8(4)	Mn(10)-O(8)-Mn(14)	99.8(3)
Mn(4)-O(4)-Mn(9)	96.8(3)	Mn(10)-O(14)-Mn(11)	95.1(2)
Mn(4)-O(5)-Na(1)	97.9(3)	Mn(11)-O(7)-Mn(12)	126.8(4)
Mn(4)-O(5)-Mn(8)	131.6(4)	Mn(11)-O(7)-Mn(14)	100.5(3)
Mn(4)-O(5)-Mn(9)	97.1(3)	Mn(11)-O(8)-Mn(13)	135.2(4)
Mn(5)-O(3)-Mn(6)	106.3(4)	Mn(11)-O(8)-Mn(14)	100.0(3)
Mn(7)-O(4)-Mn(9)	124.5(4)	Mn(12)-O(7)-Mn(14)	99.0(3)
Mn(7)-O(10)-Na(2)	100.9(3)	Mn(12)-O(9)-Na(1)	99.3(3)
Mn(7)-O(10)-Mn(15)	129.0(4)	Mn(13)-O(8)-Mn(14)	99.4(3)
Mn(8)-O(5)-Mn(9)	125.2(4)	Mn(14)-O(6)-Mn(15)	101.4(3)
Mn(8)-O(5)-Na(1)	92.6(3)	Mn(15)-O(10)-Na(2)	105.2(3)
Mn(8)-O(9)-Na(1)	88.9(3)		

Table 6.4. Selected interatomic distances and angles for complex **4**

Complex **4**			
Bond lengths			
Co(1)-N(1)	2.105(4)	Co(3)-N(7)	2.207(4)
Co(1)-N(4)	2.180(4)	Co(3)-N(10)	2.103(4)
Co(1)-N(13')	2.084(4)	Co(3)-N(13)	2.088(4)
Co(1)-N(16')	2.207(4)	Co(3)-N(16)	2.171(4)

Co(1)-N(19)	2.116(5)	Co(3)-N(23)	2.107(4)
Co(1)-N(20)	2.102(5)	Co(3)-N(24)	2.106(5)
Co(2)-N(1)	2.084(4)	Co(4)-N(4)	2.144(4)
Co(2)-N(4)	2.228(4)	Co(4)-N(4')	2.144(4)
Co(2)-N(7)	2.162(4)	Co(4)-N(7)	2.150(4)
Co(2)-N(10)	2.092(4)	Co(4)-N(4')	2.144(4)
Co(2)-N(21)	2.120(5)	Co(4)-N(7')	2.150(4)
Co(2)-N(22)	2.109(5)	Co(4)-N(16')	2.140(4)
Bond angles			
Co(1)-N(1)-Co(3)	103.01(2)	Co(2)-N(10)-Co(3)	101.97(2)
Co(1)-N(4)-Co(2)	96.11(2)	Co(3)-N(7)-Co(4)	96.61(2)
Co(1)-N(4)-Co(4)	97.65(1)	Co(3)-N(13)-Co(1')	101.42(2)
Co(2)-N(4)-Co(4)	96.12(2)	Co(3)-N(16)-Co(1')	95.03(2)
Co(2)-N(7)-Co(3)	96.48(1)	Co(3)-N(16)-Co(4)	98.01(2)
Co(2)-N(7)-Co(4)	97.91(2)	Co(4)-N(16)-Co(1')	96.95(1)

Table 6.5. Selected interatomic distances and angles for complex **5**

Complex **5**			
Bond lengths			
Ni(1)-N(4')	2.115(3)	Ni(3)-N(1)	2.156(3)
Ni(1)-N(10)	2.106(3)	Ni(3)-N(7)	2.083(4)

Ni(1)-N(10')	2.106(3)	Ni(3)-N(10)	2.134(3)
Ni(2)-N(1)	2.139(3)	Ni(3)-N(13)	2.071(4)
Ni(2)-N(4')	2.157(3)	Ni(3)-N(21)	2.050(4)
Ni(2)-N(7)	2.073(4)	Ni(3)-N(22)	2.059(4)
Ni(2)-N(16')	2.073(4)	Ni(4)-N(4)	2.160(3)
Ni(2)-N(19)	2.062(5)	Ni(4)-N(10)	2.150(4)
Ni(2)-N(20)	2.044(4)	Ni(4)-N(13)	2.067(4)
Ni(1)-N(4')	2.115(3)	Ni(4)-N(16)	2.077(4)
Ni(1)-N(10)	2.106(3)	Ni(4)-N(23)	2.055(4)
Ni(1)-N(10')	2.106(3)	Ni(4)-N(24)	2.045(4)
Bond angles			
Ni(1)-N(1)-Ni(2)	97.98(1)	Ni(2)-N(1)-Ni(3)	97.02(1)
Ni(1)-N(1)-Ni(3)	97.43(1)	Ni(2)-N(7)-Ni(3)	101.47(2)
Ni(1)-N(4)-Ni(2')	97.20(1)	Ni(3)-N(10)-Ni(4)	95.95(1)
Ni(1)-N(4)-Ni(4)	97.54(1)	Ni(3)-N(13)-Ni(4)	100.55(2)
Ni(1)-N(10)-Ni(3)	98.15(1)	Ni(4)-N(4)-Ni(2')	96.68(1)
Ni(1)-N(10)-Ni(4)	98.13(1)	Ni(4)-N(16)-Ni(2')	102.01(2)

Table 6.6. Selected interatomic distances and angles for complex **6**

Complex **6**			
Bond lengths			
Fe(1)-N(1)	2.161(4)	Fe(2)-N(11)	2.121(3)

Fe(1)-N(1′)	2.161(4)	Fe(2)-N(14)	2.081(3)
Fe(1)-N(2)	2.157(3)	Fe(2)-N(17)	2.115(3)
Fe(1)-N(2′)	2.157(3)	Fe(3)-N(8)	2.176(3)
Fe(1)-N(5)	2.179(3)	Fe(3)-N(8″)	2.176(3)
Fe(1)-N(5′)	2.179(3)	Fe(3)-N(14)	2.170(3)
Fe(2)-N(2)	2.060(3)	Fe(3)-N(14″)	2.170(3)
Fe(2)-N(5)	2.065(3)	Fe(3)-N(20)	2.160(4)
Fe(2)-N(8)	2.049(3)	Fe(3)-N(20″)	2.160(4)
Bond angles			
Fe(1)-N(2)-Fe(2)	104.9(1)	Fe(2)-N(11)-Fe(2‴)	106.3(2)
Fe(1)-N(5)-Fe(2)	103.9(2)	Fe(2)-N(14)-Fe(3)	102.5(2)
Fe(2)-N(8)-Fe(3)	103.4(2)	Fe(2)-N(17)-Fe(2‴)	106.7(2)

Table 6.7. Selected interatomic distances for complex **7**

Complex **7**			
Intermetallic distances			
Mn(1)···Mn(2)	3.2259(6)	Mn(2)···Mn(3)	3.2189(5)
Mn(1)···Mn(3)	3.2175(8)		
Bond lengths			
Mn(1)-O(1)	1.887(3)	Mn(2)-O(8)	2.195(3)
Mn(1)-O(3)	1.936(3)	Mn(2)-N(3)	2.024(4)
Mn(1)-O(4)	2.204(4)	Mn(2)-N(4)	2.058(4)
Mn(1)-O(9)	2.158(3)	Mn(3)-O(1)	1.894(3)

Mn(1)-N(1)	2.017(4)	Mn(3)-O(5)	1.929(4)
Mn(1)-N(6)	2.052(4)	Mn(3)-O(6)	2.184(3)
Mn(2)-O(1)	1.878(3)	Mn(3)-O(10)	2.186(3)
Mn(2)-O(2)	2.235(3)	Mn(3)-N(2)	2.010(4)
Mn(2)-O(7)	1.953(3)	Mn(3)-N(5)	2.055(4)
Bond angles			
Mn(1)-O(1)-Mn(2)	117.92(2)	Mn(2)-O(1)-Mn(3)	117.20(2)
Mn(1)-O(1)-Mn(3)	116.64(2)		
Torsion angles			
Mn(1)-N(1)-O(10)-Mn(3)	11.677(3)	Mn(3)-N(2)-O(8)-Mn(2)	11.741(3)
Mn(2)-N(3)-O(9)-Mn(1)	14.533(3)		

Table 6.8. Selected interatomic distances and angles for complex **8**

Complex **8**	
Intermetallic distances	
Mn(1)···Mn(1')	3.211(2)
Bond lengths	
Mn(1)-O(2)	1.937(5)
Mn(1)-O(3)	2.147(5)
Mn(1)-O(4)	1.875(2)
Mn(1)-N(1)	2.030(5)

Mn(1)-N(2)	2.021(6)
Bond angles	
Mn(1)-O(4)-Mn(1′)	117.78(1)
Torsion angles	
Mn(1′)-N(2)-O(3)-Mn(1)	11.997(4)

Table 6.9. Selected interatomic distances and angles for complex **12**

Complex **12**			
Intermetallic distances			
Tb(1)···Tb(2)	3.4938(5)	Tb(3)···Tb(6)	3.5765(8)
Tb(1)···Tb(7)	3.5125(4)	Tb(3)···Tb(7)	3.5886(5)
Tb(2)···Tb(3)	3.4754(4)	Tb(4)···Tb(5)	3.5946(4)
Tb(3)···Tb(4)	3.5228(4)	Tb(4)···Tb(6)	3.5964(4)
Bond lengths			
Tb(1)-O(1)	2.264(4)	Tb(4)-O(49)	2.407(4)
Tb(1)-O(5)	2.499(4)	Tb(5)-O(5)	2.407(4)
Tb(1)-O(6)	2.447(3)	Tb(5)-O(6)	2.365(3)
Tb(1)-O(11)	2.436(3)	Tb(5)-O(16)	2.317(4)
Tb(1)-O(12)	2.466(4)	Tb(5)-O(32)	2.303(4)
Tb(1)-O(15)	2.347(4)	Tb(5)-O(39)	2.423(4)
Tb(1)-O(16)	2.338(4)	Tb(5)-O(40)	2.398(6)
Tb(1)-O(46)	2.494(5)	Tb(5)-O(42)	2.459(5)

Tb(1)-O(47)	2.511(4)	Tb(5)-O(43)	2.423(5)
Tb(2)-O(1)	2.309(4)	Tb(6)-O(7)	2.367(3)
Tb(2)-O(2)	2.425(4)	Tb(6)-O(8)	2.381(3)
Tb(2)-O(3)	2.490(5)	Tb(6)-O(24)	2.321(4)
Tb(2)-O(9)	2.438(3)	Tb(6)-O(31)	2.303(4)
Tb(2)-O(10)	2.445(3)	Tb(6)-O(33)	2.434(4)
Tb(2)-O(11)	2.464(4)	Tb(6)-O(34)	2.430(4)
Tb(2)-O(12)	2.409(3)	Tb(6)-O(36)	2.449(4)
Tb(2)-O(13)	2.338(4)	Tb(6)-O(37)	2.431(4)
Tb(2)-O(14)	2.331(4)	Tb(7)-O(9)	2.390(3)
Tb(3)-O(1)	2.253(3)	Tb(7)-O(10)	2.401(4)
Tb(3)-O(7)	2.414(4)	Tb(7)-O(14)	2.337(4)
Tb(3)-O(8)	2.493(3)	Tb(7)-O(23)	2.331(4)
Tb(3)-O(9)	2.453(4)	Tb(7)-O(25)	2.434(5)
Tb(3)-O(10)	2.404(3)	Tb(7)-O(26)	2.426(5)
Tb(3)-O(23)	2.331(4)	Tb(7)-O(28)	2.455(6)
Tb(3)-O(24)	2.321(3)	Tb(7)-O(29)	2.444(6)
Tb(3)-O(45)	2.397(4)	Tb(8)-O(11)	2.384(3)
Tb(4)-O(1)	2.297(4)	Tb(8)-O(12)	2.366(3)
Tb(4)-O(2)	2.725(5)	Tb(8)-O(13)	2.316(4)
Tb(4)-O(5)	2.406(3)	Tb(8)-O(15)	2.310(4)
Tb(4)-O(6)	2.479(3)	Tb(8)-O(17)	2.433(5)
Tb(4)-O(7)	2.536(3)	Tb(8)-O(18)	2.439(5)

Tb(4)-O(8)	2.399(3)	Tb(8)-O(20)	2.423(5)
Tb(4)-O(31)	2.345(4)	Tb(8)-O(21)	2.431(5)
Tb(4)-O(32)	2.338(4)		
Bond angles			
Tb(1)-O(1)-Tb(2)	99.64(1)	Tb(2)-O(11)-Tb(8)	95.56(1)
Tb(1)-O(1)-Tb(3)	134.70(2)	Tb(2)-O(12)-Tb(8)	97.51(1)
Tb(1)-O(1)-Tb(4)	100.72(1)	Tb(2)-O(13)-Tb(8)	100.96(1)
Tb(1)-O(5)-Tb(4)	91.44(1)	Tb(2)-O(14)-Tb(7)	101.08(1)
Tb(1)-O(5)-Tb(5)	94.54(1)	Tb(3)-O(1)-Tb(4)	101.46(1)
Tb(1)-O(6)-Tb(4)	90.97(1)	Tb(3)-O(7)-Tb(4)	90.71(1)
Tb(1)-O(6)-Tb(5)	97.00(1)	Tb(3)-O(7)-Tb(6)	96.84(1)
Tb(1)-O(11)-Tb(2)	90.96(1)	Tb(3)-O(8)-Tb(4)	92.11(1)
Tb(1)-O(11)-Tb(8)	96.54(1)	Tb(3)-O(8)-Tb(6)	94.39(1)
Tb(1)-O(12)-Tb(2)	91.55(1)	Tb(3)-O(9)-Tb(7)	95.62(1)
Tb(1)-O(12)-Tb(8)	96.20(1)	Tb(3)-O(10)-Tb(7)	96.65(1)
Tb(1)-O(15)-Tb(8)	101.14(1)	Tb(3)-O(23)-Tb(7)	100.68(1)
Tb(1)-O(16)-Tb(5)	101.49(1)	Tb(3)-O(24)-Tb(6)	100.81(1)
Tb(2)-O(1)-Tb(3)	99.24(1)	Tb(4)-O(5)-Tb(5)	96.64(1)
Tb(2)-O(1)-Tb(4)	124.84(2)	Tb(4)-O(6)-Tb(5)	95.78(1)
Tb(2)-O(2)-Tb(4)	104.72(1)	Tb(4)-O(7)-Tb(6)	94.30(1)
Tb(2)-O(9)-Tb(3)	90.58(1)	Tb(4)-O(8)-Tb(6)	97.61(1)
Tb(2)-O(9)-Tb(7)	96.57(1)	Tb(4)-O(31)-Tb(6)	101.38(1)
Tb(2)-O(10)-Tb(3)	91.57(1)	Tb(4)-O(32)-Tb(5)	101.55(1)

Tb(2)-O(10)-Tb(7)	96.11(1)

Table 6.10. Selected interatomic distances and angles for complex **16**

Complex **16**			
Intermetallic distances			
Tb(1)···Tb(1')	3.7708(6)	Tb(1)···Tb(2)	3.7506(4)
Tb(2)···Tb(2′)	9.357(9)		
Bond legnths			
Tb(1)-O(1)	2.301(3)	Tb(2)-O(4)	2.275(3)
Tb(1)-O(1')	2.324(3)	Tb(2)-O(5)	2.424(4)
Tb(1)-O(2)	2.454(4)	Tb(2)-O(6)	2.395(4)
Tb(1)-O(3)	2.436(3)	Tb(2)-O(7)	2.301(3)
Tb(1)-O(4)	2.343(3)	Tb(2)-O(8)	2.447(4)
Tb(1)-O(7)	2.295(3)	Tb(2)-O(9)	2.495(4)
Tb(1)-N(1)	2.529(4)	Tb(2)-N(3)	2.542(4)
Tb(1)-N(2)	2.530(4)	Tb(2)-N(4)	2.491(4)
Bond angles			
Tb(1)-O(1)-Tb(1′)	109.3(1)	Tb(1)-O(7)-Tb(2)	109.4(1)
Tb(1)-O(4)-Tb(2)	108.6(1)		

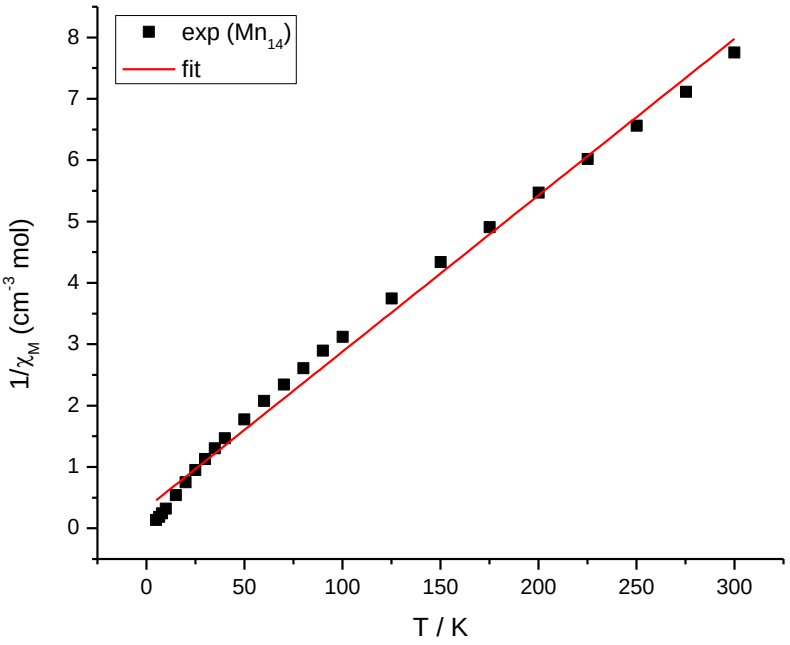

Figure 6.1. Plot of $1/\chi_M$ *vs.* *T* for complex **1**·DMF; the red thick line represents the fitting of the data to the Curie-Weiss law (C = 39.22 cm^3Kmol^{-1} and θ = -12.94 K).

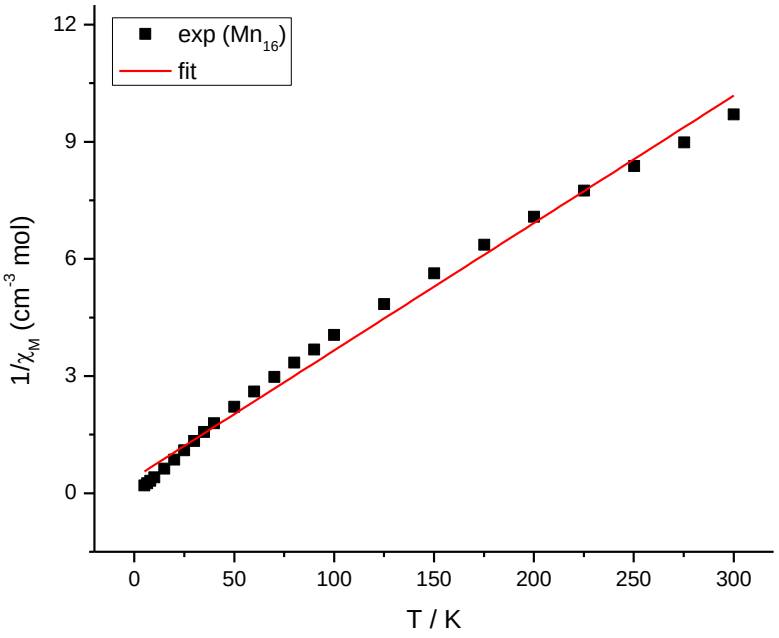

Figure 6.2. Plot of $1/\chi_M$ *vs.* *T* for complex **2**; the red thick line represents the fitting of the data to the Curie-Weiss law (C = 30.31 cm^3Kmol^{-1} and θ = -11.94 K).

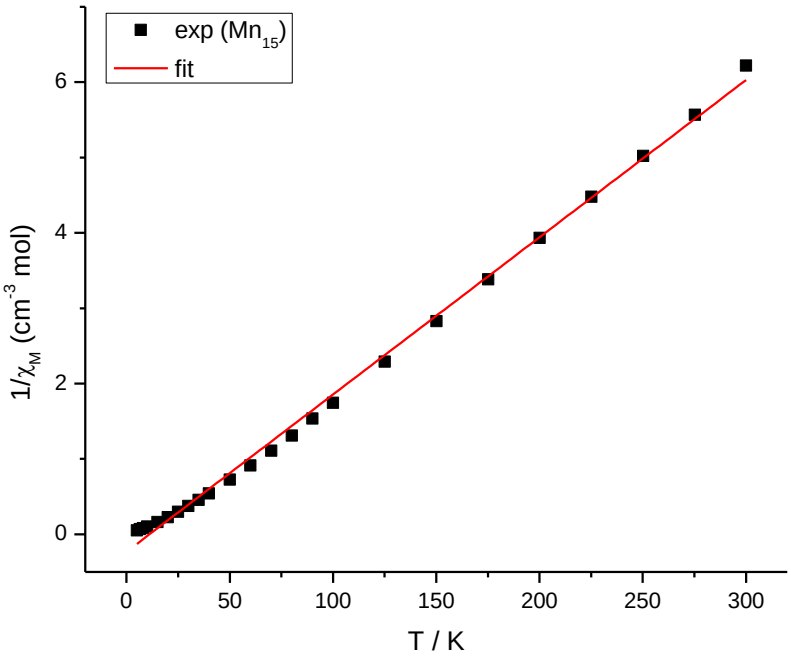

Figure 6.3. Plot of $1/\chi_M$ *vs. T* for complex **3**; the red thick line represents the fitting of the data to the Curie-Weiss law (C = 45.45 cm^3Kmol^{-1} and θ = +17.64 K).

References

1. Moore, G. E. *Electronics* **1965**, *38*, 114.

2. Feynman, R. P. *Eng. Sci.* **1960**, *23*, 22.

3. (*a*) Christou, G. *Polyhedron* **2005**, *24*, 2065. (*b*) Pringouri, K. V., MSc Thesis: New Synthetic Routes to High Nuclearity Manganese Carboxylate Clusters from the Employment of Pyrazole-Based Alkoxide Ligands; University of Florida: 2008.

4. Athanasopoulou, A. A., MSc Thesis: Polynuclear Ni(II) complexes with Schiff bases as bridging ligands: A molecular approach to nanoscience; Brock University: 2015.

5. Balzani, V.; Credi, A.; Raymo, F. M.; Stoddart, J. F. *Angew. Chem. Int. Ed.* **2000**, *39*, 3348.

6. de Silva, N.; Dahl, L. F. *Inorg. Chem*. **2005**, *44*, 9604.

7. (*a*) Badjic, J. D.; Balzani, V.; Credi, A.; Silvi, S.; Stoddart, J. F. *Science* **2004**, *303*, 1845. (*b*) Shirai, J.; Osgood, A. J.; Zhao, Y.; Kelly, K. F.; Tour, J. M. *Nano Lett.* **2005**, *5*, 2330.

8. Pardo, E.; Dul, M.- C.; Lescouëzec, R.; Chamoreau L.- M.; Journaux, Y.; Pasán, J.; Ruiz-Pérez, C.; Julve, M.; Lloret, F.; Ruiz-Garcíac, R.; Cano, J. *Dalton Trans.* **2010**, *39*, 4786.

9. Manolopoulou, E.; Stoumpos, C. C.; Siczek, M.; Lis, T.; Brechin, E. K.; Milios, C. J. *Eur. J. Inorg. Chem.* **2010**, 483.

10. (*a*) Stamatatos, Th. C.; Efthymiou, C. G.; Stoumpos, C. C.; Peplepes, S. P. *Eur. J. Inorg. Chem.* **2009**, 3361. (*b*) Pearson, R. G. *J. Chem. Educ.* **1968**, *45*, 581.

11. Cotton, F. A.; Walton, C. A.; Murillo, C. A. *Multiple Bonds Between Metal Atoms*, Springer- Verlag, New York , **2005**.

12. (*a*) Yoshizawa, M.; Tamura, M.; Fujita, M. *Science* **2006**, *312*, 251. (*b*) Sato, S.; Iida, J.; Suzuki, K.; Kawano, M.; Ozeki, T.; Fujita, M. *Science* **2006**, *313*, 1273.

13. (*a*) Whitehead, G. F. S.; Moro, F.; Timco, G. A.; Wernsdorfer, W.; Teat, S. J.; Winpenny, R. E. P. *Angew. Chem. Int. Ed.* **2013**, *12*5, 10116. (*b*) Murugesu, M.; Clérac, R.; Anson, C. E.; Powell, A. K. *Inorg. Chem.* **2004**, *43*, 7269. (*c*) Bi, Y.; Wang, X.- T.; Liao, W.; Wang, X.; Zhang, H.; Gao, S. *J. Am. Chem. Soc.* **2009**, *131*, 11650. (*d*) Liu, T.; Zhang, Y.- J.; Wang, Z.- M.; Gao, S. *J. Am. Chem. Soc.* **2008**, *130*, 10500. (*e*) Langley, S. K.; Scott, R. A.; Chilton, N. F; Moubaraki, B.; Murray, K. S. *Chem. Commun.* **2011**, *47*, 6281.

14. Liu, J. P.; Fullerton, E.; Gutfleisch, O.; Sellmyer, D. J. *Nanoscale Magnetic Materials and Applications*, Springer, **2009**.

15. Tasiopoulos, A. J.; Vinslava, A.; Wernsdorfer, W.; Abboud, K. A.; Christou, G. *Angew. Chem. Int. Ed.* **2004**, *43*, 2117.

16. Moushi, E. E.; Lampropoulos, C.; Wernsdorfer, W.; Nastopoulos, V.; Christou, C.; Tasiopoulos, A. J. *J. Am. Chem. Soc.* **2010**, *132*, 16146.

17. Manoli, M.; Inglis, R.; Manos, M. J., Nastopoulos, V.; Wernsdorfer, W.; Brechin, E. K., Tasiopoulos, A. J. *Angew. Chem. Int. Ed.* **2011**, *50*, 4441.

18. Peng, J.- B.; Kong, X.- J.; Zhang, Q.- C.; Orendáč, M.; Prokleška, J.; Ren, Y.-P.; Long, L.-S., Zheng, Z.; Zheng, L.-S. *J. Am. Chem. Soc.* **2014**, *136*, 17938.

19. Gu, X.; Xue, D. *Inorg. Chem.* **2007**, *46*, 3212.

20. (*a*) Winpenny, R. E. P. *Adv. Inorg. Chem.* **2001**, *52*, 1. (*b*) Winpenny, R. E. P. *J. Chem. Soc., Dalton Trans.* **2002**, 1.

21. Winpenny, R. E. P. in "*Transition Metals in Supramolecular Chemistry*", *Vol. 5*, (ed.: Sauvage, J. P.), Wiley, Chichester, **1999**, pp. 193-223.

22. (*a*) Brechin, E. K. *Chem. Commun.* **2005**, 5141. (*b*) Papaefstathiou, G. S.; Perlepes, S. P. *Comments Inorg. Chem.* **2002**, *23*, 249. (*c*) Stamatatos, Th. C.; Christou, G. *Inorg. Chem.* **2009**, *48*, 3308.

23. (*a*) Powell, A. K.; Heath, S. L.; Gatteschi, D.; Pardi, L.; Sessoli, R.; Spina, G.; Del Giallo, F.; Pieralli, F. *J. Am. Chem. Soc.* **1995**, *117*, 2491. (*b*) Goodwin, J. C.; Sessoli, R.; Gatteschi, D.; Wernsdorfer, W.; Powell, A. K.; Heath, S. L. *J. Chem. Soc., Dalton Trans.* **2000**, 1835.

24. (*a*) Heath, S. L.; Powell, A. K. *Angew. Chem., Int. Ed. Engl.* **1992**, *31*, 191. (*b*) Murugesu, M.; Clérac, R.; Anson, C. E.; Powell, A. K. *Chem. Commun.* **2004**, *43*, 1598.

25. Zheng, Z. *Chem. Commun.* **2001**, *17*, 2521.

26. (*a*) Baxter, P. N. W.; Lehn, J.- M.; Fisher, J.; Youinou, M.- T. *Angew. Chem. Int. Ed. Engl.* **1994**, *33*, 2284. (*b*) Lehn, J.- M. *Supramolecular Chemistry*; VCH Publishers: New York, **1995**.

27. (*a*) Fujita, M.; Umemoto, K.; Yoshizawa, M.; Fujita, N.; Kusukawa, T.; Biradha, K. *Chem. Commun.* **2001**, 509. (*b*) Fujita, M. *Chem. Soc. Rev.* **1998**, *27*, 417.

28. (*a*) Seidel, S. R.; Stang, P. J. *Acc. Chem. Res.* **2002**, *35*, 972. (*b*) Yuan, Q.- H.; Wan, L.- J.; Jude, H.; Stang, P. J. *J. Am. Chem. Soc.* **2005**, *127*, 16279. (*c*) Leininger, S.; Olenyuk, B.; Stang, P. J.; *Chem. Rev.* **2000**, *100*, 853.

29. Fielden, J; Cronin, L. in "*Encyclopedia of Supermolecular Chemistry*", Taylor & Francis, doi: 10.1081/E-ESMC-120024346, **2005**.

30. Winpenny, R. E. P. *Comprehensive Coordination Chemistry II, Vol. 7*, (Eds.: J. A. McCleverty, T. J. Meyer), Elsevier, Amsterdam, **2004**, pp. 125.

31. (*a*) Tasiopoulos, A. J.; Perlepes, S. P. *Dalton Trans.* **2008**, 5537. (*b*) Milios, C. J.; Piligkos, S.; Brechin, E. K. *Dalton Trans.* **2008**, 1809. (*c*) Milios, C. J.; Stamatatos, Th. C.; Perlepes, S. P. *Polyhedron* **2006**, *25*, 134.

32. (*a*) Maurer, J. A., PhD Thesis: I. Structure-Function Analysis of the Mechanosensitive Channel of Large Conductance. II. Design of Novel Magnetic Materials using Crystal Engineering; California Institute of Technology: 2003. (*b*) Emma, S., PhD Thesis: Novel Magnetic Materials Based on Macrocyclic Ligands: Towards High Relaxivity Contrast Agents and Mononuclear Single-Molecule Magnets; Brock University: 2015.

33. (*a*) For details, see: http://metamodern.com/2009/12/29/theres-plenty-of-room-at-the-bottom%E2%80%9D-feynman-1959/. (*b*) Chittipeddi, S.; Cromack, K. R.; Miller, J. S.; Epstein, A. J. *Phys. Rev. Let.* **1987**, *58*, 2695. (*c*) Christou, G.; Gatteschi, D.; Hendrickson, D. N.; Sessoli, R. *MRS Bull.* **2000**, *25*, 66. (*d*) Bircher, R.; Chaboussant, G.; Dobe, C.; Gudel, H. U.; Ochsenbein, S. T.; Sieber, A.; Waldman, O. *Adv. Funct. Mater.* **2006**, *16*, 209. (*e*) Murrie, M.; Price, D. J. *Annu. Rep. Prog. Chem., Sect. A* **2007**, *103*, 20.

34. (*a*) Leuenberger, M. N.; Loss, D. *Nature* **2001**, *410*, 789. (*b*) Ardavan, A.; Rival, O.; Morton, J. J. L.; Blundell, S. J.; Tyryshkin, A. M.; Timco, G. A.; Winpenny, R. E. P. *Phys. Rev. Lett.* **2007**, *98*, 057201.

35. For a tutorial review, see: Bagai, R.; Christou, G. *Chem. Soc. Rev.* **2009**, *38*, 1011.

36. Aromí, G.; Brechin, E. K. *Struct. Bonding* **2006**, *122*, 1.

37. Selected recent examples: (*a*) Qian, K.; Huang, X. C.; Zhou, C.; You, X. Z.; Wang, X. Y.; Dunbar, K. R. *J. Am. Chem. Soc.* **2013**, *135*, 13302. (*b*) Mukherjee, S.; Abboud, K. A.; Wernsdorfer, W.; Christou, G. *Inorg. Chem.* **2013**, *52*, 873. (c) Hoeke, V.; Gieb, K.; Müller, P.; Ungur, L.; Chibotaru, L. F.; Heidemeier, M.; Krickmeyer, E.; Stammler, A.; Bögge, H.; Schrö der, C.; Schnack, J.; Glaser, T. *Chem. Sci.* **2012**, *3*, 2868.

38. Gatteschi, D.; Sessoli, R. *Angew. Chem. Int. Ed.* **2003**, *42*, 268.

39. Stamatatos, Th. C.; Christou, G. *Phil. Trans. R. Soc. A* **2008**, *366*, 113.

40. Boca, R. *Coord. Chem. Rev.* **2004**, *248*, 757.

41. Sessoli, R.; Gatteschi, D.; Caneschi, A.; Novak, M. A. *Nature* **1993**, *365*, 141.

42. Milios, C. J.; Vinslava, A.; Wernsdorfer, W.; Moggach, S.; Parsons, S.; Perlepes, S. P.; Christou, G.; Brechin, E. K. *J. Am. Chem. Soc.* **2007**, *129*, 2754.

43. Ako, A. K.; Hewitt, I. J.; Mereacre, V.; Clerac, R.; Wernsdorfer, W.; Anson, C. E.; Powell, A. K. *Angew. Chem., Int. Ed.* **2006**, *45*, 4926.

44. Neese, F.; Pantazis, D. A. *Faraday Discuss.* **2011**, *148*, 229.

45. Nakano, M.; Oshio, H. *Chem. Soc. Rev.* **2011**, *40*, 3239.

46. (*a*) Rinehart, J. D.; Long, J. R. *Chem. Sci.* **2011**, *2*, 2078. (*b*) Sorace, L.; Benelli, C.; Gatteschi, D. *Chem. Soc. Rev.* **2011**, *40*, 3092. (*c*) Guo, Y. N.; Xu, G. F.; Guo, Y.; Tang, J. *Dalton Trans.* **2011**, *40*, 9953. (*d*) Sessoli, R.; Powell, A. K. *Coord. Chem. Rev.* **2009**, *253*, 2328. (*e*) Wang, B. W.; Jiang, S. D.; Wang, X. T.; Gao, S. *Sci. China*, *Ser. B: Chem.* **2009**, *52*, 1739. (*f*) Brooker, S.; Kitchen, J. A. *Dalton Trans.* **2009**, 7331.

47. Ishikawa, N.; Sugita, M.; Ishikawa, T.; Koshihara, S.; Kaizu, Y. *J. Am. Chem. Soc.* **2003**, *125*, 8694.

48. (*a*) Woodruff, D. N.; Winpenny, R. E. P.; Layfield, R. A. *Chem. Rev.* **2013**, *113*, 5110. (*b*) Layfield, R. A. *Organometallics* **2014**, *33*, 1084. (*c*) Zhang, P.; Zhang, L.; Tang, J. *Dalton Trans.* 2015, *44*, 3923.

49. Tang, J. K.; Hewitt, I.; Madhu, N. T.; Chastanet, G.; Wernsdorfer, W.; Anson, C. E.; Benelli, C.; Sessoli, R.; Powell, A. K. *Angew. Chem. Int. Ed.* **2006**, *45*, 1729.

50. Hewitt, I. J.; Tang, J. K.; Madhu, N. T.; Anson, C. E.; Lan, Y.; Luzon, J.; Etienne, M.; Sessoli, R.; Powell, A. K. *Angew. Chem. Int. Ed.* **2010**, *49*, 6352.

51. Luzon, J.; Sessoli, R. *Dalton Trans.* **2012**, *41*, 13556.

52. (*a*) Stokes, G. G. *Phil. Trans. R. Soc London* **1852**, *142*, 463. (*b*) Krasovickij, B. M.; Bolotin, B. M. *Org. Luminesc. Mater.*, VCH, Weinheim, **1988**.

53. Omary, M. A.; Patterson, H. H. "Electronic Spectroscopy: Luminescence Theory": *Encyclopedia of Spectroscopy & Spectrometry*, Academic Press, London, UK, **2000**, pp. 1186 1207.

54. (*a*) Nijegorodov, N; Luhanga, P. V. C.; Nkoma, J. S.; Winkoun, D. P. *Spectrochim. Acta A* **2006**, *64*, 1. (*b*) McClure, D. S. *J. Chem. Phys.* **1949**, *17*, 665. (*c*) McClure, D. S. *J. Chem. Phys.* **1949**, *17*, 905. (*d*) Lakowicz, J. R. *Principles of Fluorescence Spectroscopy*, Springer, New York, **2006**.

55. Visser, A. J. W; Rolinski O. J. in *Basic Photophysics on Photobiological Sciences Online* (K. C. Smith, ed.), American Society for Photobiology, http://www.photobiology.info/.

56. Valeur, B. *Molecular Fluorescence: Principles and Applications*, VCH, New York, **2001**.

57. Winnik F. M. *Chem. Rev.* **1993**, *93*, 587.

58. Voshinaga, T.; Hiratsuka, H.; Tanizaki, Y. *Bull. Chem. Soc. Jpn.***1977**, *12*, 3096.

59. Duhamel, J. *Langmuir* **2012**, *28*, 6527.

60. Bains, G. K.; Kim, S. H.; Sorin, E. J.; Narayanaswami, V. *Biochemistry* **2012**, *51*, 6207.

61. Filipescu, N.; Sager, W. F.; Serafin, F. A. *J. Phys. Chem.* **1964**, *68*, 3324.

62. (*a*) Petoud, S.; Bünzli, J.-C. G.; Glanzman, T.; Piguet, C.; Xiang, Q.; Thummel, R. P. *J. Lumin.* **1999**, *82*, 69. (*b*) Faustino, W. M.; Malta, O. L.; de Sa, G. F. *J. Chem. Phys.* **2005**, *122*, 054109. (*c*) Malta, O. L. *J. Lumin.* **1997**, *71*, 229. (*d*) D'Aleo, A.; Picot, A.; Beeby, A.; Williams, J. A. G.; Le Guennic, B.; Andraud, C.; Maury, O. *Inorg. Chem.* **2008**, *47*, 10258. (*e*) Fonger, W. H.; Struck, C. W. *J. Chem. Phys.* **1970**, *52*, 6364.

63. (*a*) Lazarides, T.; Sykes, D.; Faulkner, S.; Barbieri, A.; Ward, M. D. *Chem.-Eur. J.* **2008**, *14*, 9389. (*b*) Ward, M. D. *Coord. Chem. Rev.* **2007**, *251*, 1663. (*c*) Ronson, T. K.; Lazarides, T.; Adams, H.; Pope, S. J. A.; Sykes, D.; Faulkner, S.; Coles, S. J.; Hursthouse, M. B.; Clegg, W.; Harrington, R. W.; Ward, M. D. *Chem.-Eur. J.* **2005**, *12*, 9299. (*d*) Lazarides, T.; Adams, H.; Sykes, D.; Faulkner, S.; Calogero, G.; Ward, M. D. *Dalton Trans.* **2008**, 691. (*e*) Shavaleev, N. M.; Moorcraft, L. P.; Pope, S. J. A.; Bell, Z. R.; Faulkner, S.; Ward, M. D. *Chem. Commun.* **2003**, 1134. (*f*) Chen, F. F.; Bian, Z. Q.; Liu, Z. W.; Nie, D. B.; Chen, Z. Q.; Huang, C. H. *Inorg. Chem.* **2008**, *47*, 2507. (*g*) Imbert, D.; Cantuel, M.; Bünzli, J.-C. G.; Bernardinelli, G.; Piguet, C. *J. Am. Chem. Soc.* **2003**, *125*, 15698.

64. (*a*) Whan, R. E.; Crosby, G. A. *J. Mol. Spectrosc.* **1962**, *8*, 315. (*b*) Crosby, G. A.; Whan, R. E.; Alire, R. M. *J. Chem. Phys.* **1961**, *34*, 743. (*c*) Crosby, G. A.; Whan, R. E.; Freeman, J. J. *J. Phys. Chem.* **1962**, *66*, 2493.

65. Binnemans, K. *Chem. Rev.* **2009**, *109*, 4283.

66. (*a*) Sato, S.; Wada, M. Bull. *Chem. Soc. Jpn.* **1970**, *43*, 1955. (*b*) Latva, M.; Takalo, H.; Mukkala, V. M.; Matachescu, C.; Rodriguez-Ubis, J. C.; Kankare, J. *J. Lumin.* **1997**, *75*, 149. (*c*) Balzani, V.; Moggi, L.; Manfrin, M. F.; Bolletta, F. *Coord. Chem. Rev.* **1975**, *15*, 321. (*d*) Wilkinson, F. *Pure Appl. Chem.* **1975**, *41*, 661.

67. Miller, J. S. *Adv. Mater.* **1990**, *2*, 98.

68. (a) Gomez-Romero, P.; Sanchez, C. *Functional Hybrids Materials*; Wiley-VCH Verlag GmbH & Co. KGaA: Weinheim, Germany, **2004**, p 15-44. (b) Weigert, E. C.; South, J.; Rykov, S. A.; Chen, J. G. *Catal. Today* **2005**, *99*, 285. (c) Galán-Mascarós, J. R.; Coronado, E. *C. R. Chimie* **2008**, *11*, 1110. (d) Torquato, S.; Hyun, S.; Donev, A. *Phys. Rev. Lett.* **2002**, *89*, 266601.

69. (a) Maspoch, D.; Ruiz-Molina, D.; Veciana, J. *Chem. Soc. Rev.* **2007**, *36*, 770. (b) Gaspar, A. B.; Ksenofontov, V.; Seredyuk, M.; Guetlich, P. *Coord. Chem. Rev.* **2005**, *249*, 2661. (c) Coronado, R.; Galán-Mascarós, J. R.; Romero, F. *Functional Hybrids Materials*; Wiley-VCH Verlag GmbH & Co. KGaA: Weinheim, Germany, **2004**, p 317-346 and references therein.

70. Train, C.; Grusellec M.; Verdaguer M. *Chem. Soc. Rev.* **2011**, *40*, 3297.

71. (a) Coronado, E.; Day, P. *Chem. Rev.* **2004**, *104*, 5419. (b) Enoki, T.; Miyazaki, A. *Chem. Rev.* **2004**, *104*, 5449. (c) Ouahab, L. *Chem. Mater.* **1997**, *9*, 1909.

72. Kurmoo, M.; Graham, A. W.; Day, P.; Coles, S. J.; Hursthouse, M. B.; Caulfield, J. L.; Singleton, J.; Pratt, F. L.; Hayes, W.; Ducasse, L.; Guionneau, P. *J. Am. Chem. Soc.* **1995**, *117*, 12209.

73. Ojima, E.; Fujiwara, H.; Kato, K.; Kobayashi, H.; Tanaka, H.; Kobayashi, A.; Tokumoto, M.; Cassoux, P. *J. Am. Chem. Soc.* **1999**, *121*, 5581.

74. (a) Coronado, E.; Galán-Mascarós, J. R.; Gómez-Garcia, C. J.; Laukhin, V. *Nature* **2000**, *408*, 447. (b) Alberola, A.; Coronado, E.; Galán-Mascarós, J. R.; Giménez-Saiz, C.; Gómez-García, C. J. *J. Am. Chem. Soc.* **2003**, *125*, 10774.

75. Hiraga, H.; Miyasaka, H.; Nakata, K.; Kajiwara, T.; Takaishi, S.; Oshima, Y.; Nojiri, H.; Yamashita, M. *Inorg. Chem.* **2007**, *46*, 9661.

76. (a) Kulzer, F.; Orrit, M. *Annu. Rev. Phys. Chem.* **2004**, *55*, 585. (b) Moerner, W. E.; Kador, L. *Phys. Rev. Lett.* **1989**, *62*, 2535.

77. (a) Jo, M. H.; Grose, J. E.; Baheti, K.; Deshmukh, M. M.; Sokol, J. J.; Rumberger, E. M.; Hendrickson, D. N.; Long, J. R.; Park, H.; Ralph, D. C. *Nano Lett.* **2006**, *6*, 2014. (b) Ni, C.; Shah, S.; Hendrickson, D.; Bandaru, P. R. *Appl. Phys. Lett.* **2006**, *89*, 212104. (c) Bogani, L.; Wernsdorfer, W. *Nat. Mater.* **2008**, *7*, 179. (d) Coronado, E.; Martí-Gastaldo, C.; Tatay, S. *Appl. Surf. Sci.* **2007**, *254*, 225. (e) Abdi, A. N.; Bucher, J. P.; Rabu, P.; Toulemonde, O.; Drillon, M.; Gerbier, P. *J. Appl. Phys.* **2004**, *95*, 7345.

78. Beedle, C. C.; Stephenson, C. J.; Heroux, K. J.; Wernsdorfer, W.; Hendrickson, D. N. *Inorg. Chem.* **2008**, *47*, 10798.

79. Rikken, G. L. J. A.; Raupach, E. *Nature* **1997**, *390*, 493.

80. Liu, C.-M.; Xiong, R.-G.; Zang, D.-Q.; Zhu, D.-B. *J. Am. Chem. Soc.* **2010**, *132*, 4044.

81. (*a*) Williams, S. L.; Kirkpatrick, I.; Worrall, D. R. *Photochem. Photobiol. Sci.* **2010**, *9*, 937. (*b*) Feringa, B. L. *Molecular Switches* **2001**, Wiley-VCH. (*c*) Demchenko A. P. *Introduction to Fluorescence Sensing* **2009**, Springer.

82. (*a*) Escuer, A.; Aromi, G. *Eur. J. Inorg. Chem.* **2006**, *23*, 4721. (*b*) Escuer, A.; Esteban, J.; Perlepes, S. P.; Stamatatos, Th. C. *Coord. Chem. Rev.* **2014**, *275*, 87.

83. (*a*) Stamatatos, Th. C.; Abboud, K. A.; Wernsdorfer, W.; Christou, G. *Angew. Chem. Int. Ed.* **2007**, *46*, 884. (*b*) Boudalis, A. K.; Donnadieu, B.; Nastopoulos, V.; Clemente-Juan, J. Modesto; M., Alain; S., Yiannis; T., Jean-Pierre; Perlepes, S. P. *Angew. Chem. Int. Ed.* **2004**, *43*, 2266. (*c*) Stamatatos, Th. C.; Foguet-Albiol, D.; Lee, S.- C., Stoumpos, C. C.; Raptopoulou, C. P.; Terzis, A; Wernsdorfer, W.; Hill, S.; Perlepes, S. P.; Christou, G. *J. Am. Chem. Soc.* **2007**, *129*, 9484.

84. Gatteschi, D.; Sessoli, R.; Cornia, A. *Chem. Commun.* **2000**, *36*, 725.

85. Atanasov, M.; Zadrozny, J. M.; Long, J. R.; Neese F. *Chem. Sci.* **2013**, *4*, 139.

86. (*a*) Murrie, M. *Chem. Soc. Rev.* **2010**, *39*, 1986. (*b*) Craiq, G. A.; Murrie, M. *Chem. Soc. Rev.* **2015**, *44*, 2135.

87. Rorez, G.; Rebilly, J. N.; Barra, A. L.; Sorace, L.; Blondin, G.; Kirchner, N.; Duran, M.; van Slageren, J.; Parsons, S.; Richard, L.; Marvilliers, A.; Mallah, T. *Angew. Chem. Int. Ed.* **2005**, *44*, 1876.

88. Feltham, H. L. C.; Brooker, S. *Coord. Chem. Rev.* **2014**, *276*, 1.

89. (*a*) Habib, F.; Murugesu, M. *Chem. Soc. Rev.* **2013**, *42*, 3278. (*b*) Roy, L. E.; Hughbanks, T. *J. Am. Chem. Soc.* **2006**, *128*, 568.

90. Richardson, F. S. *Chem. Rev.* **1982**, *82*, 541.

91. Deng, Z.; Bai, F.; Xing, Y.; Xing, N; Xu, L. *Open J. Inorg. Chem.* **2013**, *3*, 76.

92. Bain, G. A.; Berry, J. F. *J. Chem. Educ.* **2008**, *85*, 532.

93. Wernsdorfer, W. *Adv. Chem. Phys.* **2001**, *118*, 99.

94. Glynn, C. W.; Turnbull, M. M. *Transition Met. Chem.* **2002**, *27*, 822.

95. *Oxford Diffraction, CrysAlis CCD and CrysAlis RED, version 1.171.32.15*; Oxford Diffraction Ltd: Abingdon, England, **2008**.

96. Sheldrick, G. M. in *SHELXS-97, Program for Crystal Structure Solution, University of Göttingen*, **1997**.

97. Sheldrick, G. M. *Acta Cryst. A* **2008**, *64*, 112.

98. Farrugia, L. I. *J. Appl. Crystallogr.* **1999**, *32*, 837.

99. Kottke, T.; Stalke, D. *J. App. Cryst.* **1993**, *26*, 615.

100. APEX2, *Data Collection Software Version 2.1-RC13, Bruker AXS, Delft, The Netherlands*, **2006**.

101. Cryopad, *Remote monitoring and control, Version 1.451, Oxford Cryosystems, Oxford, United Kingdom* **2006**.

102. SAINT+, *Data Integration Engine v. 7.23a* © **1997-2005**, Bruker AXS.

103. Sheldrick, G. M. in *SADABS v.2.01, Bruker/Siemens Area Detector Absorption Correction Program* **1998**, Bruker AXS.

104. Spek, A. L., *J. Appl. Crystallogr.* **2003**, *36*, 7.

105. Van der Sluis, P.; Spek, A. L. *Acta Crystallogr., Sect. A* **1990**, *A46*, 194.

106. Bruno, I. J.; Cole, J. C.; Edgington, P. R.; Kessler, M. K.; Macrae, C. F.; McCabe, P.; Pearson, J.; Taylor, R. *Acta Crystallogr.* **2002**, *B58*, 389.

107. Bradenburg K., *Release 3.1f, Crystal Impact GbR; Bonn*, Germany, **2008**.

108. Stamatatos, Th. C.; Foguet-Albiol, D.; Wernsdorfer, W.; Abboud, K.; Christou. G. *Chem. Commun.* **2011**, *47*, 274.

109. Scott, R. T. W.; Parsons, S.; Murugesu, M.; Wernsdorfer, W.; Christou, G.; Brechin, E. K. *Angew. Chem. Int. Ed.* **2005**, *44*, 6540.

110. Escuer, A.; Cordero, B.; Bardia, M. F.; Calvet, T.; Roubeau, O.; Teat, S. J.; Fedie, S.; Bianie, F. F. *Dalton Trans.* **2010**, *39*, 4817.

111. Khanra, S.; Weyhermuller, T.; Chaudhuri, P. *Dalton Trans.* **2008**, *37*, 4885.

112. For example, see: (*a*) Schmidt, S.; Prodius, D.; Novitchi, G.; Mereacre, V.; Kostakis, G. E.; Powell, A. K. *Chem. Commun.* **2012**, *48*, 9825. (*b*) Mereacre, V.; Prodius, D.; Lan, Y.; Turta, C.; Anson, C. E.; Powell, A. K. *Chem. Eur. J.* **2011**, *17*, 123. (*c*) Khan, M. I.; Tabussum, S.; Doedens, R. J.; Golub, V. O.; O'Connor, C. J. *Inorg. Chem. Commun.* 2004, *7*, 54. (*d*) Baniodeh, A.; Hewitt, I. J.; Mereacre, V.; Lan, Y.; Novitchi, G.; Anson, C. E.; Powell, A. K. *Dalton Trans.* 2011, *40*, 4080. (*e*) Wang, W.- G.; Zhou, A.- J.; Zhang, W.- X.; Tong, M.- L.; Chen, X.- M.; Nakano, M.; Beedle, C. C.; Hendrickson, D. N. *J. Am. Chem. Soc.* **2007**, *129*, 1014. (*f*) Jones, L. F.; Jensen, P.; Moubaraki, B.; Berry, K. J.; Boas, J. F.; Pilbrow, J. R.; Murray, K. S. *J. Mater. Chem.* 2006, *16*, 2690. (*g*) Langley, S. K.; Chilton, N. F.; Moubaraki, B.; Murray, K. S. *Dalton Trans.* 2011, *41*, 1033.

113. For example, see: (*a*) Biswas, B.; Khanra, S.; Weyhermüller, T.; Chaudhuri, P. *Chem. Commun.* **2007**, 1059. (*b*) Papatriantafyllopoulou, C.; Stamatatos, Th. C.; Wernsdorfer, W.; Teat, S. J.; Tasiopoulos, A. J.; Escuer, A.; Perlepes, S. P. *Inorg. Chem.* 2010, *49*, 10486.

114. (*a*) Liu, W.; Thorp, H. H. *Inorg. Chem.* **1993**, *32*, 4102. (*b*) Brown, I. D.; Altermatt, D. *Acta Crystallogr. Sect. B* **1985**, 244.

115. Addison, A. W.; Rao, T. N.; Reedijk, J.; Rijn, J.; Verschoor, G. C. *J. Chem. Soc., Dalton Trans.* **1984**, 1349.

116. Koumousi, E. S.; Routzomani, A.; Nguyen, T. N.; Giannopoulos, D. P.; Raptopoulou, C. P.; Psycharis, V.; Christou, G.; Stamatatos Th. C. *Inorg. Chem.* **2013**, *52*, 1176.

117. (*a*) Chakov, N. E.; Lee, S.– C.; Harter, A. G.; Kuhns, P. L.; Reyes, A. P.; Hill, S. O.; Dalal, N. S.; Wernsdorfer, W.; Abboud, K. A.; Christou, G. *J. Am. Chem. Soc.* **2006**, *128*, 6975. (*b*) Stamatatos, Th. C.; Abboud, K. A.; Wernsdorfer, W.; Christou, G. *Angew. Chem. Int. Ed.* **2008**, *47*, 6694. (*c*) Stamatatos, Th. C.; Luisi, B. S.; Moulton, B.; Christou, G. *Inorg. Chem.* **2008**, *47*, 1134.

118. Stamatatos, Th. C.; Abboud, K. A.; Christou, G. *J. Clust. Sci.* **2010**, *21*, 485.

119. Alexandropoulos, D. I.; Papatriantafyllopoulou, C.; Aromi, G.; Roubeau, O.; Teat, S. J.; Perlepes, S. P.; Christou, G.; Stamatatos, Th. C. *Inorg. Chem.* **2010**, *49*, 3962.

120. Wang, M.; Ma, C.; Wen, H.; Chen, C *Dalton Trans.* **2009**, 994.

121. John, R. P.; Park, M.; Moon, D.; Lee, K.; Hong, S.; Zou, Y.; Hong, C. H.; Lah, M. S. *J. Am. Chem. Soc.* **2007**, *129*, 14142.

122. Zheng, Y.- Z.; Xue, W.; Zhang, W.- X.; Tong, M.- L.; Chen, X.- M. *Inorg. Chem.* **2007**, *46*, 6437.

123. Moushi, E. E.; Masello, A.; Wernsdorfer, W.; Nastopoulos, V.; Christou, G.; Tasiopoulos, A. J. *Dalton Trans.* **2010**, *39*, 4978.

124. Mautner, F. A.; Fischer, R. C.; Salah El Fallah, M.; Speed, S.; Vicente, R. *Polyhedron* **2012**, *36*, 92.

125. Liu, J.- L.; Leng, J.- D.; Lin, Z.; Tong, M.- L. *Chem. Asian J.* **2011**, *6*, 1007.

126. Novak, M. A.; Sessoli, R. In *Quantum Tunnelling of Magnetization*, QTM'94, Gunther, L.; Barbar, B. Eds., Kluwer: Dordrecht, The Netherlands, **1995**, 171.

127. (*a*) Chakov, N. E.; Wernsdorfer, W.; Abboud, K. A.; Christou, G. *Inorg. Chem.* **2004**, *43*, 5919. (*b*) Mishra, A.; Tasiopoulos, A. J.; Wernsdorfer, W.; Abboud, K. A.; Christou, G. *Inorg. Chem.* **2007**, *46*, 3105.

128. (*a*) Friedman, J. R.; Sarachik, M. P.; Tejada, J.; Maciejewski, J.; Ziolo, R. *J. Appl. Phys.* **1996**, *79*, 6031. (*b*) Sangregorio, C.; Ohm, T.; Paulsen, C.; Sessoli, R.; Gatteschi, D. *Phys. Rev. Lett.* **1997**, *78*, 4645. (*c*) Brechin, E. K.; Soler, M.; Christou, G.; Helliwell, M.; Teat, S. J.; Wernsdorfer, W. *Chem. Commun*. **2003**, 1276.

129. Schager, F.; Goddart, R.; Seevogel, K.; Porschke, K.-R. *Organometallics* **1998**, *17*, 1546.

130. (*a*) Zhang, Y.- Z.; Wernsdorfer, W.; Pan, F.; Wang, Z. –M.; Gao, S. *Chem. Commun.* **2006**, 3302. (*b*) Zhou, Y.- L. ; Zeng, M.- H. ; Wei, L.- Q. ; Li, B.- W. ; Kurmoo, M. *Chem. Mater.* **2010**, *22*, 4295.

131. Brunet, G.; Habib, F.; Cook, C; Pathmalingam, T.; Loiseau, F.; Korobkov, I.; Burchell, T. J.; Beauchemin, A. M.; Murugesu, M. *Chem. Commun.* **2012**, *48*, 1287.

132. Zhang, Y.- Z.; Wernsdorfer, W.; Pan, F.; Wang, Z.- M.; Gao, S. *Chem. Commun.* **2006**, 3302.

133. Chilton, N. F.; Anderson, R. P.; Turner, L. D.; Soncini, A.; Murray, K. S. *J. Comput. Chem.* **2013**, *34*, 1164.

134. For a Co4 with an $\Delta E/k\mathrm{B}$ = 39 K, see: Wu, D.; Guo, D.; Song, Y.; Huang, W.; Duan, C.; Meng, Q.; Sato, O. *Inorg. Chem.* **2009**, *48*, 854.

135. (*a*) Wei, L.- Q.; Zhang, K.; Feng, Y.- C.; Wang, Y.- H.; Zeng, M.- H.; Kurmoo, M. *Inorg. Chem.* **2011**, *50*, 7274. (*b*) Meally, S. T. ; Karotsis, G.; Brechin, E. K.; Papaefstathiou, G. S.; Dunne, P. W.; McArdle, P.; Jones, L. F. *CrystEngComm* **2010**, *12*,

59. (*c*) Meally, S. T.; McDonald, C.; Karotsis, G.; Papaefstathiou, G. S.; Brechin, E. K.; Dunne, P. W.; McArdle, P.; Power, N. P.; Jones, L. F. *Dalton Trans.* **2010**, *39*, 4809.

136. (*a*) Zeng, Y.- F.; Hu, X.; Liu, F.- C.; Bu, X.- H. *Chem. Soc. Rev.* **2009**, *38*, 469. (*b*) Wang, X.- Y.; Wang, Z.- M.; Gao, S. *Chem. Commun.* **2008**, 281.

137. (*a*) Coronado, E.; Martí-Gastaldo, C.; Galán-Mascarós, J. R.; Cavallini, M. *J. Am. Chem. Soc.* **2010**, *132*, 5456. (*b*) Gao, E.- Q.; Liu, P.- P.; Wang, Y.- Q.; Yue, Q.; Wang, Q.- L. *Chem. Eur. J.* **2009**, *15*, 1217.

138. Stamatatos, Th. C.; Foguet-Albiol, D.; Stoumpos, C. C.; Raptopoulou, C. P.; Terzis, A.; Wernsdorfer, W.; Perlepes, S. P.; Christou, G. *J. Am. Chem. Soc.* **2005**, *127*, 15380.

139. (*a*) Boulon, M.- E.; Cucinotta, G.; Luzon, J.; Degl'Innocenti, G.; Perfetti, M.; Bernot, K.; Calvez, C.; Caneschi, A.; Sessoli, R. *Angew. Chem. Int. Ed*. **2013**, *52*, 350. (*b*) Cucinotta, G.; Perfetti, M.; Luzon, J.; Etienne, M.; Car, P.- E.; Caneschi, A.; Calvez, G.; Bernot, K.; Sessoli, R. *Angew. Chem. Int. Ed*. **2012**, *51*, 1606. (*c*) Pointillart, F.; Guennic, B. L.; Golhen, S.; Cador, O.; Maury, O.; Ouahab, L. *Chem. Commun.* **2013**, *49*, 615.

140. Fleischauer, P. D.; Fleischauer, P. *Chem. Rev.* **1970**, *70*, 199, and references cited therein.

141. (*a*) Eppley, H. J.; Tsai, H. L.; Devries, N.; Folting, K.; Christou, G.; Hendrickson, D. N. *J. Am. Chem. Soc.* **1995**, *117*, 301.

142. Chakov, N. E.; Lee, S.- C.; Harter, A. G.; Kuhns, P. L.; Reyes, A.; Hill, S. O.; Dalal, N. S.; Wernsdorfer, W.; Abboud, K.; Christou, G. *J. Am. Chem. Soc.* **2006**, *128*, 6975.

143. Schwarz, F. P.; Wasik, S. P. *Anal. Chem.* **1976**, *48*, 524-528.

144. Lever, A. B. P. *Inorganic Electronic Spectroscopy*; Elsevier: Amsterdam, 1997.

145. (a) Bagai, R.; Christou, G. *Inorg. Chem.* **2007**, *46*, 10810-10818. (b) Soler, M.; Wernsdorfer, W.; Abboud, K. A.; Huffman, J. C.; Davidson, E. R.; Hendrickson, D. N.; Christou, G. *J. Am. Chem. Soc*. **2003**, *125*, 3576.

146. Sessoli, R.; Tsai, H.- L.; Schake, A. R.; Wang, S.; Vincent, J. B.; Folting, K.; Gatteschi, D.; Christou, G.; Hendrickson, D. N. *J. Am. Chem. Soc.* **1993**, *115*, 1804.

147. (*a*) Katsenis, A. D.; Inglis, R; Prescimone, A; Brechin, E. K.; Papaefstathiou, G. S. *CrystEngComm* **2012**, *14*, 1216. (*b*) Inglis, R.; Taylor, S. M.; Jones, L. F.; Papaefstathiou, G. S.; Perlepes, S. P.; Datta, S.; Hill, S.; Wernsdorfer, W.; Brechin, E. K. *Dalton Trans.* **2009**, 9157.

148. (*a*) Schawrz, F. P.; Wasik, S. P. *Anal. Chem.* **1976**, *48*, 524. (*b*) Uchida, K.; Takahashi, Y. *Int. J. Quantum Chem.* **1980**, *18*, 301.

149. (*a*) Yang, P.- P.; Gao, X.- F.; Song, H.- B.; Zhang, S.; Mei, X.- L.; Li, L.- C.; Liao, D.- Z. *Inorg. Chem.* **2011**, *50*, 720-722. (*b*) Yang, P.- P. *Z. Anorg. Allg. Chem.* **2011**, *637*, 1234-1237.

150. Stamatatos, Th. C.; Christou, A. G.; Mukherjee, S.; Poole, K. M.; Lampropoulos, C.; Abboud, K. A.; O'Brien, T. A.; Christou, G. *Inorg. Chem.* **2008**, *47*, 9021.

151. Boudalis, A. K.; Dahan, F.; Bousseksou, A.; Tuchagues, J.- P.; Perlepes, S. P. *Dalton Trans.* **2003**, 3411.

152. Alvarez, S.; Alemany, P.; Casanova, D.; Cirera, J.; Llunell, M.; Avnir, D. *Coord. Chem. Rev.* **2005**, *249*, 1693.

153. Zabrodsky, H.; Peleg, S.; Avnir, D. *J. Am. Chem. Soc.* **1992**, *114*, 7843.

154. Ruiz-Martinez, A.; Casanova, D.; Alvarez, S. *Chem. Eur. J.* **2008**, *14*, 1291.

155. Llunell, M.; Casanova, D.; Girera, J.; Alemany, P.; Alvarez, S. *SHAPE*, version 2.0, Barcelona, Spain, **2010**.

156. (*a*) Guo, Y.-N.; Xu, G.-F.; Gamez, P.; Zhao, L.; Lin, S.-Y.; Deng, R; Tang, J.; Zhang, H.-J. *J. Am. Chem. Soc.* **2010**, *132*, 8538. (*b*) Yang, X.; Chan, C.; Lam, D.; Schipper, D.; Stanley, J. M.; Chen, X.; Jones, R. A.; Holiday, B. J.; Wong, W.-K.; Chen, S.; Chen, Q. *Dalton Trans.* **2012**, *41*, 11449. (*c*) Lin, S.-Y.; Zhao, L.; Ke, H.; Guo, Y.-N.; Tang, J.; Dou, J. *Dalton Trans.* **2012**, *41*, 3248. (*d*) Ke, H.; Xu, G.-F.; Guo, Y.-N.; Gamez, P.; Beavers, C. M.; Teat, S. J.; Tang, J. *Chem. Commun.* **2010**, *46*, 6057. (*e*) Yang, X.; Jones, R. A.; Wong, W.-K. *Chem. Commun.* **2008**, 3266.

157. (*a*) Franklin, S. J.; Raymond, K. N. *Inorg. Chem.* **1994**, *33*, 5794. (*b*) Miyashita, Y.; Sanada, M.; Islam, M. M.; Amir, N.; Koyano, T.; Ikeda, H.; Fujisawa, K.; Okamoto, K. *Inorg. Chem. Commun.* **2005**, *8*, 785. (*c*) Ronson, T. K.; Adams, H.; Harding, L. P.; Pope, S. J. A.; Sykes, D.; Faulkner, S.; Ward, M. D. *Dalton Trans.* **2007**, 1006. (*d*) Boyle, T. J.; Ottley L. A. M.; Daniel-Taylor, S. D.; Tribby, L. J.; Bunge S. D.; Costello, A. L.; Alam, T. M.; Gordon, J. C.; McCleskey, T. M. *Inorg. Chem.* **2007**, *46*, 3705. (*e*) Regueiro-Figueroa, M.; Esteban-Gomez, D.; de Blas, A.; Rodriguez-Blas, T.; Platas-Iglesias, C. *Eur. J. Inorg. Chem.* **2010**, 3586.

158. For representative references, see: (*a*) Xue, S.; Zhao, L.; Guo, Y.-N.; Tang, J. *Dalton Trans.* **2012**, *41*, 351. (*b*) Coles, M. P.; Hitchcock P. B.; Khvostov, A. V.; Lappert, M. F.; Li, Z.; Protchenko, A. V. *Dalton Trans.* **2010**, *39*, 6780. (*c*) Bi, Y.; Wang, X.-T.; Liao, W.; Wang, X.; Deng, R.; Zhang, H.; Gao, S. *Inorg. Chem.* **2009**, *48*, 11743. (*d*) Bilyk, A.; Dunlop, J. W.; Fuller, R. O.; Hall, A. K.; Harrowfield, J. M., Hosseini, M. W.; Koutsantonis, G. A.; Murray, I. W.; Skelton, B. W.; Sobolev, A. N.; Stamps, R. L.;

White, A. H. *Eur. J. Inorg. Chem.* **2010**, 2127. (*e*) Anwar, M. U.; Thompson, L. K.; Dave, L. N.; Habib, F.; Murugesu, M. *Chem. Commun.* **2012**, *48*, 4576. (*f*) Randell, N. M.; Anwar, M. U.; Drover, M. W.; Dawe, L. N.; Thompson, L. K. *Inorg. Chem.* **2013**, *52*, 6731.

159. (*a*) Guo, P.-H.; Lui, J.-L.; Zhang, Z.-M.; Ungur, L.; Chibotaru, L. F.; Leng, J.-D.; Guo, F.-S.; Tong, M.-L. *Inorg. Chem.* **2012**, *51*, 1233. (*b*) Thompson, M. K.; Lough, A. J.; White, A. J. P.; Williams, D. J.; Kahwa, I. A. *Inorg. Chem.* **2003**, *42*, 4828. (*c*) Yan, P.-F.; Lin, P.-H.; Habib, F; Aharen, T.; Murugesu, M.; Deng, Z.-P.; Li, G.-M.; Sun, W.-B. *Inorg. Chem.* **2011**, *50*, 7059. (*d*) Abbas, G.; Lan, Y.; Kostakis, G. E.; Wernsdorfer, W.; Anson, C. E.; Powell, A. K. *Inorg. Chem.* **2010**, *49*, 8067. (*e*) Xue, S.; Zhao, L.; Guo, Y.-N.; Deng, R.; Guo, Y.; Tang, J. *Dalton Trans*. **2011**, *40*, 8347. (*f*) Zheng, Y.-Z.; Lan, Y.; Anson, C. E.; Powell, A. K. *Inorg. Chem.* **2008**, *47*, 10813. (*g*) Langley, S. K.; Chilton, N. F.; Gass, I. A.; Moubaraki, B.; Murray, K. S. *Dalton Trans.* **2011**, *40*, 12656. (h) Lin, P.-H.; Burchell, T. J.; Ungur, L.; Chibotaru, L. F., Wernsdorfer, W.; Murugesu, M. *Angew. Chem., Int. Ed.* **2009**, *48*, 9489. (*i*) Andrews, P. C.; Deacon, G. B.; Gee, W. J.; Junk, P. C.; Urbatsch, A. *Eur. J. Inorg. Chem.* **2012**, 3273. (*j*) Chandrasekhar, V.; Hossain, S.; Biswas, S.; Sutter, J.- P. *Inorg. Chem.* **2013**, *52*, 6346.

160. For recent literature on discrete Ln cubanes, see: (*a*) Gao, Y.; Xu, G.-F.; Zhao, L.; Tang, J.; Liu, Z. *Inorg. Chem.* **2009**, *48*, 11495. (*b*) Ke, H.; Gamez, P.; Zhao, L.; Xu, G.-F.; Xue, S.; Tang J. *Inorg. Chem.* **2010**, *49*, 7549. (*c*) Liu, C.-M.; Zhang, D.-Q.; Hao, X.; Zhu, D.-B. *Cryst. Growth Des.* **2012**, *12*, 2948. (*d*) Gerasko, O. A.; Mainicheva, E. A.; Naumova, M. I.; Yurjeva, O. P.; Antonio, A.; Vincent, C.; Llusar, R.; Fedin, V. P. *Eur. J.*

Inorg. Chem. **2008**, 416. (*e*) Kong, X.-J.; Long, L.-S.; Zheng, L.-S.; Wang, R.; Zheng, Z. *Inorg. Chem.* **2009**, *48*, 3268.

161. (*a*) Guo, F.-S.; Leng, J.-D.; Lui, J.-L.; Meng, Z.-S.; Tong, M.-L. *Inorg. Chem.* **2012**, *51*, 405. (*b*) Bretonniere, Y.; Mazzanti, M.; Pecaut, J.; Bunand, F. A.; Merbach, A. E. *Inorg. Chem.* **2001**, *40*, 6737. (*c*) Du, Z.; Zhang, Y.; Yao, Y.; Shen, Q. *Dalton Trans.* **2011**, *40*, 7639. (*d*) Chandrasekhar, V.; Das, S.; Dey, A.; Hossain, S.; Sutter, J.- P. *Inorg. Chem.* **2013**, *52*, 11956.

162. (*a*) Koo, B. H.; Lim, K. S.; Ryu, D. W.; Lee, W. R.; Koh, E. K.; Hong, C. S. *Chem. Commun.* **2012**, *48*, 2519. (*b*) Carretas, J.; Branco, J.; Marcalo, J.; Isolani, P.; Domingos A.; de Matos, A. P. *J. Alloys and Compounds* **2001**, *323-324*, 169. (*c*) Chen, Y.- H.; Tsai, Y.- F.; Lee, G.- H.; Yang, E.- C. *J. Solid State Chem.* **2012**, *185*, 166. (*d*) Yang, P.- P.; Gao, X.- F.; Song, H.- B.; Zhang, S.; Mei, X.- L.; Li, L.- C.; Liao, D.- Z. *Inorg. Chem.* **2011**, *50*, 720. (*e*) Yang, P.- P. *Z. Anorg. Allg. Chem.* **2011**, *637*, 1234.

163. George G. A.; Morris G. C., *J. Mol. Spectr.* **1968**, *26*, 67.

164. Moll H.; Glorius M.; Barkleit A.; Robberg A., Bernhard G., Wiss.-Tech Ber., **2009**, *552*,17.

165. (*a*) Kaljurand, I.; Rodima, T.; Leito, I.; Koppel, I. A.; Schwesinger, R. *J. Org. Chem.*, **2000**, *65*, 6202. (*b*) Lorentzo, J.; Fülscher, M. P.; Roos, B.O. *Theor. Chim. Acta*, **1995**, *92*, 67. (*c*) Komy, Z. R.; Abu-Gharib, E. A.; Desoky, A. *American J. Applied Sci.*, **2005**, 2(*4*), 847.

166. Bartolomé, J.; Filoti, G.; Kuncser, V.; Schinteie, G.; Mereacre, V.; Anson, C. E.; Powell, A. K.; Prodius, D.; Turta, C. *Phys. Rev. B* **2009**, *80*, 014430.

167. (*a*) Kahn, O. *Molecular Magnetism*; VCH Publishers: New York, **1993**. (*b*) Benelli, C.; Gatteschi, D. *Chem. Rev.* **2002**, *102*, 2369.

168. MAGMUN4.1. and MAGMUN4.1/OW01.exe are available free of charge from the authors (http://www.ucs.mun.ca/~lthomp/magmun.html).

169. Brockman, J. T.; Stamatatos Th. C.; Wernsdorfer, W.; Abboud, K. A.; Christou, G. *Inorg. Chem.* **2007**, *46*, 9160

170. (*a*) Lehn, J.- M. *Angew. Chem. Int. Ed.* **1990**, *29*, 1304-1319. (*b*) Binnemans, K. *Chem. Rev.* **2009**, *109*, 4283-4374. (*c*) Bekiari, V.; Lianos, P. *Adv. Mater.* **2000**, *12*, 1603.

171. Alexandropoulos, D. I.; Mowson, A. M.; Pilkington, M.; Bekiari, V.; Christou, G.; Stamatatos, Th. C. *Dalton Trans.* **2014**, *43*, 1965.

172. Katsoulakou, E.; Dermitzaki, D.; Konidaris, K. F.; Moushi, E. E.; Raptopoulou, C. P.; Psycharis, V.; Tasiopoulos, A. J.; Bekiari, V.; Manessi-Zoupa, E.; Perlepes, S. P.; Stamatatos, Th. C *Polyhedron* **2013**, *52*, 467.

173. (*a*) Canaj, A. B.; Tzimopoulos, D. I.; Philippidis, A.; Kostakis, G. E.; Milios, C. J. *Inorg. Chem.* **2012**, *51*, 7451-7453. (*b*) Alexandropoulos, D. I.; Mukherjee, S.; Papatriantafyllopoulou, C.; Raptopoulou, C. P.; Psycharis, V.; Bekiari, V.; Christou, G.; Stamatatos, Th. C. *Inorg. Chem.* **2011**, *50*, 11276-11278. (*c*) Menelaou, M.; Ouharrou, F.; Rodríguez, L.; Roubeau, O.; Teat, S. J.; Aliaga-Alcalde, N. *Chem. Eur. J.* **2012**, *18*, 11545-11549. (*d*) Yamashita, K.; Miyazaki, R.; Kataoka, Y.; Nakanishi, T.; Hasegawa, Y.; Nakano, M.; Yamamura, T.; Kajiwara, T. *Dalton Trans.* **2013**, *42*, 1987-1990. (*e*) Burrow, C. E.; Burchell, T. J.; Lin, P.- H.; Habib, F.; Wernsdorfer, W.; Clérac, R.; Murugesu, M. *Inorg. Chem.* **2009**, *48*, 8051-8053.

174. Dermitzaki, D.; Lorusso, G.; Raptopoulou, C. P.; Psycharis, V.; Escuer, A.; Evangelisti, M.; Perlepes, S. P.; Stamatatos, Th. C. *Inorg. Chem.* **2013**, *52*, 10235.

175. (*a*) Magennis, S. W.; Parsons, S.; Pikramenou, Z. *Chem. Eur. J.* **2003**, *8*, 5761. (*b*) Mancino, G.; Ferguson, A. J.; Beeby, A.; Long, N. J.; Jones, T. S. *J. Am. Chem. Soc.* **2005**, *127*, 524.